Digital hologram processing methods and its applications in particle imaging

A

Thesis submitted

for the award of the degree of

DOCTOR OF PHILOSOPHY

By

Anik Ghosh

DEPARTMENT OF ELECTRONICS AND ELECTRICAL ENGINEERING

INDIAN INSTITUTE OF TECHNOLOGY GUWAHATI

GUWAHATI - 781 039, ASSAM, INDIA

JUNE 2023

Certificate

This is to certify that the thesis titled "**Digital hologram processing methods and its applications in particle imaging**", submitted by **ANIK GHOSH** (186102102), a research scholar in the *Department of Electronics and Electrical Engineering, Indian Institute of Technology Guwahati*, for the award of the degree of **Doctor of Philosophy**, is a record of an original research work carried out by him under my supervision and guidance. The thesis has fulfilled all requirements as per the regulations of the institute and in my opinion has reached the standard needed for submission. The results embodied in this thesis have not been submitted to any other University or Institute for the award of any degree or diploma.

Dated: 24-06-2023

Guwahati.

Dr. Rishikesh D. Kulkarni

Assistant Professor

Dept. of Electronics and Electrical Engineering

Indian Institute of Technology Guwahati

Guwahati - 781 039, Assam, India.

To

My father

Late Nirmal Ghosh

Acknowledgements

This thesis would not have been possible without the immense help and support of several people in various measures. I would like to convey my acknowledgment to all of them. First and foremost,I express my deepest gratitude and sincere regards to my advisor, Dr. Rishikesh D. Kulkarni (Assistant Professor at the Department of Electronics and Electrical Engineering in Indian Intsitute of technology, Guwahati), who has given his continuous and persuasive support in my Ph.D. study and research with his patience, enthusiasm, motivation and immense experience. His guidance helped me throughout the research and writing of this thesis and made this a thoughtful and rewarding journey. I have been amazingly fortunate to have an advisor who gave me the freedom to explore on my own and at the same time the guidance to recover when my steps faltered. Prof. Kulkarni taught me how to question thoughts and express ideas. I would like to thank him for encouraging my research and for allowing me to grow as a research scientist along with his thorough review. His insightful comments and constructive criticisms at different stages of my research were thought-provoking and they helped me focus and sharpen my ideas. His patience and support helped me overcome many crisis situations and finish this dissertation. I would also like to thank him for providing a laboratory environemnt to gain hand-on experiance and financial support for conference. I am also thankful to him for encouraging the use of correct grammar and consistent notation in my writings and for carefully reading and commenting on countless revisions of this dissertation. I could not have imagined having a better advisor and mentor for my Ph.D. study. Without his supervision and constant help this dissertation would not have been possible.

Besides my advisor, I would like to thank all the members of the my doctral committee, Indian Institute of Technology Guwahati, Prof. Rohit Sinha, Dr. Prithwijit guha, Dr. Pranab Kumar Mondal, for their encouragement, valuable suggestions and feedback on my work. I would like to thank Prof. Sreedeep Sekharan (Professor at the Department of Civil Engineering in Indian Intsitute of technology, Guwahati) and Dr. Pranab Kumar Mondal (Associate Professor at the Department of Mechanical Engineering in Indian Intsitute of technology, Guwahati) for their constant help and laboratory support durig my thesis work. I am also thankful to Dr. Rajshekhar Gannavarpu (Associate Professor at the Department of Electrical Engineering in Indian Intsitute of technology, Kanpur) for providing their experimental data. I would like to thank faculty members and the office staffs of the Department of Electronics and Electrical Engineering, IIT Guwahati, for their help in carrying out this research work.

I am grateful for colleagues from the Signal Processing Laboratory (Department of Electronics and Electrical Engineering), Signal Informatics Laboratory (Department of Electronics and Electrical Engi-

neering), Image processing and computer Vision Laboratory (Department of Electronics and Electrical Engineering), Microfluidics Laboratory (Department of Mechanical Engineering), Geotechinal Laboratory (Department of Civil Engineering).

Most importantly, none of this would have been possible without the love and patience of my family. My father late Nirmal Ghosh to whom this dissertation is dedicated, had been a constant source of love, concern, support and strength from my birth till the time of his unfortunate demise; however his ideas, love and spirit had strong enough power and influence to motivate me throughout all these years of my study. I would like to express my heart-felt gratitude to my mother Mrs. Sulata Ghosh who have aided and encouraged me throughout this endeavor and always supported me in both good times and bad. I am thankful to my wife, Mrs. Pamela Saha Mondal (pursuing Ph. D. in Indian Institute of Technology, Kharagpur) for her sacrifice and support throughout my entire Ph. D. study. I also express my gratitude to my elder brother Dr. Abhik Ghosh (Associate Professor, Indian statistical Institute) his support and enthusiasm.

Above all, I thank God for all His blessings !

Anik Ghosh

Abstract

Digital holography is a three-dimensional imaging technique, which involves digital recording of a hologram as the intensity of interference pattern of an object scattered light and a reference light. The complex light field at the object plane is retrieved by numerical reconstruction of the hologram. As a result, digital holography provides both amplitude and quantitative phase imaging which is one of its unique features. Especially, digital in-line holographic microscopy (DIHM) has found its way in microscopic imaging applications and microfluidic studies due to its unique features and cost effectiveness. DIHM has found numerous applications in particle imaging due to its three-dimensional particle localization capability, compact and cost-effective experimental setup. The particle objects placed at any given distance between source to camera can be detected in reconstructed images numerically. In general, the reconstructed images in digital in-line holography suffers from twin image effect and background noise. This affect the particle detection and its size estimation accuracy. The improvement of reconstructed image quality can result in improved particle detection accuracy. Conventional reconstruction method takes high computation time for the accurate particle localization as the hologram reconstruction is required to be performed at different planes within the measurement. This problem can be overcome with a computationally efficient reconstruction algorithm. Accurate detection of object focal plane is of crucial importance in digital holography as it offers numerical autofocusing capability. In that context, establishing an appropriate autofocusing criteria is essential. Thus, taking these observations into consideration, a number of digital hologram processing algorithms are reported in the thesis. Novel hologram reconstruction algorithms are developed which provide computational efficiency without compromising the reconstruction quality. In the case of quantitative phase imaging, an important problem of phase unwrapping is addressed by developing an quality-guided, computationally efficient phase unwrapping algorithm. The thesis proposes different autofocusing algorithm for accurate detection of focal plane of amplitude, phase and mixed type objects. The performance of all these algorithms were evaluated and compared with state-of-art method with different simulation examples. Furthermore, practical validation of the algorithms were performed with experimental data. A comprehensive study on the particle size distribution of fly ash samples is also reported. We believe that the proposed hologram processing methods can be important additions in the field of digital holography.

Contents

List of Figures

List of Tables

List of Acronyms

2D	Two dimension
3D	Three dimension
AF	Autofocusing
AMS	Autofocusing algorithm based on amplitude measure
AR	Autoregressive
BC	Bicubic
BFA	Badarpur fly ash
BFS	Breadth-first-search
BIPEPI	Bicubic interpolation and extrapolation iteration
BL	Bilinear
CCD	Charged coupled device
CEC	Cation exchange area
CFB	circulating fluidized bed
CMOS	Complementary metal oxide semiconductor
Conv.	Conventional
CT	Computed tomography
DFS	Autofocusing algorithm based on dark focusing
DH	Digital holography
DHM	Digital holograpic microscopy
DIH	Digital in-line holography
DIHM	Digital in-line holograpic microscopy
EIG	Autofocusing algorithm based on eigenvalues
FastPU	Fast phase unwrapping
FESEM	Field emission scanning electron micrscope
FFA	Farakka fly ash

FFT	Fast fourier transform
FrT	Fresnel transform
GPU	Graphics Processing unit
GRA	Autofocusing algorithm based on gradient
HR	High Resolution
IPI	Interferometric particle imaging
ITR	Autofocusing based on iterative algorithm
LR	Low Resolution
LZ	Lanczos
MLE	Maximum likelihood estimation
NCC	Normalized cross-correlation
NFA	Neyveli fly ash
NI	Nin-interpolated
NN	Nearest neighbour
PA	Pond ash
PF	Parcentage finer
PSD	Particle size distribution
PSF	Point spread function
PSNR	Peak Signal to Noise ratio
PSO	Particle swarm optimization
PUMA	Maximum Flow
PVE	Peak-to-Valley error
QI	Quality index
QPI	Quantitative phase unwrapping
RBC	Red blood cell
RMSE	Root mean square error
SEN	Autofocusing algorithm based on self entropy
SLM	Spatial light modulator
SNR	Signal to Noise ratio
SPA	Autofocusing algorithm based on sparsity
SSA	Specific surface area
SSIM	Structural Similarity

TOW	Autofocusing algorithm based on distribution of eigenvalues
TMD	Toeplitz matrix based deconvolution
VAR	Autofocusing algorithm based on variance
XRD	X-ray diffraction

भारतीय प्रौद्योगिकी संस्थान गुवाहाटी
Indian Institute of Technology Guwahati

Part I

Background

भारतीय प्रौद्योगिकी संस्थान गुवाहाटी
Indian Institute of Technology Guwahati

1

Introduction

1.1 Digital holography

Holography involves recording of light field scattered from an object surface and its reconstruction in a manner that appears to reproduce a three-dimensional (3D) image of the object. The idea of holography was first developed by Dennis Gabor in 1940s, while working on improving the resolving power of electron microscope. In absence of a coherent light source, the applications of holography were limited. However, with the advent of laser source in 1960's, hologram recording and reconstruction could become possible. The conventional holography typically involves recording of a hologram on a photographic film as an intensity of interference pattern generated by a reference light and the light scattered from an object surface. The photographic film upon development produces 3D image of the object when illuminated with the reference light beam. This process of optical recording and optical reconstruction of hologram was found to be cumbersome for practical applications mainly due to the involvement of photographic film development and stringent requirement of optical setup stability. The arrival of CCD and CMOS image sensors allowed for the digital recording of holograms. This resulted in faster and easier hologram recording from the perspective of practical applications. However, the digital recording of hologram necessitates numerical reconstruction of scattered light field associated with the object instead of optical reconstruction as performed in classical holography. The digital holography on account of its advantages over conventional holography has found applications in various engineering domains such as biomedical,

[1] A brief introduction to basic principles of digital holography is provided in this chapter.

chemical, civil, mechanical, particle physics, etc. Especially, digital holographic microscopy (DHM) has found its way in microscopic imaging applications and microfluidic studies due to its unique features and cost effectiveness.

Digital holography involves two main operations: optical recording of digital hologram and numerical reconstruction of recorded hologram. In the optical recording process, the light scattered from the object surface or diffracted through it, interferes with a reference light beam at the hologram recording plane, i.e., charge couple device (CCD)/complementary metal oxide semiconductor(CMOS) image sensor plane. It is important to note that the object illuminating beam and the reference beam are derived from the same coherent light source. The intensity of resulting interference pattern is recorded by the image sensor. This intensity pattern is called as *hologram*. The information on amplitude and phase of object beam is recorded in the form of intensity variations of the hologram. In the process of numerical reconstruction, the hologram is multiplied with the simulated reference beam which is as close as possible to the actual reference beam used during the hologram recording. This multiplication simulates the process of diffraction and provides the diffracted light beam at the hologram plane. Subsequently, this light is propagated to object plane to obtain the object field distribution [1, 2, 3, 4].

The recent advancements in electronic devices such as spatial light modulators (SLM), image sensors and computers have helped holography to improve its resolution power. SLMs with high pixel density helps 3D image reconstruction with higher resolution and quality on a holographic display [5, 6]. Lens-less holography can be performed using lens-free image sensor, which have high pixel density. High performance computers then help to reconstruct a digitally recorded hologram numerically to produce high throughput 3D image [7, 8] as well as additional quantitative phase images [9]. Digital holography [10, 11, 12, 13, 14] has several potential applications in various fields covering microscopy [15, 16, 12, 17, 18, 19, 20, 21, 22], particles and flow measurement in 3D space [23], quantitative phase imaging (QPI) [12, 21, 24], 3D object recognition [25], 3D surface shape measurements [26], 3D image encryption [27], ultra-fast 3D optical imaging with ultrashort pulsed laser [28], holographic 3D imaging with single photo detector [29, 30], 3D tomography of amplitude and phase distributions [31], particle tracking in microfluidics [32, 33, 34, 35, 36, 17, 37, 38, 39, 40, 41, 42], space biotechnology [32] and many others.

1.1.1 Holographic configurations

Two basic optical configurations commonly used in digital holography are Gabor in-line holography (DIH) and off-axis holography, as shown in Figs. 1.1(a) and 1.1(b), respectively. The output of the laser

source (LS) is filtered using the spatial light filter (SF) module and collimated using a lens (C). The laser beam width can be expanded using a beam-expander (BE). Whereas in Gabor in-line holography, the object (OB) scattered and unscattered light acts as reference and object beam, respectively, these beams are separately generated using a beamsplitter (BS) and later combined in off-axis configuration. Figure 1.1(b) represents an off-axis holography set-up, where laser light is divided into two parts with a beam splitter (BS). One part (black solid line in Fig. 1.1(b)) illuminates the object and another part (red dashed line in Fig. 1.1(b)) acts as the reference beam. Object scattered beam and reference beam are magnified with two microscopic objectives (MO). The intensity of the interference pattern generated by these beams is recorded as the hologram by camera sensor. The angle θ between object and reference beams in the off-axis setup introduces spatial carrier fringe pattern in the recorded hologram. It can be noted that this angle is zero for the in-line configuration [43]. Digital Gabor in-line holography configuration is most commonly used for particle imaging due to object sparsity and easy experimental set-up [44]. Figures 1.1(c) and 1.1(d) represent schematics of lensless in-line holography setup with plane and spherical wave illumination, respectively. In digital lensless in-line holography setup with spherical wave illumination,the point source is placed at z_1 distance from the object plane. The object scattered beam and reference beam propagate further to the hologram recording sensor plane at a distance z_2.

1.2 Digital off-axis holographic microscopy

The off-axis configuration in DHM has found numerous applications in quantitative phase imaging. Especially , it has been shown to be powerful technique for the analysis of biological cells. Digital holographic microscopy is found to provide similar to the electron microscope at high frame rates. DHM has ability to track particles with their rotations in 3D with high spatial resolution [15, 16, 12, 17, 45, 19, 20, 21, 22, 46]. Least/no sample preparation, numerical autofocusing, simultaneous amplitude and phase imaging are some of the unique features offered by DHM [47]. The carrier fringes introduced by the angle between the object and reference beams allows for the separation of the twin images in the spatial frequency plane of the hologram. Off-axis holographic microscopy has been used to achieve variable magnification [48] and in various live cell applications and technical inspections [49]. The need of a separate reference beam makes off-axis configuration slightly more complicated in comparison to in-line. In addition, the experimental stability requirement is more stringent in the case of off-axis compared to in-line configuration.

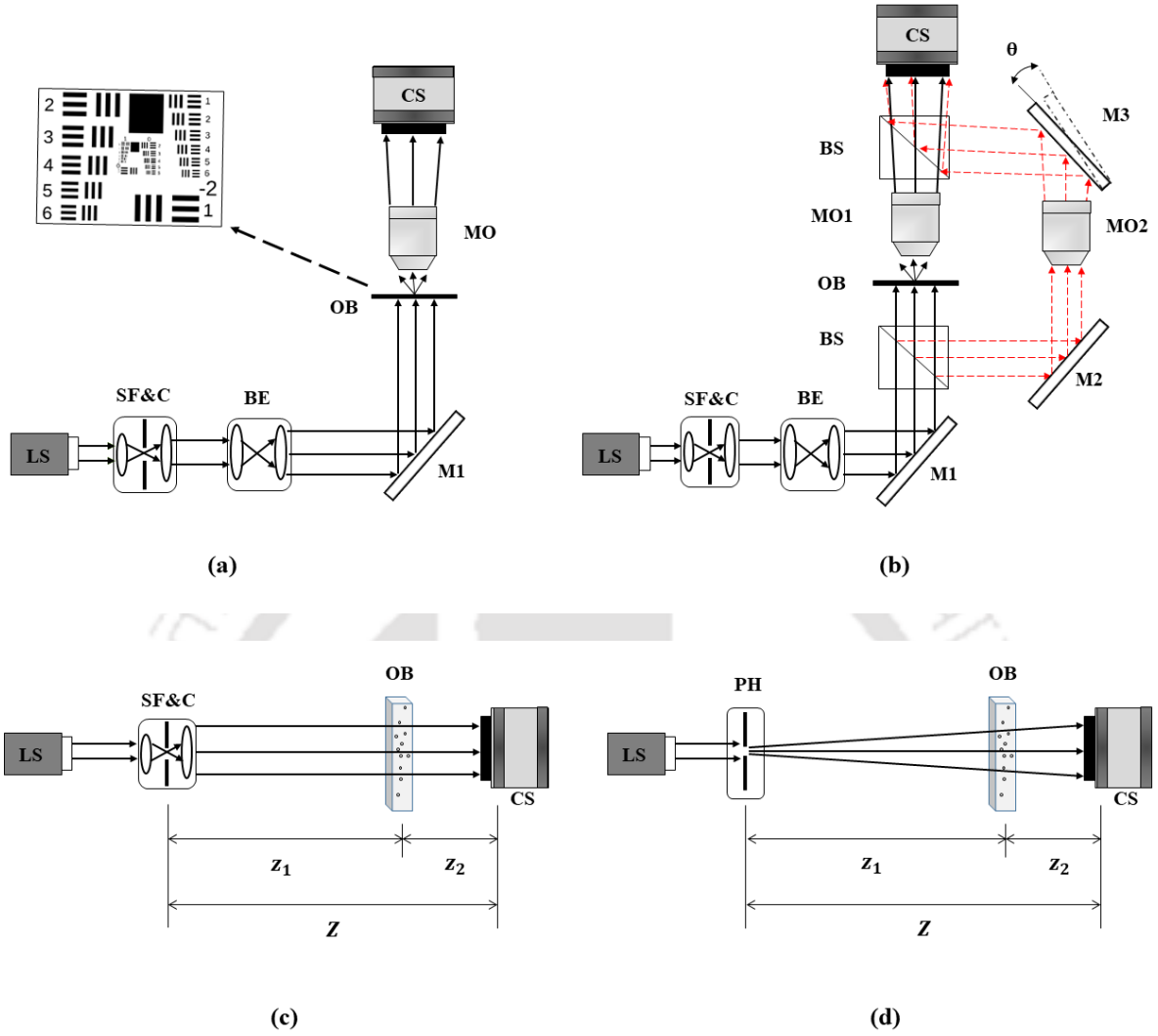

LS: Laser Source, SF&C: Spatial Filter & Collimator block, BE: Beam Expander, M: Mirrors, BS: Beam Splitter, OB: Object, MO: Microscopic Objectives, CS: Camera Sensor, PH: Pinhole, z_1: Source to Object distance, z_2: Object to Sensor distance, Z: Source to Sensor distance, θ: Off − axis angle

Figure 1.1: *Schematics of holographic configurations: (a) in-line with plane wave illumination, (b) off-axis, (b) in-line lensless with plane wave illumination, (d) in-line lensless with spherical wave illumination.*

1.3 Digital in-line holographic microscopy: plane wave illumination

Digital in-line holographic microscopy (DIHM) approach has the advantage of achieving variable magnification/ field-of-view by moving the sample between the light source and the sensor. However, the reconstructed image is affected by the presence of the DC term and the twin image. As a result, this method is mainly applicable in particle imaging, compution of particle size distribution, particle tracking, microfluidics, etc [32, 33, 34, 35, 36, 17, 37, 38, 39, 40, 41, 42]. This micro-particle can be

tracked inside a microfluidic channel using high-speed camera. The 3D information of the micon-scaled particle (mostly the opaque particles) can be observed [32, 33, 34, 35, 36, 17, 37, 38, 39, 40, 41, 42]. Figure (1.1) shows a typical set-up of holographic microscopy in particle imaging applications using microfluidic channel [50, 51].

In the digital in-line holographic microscopy setup with plane wave illumination, described in Figure 1.1(a), let us consider a plane wave is coming from the origin of coordinate system $(x_0, y_0; z = 0)$. The light is considered to be propagating along z-axis. The object plane $(x, y; z)$ is placed at distance z_1 from the source plane. Consider the object illumination with a plane beam of unity amplitude, the amplitude transmittance function associated with the object, defined as $O(x, y)$, can be expressed as [1, 15],

$$O(x, y) = 1 + \tilde{O}(x, y) \tag{1.1}$$

where, $\tilde{O}(x, y)$ is the perturbation imposed by the object. The wave passing through the object in the plane immediately next to object can be described as [1, 15],

$$U_{ex}(x, y) = O(x, y). \tag{1.2}$$

The object scattered wave and unperturbed reference wave further propagate z_2 distance to sensor plane. The intensity of the interference pattern of these two waves is recorded as the hologram at sensor plane. The field distribution at the detector plane $(X, Y; z = Z)$ can be computed using Fresnel diffraction formula as [1, 15],

$$U_s(X, Y) = -\frac{i}{\lambda}\iint U_{ex}(x, y)\ \frac{\exp(ik|r|)}{|r|}dxdy, \tag{1.3}$$

where, $i = \sqrt{-1}$; $r = \sqrt{x^2 + y^2 + z_2^2}$; λ is the wavelength of laser source and $k = 2\pi/\lambda$ represents wave number; Considering the paraxial approximation,

$$|r| \approx z_2\left[1 + \frac{(x - X)^2 + (y - Y)^2}{2z_2^2}\right], \tag{1.4}$$

Accordingly, Equation 1.3 can be rewritten as,

$$U_s(X, Y) \;=\; -\frac{i}{\lambda z_2}\iint O(x, y)\exp\left\{\frac{i\pi}{\lambda z_2}\left[(x - X)^2 + (y - Y)^2\right]\right\}dxdy. \tag{1.5}$$

The hologram recorded at the sensor plane can be expressed as [1, 15],

$$\begin{aligned} H(X, Y) \;&=\; |U_s(X, Y)|^2. \\ &=\; |U_R(X, Y)|^2 + |U_O(X, Y)|^2 \\ &\quad + U_R^*(X, Y)U_O(X, Y) + U_R(X, Y)U_O^*(X, Y). \end{aligned} \tag{1.6}$$

where, $U_R(X,Y)$ and $U_O(X,Y)$ represent the complex wavefields associated with reference and object scattered waves at the detector plane, respectively; $(.)^*$ represents complex conjugate operation. The first and second term in Eq.1.6 represent the intensity of reference and object wave, respectively, at sensor plane. The intensity modulation in the interference pattern observed in the hologram is the result of last two terms in Eq.1.6.

1.3.1 Reconstruction of hologram using Fresnel Transform

Equation 1.5 basically represents a convolution operation. Without loss of generality, we can neglect the constant and quadratic phase terms appearing before the integration, as they are independent of the object. The expression for hologram recording can be represented as [1, 15],

$$H(X,Y) = |[O \circledast p](X,Y)|^2, \tag{1.7}$$

where, $\circledast$ represents the convolution operator, and

$$p(x,y) = \frac{-i}{\lambda z_2} \exp\left[\frac{i\pi}{\lambda z_2}\left(x^2+y^2\right)\right]. \tag{1.8}$$

The parameter z is set as $\tilde{z} = z_2$. Using the Fourier transform property of the convolution operation, Eq. (1.7) can be evaluated as [1, 15].

$$H(X,Y) = |\mathcal{F}^{-1}\left[\mathcal{F}\left(O\right) \times \mathcal{F}\left(p\right)\right]|^2, \tag{1.9}$$

where, $\mathcal{F}$ and $\mathcal{F}^{-1}$ represent Fourier and inverse Fourier transform operations, respectively. Fourier and inverse Fourier Transform are evaluated using FFT routines available in MATLAB.

Since the hologram reconstruction process is an inverse operation as that of the hologram recording process, under the paraxial approximation of wavefield propagation, the complex amplitude of the object wavefield at z_2 distance from the sensor plane can be computed as,

$$U_{r_z}(x,y) = \mathcal{F}^{-1}\left[\mathcal{F}\left(H\right) \times \mathcal{F}\left(p^*\right)\right]. \tag{1.10}$$

where, $p^*(x,y)$ is the complex conjugate of $p(x,y)$. This approach of hologram reconstruction is named as Fresnel transform (FrT) method. In the case of plane beam illumination, the size of the reconstructed object area is equal to the size of the hologram, that is, the magnification (M_g) is unity

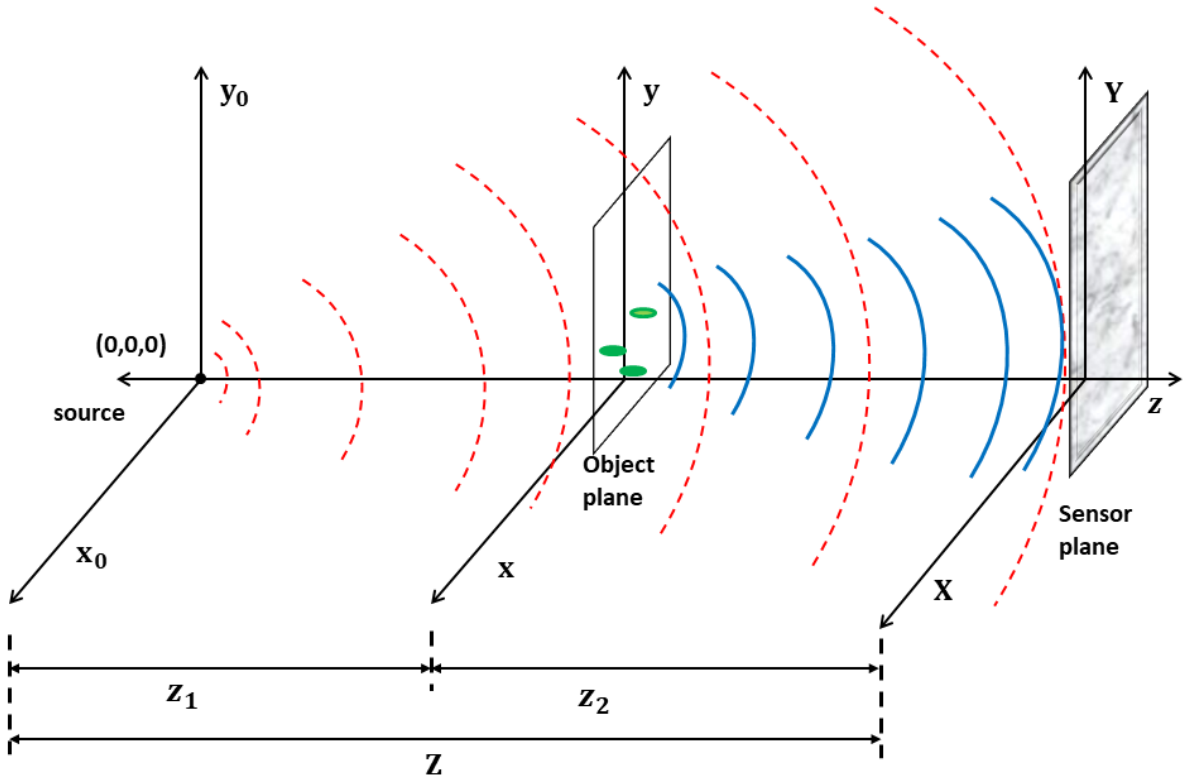

Figure 1.2: Digital lensless in-line holographic microscopic setup with sperical wave illumination [52].

1.4 Digital in-line holographic microscopy: spherical wave illumination

In the digital in-line holographic microscopy setup with spherical wave illumination, described in Figure 1.2, let us consider a point source placed at the origin of coordinate system $(x_0, y_0; z = 0)$. The light is considered to be propagating along z-axis. The object plane $(x, y; z)$ is placed at distance z_1 from the source plane. The spherical beam illuminating the object can be represented as,

$$U_{in}(x, y) = \frac{\exp(ikr)}{r}, \tag{1.11}$$

where, $i = \sqrt{-1}$; $r = \sqrt{x^2 + y^2 + z_1^2}$; Considering paraxial approximation of wave propagation, the term r in the exponential can be replaced with,

$$r = z_1 \left(1 + \frac{x^2 + y^2}{2z_1^2}\right). \tag{1.12}$$

At the same time, the r term in the denominator of Eq. 1.11 is replaced with z_1. The wave passing through the object immediately next to the object plane can be described as the combination of unperturbed reference wave ($U_i(x, y)$, red dashed curves in Fig. 1.2) and object scattered wave ($U_i(x, y)\tilde{O}(x, y)$,

blue solid curves in Fig. 1.2) as,

$$\begin{aligned} U_{ex}(x,y) &= U_{in}(x,y)O(x,y), \\ &= U_{in}(x,y) + U_{in}(x,y)\ \tilde{O}(x,y). \end{aligned} \tag{1.13}$$

The object scattered wave and unperturbed reference wave further propagate z_2 distance to sensor plane, where $Z = (z_1 + z_2)$ is the source to sensor plane distance. The intensity of the interference pattern of these two waves is recorded as the hologram at sensor plane. The field distribution at the detector plane $(X, Y; z = Z)$ can be computed using Fresnel diffraction formula as,

$$U_s(X,Y) = -\frac{i}{\lambda}\iint U_{ex}(x,y)\ \frac{\exp(ik|r-R|)}{|r-R|}dxdy, \tag{1.14}$$

where, $R = \sqrt{X^2+Y^2+Z^2}$. Considering the paraxial approximation and by taking into account that $z_1 << Z$,

$$|r-R| \approx Z\left[1 + \frac{(x-X)^2+(y-Y)^2}{2Z^2}\right], \tag{1.15}$$

Accordingly, Equation 1.14 can be rewritten as,

$$\begin{aligned} U_s(X,Y) &= -\frac{i}{\lambda z_1 Z}\exp\left[\frac{2\pi i(Z+z_1)}{\lambda}\right]\exp\left[\frac{i\pi}{\lambda Z}(X^2+Y^2)\right] \\ &\times\iint O(x,y)\exp\left\{\frac{i\pi}{\lambda z_1}\left[\left(x - X\frac{z_1}{Z}\right)^2 + \left(y - Y\frac{z_1}{Z}\right)^2\right]\right\}dxdy. \end{aligned} \tag{1.16}$$

The magnification associated with this imaging setup is $M_g = Z/z_1$.

1.4.1 Reconstruction of hologram using Fresnel Transform

Equation 1.16 basically represents a convolution operation. Without loss of generality, we can neglect the constant and quadratic phase terms appearing before the integration, as they are independent of the object. The expression for hologram recording can be represented as,

$$H(X,Y) = |[O \circledast p](X,Y)|^2, \tag{1.17}$$

with

$$p(x,y) = \frac{-i}{\lambda z_1 Z}\ \exp\left[\frac{i\pi}{\lambda z_1}\left(x^2+y^2\right)\right], \tag{1.18}$$

where, the parameter z is set as $\tilde{z} = z_1$. Using the Fourier transform property of the convolution operation, Eq. 1.17 can be evaluated using Fourier transform routines as given in Eq. 1.9.

Since the hologram reconstruction process is an inverse operation as that of the hologram recording process, under the paraxial approximation of wavefield propagation, the complex amplitude of the object

wavefield at z distance from the sensor plane can be computed as Eq. 1.10. In this case, the size of the reconstructed object area is equal to the size of the hologram divided by the magnification factor M_g.

भारतीय प्रौद्योगिकी संस्थान गुवाहाटी
Indian Institute of Technology Guwahati

2

Literature review, Motivation and Objectives

2.1 Digital hologram processing methods

2.1.1 Literature review

As described previously, in digital holography, the light field in the object plane is numerically reconstructed based on wave propagation phenomenon. One of the key feature of DH is its ability to provide numerical reconstruction of the optical field at any given reconstruction plane in the measurement volume. As a result, focusing of the object can be achieved in a numerical manner. A number of hologram reconstruction algorithms have been reported in the literature, for example, Fresnel transform [53, 54], angular spectrum [55, 56, 57, 58], Fourier transform holography [54, 1, 15], Bayesian method [59], wavelet transform [60, 61, 62], fractional Fourier transform [63, 64], etc. Wavelength-scanning digital holography using a tunable laser source has also been proposed [65] for surface mapping applications.

Methods have been reported to enhance the hologram resolution for better particle detection. For example, spatial dynamic range of digital in-line holography (DIH) is improved with super-sampling using Lanczos interpolation [66]. Bicubic interpolation of the hologram is used to enhance the low-frequency terms of the object in conjunction with the iterative extrapolation approach for high resolution hologram imaging [67]. The reconstruction of in-line hologram suffers from twin image artifacts. The twin image effect and background noise of the reconstructed images also affect the particle detection

[2]The chapter includes the literature survey on the digital holography, motivation and objectives of the thesis work.

accuracy in DIH. Twin image effect can be suppressed by phase retrieval techniques, which was initially proposed by **Gerchberg** and **Saxton** [68] and further modified by Fienup. This class of techniques restore the phase information of object with a priori knowledge [69, 70]. In the case of opaque particles, however, the variation in amplitude need to be captured which requires modifications in the model of hologram generation. The improvement of reconstructed image quality plays significant role in particle imaging with DIH.

In the case of phase or mixed (both amplitude and phase) type objects, the quantitative information on the physical quantity under investigation is available in the form of phase. The phase retrieval in digital holography is such that phase values lie in the range $(-\pi, \pi]$. Phase unwrapping is also a key step in DH measurement techniques [71]. Consequently, a number of phase unwrapping algorithms have been reported in the literature that can be broadly classified into quality-guided (path following), least-squares and model based. Some of the popular unwrapping algorithms are branch cut algorithm [72, 73, 74], minimum Lp-norm [75], the $Z\pi M$ algorithm [76], regularized phase tracking [77], local polynomial phase approximation (PhaseLa) [78], recursive phase unwrapping [79], piecewise polynomial phase approximation [80], state-space analysis based methods [81, 82, 83, 84, 85, 86] and least-squares algorithms [75, 87, 88, 89, 90]. Although these algorithms are noise-robust to certain extent, wrapped phase denoising [91, 92, 93] is usually needed as a preprocessing step to simply the unwrapping operation. Algorithms based on simultaneous noise filtering and phase unwrapping have also been reported [79, 94, 95, 96]. Under the category of quality-guided phase unwrapping algorithms [97, 98, 99, 100, 101, 102, 103, 104] typically a phase quality map is utilized to guide the phase unwrapping process. The algorithms mainly differ in the strategies of sorting and processing pixels depending on their quality values. In digital holographic microscopy, quality guided [101] and least square [105] phase unwrapping methods have been utilized. Some of the recent works that have reported phase unwrapping algorithms applied in digital holography are based on modulo wavelet [106, 107], total variance [108], deep learning [109] and contourlet transform [110].

Several works have been reported on digital hologram processing methods in recent years. In the following, we have discussed some of the representative methods. In the work of **Hennely and Sheridon (2005)** [111], a simple, easy and automated method has been proposed to track the space-bandwidth product of a signal, which is passing through an arbitrary quadratic phase system and undergoing deformation of its Wigner distribution function (WDF). The WDF of a complex optical amplitude distribution can graphically show the signal's spatial frequency distributions and is useful for visualization of localized signals. The total system matrix has been defined in terms of product of three different matrices,

each of which represents an optical process; Fourier transformation, magnification and chirp multiplication. This technique is used to simulate optical systems for any given input function.

A scaled down distance approach for hologram reconstruction is proposed by **Molony et al. (2009)** [112] in DIH setup. This paper discusses the performance dependence of Fresnel approximation based methods on reconstruction distance, image sensor pixel size, etc. The ABCD matrix formulation is considered to derive the matrix description of hologram recording and reconstruction process. The authors concluded that direct and angular spectrum methods of reconstruction are suitable for large and small reconstruction distances, respectively. The scaled down distance approach is capable of providing the suitable output image size.

In the work of **Latychevskaia et al. (2010)**, a depth-resolved holographic reconstruction method is proposed using 3D-volumetric deconvolution [113]. A point-spread-function (PSF) is simulated considering point object at central plane of the measurement volume. The 3D deconvolution is performed to achieve noise-reduced sharp reconstructed image and depth information or 3D shape of the object. The improvement of the results are shown by applying the algorithm iteratively. The application of proposed method was demonstrated in holographic particle tracking velocimetry. The main limitation of this work is that, the PSF is evaluated only at the center of measurement volume. **Latychevskaia and Fink** [15] have developed algorithms for simulation and reconstruction of digital in-line holograms with plane wave and spherical wave under paraxial approximation. The object position is considered to be close to either source or the sensor. **Tatiana Latchevskaia (2019)** has also proposed iterative phase retrieval algorithm [114] and twin-image-free iterative reconstruction algorithm [115] for digital holography. In this method, hologram extrapolation is incorporated to enhance the reconstructed image resolution. The applications of this method are shown for 3D samples such as 3D distribution of particles, thick biological samples, and other 3D phase objects. Figure 2.1a shows the result for iterative phase retrieval algorithm. The paper [115] describes an iterative reconstruction algorithm to retrieve twin-image free true absorption and phase distributions from a single hologram. The method can be applied without limitations to wavelength or wave front shapes (planar or spherical), for imaging objects of arbitrary size, exhibiting absorbing and/or phase shifting properties. Figure 2.1b shows a comparative result for conventional and iterative reconstruction.

In a recent work by **Kumar et al. (2020)** [18], they have used photonic crystal fiber for high resolution lens-less in-line holographic microscopy. Highly divergent beam helps to overcome the spatial sampling limitation of the image sensor. Maximum-likelihood estimation (MLE) based blind deconvolution is incorporated to achieve high resolution reconstructed images. Figure 2.2a shows the result for

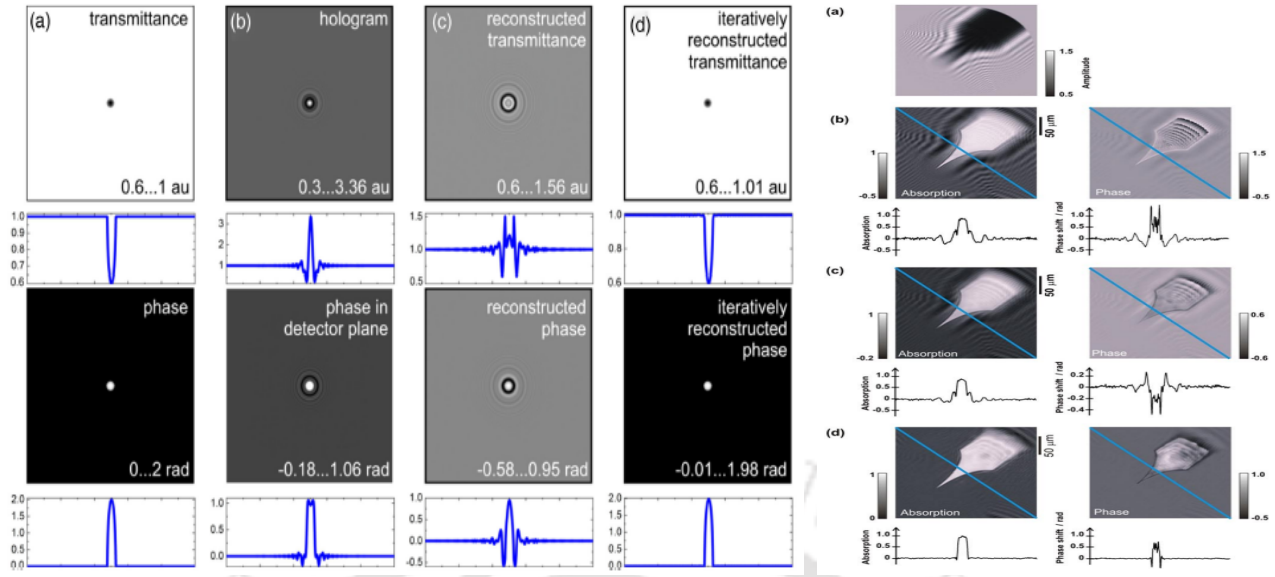

(a) (b)

Figure 2.1: *(a) Iteratively reconstructed amplitude and phase distributions in the object plane [114], (b) Iteratively reconstructed experimental optical hologram of a tungsten tip [115].*

lensless microscopic reconstructed image (magnification $\sim$ 3) compared with bright field microscope with $10X$ objective lens. Figure 2.2b shows the reconstructed image of RBC samples at optical magnification $\sim$ 2 and improvement of resolution after applying MLE blind deconvolution.

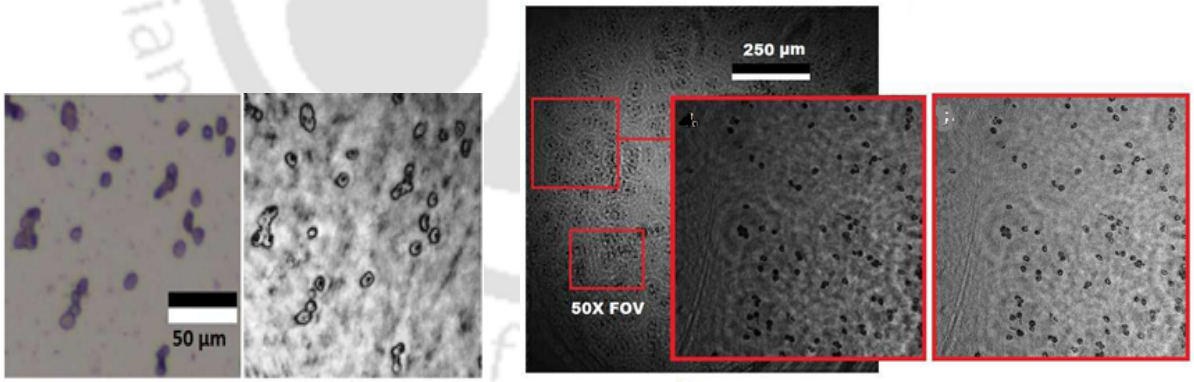

(a) (b)

Figure 2.2: *(a) Lensless microscopy reconstructed image (magnification $\sim$ 3) compared with bright field microscope with 10X objective lens, (b) reconstructed image of RBCs samples at optical magnification $\sim$ 2 and improvement of resolution after aplying MLE blind deconvolution [18].*

Momey et al.(2019) have described reconstruction of in-line holograms using an inverse problems approach in [70]. This work involves modeling the observations, selecting regularizations and constraints, and design of a reconstruction algorithm. It is shown that Fienup's method is analogous to a particular formulation of this phase retrieval problem when solved by proximal gradient descent itera-

tions. Figure 2.3 shows the phase image reconstructed in the above work with different methods and regularization techniques.

In another work by **Huang et al.(2020)**, the resolution of reconstructed image is improved using a bicubic interpolation and extrapolation iteration (BIPEPI) method[67], which compensates the limited size of the digital holograms. Based on the prior knowledge of the model of Fresnel zone plate with circular diffraction gratings, the pixel density is increased by the bicubic interpolation method inside the hologram to enhance the low-frequency terms of the object and by extrapolation iterations method to generate more high order fringes outside the hologram to enhance the high-frequency terms of the object. The resolution of the reconstructed image is improved by combining this predicted low and high frequency terms. Figures 2.4a and 2.4b show the optical setup used for this work and experimental results, respectively.

Herraez et al.(2002) proposed a novel phase unwrapping technique (FastPU)[116]. This work described a different type of reliability function and does not follow a continuous path to perform the unwrapping operation. The phase unwrapping method described by them operates faster with compromising some unwrapping accuracy. In another work by **Bioucas-Dias et al.(2007)**, a new energy minimization framework is introduced for phase unwrapping, named PUMA [117]. The first-order Markov random fields are cosidered as the objective functions. NP-hard problem for owing discontinuity preserving ability are solved with an approximate solution by using graph cut techniques. The proposed algorithm is able to provide good unwrapping quality, but the computation time is significantly high.

The phase retrieval in digital holography can be achieved using the phase shifting method [118, 119]. Multiple phase-shifted holograms are recorded by introducing known phase shifts in the reference beam using phase modulators such as piezo-driven mirror, acousto-optic modulator, spatial light modulators, electro-optic modulator, etc. The phase shifting algorithm provides the object scattered light field in the hologram plane. Subsequently, the light field in the object plane can be evaluated based on wave propagation [10, 11, 13, 14]. This techniques makes it possible to utilize the full space-bandwidth product of the image sensor which results in wide field-of-view and high resolution in imaging. The time-consuming process of recording phase-shifted holograms has been circumvented using parallel phase-shifting digital holography [120, 121, 122]. Real-time holographic imaging depends on the frame rate of image sensor, frame transfer speed and hologram reconstruction computation time. Modern high-speed cameras are capable of recording images at high frame rates. The computation time required for hologram reconstruction based on 2D FFTs can be reduced with the help of graphics processing units (GPUs) [123]. Some other digital hologram processing methods can be found in [124, 125, 126, 127,

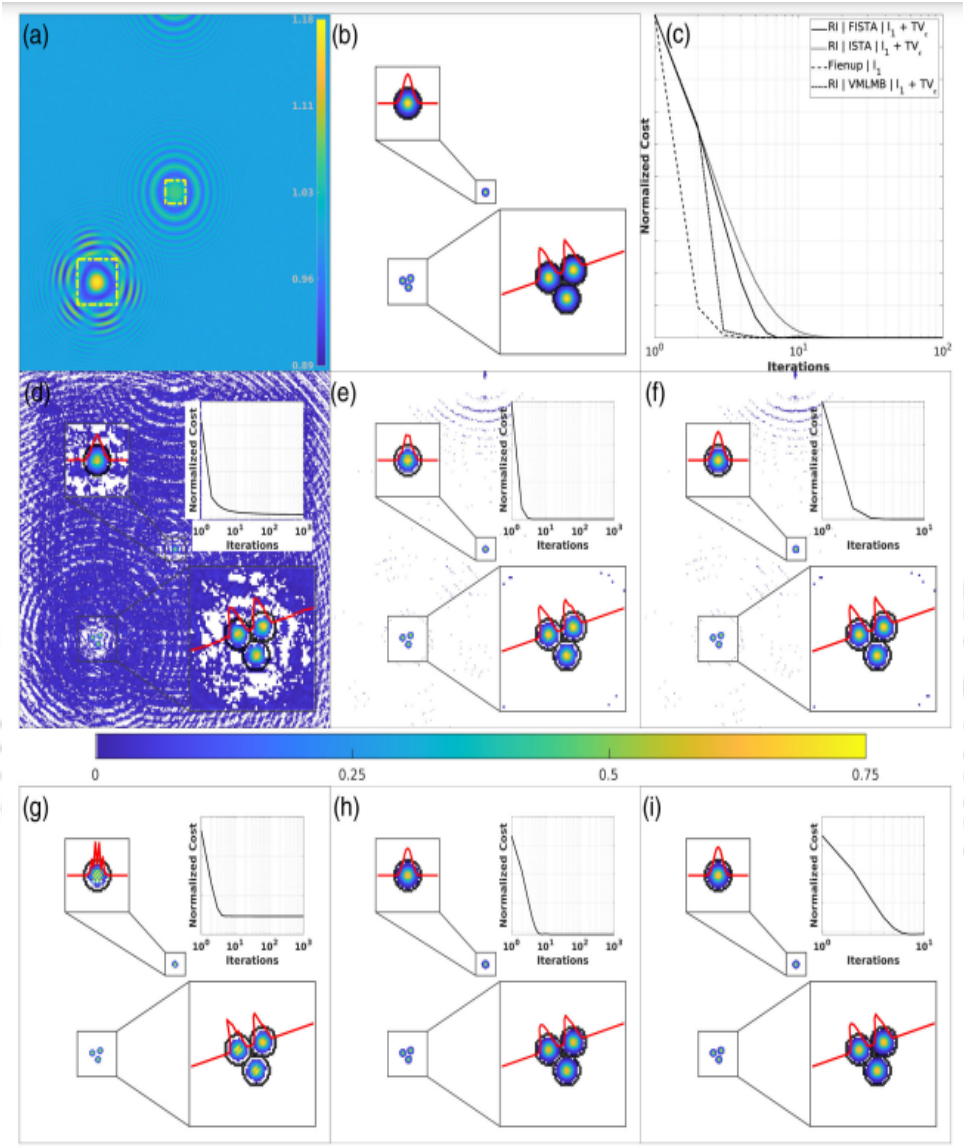

Figure 2.3: (a) In-line hologram. The yellow frames indicate the regions of interest that are extracted from the field of view for visualization. (b) Ground truth phase. (c) Evolution of the normalized cost criterion (minimum and maximum values ranged between zero and one) for each reconstruction. Reconstructed images using (d) Fienup method, (e) Fienup method + soft-thresholding, (f) Fienup method + soft-thresholding, 10 iterations, (g) RI method using FISTA + soft-thresholding, (h) RI method using FISTA + soft-thresholding + edge-preserving, (i) RI method using FISTA + softthresholding + edge-preserving, 10 iterations [70].

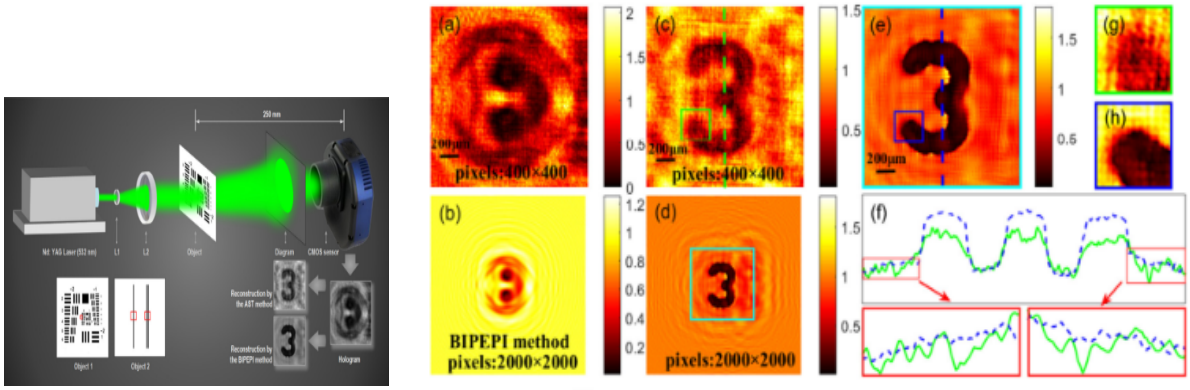

(a) (b)

Figure 2.4: (a) Optical setup for inline digital holography, (b) Experimental result [67].

128, 45, 37, 32, 39, 41, 40, 51, 129, 35, 19, 20, 130, 131].

2.1.2 Motivation

Based on the literature survey described in the previous sections, the motivations for this thesis work are described below.

(i) In the case of object illumination with spherical beam in digital lens-less holography, the reconstruction algorithm described in [15] considers the assumption that the source-to-object distance is less compared to source-to-detector distance. Such an assumption may not be valid in the practical scenario wherein the object may be placed anywhere between source and detector. It is beneficial to develop a hologram reconstruction algorithm considering plane and spherical beam illumination of the object in digital lens-less holography for any given source-to-object distance.

(ii) The reconstructed images of the conventional in-line holography methods suffer from twin image effects and background noise. Development of a twin image free reconstruction algorithm to obtain high quality images is required mainly in particle imaging applications.

(iii) The reduction in computation time in hologram processing is essential especially in applications which involve multiple hologram recording.

(iv) Although, DHM provides quantitative phase imaging of objects, in general, the measured phase is in wrapped form. Therefore, phase unwrapping is essential for absolute phase retrieval for quantitative measurement of physical parameters under investigation. In the presence of noise and object

discontinuities, phase unwrapping becomes non-trivial. Desirable features of phase unwrapping algorithm are acceptable accuracy and low computation cost. In general, fast unwrapping algorithms suffer from inaccuracies in the presence of noise, whereas, algorithms providing high accuracy are computationally not efficient.

2.1.3 Objective

Based on the motivation described above, objectives of the thesis work are outlined below:

- Development of hologram reconstruction algorithm by extending the work presented in Ref. [15] for any given source-to-object distance. In that case, the algorithm described in Ref. [15] can become special case of proposed algorithm.
- Modification of model based iterative algorithm for phase retrieval to amplitude type particle imaging applications.
- Development of a computationally efficient hologram reconstruction algorithm compared to state-of-art Fourier transform-based method without compromising reconstruction quality.
- Development of a phase unwrapping algorithm in DHM which can provide an optimal compromise between the acceptable accuracy and computation time in comparison to state-of-art methods.

2.2 Autofocusing methods in digital holography

2.2.1 Literature review

Numerical autofocusing is one of the unique features associated with digital holographic imaging. The numerical hologram reconstruction allows to evaluate the object field at any plane within the measurement volume. Accordingly, the image of object under investigation can be brought to focus numerically. However, finite depth-of-focus requires an image-based measure to identify the exact object plane location. As a result, numerous autofocusing algorithms in digital holography have been reported in the literature over the years. At the core of most of these algorithms is the development of a metric to measure the quality of reconstructed images of the object as a function of the reconstruction distance. Usually, the metric is based on the sharpness of the reconstructed image. The plot of reconstructed image quality metric as a function of reconstruction distance achieves maximum or minimum at a location which corresponds to the object plane. The desirable characteristics of an autofocusing algorithm have

been described in [132]. Among different autofocusing metrics reported in the literature, some of them are mentioned in the following.

Gillespie et al. established an autofocusing criterion [133] based on self-entropy of the reconstructed image intensity (SEN) for amplitude objects. Another commonly used autofocusing method is based on the gradient of the reconstructed image (GRA) [134]. **Dubois et al. (2006)** [135] proposed autofocusing algorithm based on the total amplitude measure (AMS). In this work, focal plane detection criterion has been designed for pure amplitude and pure phase type objects. Figure 2.5a shows the hologram and reconstructed image in focus of an object. The plot of AMS in function of reconstruction distance is given in Fig. 2.5b. The minimum of the curve is observed at $55\mu m$ which corresponds to the object plane. Alternatively, by applying the theory of Fresnelet, a sharpness sparsity metric is calculated to find the

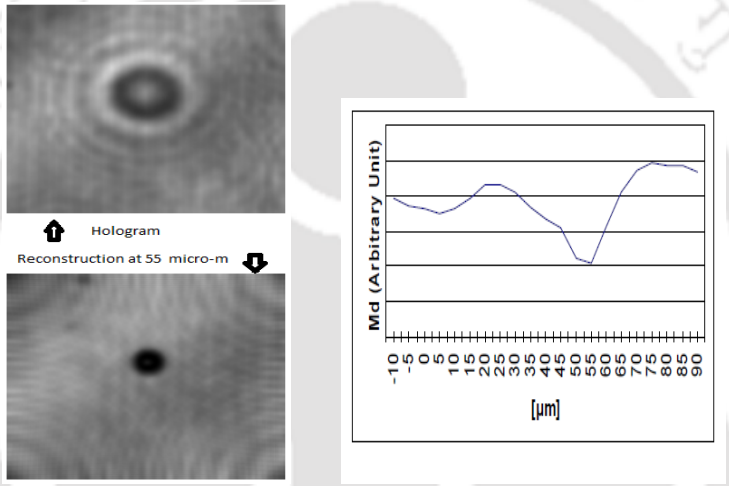

(a) (b)

Figure 2.5: *(a) Hologram and reconstructed image at* $55\ \mu m$ *and (b) magnitude map [135].*

focus position [136]. On the similar lines, an algorithm using the sparsity of the sample (SPA) [137] has also been proposed. The maximum intensity local variance (VAR) based approach has been employed in [138, 139]. Recently, **Lyu et al.** developed a method based on the axial magnitude differential [140] which is found to work for both amplitude and phase objects. Dark-focusing (DFS) algorithm reported in [132] is based on the local variance of the gradient of the reconstructed image. Most of these algorithms seem to work well for a pure amplitude or pure phase objects. Only the DFS algorithm is found to work with mixed type objects among the above mentioned autofocusing algorithms. A recent work pertaining to the complex amplitude-phase mixed object has been discussed [141] in the context of in-line holographic microscopy. Some other autofocusing algorithms can be found in [142, 143, 144, 145]. A comparison of some of the autofocusing criterias has been reported in Ref. [146].

2.2.2 Motivation

Based on the literature survey described in the previous sections, the motivations for this thesis work are described below.

(i) In the iterative in-line hologram reconstruction, it is assumed that the location of object plane is known accurately. The object field and hologram reconstruction is performed iteratively based on this assumption. However, it has been observed that a small departure from true value of the reconstruction distance results in significant changes in the reconstructed amplitude and phase images. Thus, inaccurate object plane distance in the iterative reconstruction algorithm results in inaccurate amplitude and phase images.

(ii) In particle imaging application, for example in microfluidics, the particles may lie in different plane at different time instances. In that case, the autofocusing algorithm should be able to identify multiple focal planes.

(iii) In general, the evaluation of autofocusing metric is performed at a number of planes within measurement volume. The overall computation time for focal plane detection increases with increase in this number. Consequently, it is desirable to have a computationally efficient autofocusing algorithm.

2.2.3 Objectives

Based on the motivation described above, objectives of the thesis work are outlined below:

- Development of a novel autofocusing algorithm for amplitude, phase and mixed type objects.
- Development of a novel and computationally efficient autofocusing algorithm.

2.3 Digital holographic microscopy for particle imaging applications

2.3.1 Literature review

Particles with varying shapes and sizes, i.e., fly ash particles produced in thermal power plant [147], sand particles, aerosols[148] in the air, various food and medicine powders, fossil fuel particles in energy and milling engineering, are widely encountered in both nature and industry. It is a great challange to manipulate and utilize such particles due to their morphological complexity [149]. Thus, numerous work have been reported on particle characterization with mathematical and numerical models [150], as well

as with measurement tools. A large number of shape descriptors technologies have been introduced to investigate the 1D parameters (size, length, width, and thickness), 2D projection image (roundness, area, 2D shape, and texture), and 3D geometrical properties (volume, sphericity, concavity, convexity, and 3D boundary) of particles [151, 152, 153, 154, 155]. The 1D parameters are usually measured experimentally by the laser diffraction-based particle size analyzer and phase Doppler particle analyzer [156, 157]. Traditional passive direct imaging or shadowgraphy, are robust approaches for 2D characterization of particle. The 3D surface of the particles can be measured by Laser scanner (LS) technique with laser sheet illumination [158]. Computed tomography (CT) methods are able to measure 3D morphology of the interrogated irregular particle. The X-ray CT provides the internal 3D information, which is encoded as the inner absorption and scattering process while X-ray wave penetrating through the particle [159].

Digital holographic 3D imaging technique is a mature tool for micron-sized particle measurement in last two decades. The previous investigations have demonstrated its capability of measuring the size, 3D position, 2D shape, and 3D morphology of the particle [160, 161, 162]. Interferometric particle imaging (IPI), an interferometric laser imaging determines the size and 2D position of a transparent spherical particle or droplet [163, 164] from the angular spacing (or spatial frequency) of Mie scattering at the off-axis forward direction [165, 166, 167, 168]. A special receiving optical system is developed to compress the circular image with fringes into a linear image by a cylindrical lens. This reduces the overlapping of neighboring fringes and enhances the spatial resolution [169]. The depth position of a transparent particle in the measurement volume can be determined through the fringe orientation tracking, with a cylindrical interferometric out-of-focus imaging configuration [170, 171]. The irregular particles are modeled with cluster of point emitters and measured the shape using 2D-autocorrelation [172]. A dual-beam interferometric particle imaging method is proposed to measure spherical opaque particles [173]. Microfluidic chip is used to measure the fly ash particle distribution after the wet electrostatic precipitators [38]. Using machine learning three-dimensional particle size distribution is obtained in DIH [174]. Two-dimensional position of opaque particles is detected using dual-beam interferometry. Rod-shaped particle's size is also detected using Wigner-Ville distribution [175]. Minimum intensity projection [176, 177] and hybrid method [178] are two commonly used method for particle size measurement. The focal plane detection in DIH offers an important advantage of accurate particle size and depth determination. There are several automatic algorithms which determine accurate particle depths and sizes from hologram reconstructed images by applying one of the image quality metrics to identify in-focus particle positions. The particle detection and size estimation accuracy is limited due to the fixed camera field-of-view and resolution of DIH setup. The improvement of reconstructed image quality has very significant role in particle imaging

with DH. The DH techniques measure the size, shape, and 3D position of particles. In real industrial scenarios, the configuration is also an important consideration. Instruments that have discrete assemblies placed at opposite sides (laser diffraction particle analyzer) or off-axis sides (traditional IPI) might have limitations with their applications, because of the implication of multiple optical windows. Compact devices that integrate the light source and acquisition components in one box is preferable, since they only require one window [179]. DIH is more suitable for its compact and easy experimental setup [44].

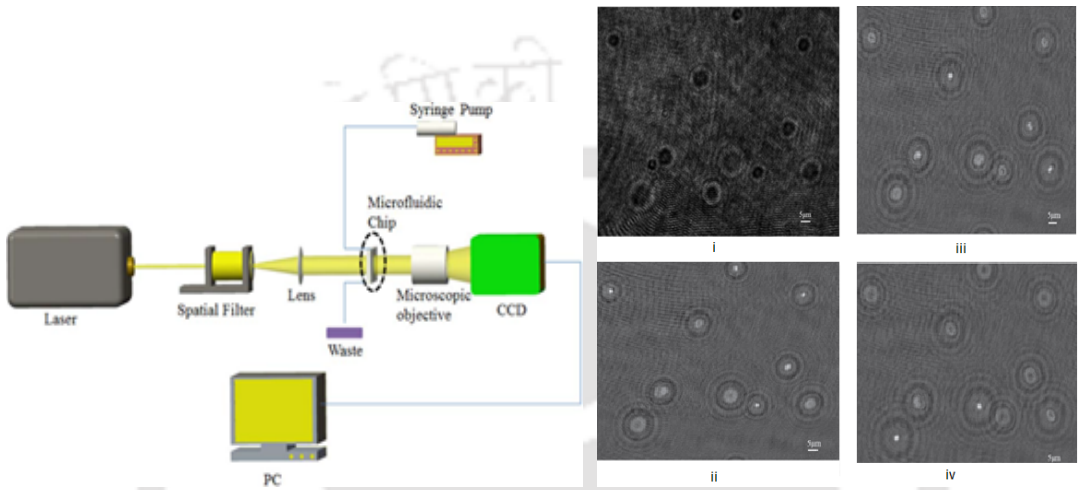

Figure 2.6: *(a) Experimental set-up, (b) raw Hologram (i), reconstructed image at distance* $Z = 20\ \mu m$ *(ii),* $Z = 33\ \mu m$ *(iii),* $Z = 44\ \mu m$ *(iv) [38].*

In the work by **Zhou et al. (2018)** [38], they have applied digital in-line holographic microscopy and microfluidic chips for measurement of particle size distribution of fly ash particles (size of less than $5\ \mu m$) after a wet electrostatic precipitator. The obtained results are compared with that from a laser particle size analyzer and a acceptable deviation indicates that the method is feasible and accurate. Figure 2.6a shows the experimental set-up. In Fig. 2.6b, (i) a raw hologram, reconstructed images at distance (i) 20 μm, (ii) 33 μm, (iii) 44 μm are shown.

Another group of **Chen et al. (2020)** [180] have designed a on-chip set-up for lens-free in-line holographic microscopy for complete blood analysis. They were able to detect all the blood particle and the total RBC count with their compact lens-free set-up. Figure 2.7a shows the 20X microscopic images, holograms and reconstructed images of blood particles. Figure 2.7b shows the total RBC count, where it is shown that holographic result is almost same as the real data. Figure 2.7c shows the reconstruction of particles in holography and their 4X microscopic images.

Recently another group of **Kumar et al. (2020)** [181] have developed a common-path multi-modal three-dimensional fluorescence and phase imaging setup for digital holography. A 3D fluorescence

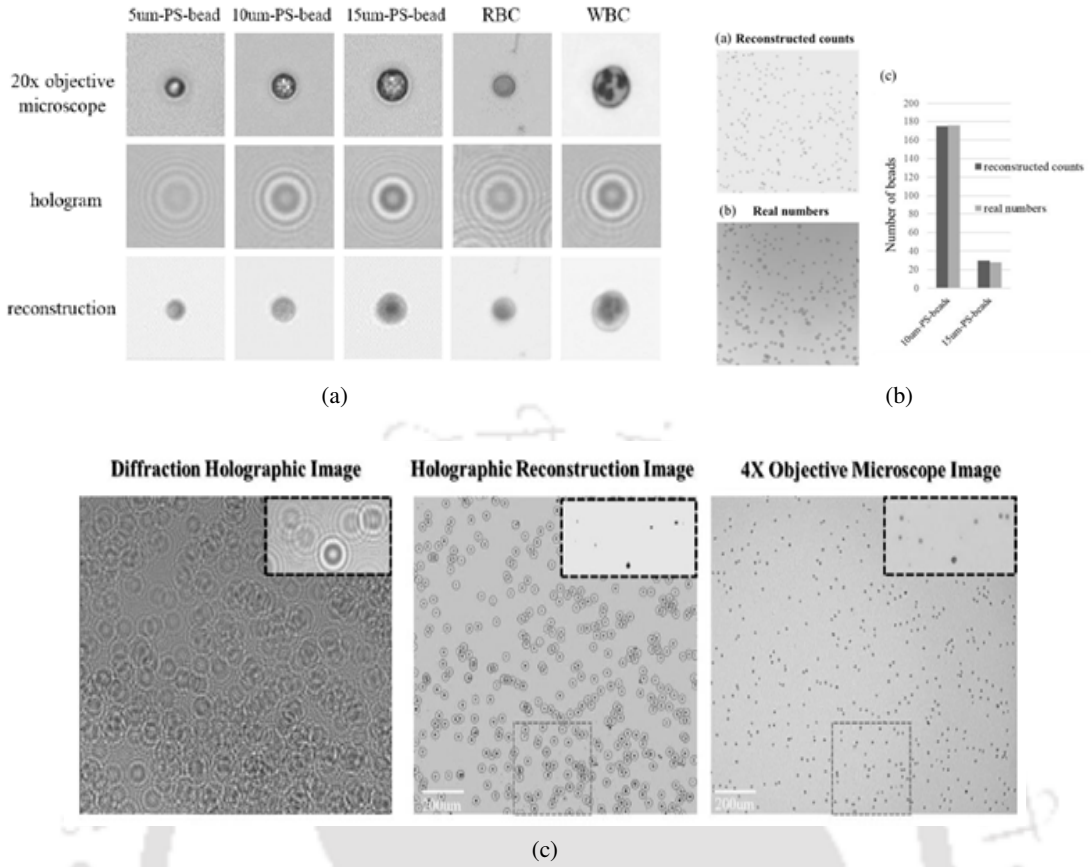

Figure 2.7: *(a) Detection of all the Blood particles, (b) Total RBC count (Comparison with real data), (c) Reconstruction of Particles with Holography [180].*

imaging system and 3D phase imaging system is designed individually and both are combined to invent a multi-modal configuration as shown in Fig. 2.8a. Multi-modal system simultaneously provide the molecular-specific quantitative analysis and specific localized regions of the sample. It also performs comprehensive analysis of the living biological materials with specific molecular and biophysical dynamics, and physiological and pathological processes at a single platform as shown in Fig. 2.8b.

2.3.2 Motivation

Based on the literature survey described in the previous sections, the motivations for this thesis work are described below.

(i) Although fly ash particle size characterization has been reported in the literature, the system is not compact due to the use of microfluidic system.

(ii) Exploring the possibilities of using compact DIH setup in different measurement applications.

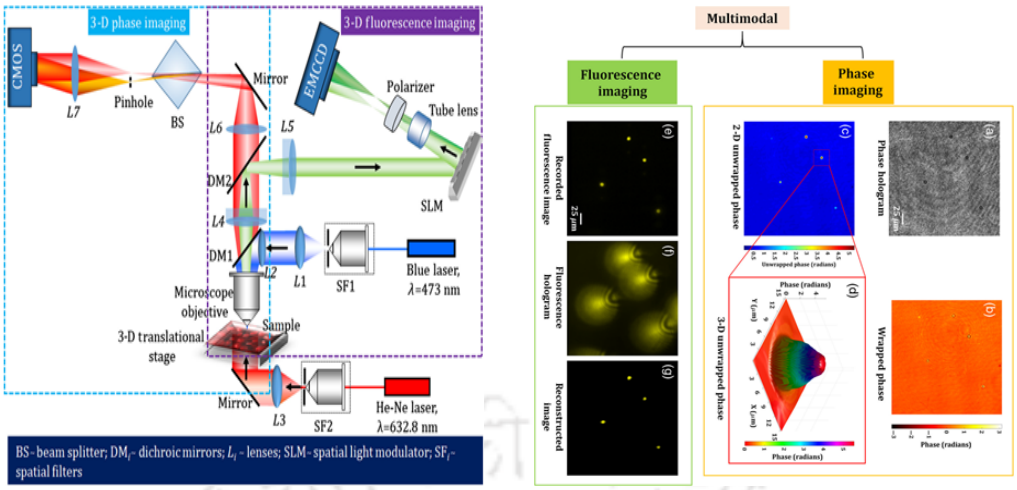

(a) (b)

Figure 2.8: *(a) Optical schematic of the proposed multimodal system for the measurement of the 3-D fluorescence and the 3-D phase of the specimen, (b) Experimental results of the multimodal system of microsphere beads [181].*

2.3.3 Objectives

Based on the motivation described above, the objectives of the thesis work are outlined below:

- Development of lens-less DIH setup for imaging of particles of known size and shape.
- Performance evaluation of proposed particle size estimation method.
- Development of lens-less DIH setup for imaging of fly ash samples.
- Performance evaluation of the proposed method for the characterization of fly ash particle size distribution and comparison with hydrometer and laser scattering based methods.

Part II

Digital Hologram Processing

भारतीय प्रौद्योगिकी संस्थान गुवाहाटी
Indian Institute of Technology Guwahati

3

Hologram Reconstruction methods

3.1 Reconstruction of digital in-line hologram using iterative algorithm

This section proposes an iterative algorithm based reconstruction method in digital in-line holography to reduce the twin image effect and background noise in the reconstructed images. The proposed method estimates object wavefield by applying physical constraint at the object plane in each iteration. The reconstruction algorithm also considers a general case of any source-to-object distance.

3.1.1 Methodology

3.1.1.1 Digital in-line holographic microscopy: spherical wave illumination

In the digital in-line holographic microscopy setup with spherical wave illumination, described in section 1.4, it is considered that object plane is close to source plane ($z_1 << Z$), which may not be always the case in certain practical scenarios. The object can be placed at any plane between the source and camera. Considering this general case, the holographic recording and reconstruction process is derived here. The spherical beam illuminating the object can be represented as Eq. 1.11. Considering paraxial approximation of wave propagation, the term r in the exponential can be replaced with Eq. 1.12. At the same time, the r term in the denominator of Eq. 1.11 is replaced with z_1. The amplitude transmittance function associated with the object, defined as $O(x, y)$, can be expressed as Eq. 1.1. The wave immediately passing through the object ($U_{ex}(x, y)$) can be described as the combination of unperturbed reference wave ($U_{in}(x, y)$, red dashed curves in Fig. 1.2) and object scattered wave ($U_{in}(x, y)\tilde{O}(x, y)$,

[3]The chapter includes the iterative and the Toeplitz matrix deconvoltion based hologram reconstruction algorithms.

blue solid curves in Fig. 1.2) as Eq. 1.13. The object scattered wave and unperturbed reference wave further propagate z_2 distance to sensor plane, where $Z = (z_1 + z_2)$ is the source to sensor plane distance. The intensity of the interference pattern of these two waves is recorded as the hologram at sensor plane. The field distribution at the detector plane $(X, Y; z = Z)$ can be computed using Fresnel diffraction formula as,

$$U_s(X,Y) = -\frac{i}{\lambda}\iint U_{ex}(x,y)\,\frac{\exp(ik|r-R|)}{|r-R|}dxdy, \tag{3.1}$$

where, $R = \sqrt{X^2+Y^2+Z^2}$. Considering the paraxial approximation we have,

$$|r-R| \approx z_2\left[1+\frac{(x-X)^2+(y-Y)^2}{2z_2^2}\right], \tag{3.2}$$

Accordingly, Equation 3.1 can be rewritten as,

$$\begin{aligned} U_s(X,Y) \;=\; & -\frac{i}{\lambda z_1 z_2}\exp\left(\frac{2\pi i Z}{\lambda}\right)\exp\left[\frac{i\pi}{\lambda Z}(X^2+Y^2)\right] \\ & \times\iint O(x,y)\exp\left\{\frac{i\pi Z}{\lambda z_1 z_2}\left[\left(x-X\frac{z_1}{Z}\right)^2+\left(y-Y\frac{z_1}{Z}\right)^2\right]\right\}dxdy. \end{aligned} \tag{3.3}$$

Now, the magnification associated with the imaging setup is $M_g = Z/z_1$.

3.1.1.2 Reconstruction of hologram using Fresnel Transform

Equation 3.3 basically represents a convolution operation. Without loss of generality, we can neglect the constant and quadratic phase terms appearing before the integration, as they are independent of the object. The expression for hologram recording can be represented as,

$$H(X,Y) = \Big|[O \circledast p](X,Y)\Big|^2, \tag{3.4}$$

with

$$p(x,y) = \frac{-i}{\lambda\tilde{z}Z}\exp\left[\frac{i\pi}{\lambda\tilde{z}}\left(x^2+y^2\right)\right], \tag{3.5}$$

where, the parameter z is set as $\tilde{z} = z_1 z_2/Z$. Using the Fourier transform property of the convolution operation, Eq. 3.4 can be evaluated as Eq. 1.9. Since the hologram reconstruction process is an inverse operation as that of the hologram recording process, under the paraxial approximation of wavefield propagation, the complex amplitude of the object wavefield at z distance from the sensor plane can be computed as Eq. 1.10. In this case, the size of the reconstructed object area is equal to the size of the hologram divided by the magnification factor M_g. Thus, the holographic microscopy described in Ref. [15] becomes a special case of this generalized method.

3.1.1.3 Reconstruction of hologram based on iterative algorithm

In the proposed method, the in-line hologram is reconstructed using iterative algorithm similar to the one described in Ref. [70] for the object phase reconstruction. Since we consider imaging of particles, we consider the object type such that it alters only the amplitude of illuminating optical wavefield. The algorithm starts an initial estimate of the object field which is considered to be random distribution. The algorithm proceeds by alternately propagating the field between the object and the hologram planes by applying some constrains at each plane. After a fixed number of iterations, the final estimate of the object field is obtained which is free of twin image. The detailed method is discussed below.

In general, the object field can be modelled as a two-dimensional (2D) complex transmittance function as,

$$O(x, y) = A(x, y) \exp(i\phi(x, y)), \tag{3.6}$$

where, $O(x, y)$ is the quantity of interest consists of both amplitude $A(x, y)$ and phase $\phi(x, y)$ distributions. Since in particle imaging applications, the particles can be considered to be opaque in nature, the object field can be simply modelled as the amplitude distribution $O(x, y) = A(x, y)$. Let, $m(O) = |[p \circledast O](X, Y)|^2$ represent the intensity of field distribution that has propagated to the hologram plane. Accordingly, the recorded hologram intensity can be modelled as [70],

$$H = c\, m(O) + \eta \tag{3.7}$$

$$H = c|PO|^2 + \eta \tag{3.8}$$

where, P is the complex-valued convolution matrix operator corresponding to $p(x, y)$ that performs the discrete propagation of the object field; η represents the additive noise in the recorded hologram intensity. It also incorporates the model approximation error. P^* is the back-propagation operator.

At first, the proposed iterative algorithm is used to retrieve the unknown object field based on the hologram formation model in Eq. 3.7 and 3.8 using a single hologram. The hologram is normalized by dividing by its mean/median to make background equal to 1. As a result the retrieved object image is normalized in the same way. The iterative algorithm is described below:

- At the n^{th} iteration, the estimate $\bar{O}^{(n)}$ is propagated to the hologram plane to obtain a complex wave-field $C^{(n+1)}$, where n represent the iteration number.

- The amplitude of $C^{(n+1)}$ is replaced with the square root of the normalized measurement data H_{norm} to obtain the modified wave-field $\dot{a}^{(n+1)}$.

Algorithm 1 : Reconstruction of hologram using iterative estimation

Input:

H // {hologram}
p // {propagation kernel}
p^* // {backpropagation kernel}
Δ_{min} // {minimum bound constraint}
Δ_{max} // {maximum bound constraint}
$maxIter$ // {maximum number of iteration}

Output:

$\bar{O}$ // {reconstructed Image}

begin:

// {Step 0: Initializations}
$H_{norm} \leftarrow normalize(H)$ // {normalize the data hologram (dividing by its mean/median)}
$\bar{O} = rand(x, y)$ // {first estimate as random values of object size}
for $n = 1 : maxIter$ **do**
  $C = p \circledast \bar{O}$ // {Step 1: propagation of O^* to hologram plane}
  for $j = 1 : x$ **do**
    for $l = 1 : y$ **do**
      if $C(j, l) \neq 0$ **then**
        $\dot{a}(j, l) = \sqrt{H_{norm}(j, l)} \times \frac{C(j,l)}{|C(j,l)|}$ // {Step 2: Replacing the field amplitude in the hologram plane using measured hologram intensity}
      else
        $\dot{a}(j, l) = 0$
      end
    end
  end
  $A = |p^* \circledast \dot{a}|$ // {Step 3: backpropagation of a to object plane}
  for $j = 1 : x$ **do**
    for $l = 1 : y$ **do**
      $A(j, l) = min(A(j, l), \Delta_{max})$
      $A(j, l) = max(A(j, l), \Delta_{min})$ // {Step 4: application of physical constraints in the object plane}
    end
  end
  $\bar{O} \leftarrow A$
end

- The modified wave $\dot{a}^{(n+1)}$ is back-propagated to the object plane to get obtain the amplitude image $A^{(n+1)}$.
- At the object plane, minimum and maximum bound constraints based on some prior knowledge of the object are applied to obtain $\bar{O}^{(n+1)}$.
- The above steps are repeated for a maximum number of iterations denoted as $maxIter$.
- The final estimate $\bar{O}^{\,maxIter}$ is considered as the final reconstructed object image.

3.1.2 Results and Discussion

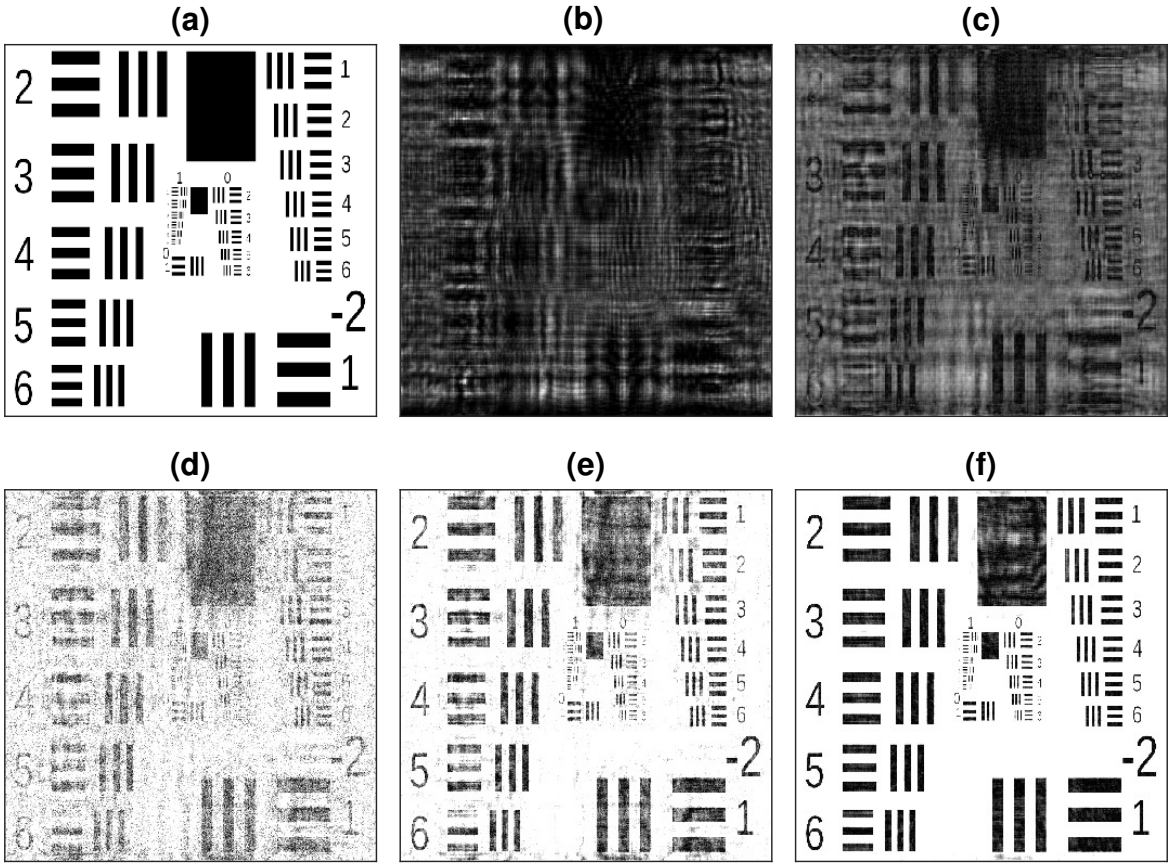

Figure 3.1: Simulated result: (a) USAF target amplitude object of size 583×800 pixels, (b) in-line hologram, (c) reconstructed amplitude images in conventional in-line holography, (d-f) reconstructed amplitude images using proposed method after $2, 5$ and 20 iterations, respectively [182].

The simulation study is performed considering a digital in-line holographic setup with a plane beam illumination of the object using a He-Ne laser source of wavelength $\lambda = 632.8\ nm$ and camera pixel size $4.8\ \mu m$. The USAF target amplitude object of size 583×800 pixels as shown in Fig. 3.1(a) is used as test objects placed at $z_2 = 80\ mm$. The simulated hologram is shown in Fig. 3.1(b). Figure 3.1(c) shows the reconstructed amplitude image with conventional in-line holography reconstruction. Reconstructed amplitude using proposed method after $2, 5$ and 20 iterations are shown in Fig. 3.1(d), (e) and (f), respectively. It can be clearly observed that, the twin image effect and background noise reduced significantly in the reconstructed amplitude obtained using the proposed method.

Another similar simulation study is performed with simulated amplitude type object of size 400×400 pixels as shown in Fig. 3.2(a). In this simulated object, amplitude of each letter in the word "IITG" is varying. The in-line hologram is shown in Fig. 3.2(b). Figure 3.2(c) represents the reconstructed

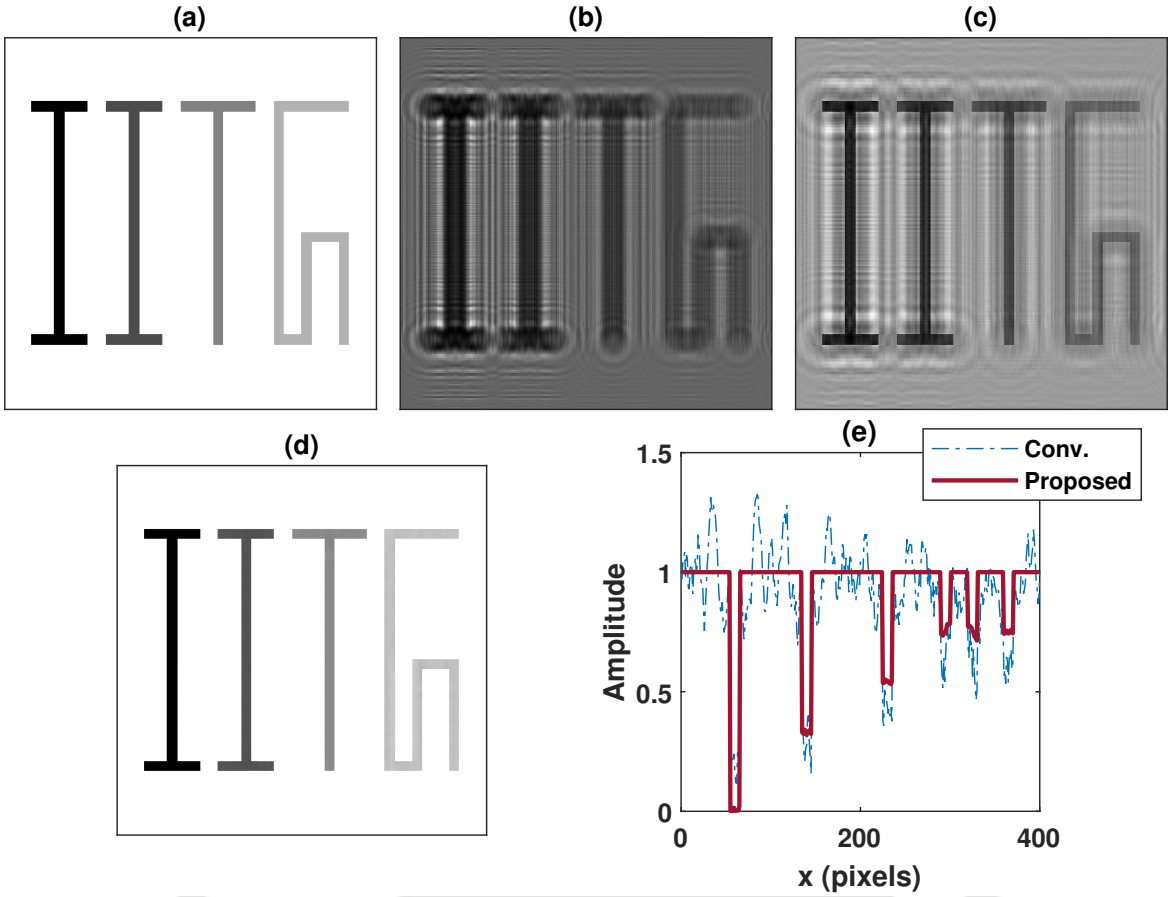

Figure 3.2: Simulated result: (a) Simulated object of size 400×400 pixels, (b) in-line hologram, (c) reconstructed amplitude images in conventional in-line holography, (d) reconstructed amplitude images using proposed method after 20 iterations, (e) comparison of the reconstructed amplitude profile in row $y = 250$ of both conventional and proposed method.

amplitude image with conventional holography. Figure 3.2(d) represents the reconstructed amplitude image with proposed method after 20 iterations. Comparison of the reconstructed amplitude profile in the row $y = 250$ in the reconstructed images using conventional DIH and proposed algorithm are shown in Fig. 3.2(e). It can be clearly seen that, the twin image and background noise are reduced significantly in the reconstructed image obtained using the proposed method.

Next, a simulation study is performed with simulated amplitude type particle object of size 400×400 pixels as shown in Fig. 3.3(a). The in-line hologram is shown in Fig. 3.3(b). Figure 3.3(c) represents the reconstructed amplitude image with conventional holography. Figure 3.3(d-f) represent the reconstructed amplitude images with proposed method after $2, 5$ and 20 iterations, respectively.

The experimental validation of the proposed method is provided with a hologram recorded in a digital in-line holographic setup with spherical wave illumination of wavelength $\lambda = 632.8\ nm$. A

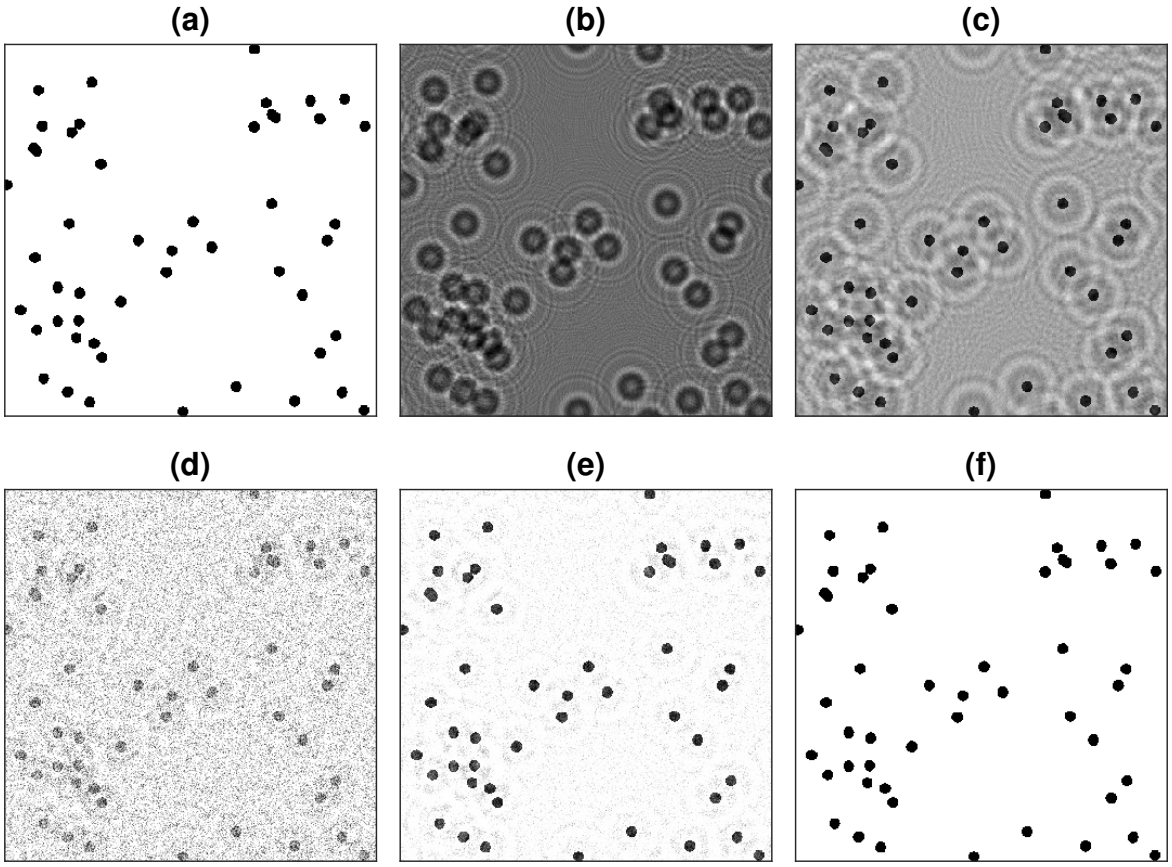

Figure 3.3: Simulated result: (a) Simulated particle object of size 400×400 pixels, (b) in-line hologram, (c) reconstructed amplitude images using conventional reconstruction method and (d-f) proposed method after $2, 5$ and 20 iterations, respectively.

glass cuvette of $1\ cm$ width containing polystyrene particles of diameter $40\ \mu m$ suspended in water is considered as the object. The hologram (shown in Fig. 3.4(a)) is recorded using a CMOS camera VEXG-13M with 1024×1280 pixels and $4.8\ \mu m$ pixel size. The hologram is reconstructed in the range of cuvette distance using both conventional and proposed method. The maximum intensity map of the reconstructed amplitudes for conventional and proposed method are shown Fig. 3.4(b) and Fig. 3.4(c), respectively.

In the results shown in Figs.3.1-3.4, it can be clearly seen that the proposed method is able to provide improvment in the reconstruction quality in comparison with the conventional method. The twin image effect and background noise are significantly reduced. In order to quantify the improvement, following image quality metrics are used: root mean square error (RMSE), peak signal to noise ratio (PSNR), structural similarity (SSIM), normalized cross correlation (NCC) and quality index (QI). These metrics were evaluated for conventional and iterative estimation based reconstructed images considering 20 iterations.

Table 3.1: Comparison of reconstructed image quality for conventional and Fienup's iterative estimation based methods with 20 iterations.

	Quality index									
	RMSE		PSNR (dB)		SSIM		NCC		QI	
	Conv.	Proposed	Conv.	Proposed	Conv.	Proposed	Conv.	Proposed	Conv.	Proposed
Fig. 3.1(a)	0.490	0.082	14.25	49.94	0.199	0.830	0.357	1.0	0.473	0.883
Fig. 3.2(a)	0.429	0.004	16.92	109.58	0.361	0.991	0.556	1.0	0.544	0.995
Fig. 3.3(a)	0.364	0.0003	20.23	165.14	0.370	0.999	0.638	1.0	0.650	0.999

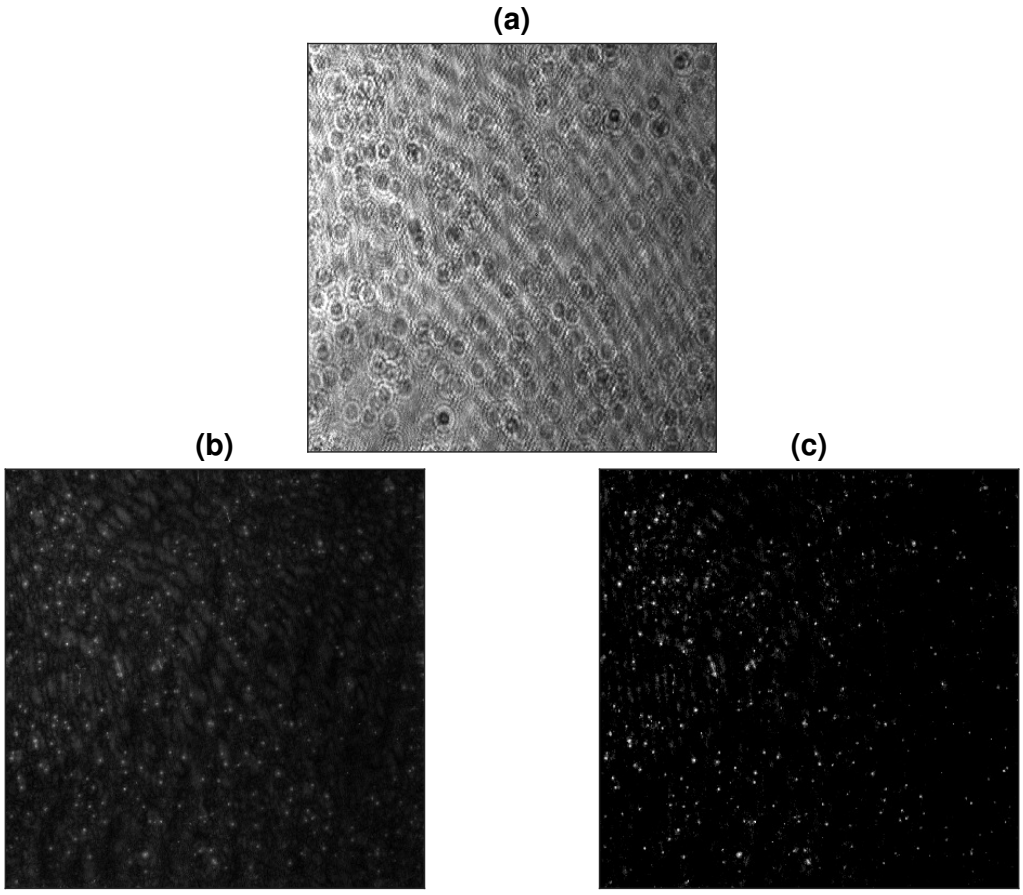

Figure 3.4: Experimental result: (a) Recorded hologram of size 1024×1280 pixels with polystyrene particles of diameter $40\ \mu m$. (b) maximum amplitude map of the reconstructed images with conventional reconstruction method and (c) proposed method. [182].

Table 3.1 provides the quality metrics evaluated for objects shown in Fig. 3.1(a), Fig. 3.2(a) and Fig. 3.3(a), respectively, using the conventional and proposed methods.

3.1.3 Conclusion

A new iterative estimation based reconstruction technique in digital in-line holography is discussed. The simulation and experimental results substantiate the practical applicability of the proposed method.

3.2 Fast Reconstruction of digital in-line hologram using Toeplitz Matrix based Deconvolution

In this section, we propose a hologram reconstruction algorithm based on Toeplitz matrix based deconvolution (TMD) applicable for digital in-line holographic configuration. The reconstructed image quality obtained using the proposed method is similar to with that obtained using conventional reconstruction algorithms, for example, the Fresnel transform (FrT) based method. However, the proposed method is found to achieve the reconstruction in comparatively less time. The improvement of the reconstructed image quality using the TMD in association with iterative reconstruction algorithm is also discussed.

3.2.1 Methodology

The methodology of the proposed method is described using a digital in-line lens-less holography setup described in Fig. 1.2. The light wave coming from a point source, placed at the origin in the $(x_0, y_0; z = 0)$ plane illuminates the object placed at $(x, y; z = z_1)$ plane. The object scattered beam and reference beam propagate to sensor plane and the intensity of interference pattern is recorded as hologram as described in Eq. 3.3.

3.2.1.1 Reconstruction of hologram using Toeplitz Matrix based Deconvolution

As described in Eq. 3.3, the hologram recording is basically a convolution operation of amplitude transmittance function associated with the object O with the convolution kernel p. Without loss of generality, we can neglect the constant and quadratic phase term appearing before the integration, as they are independent of the object, the complex wavefield at the sensor plane can be expressed as,

$$U_s(X, Y) = \iint O(x, y)\, p_{z_1,Z}(x, y, X, Y) dx dy, \tag{3.9}$$

which is a first-kind Fredholm integral equation. The convolution kernel p can be defined as,

$$p_{z_1,Z}(x, y, X, Y) = \frac{-i}{\lambda z_1 z_2} \exp\left\{\frac{i\pi Z}{\lambda z_1 z_2}\left[\left(x - X\frac{z_1}{Z}\right)^2 + \left(y - Y\frac{z_1}{Z}\right)^2\right]\right\} \tag{3.10}$$

The terms associated with variables (x, X) and (y, Y) of the convolution kernel p are separable, which gives p a special form: $p_{z_1,Z}(x, y, X, Y) = \frac{-i}{\lambda z_1 z_2} g_{z_1,Z}(x, X) h_{z_1,Z}(y, Y)$, where, $g_{z_1,Z}(x, X) = \exp\left[\frac{i\pi Z}{\lambda z_1 z_2}\left(x - X\frac{z_1}{Z}\right)^2\right]$ and $h_{z_1,Z}(y, Y) = \exp\left[\frac{i\pi Z}{\lambda z_1 z_2}\left(y - Y\frac{z_1}{Z}\right)^2\right]$. For the purpose of discretization of convolution and deconvolution operations, the Toeplitz matrices can be defined as

[183]

$$B_{mn} = \exp\left[\frac{i\pi Z}{\lambda z_1 z_2}(m-n)^2\right], D_{pq} = \exp\left[\frac{i\pi Z}{\lambda z_1 z_2}(q-p)^2\right], \tag{3.11}$$

where, B and D represent the Toeplitz matrices consisting of discrete samples of $g_{z_1,Z}(x,X)$ and $h_{z_1,Z}(y,Y)$, respectively. Considering the $M \times N$ sized digital hologram, we have $m,n \in [1,N]$ and $p,q \in [1,M]$.

Accordingly, the hologram recording process can be represented as

$$H = |BOD|^2, \tag{3.12}$$

where H and O represent the matrices corresponding to $H(X,Y)$ and $O(x,y)$, respectively. In a similar manner, the hologram reconstruction can also be formulated as,

$$U_{r_z} = B^* H D^*, \tag{3.13}$$

where B^* and D^* represent the complex conjugate of B and D, respectively.

In the case of plane-wave illumination of the object, the matrices B and D are evaluated as,

$$B_{mn} = \exp\left[\frac{i\pi}{\lambda z_2}(m-n)^2\right], D_{pq} = \exp\left[\frac{i\pi}{\lambda z_2}(q-p)^2\right]. \tag{3.14}$$

where z_2 represents the object plane to sensor plane distance. Figure 3.5(a) shows the real part of B evaluated for $z_2 = 1000$ mm, $\lambda = 632.8$ nm, $m,n \in [1,580]$ and $p,q \in [1,580]$. In the case of plane-wave illumination, only that part of B should be used in the hologram reconstruction wherein the phase gradient do not exceed the range of $[-\pi,\pi]$ to avoid the aliasing effect. Figure 3.5(b) shows the phase and phase gradient of B along its antidiagonal indicated with red color line in Fig. 3.5(a). It can be observed that the phase gradient crosses the value of $-\pi$ and π at indexes 187 and 393, respectively. The entries of B below and above the diagonal passing through these index locations are set to zero as shown in Fig. 3.5(c). On the other hand, in the case of spherical wave illumination, it is observed that the limit to phase gradient variation range should be selected as $[-2\pi,2\pi]$ because of the quadratic phase term associated with the wavefront.

Let $M = N$ and Δ represent the pixel size. The theoretical lateral resolution in digital in-line holography setup under the plane wave illumination is $\delta_{plane} = \lambda z_2/N\Delta$ [15]. In the case of spherical illumination, the imaging resolution varies depending on the source to object distance. If source to object distance is less (z_1 <<), the imaging resolution is $\delta_{spherical} = \lambda z_1/N\Delta\sqrt{((N\Delta/2)^2 + z_2^2)}$. On the other hand, if source to object distance is large (z_1 >>), the imaging resolution is $\delta_{spherical} = \Delta z_1/Z$ [184]. In practice, the achievable resolution in in-line holography depends upon the ability of

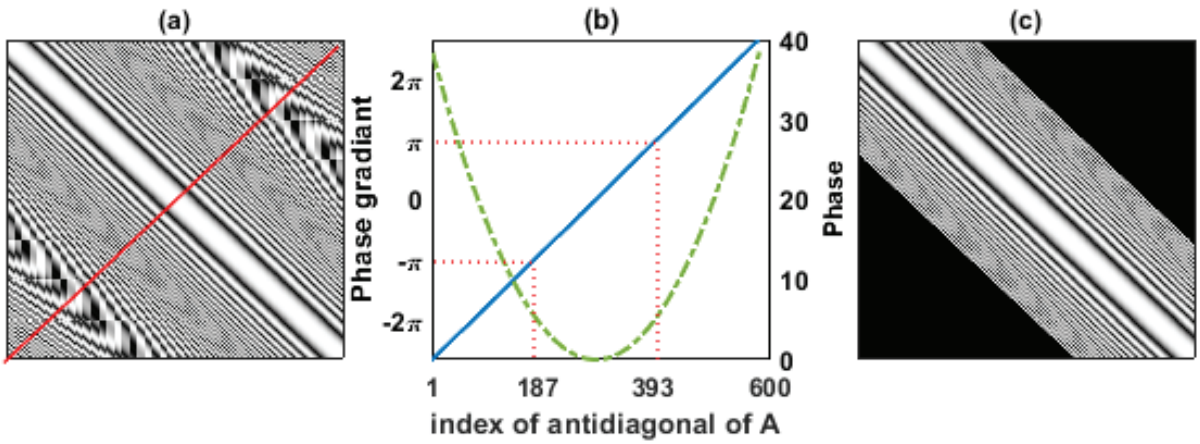

Figure 3.5: (a) Real part of B. Red color line indicates the antidiagonal of B (b) phase and phase gradient plots corresponding to the antidiagonal of B, and (c) real part of B after replacing its elements below and above specific diagonals with zeros to avoid the effect of aliasing [52].

the digital sensor to record finest interference fringes [15]. Therefore, the maximum achievable imaging resolution in digital in-line holography with plane wave and spherical wave illumination are Δ and $\Delta z_1/Z$, respectively.

3.2.2 Results and Discussion

Digital lensless in-line holographic setup with a spherical beam illumination of the object is considered for simulation study. A laser source of wavelength $\lambda = 632.8$ nm and camera pixel size of 4.8 μm was considered. An USAF target amplitude object of size 580×580 pixels as shown in Fig. 3.6(a) was placed such that $z_1 = 80$ mm and $Z = 100$ mm. The corresponding simulated hologram is shown in Fig. 3.6(b). The reconstructed object images evaluated using the FrT and TMD methods are shown in Fig. 3.6(c) and Fig. 3.6(d), respectively. Both the methods are found to provide similar reconstruction results. Similar study was performed considering DIH with plane-wave illumination of the same USAF object. The hologram shown in Fig. 3.7(a) was simulated considering object to sensor plane distance $z_2 = 20$ mm. The reconstructed object images obtained using the FrT and TMD methods are shown in Fig. 3.7(b) and Fig. 3.7(c), respectively. In this case too, similar reconstruction results were obtained using both methods. For the purpose of quantitative performance comparison between TMD and FrT, image quality metrics RMSE, PSNR, SSIM, NCC and QI were evaluated as a function of z_1 for spherical-wave illumination based setup with the source-to-sensor distance fixed at $Z = 100$ mm. Table 3.2 provides the quality metrics evaluated for the USAF target amplitude object shown in Fig. 3.6(a) using the FrT and TMD methods. It can be noted that both methods provide almost similar reconstruction quality results.

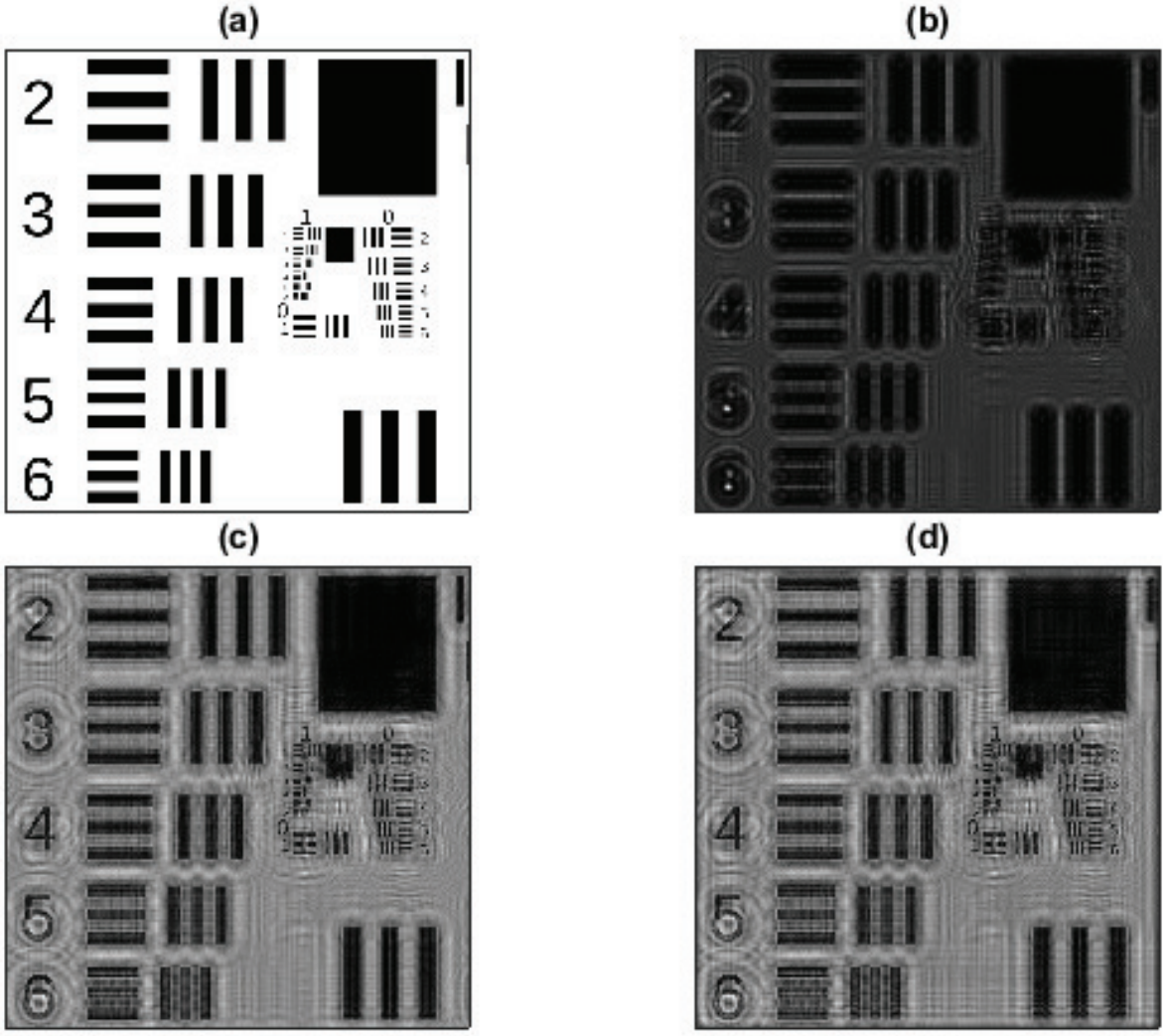

Figure 3.6: Simulation result of hologram reconstruction using TMD for lensless DIH with spherical wave illumination: (a) 580×580 pixels USAF target object, (b) simulated hologram considering $z_1 = 80$ mm and $Z = 100$ mm, reconstructed images obtained using the (c) FrT and (d) TMD methods [52].

Table 3.2: Comparison of quality of reconstructed images obtained using the FrT and TMD methods with 580×580 pixels USAF target amplitude object in function of z_1 ($Z = 100$ mm)

Distance z_1 **(mm)**	Quality Metric									
	RMSE		PSNR (dB)		SSIM		NCC		QI	
	FrT	TMD	FrT	TMD	FrT	TMD	FrT	TMD	FrT	TMD
95	0.412	0.410	17.71	17.83	0.288	0.268	0.542	0.547	0.473	0.472
90	0.456	0.458	15.69	15.61	0.251	0.238	0.494	0.494	0.516	0.515
85	0.489	0.481	14.31	14.63	0.243	0.237	0.455	0.467	0.530	0.526
80	0.469	0.473	15.15	14.96	0.242	0.233	0.485	0.482	0.536	0.537

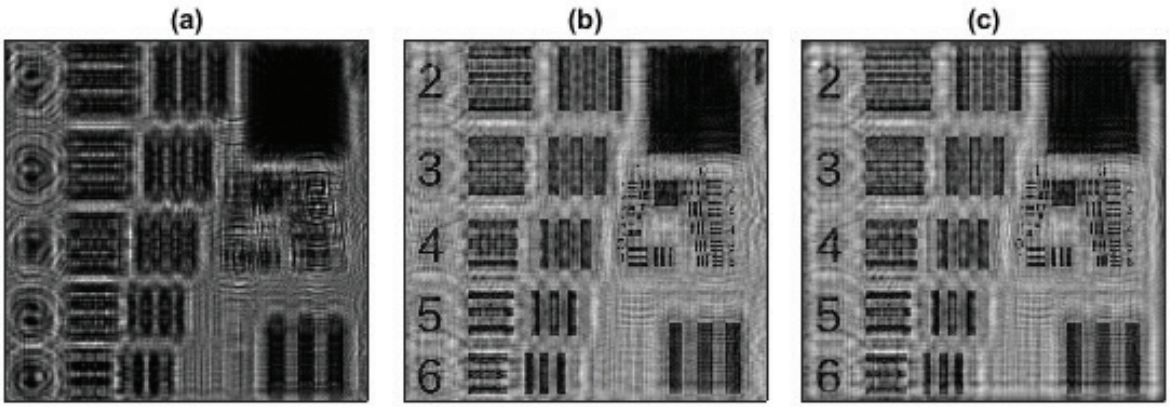

Figure 3.7: Simulation result of hologram reconstruction using TMD for DIH with plane wave illumination: (a) simulated hologram considering $z_2 = 20$ mm, reconstructed image obtained using the (b) FrT and (c) TMD methods [52].

The performance of the proposed method is validated with particle objects. Figure 3.8(a) shows the simulated object of size 1200×1200 consisting of 100 number of particles each of diameter 24 pixels. Considering DIH with plane-wave illumination of the object, Fig. 3.8(b) shows the simulated hologram obtained for $z_2 = 50$ mm. The hologram is numerically reconstructed using the FrT and TMD method as shown in Figs. 3.8(c) and 3.8(d), respectively. It can be deduced from this result that the proposed TMD method is capable of providing particle image reconstruction similar to the FrT method.

The experimental validation of the proposed method is performed using a digital in-line holographic setup with a plane beam object illumination as shown in Fig 1.1(a). A solid-state laser source (MSL-III-532/20 mW) of wavelength $\lambda = 532$ nm was used to illuminate 1951-USAF test target object (R3L3S1P, THORLABS) placed at a defocus distance of $z_2 = 724$ μm from a microscope objective (MO). The camera sensor is placed at a distance from the MO such that 15X magnification is obtained. The hologram of size 2048×2048 pixels was recorded using a CMOS camera (Pixelink, PL-D734MU-T) having pixel size of 5.5 μm. The practical laboratory system of above holographic setup is shown in Fig. 3.9. Figure 3.10(a) shows the experimentally recorded hologram. The reconstructed images computed using the FrT and TMD methods are shown in Figs. 3.10(b) and 3.10(c), respectively. It can be seen that both methods provided equally good reconstruction results. The computation time taken by the FrT and TMD methods were 0.99 seconds and 0.73 seconds, respectively.

Another experiment was performed using the holograms recorded in digital lens-less in-line holographic setup with spherical beam object illumination similar to that shown in Fig. 1.1(d). A He-Ne laser source (LASOS, LGK 7628) of wavelength $\lambda = 632.8$ nm was used to illuminate object sam-

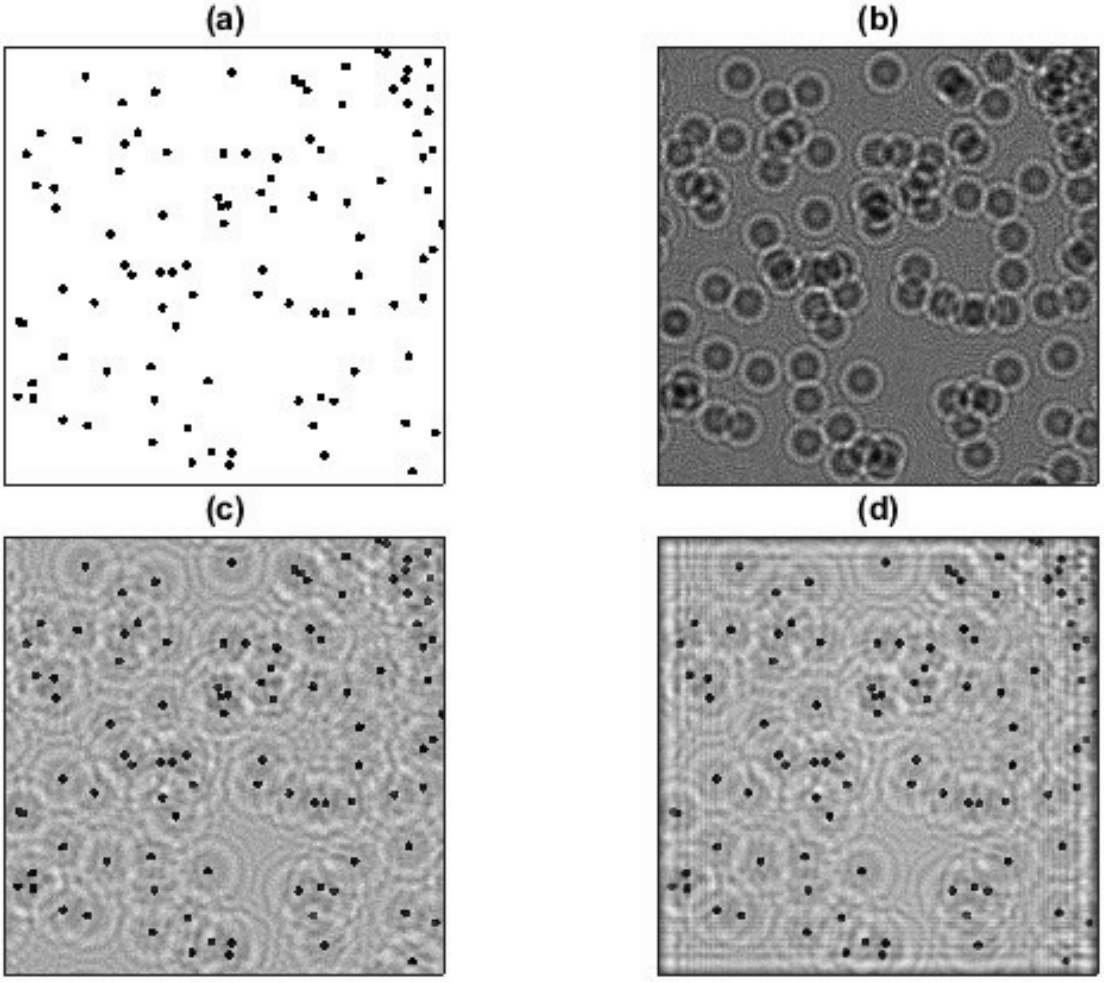

Figure 3.8: Simulation result of hologram reconstruction using TMD for DIH with plane wave illumination: (a) 1200 × 1200 pixels object consisting of 100 particles, (b) simulated hologram considering $z_2 = 50$ mm, reconstructed images obtained using the (c) FrT and (d) TMD methods [52].

ple, a 3.5 μl glass cuvette containing polystyrene micro-beads of diameter 40 μm immersed in distilled water. The center of the cuvette was placed at a distance of $z_1 = 583$ mm from point source, where source-to-camera distance was $Z = 600$ mm. The holograms of size 1280 × 1024 pixels were recorded using a CMOS camera (Baumer, VEXG-13M) having pixel size of 4.8 μm. Figure 3.11(a) shows the experimentally recorded hologram of particle object. The reference hologram shown in Fig. 3.11(b) was subtracted from the object hologram. The reconstructed images computed using the FrT and TMD methods are shown in Figs. 3.11(c) and 3.11(d), respectively. The circular Hough transform based edge detection algorithm was applied to detect and estimate size of the particles. The FrT method resulted in detection of 48 number of particles with average diameter of $d_{avg} = 46.1$ μm and standard deviation $\sigma = 9.5$ μm. On the other hand, the TMD method provided detection of 51 number of particles with $d_{avg} = 47.04$ μm and $\sigma = 10.4$ μm. The computation time taken by the FrT method was 0.3

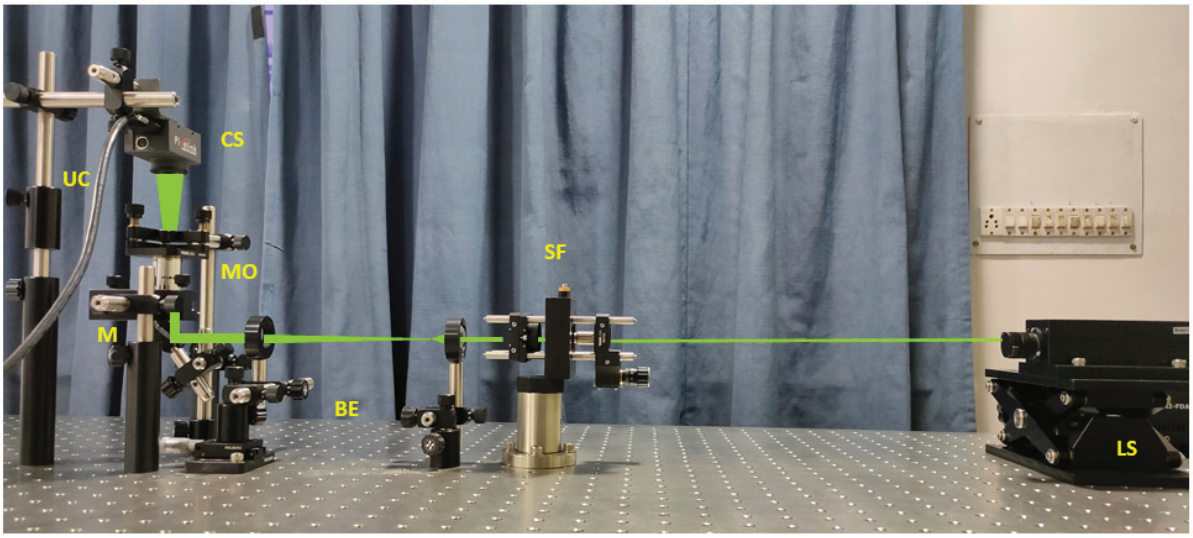

Figure 3.9: Practical lab system of the digital in-line holography setup with plane beam illumination, as shown in schematic Fig. 1.1(a).

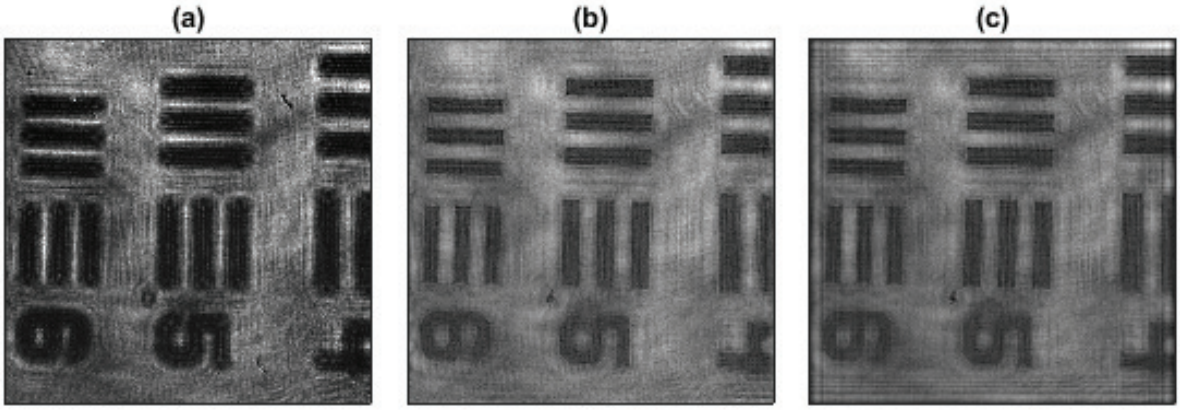

Figure 3.10: Experimental result of hologram reconstruction using TMD with plane wave illumination: (a) experimentally recorded hologram of size of the 1951-USAF test target object with $z_2 = 724$ μm. Reconstructed images obtained using the (b) FrT and (c) TMD methods [52].

seconds whereas the same for TMD method was only 0.15 seconds. The quality of hologram reconstruction was further improved by using the FrT and TMD methods in association with iterative estimation based algorithm [70]. The reconstructed images obtained using the iterative algorithm are shown in Fig. 3.12(a) and Fig. 3.12(b), respectively. In this case, while the FrT method detected 49 number of particles with $d_{avg} = 40.6$ μm and $\sigma = 3.35$ μm, the TMD method detected 51 number of particles with $d_{avg} = 38.85$ μm and $\sigma = 3.32$ μm. Since the polystyrene micro-bead sizes have a tolerance of 5%

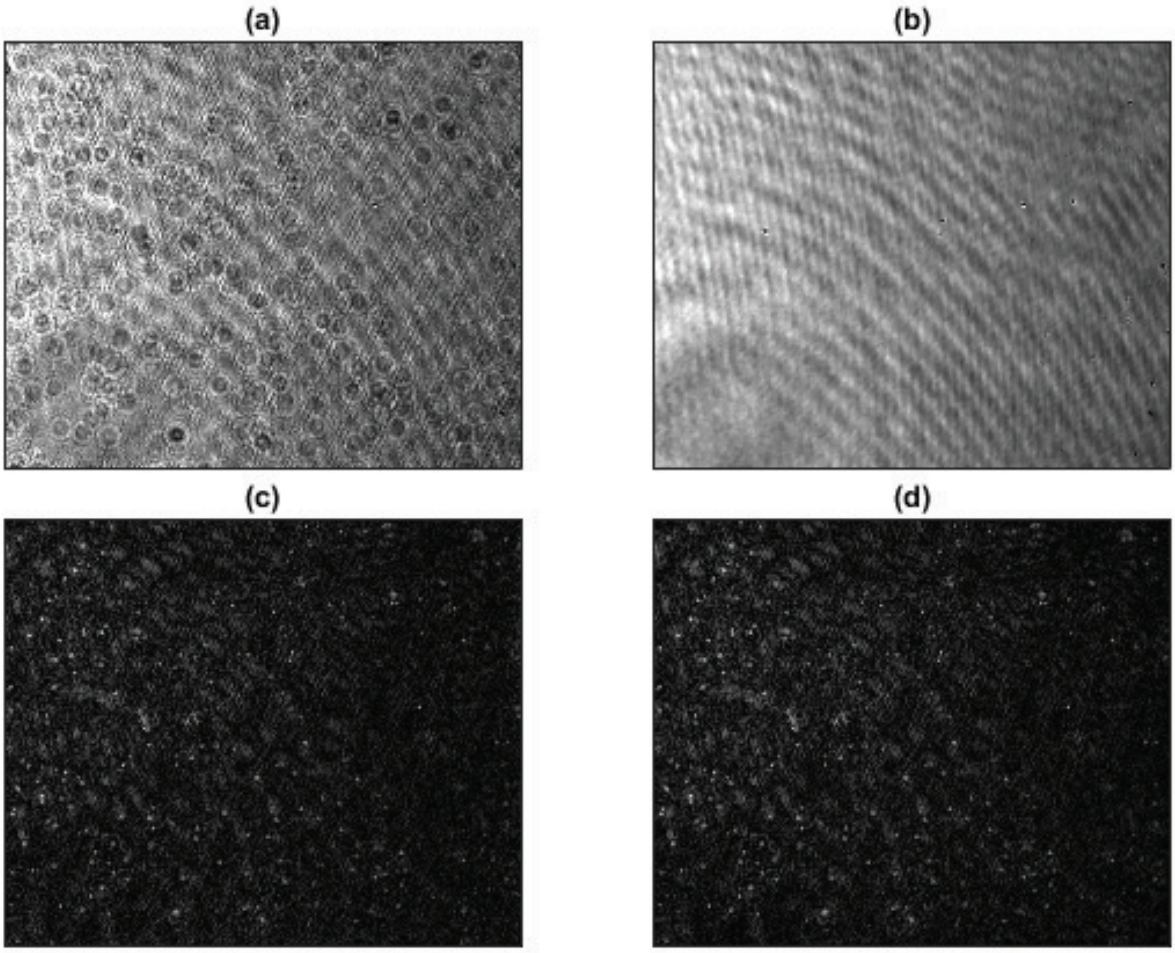

Figure 3.11: Experimental result of hologram reconstruction using TMD with spherical wave illumination: (a) 1280×1024 pixels recorded hologram using 40 μm polystyrene particles kept in a cuvette placed such that $z_1 = 583$ mm and $Z = 600$ mm, (b) reference hologram, reconstructed images obtained using the (c) FrT and (d) TMD methods [52].

as specified by the manufacturer, the proposed method is found to provide particle size estimation with good accuracy. The computation time taken for iterative algorithm implementation with the FrT and TMD methods were 7.32 seconds and 5.59 seconds, respectively.

The computation time taken by the FrT and TMD methods in hologram reconstruction are tabulated in Table 3.3 as a function of hologram sizes. It can be noted that the TMD method provides higher computational efficiency in comparison to the FrT based method while maintaining the similar reconstruction quality. This improvement is particularly evident in the case of iterative reconstruction algorithm as it involves the reconstruction to be performed multiple times. The twin image effect as well as background noise of the reconstructed images can be reduced by integrating the proposed TMD method with our proposed iterative estimation based reconstruction algorithm. All the algorithms are implemented using

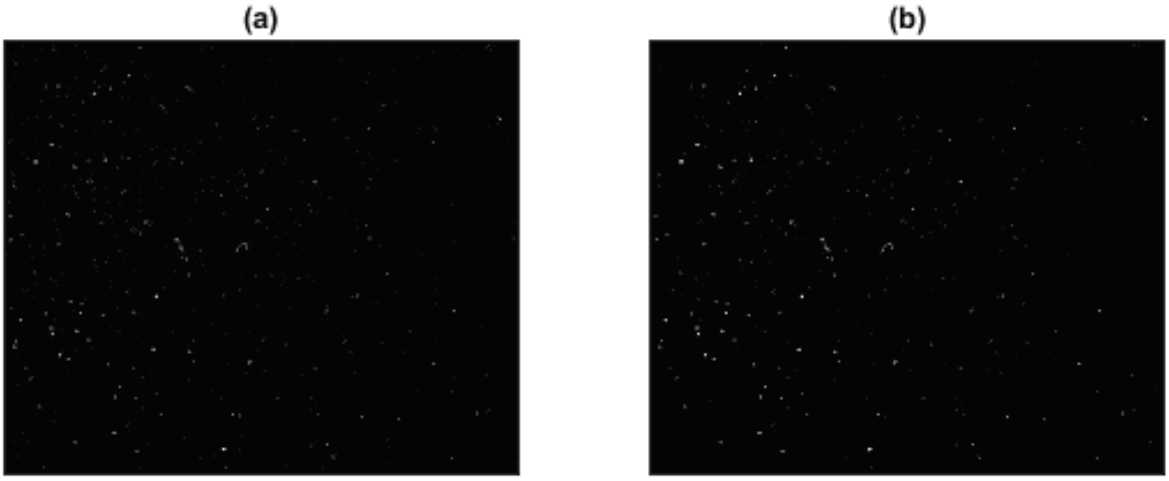

Figure 3.12: Experimental result of hologram reconstruction using iterative estimation with TMD: (a) reconstructed image from from iterative estimation with FrT, (b) reconstructed image from iterative estimation with TMD [52].

MATLAB-19a on a computer with the Intel(R) Core(TM) i7-8700 processor with 3.2 GHz Octacore and 16 GB RAM.

Table 3.3: Computation time for FrT and TMD in function of hologram sizes (in seconds)

Reconstruction methods	Hologram size (pixels)						
	200×200	400×400	580×580	800×800	1000×1000	1200×1200	2000×2000
FrT	0.02	0.03	0.063	0.1	0.226	0.236	0.72
TMD	**0.001**	**0.008**	**0.02**	**0.04**	**0.105**	**0.112**	**0.48**

3.2.3 Conclusion

The proposed digital hologram reconstruction algorithm based on TMD is found to provide the reconstruction quality similar to the conventional algorithm with better computational efficiency. This increase in computational efficiency is more prominent when the hologram reconstruction is performed in an iterative manner. The TMD based algorithm is currently limited to the digital in-line holographic configuration. In the future study, its applicability to other holographic configurations can be explored.

भारतीय प्रौद्योगिकी संस्थान गुवाहाटी
Indian Institute of Technology Guwahati

4

Hologram Interpolation method

4.1 Improvement of Reconstructed Image quality using Autoregressive Interpolation of hologram

We have developed an autoregressive interpolation based technique for the improvement of quality of hologram reconstructed images especially the low-frequency terms associated the object. The proposed method along with the iterative extrapolation technique can help improve the resolution of the reconstructed images.

4.1.1 Methodology

In the proposed algorithm, the hologram interpolation is performed by modelling the hologram intensity as a two-dimensional autoregressive (AR) process within a given window. The sub-pixel intensity is estimated using the AR model parameters. The original hologram pixels are treated as low-resolution (LR) pixels, whereas the sub-pixels are considered to be high-resolution (HR) pixels. The interpolation operation effectively provides higher pixel density in a given sensor area. Fig. 4.1(a) describes the formation of HR hologram from the given LR hologram [185]. As shown in the figure, interpolation is performed by inserting rows and columns between two consecutive rows and columns of LR hologram. The solid dots represent the LR image pixels (I). The interpolation is performed in two stages: In the first stage, the shaded circle HR pixel intensities are estimated, and in the second stage, the remaining

[4]The chapter includes an algorithm based on autoregressive hologram interpolation for improvement in the reconstructed image quality.

white circle HR pixel intensities are estimated. The HR pixels are denoted by $\tilde{I}$.

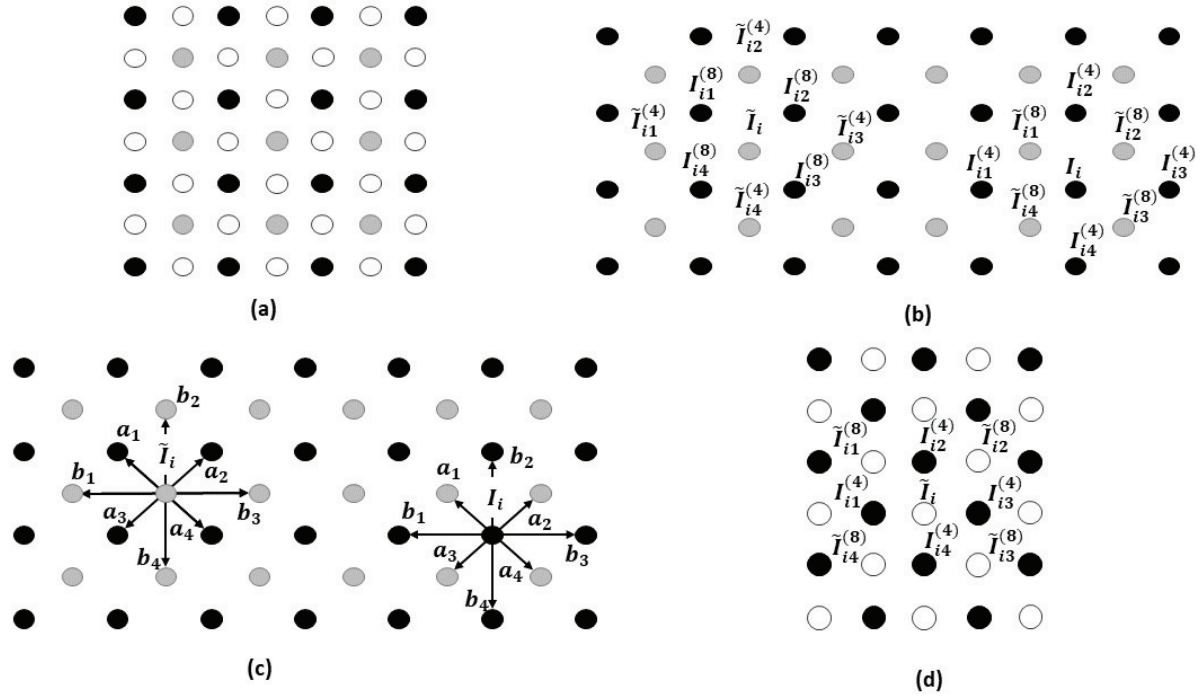

Figure 4.1: (a) HR image formation by inserting rows and column between two consecutive rows and columns of LR hologram (b) pixel configuration in the first stage of hologram interpolation (c) model parameter $\hat{\boldsymbol{a}} = (a_1, a_2, a_3, a_4)$ and $\hat{\boldsymbol{b}} = (b_1, b_2, b_3, b_4)$ defined as per the spatial pixel correlation and (d) pixel configuration in the second stage of interpolation.[186]

4.1.1.1 First stage AR interpolation:

Figure 4.1(b) shows the spatial relation of LR and HR pixels involved in the first stage of AR interpolation. For a HR pixel $\tilde{I}_i$ at the ith location, its four 8-connected neighbour LR pixels are denoted by $I_{it}^{(8)}$ and its four 4-connected neighbour HR pixels are denoted as $\tilde{I}_{it}^{(4)}$, where $t = 1, 2, 3, 4$. Similarly, for a LR pixel I_i at the ith location, its 8-connected neighbour HR pixels and 4-connected neighbour LR pixels are denoted as $\tilde{I}_{it}^{(8)}$ and $I_{it}^{(4)}$ respectively, where $t = 1, 2, 3, 4$.

In the proposed algorithm, a piecewise AR interpolation scheme as described in [185] is used where, a soft-decision interpolation technique is performed to estimate the missing pixels in groups using a 2-D piecewise autoregressive model. The HR pixels are estimated in a local window and provides better spatial coherence of interpolated images. The AR parameters are considered to be constant within the local window W where $i \in W$. Considering that there exists n HR pixels $\tilde{I} = (\tilde{I}_1, \tilde{I}_2, .., \tilde{I}_n)$ in the local

window W, the piecewise AR model can be represented as

$$\tilde{I}_i = \sum_{1 \leq t \leq 4} a_t I_{it}^{(8)} + \rho_i, \tag{4.1}$$

where, $\hat{\boldsymbol{a}} = (a_1, a_2, a_3, a_4)$ represent the AR model parameters. As shown in Fig. 4.1(c), $\hat{\boldsymbol{a}}$ characterizes diagonal correlation among pixel intensities, and ρ represents the random perturbation independent of spatial location and image intensity. The parameter ρ defines the AR model noise, which is considered to be white Gaussian noise of zero mean and non-zero variance. Furthermore, the same AR model in Eq. 4.1 can represent the known LR pixel intensity in terms of unknown HR pixel intensities. Accordingly,

$$I_i = \sum_{1 \leq t \leq 4} a_t \tilde{I}_{it}^{(8)} + \rho_i \tag{4.2}$$

Thus, given AR model parameters, the set of unknown HR pixel intensities $\tilde{\boldsymbol{I}} = (\tilde{I}_1, \tilde{I}_2, \cdots, \tilde{I}_n)$ can be estimated as,

$$\tilde{\boldsymbol{I}} = \arg\min_{\tilde{\boldsymbol{I}}} \left\{ \sum_{i \in W} |\tilde{I}_i - \sum_{1 \leq t \leq 4} a_t I_{it}^{(8)}| + \sum_{i \in W} |I_i - \sum_{1 \leq t \leq 4} a_t \tilde{I}_{it}^{(8)}| \right\} \tag{4.3}$$

The feedback mechanism used in Eq. 4.3 allows to establish the mutual influence among the known LR and unknown HR pixels. Further, in order to include the pixel intensity correlation among pixels in the horizontal and vertical directions, another set of AR parameter $\hat{\boldsymbol{b}} = (b_1, b_2, b_3, b_4)$ is considered such that

$$\tilde{I}_i = \sum_{1 \leq t \leq 4} b_t \tilde{I}_{it}^{(4)} + \rho_i, \tag{4.4}$$

$$I_i = \sum_{1 \leq t \leq 4} b_t I_{it}^{(4)} + \rho_i \tag{4.5}$$

Thus, based on the knowledge of AR parameters, the unknown HR pixel intensities can be estimated by combining Eqs. 4.1-4.5 as,

$$\tilde{\boldsymbol{I}} = \arg\min_{\tilde{\boldsymbol{I}}} \left\{ \sum_{i \in W} |\tilde{I}_i - \sum_{1 \leq t \leq 4} a_t I_{it}^{(8)}| + \sum_{i \in W} |I_i - \sum_{1 \leq t \leq 4} a_t \tilde{I}_{it}^{(8)}| + \eta \sum_{i \in W} |\tilde{I}_i - \sum_{1 \leq t \leq 4} b_t \tilde{I}_{it}^{(4)}| \right\} \tag{4.6}$$

subject to the constrain that

$$\sum_{i \in W} |\tilde{I}_i - \sum_{1 \leq t \leq 4} b_t \tilde{I}_{it}^{(4)}| \approx \sum_{i \in W} |I_i - \sum_{1 \leq t \leq 4} b_t I_{it}^{(4)}| \tag{4.7}$$

Here, in the third term of Eq. 4.6, as unknown HR pixels $\tilde{I}$ are estimated from neighbouring unknown horizontal pixels in a local window, the chance of the estimation error is very high. To overcome this, the

Lagrangian multiplier η is multiplied with this to regulate its contribution. Although, η can take values between 0.2 and 0.7, we have selected $\eta = 0.5$ as suggested in [185]. It has been found that the variation in η does not change the particle detection accuracy significantly.

The AR parameters are required in order to obtain the estimate of unknown pixel intensities $\tilde{\boldsymbol{I}}$ in a given window W using Eq. 4.7. These parameters can be computed as

$$\hat{\boldsymbol{a}} = \arg\min_{\boldsymbol{a}} \sum_{i \in W} \left(I_i - \sum_{1 \le t \le 4} a_t I_{it}^{(8)} \right)^2 \tag{4.8}$$

$$\hat{\boldsymbol{b}} = \arg\min_{\boldsymbol{b}} \sum_{i \in W} \left(I_i - \sum_{1 \le t \le 4} b_t I_{it}^{(4)} \right)^2 \tag{4.9}$$

Note that these AR parameter estimates are obtained using the known LR pixel intensities only. These estimates are subsequently used to solve Eq. 4.6 based on a matrix formulation as described in [185]. In the implementation of the proposed method, an octagonal window W has been considered such that it consists of 12 unknown HR pixels $\tilde{I}$. The interpolation is performed in a moving window manner. Accordingly, only four pixels are updated with their average interpolated intensity estimates evaluated in respective overlapping windows.

4.1.1.2 Second stage AR interpolation:

In the first stage, the gray pixels shown in Fig. 4.1(a) are estimated. At the end of first stage, the pixel configuration is shown in Fig. 4.1(d). It can be observed that it is basically 45^o rotated version of the pixel configuration shown in Fig. 4.1(a). Therefore, the same approach of unknown HR pixel intensity estimation considered in the first stage is used in the second stage with the appropriate window orientation.

4.1.2 Results and Discussion

A simulation study is performed considering a DIH setup with a plane wave illumination of an amplitude object with a laser source of wavelength $\lambda = 450\ nm$. The hologram recording camera pixel size is 5.5 μm. The hologram simulation and reconstruction are performed based on the paraxial approximation of light propagation implemented using fast Fourier transform routines [187]. In the following, simulation results are provided for single and multiple number of particles of same and different sizes.

4.1.2.1 Single Particle:

A simulated single particle object of diameter $d = 27.5\ \mu m$ is shown in the Fig. 4.2(a). A hologram of size 400×400 pixels was generated with $z_2 = 80\ mm$. Figure 4.2(b) shows the simulated hologram intensity map. The hologram was interpolated using the proposed method to 800×800 ($2\times$) and 1600×1600 ($4\times$) as shown in Figs. 4.2(c) and 4.2(d), respectively. The reconstructed images computed using the original and interpolated holograms are shown in Figs. 4.2(f)-4.2(h), respectively. The $y = 200$ rows of the LR reconstructed image and corresponding row of HR reconstructed images are plotted in Fig. 4.2(e) for the purpose of comparison. It can be observed that the hologram interpolation resulted in the reconstruction image with a better visual quality. In addition, the interpolation has not resulted in any spurious components in the reconstructed image. The number of pixels associated with the object has increased with the application of AR interpolation. To further quantify the improvement in reconstruction image quality, the Hough transform based edge detection algorithm is applied to the reconstructed images. The diameter estimates of the particles in the reconstructed images from the original, $2\times$ and $4\times$ interpolated holograms are found to be $31.6\ \mu m$, $28.1\ \mu m$ and $27.6\ \mu m$, respectively. It is quite clear that the proposed hologram interpolation algorithm provides improvement in the reconstructed image quality by increasing number of pixels containing object information.

4.1.2.2 Two closely spaced particles:

Next simulation example is considered with two closely spaced particles. Figure 4.3(a) shows two particles each of diameter $d = 24.5\ \mu m$ with a spacing of $5.5\ \mu m$ corresponding to a single pixel. A hologram of size 400×400 pixels was generated with $z_2 = 80\ mm$ as shown in Fig. 4.3(b). The $2\times$ and $4\times$ interpolated holograms are shown in Figs. 4.3(c) and 4.3(d), respectively. Figures 4.3(f)- 4.3(h) show the close view of the reconstructed particle image areas corresponding to the original, $2\times$ and $4\times$ interpolated holograms, respectively. The $y = 200$ rows of the LR reconstructed image and corresponding row of HR reconstructed images are plotted in Fig. 4.3(e) for the purpose of comparison. The particle size estimation is performed for the quantitative evaluation of the effect of hologram interpolation. No particles were detected in the object image obtained with the original hologram reconstruction due to close spacing between two particles. On the other hand, both the particles were detected with diameters $23.7\ \mu m,\ 24.2\ \mu m$ and $24.4\ \mu m,\ 24.4\ \mu m$ in the images obtained from the reconstruction of $2\times$ and $4\times$ interpolated holograms, respectively. This results indicate that the proposed hologram interpolation algorithm provides better reconstructed image in the case of closely spaced particle objects.

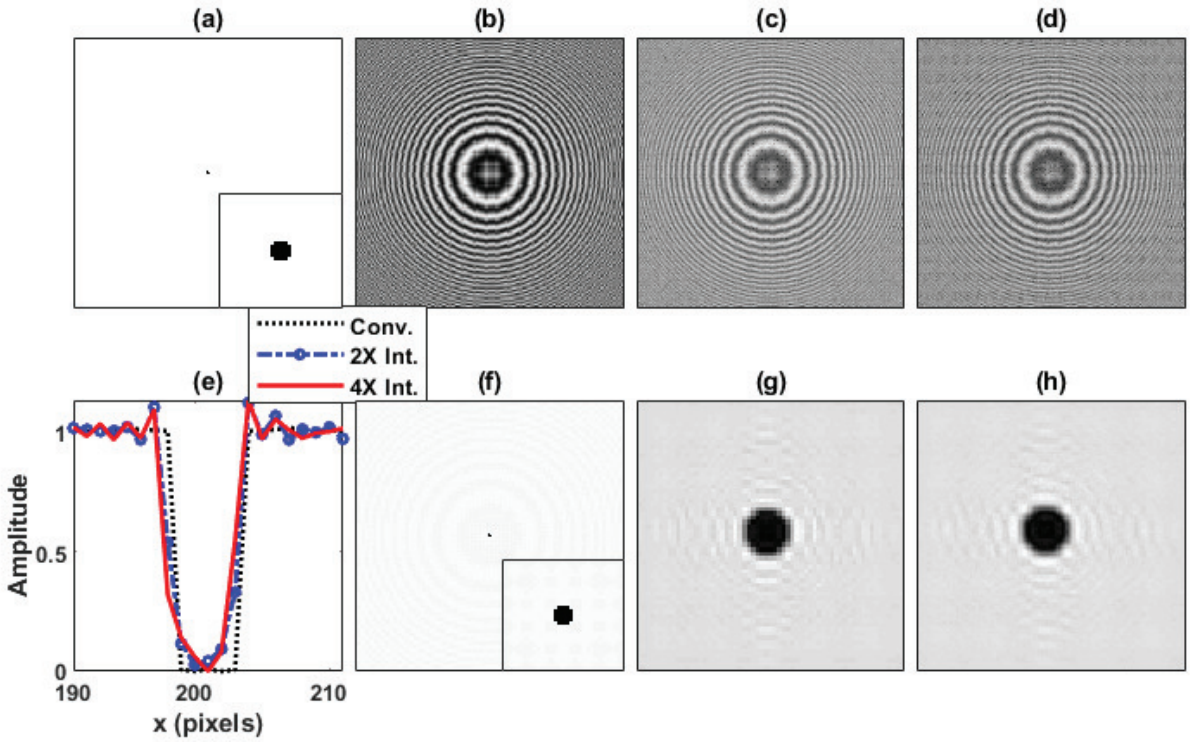

Figure 4.2: Simulation example: (a) single particle of diameter $d = 27.5\ \mu m$, (b) original hologram of size 400×400 pixels, (c) $2\times$ interpolated hologram of size 800×800 pixels, (d) $4\times$ interpolated hologram of size 1600×1600 pixels, (f-h) reconstructed images computed from the holograms shown in figure 4.2(b-d), respectively, and (e) comparison of the reconstructed amplitude profile in row $y = 200$ for LR image and corresponding row of HR images [186].

4.1.2.3 Multiple particles of same size:

A simulation example to study the effect of hologram interpolation is considered with the object plane consisting of multiple particles of same size. A 400×400 pixels size hologram was simulated with 200 particles each of diameter $d = 40\ \mu m$. Figures 4.4(a) and 4.4(b) show the randomly distributed particles and corresponding hologram recorded at $z_2 = 80\ mm$. The $2\times$ interpolated hologram is shown in Fig. 4.4(c). The reconstructed images of the original and interpolated holograms are shown in Figs. 4.4(d) and 4.4(e), respectively. In the cropped part of the red colored rectangular region, it can be clearly seen that, more number of pixels containing object information are present in the reconstructed image from interpolated hologram.

4.1.2.4 Multiple particle of different size:

The capability of the proposed algorithm is also evaluated considering distribution of multiple particles having different sizes. A random distribution of total 100 particles was simulated as shown in Fig.

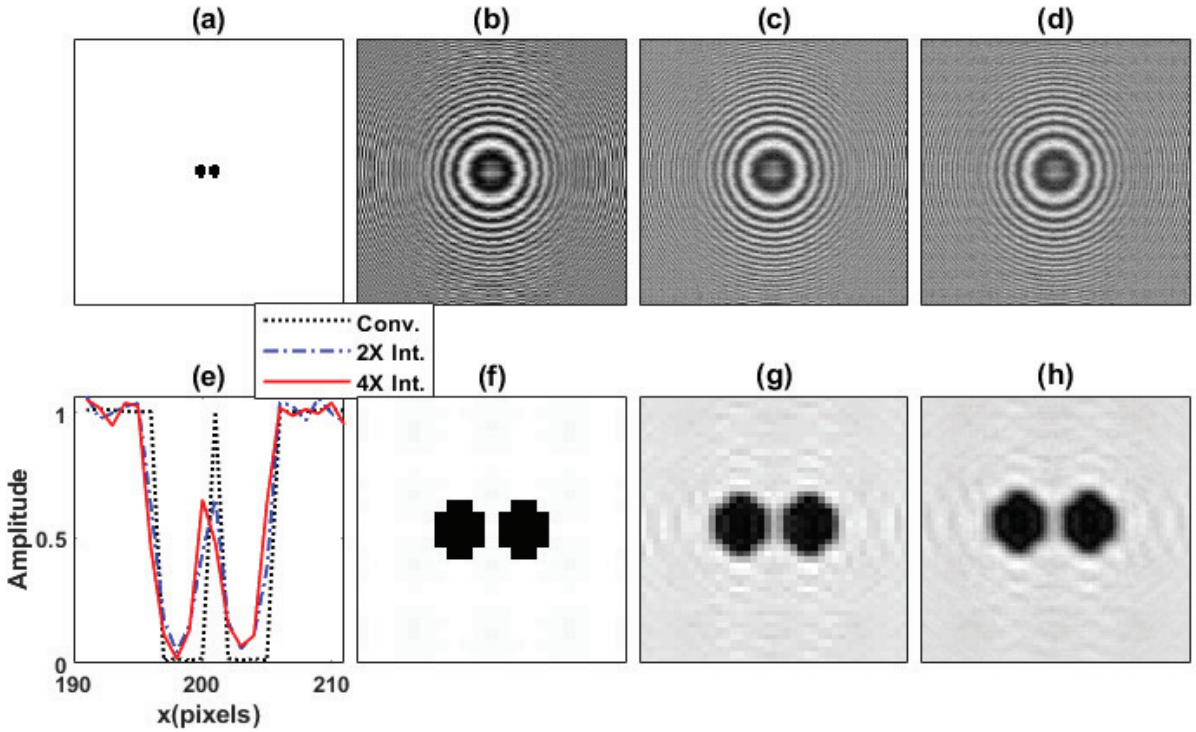

Figure 4.3: Simulation example: (a) Two closely spaced particles of diameter $d = 24.5\mu m$, (b) original hologram of size 400×400, (c) $2X$ interpolated hologram of size 800×800 pixels, (d) $4X$ interpolated hologram of size 1600×1600 pixels, (f-h) reconstructed images from holograms (b-d) respectively. (e) comparison of the reconstructed amplitude profile in row $y = 200$ for LR image and corresponding row of HR images [186].

4.5(a) with 50, 30 and 20 number of particles having diameters 20 μm, 40 μm and 80 μm, respectively. A 400×400 pixels size hologram was simulated with the object placed at $z_2 = 80\ mm$. The original and $2\times$ interpolated holograms are shown in Figs. 4.5(b) and 4.5(c), respectively. Figures 4.5(d) and 4.5(e) show the object images obtained from the reconstruction of holograms given in Figs. 4.5(b) and 4.5(c), respectively. The cropped part of the red colored rectangular region shows the improvement in the reconstructed image from interpolated hologram.

The performance of the proposed method is experimentally validated using a DIH setup with spherical beam object illumination as shown in Fig. 1.1(d). A glass cuvette of width 10 mm containing polystyrene spherical particles of diameter 40 μm suspended in distilled water was used as the object. The center of the cuvette was placed at a distance of $z_1 = 583\ mm$ from point source, and at distance of $z_2 = 17\ mm$ from the CMOS camera plane. A He-Ne laser source of wavelength $\lambda = 632.8\ nm$ was used to record the hologram of 1280×1024 size using the Baumer VEXG-13M CMOS camera having pixel size of $\Delta = 4.8\ \mu m$. Since the object is illuminated with a spherical beam, the parame-

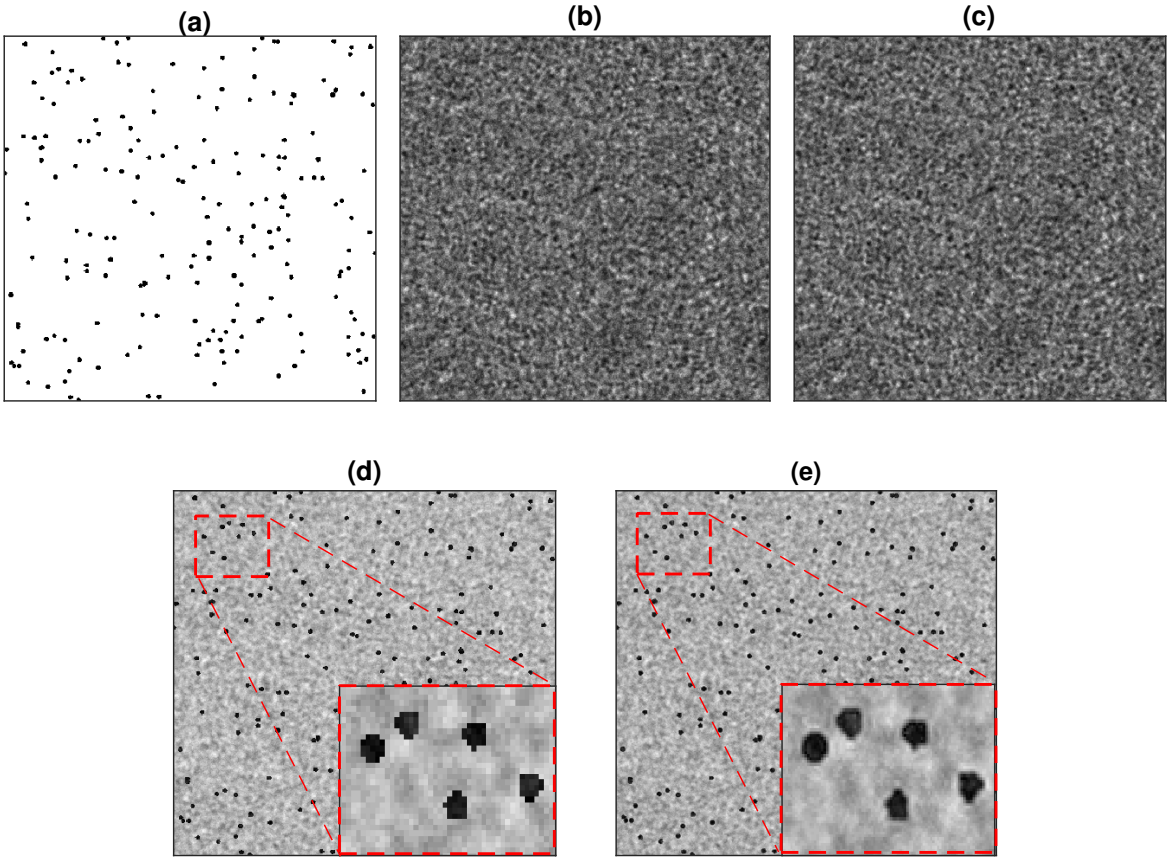

Figure 4.4: Simulation example: (a) randomly distributed particles with 200 particles each of diameter 40 μm, (b) 400×400 pixels sized hologram, (c) $2\times$ interpolated hologram, (d) and (e) reconstructed image obtained from the reconstruction of the original and $2\times$ interpolated hologram, respectively. The cropped part at the red rectangular box part are shown in inset [186].

ter z in Eq. 1.18 was set as $\tilde{z} = z_1 z_2/(z_1 + z_2)$. The magnification M_g associated with this imaging setup is $M_g = (z_1 + z_2)/z_1$. The spherical particle diameter in a given plane can be calculated as $d = d_p \Delta / M_g$, where d_p represents the particle diameter in number of pixels. The object hologram was recorded with the cuvette containing micro-particles and the reference hologram was recorded without the cuvette. Figure 4.6(a) shows the reference subtracted object hologram. As the cuvette width size 10 mm, the magnification of the setup was between $1.02 - 1.04$ and the illuminated object area was between $4.73 \times 5.91\ mm^2 - 4.82 \times 6.02\ mm^2$. Figure 4.6(b) shows the $2\times$ AR interpolated hologram. The original and interpolated holograms were reconstructed at 200 planes within the measurement volume. Using these reconstructed images, the maximum intensity maps were generated as shown in Figs. 4.6(c) and (d) indicating the particles at focus corresponding to the original and interpolated hologram, respectively. In the zoomed part (insets) it can be seen that more number of pixels containing object

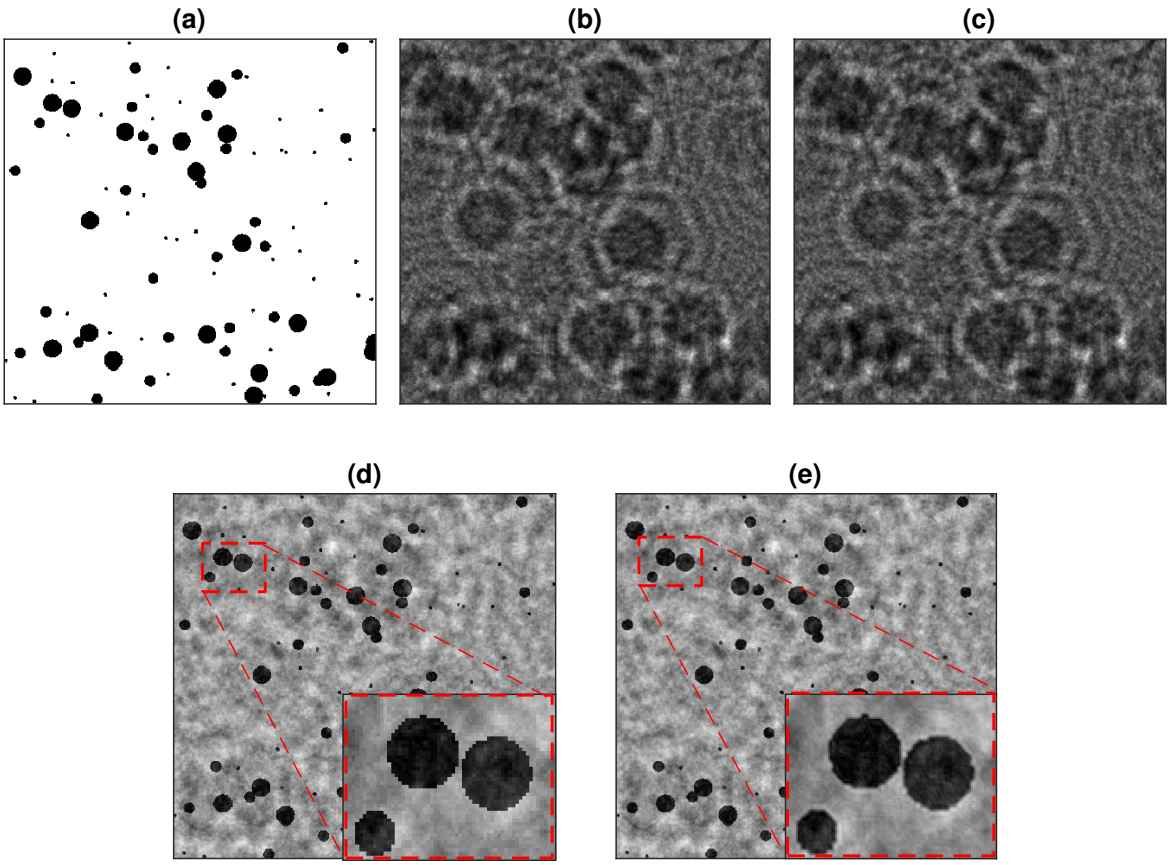

Figure 4.5: Simulation example: (a) 400 $\times$ 400 pixels object with 50, 30 and 20 particles of diameter 20 μm, 40 μm, 80 μm, respectively. (b) Original hologram, (c) 2$\times$ interpolated hologram. Object images obtained from the reconstruction of (d) original hologram and (e) 2$\times$ interpolated hologram. The cropped part at the red rectangular box part are shown in inset [186].

information are present after the application of AR interpolation on hologram. From these results, it can be deduced that the AR hologram interpolation offers significant improvement in reconstructed image quality over conventional method. The performance of AR interpolation method is comparable with the existing interpolation methods. A comparative study is shown in section 9.1 for the improvement of particle detection and size estimation accuracy using hologram interpolation.

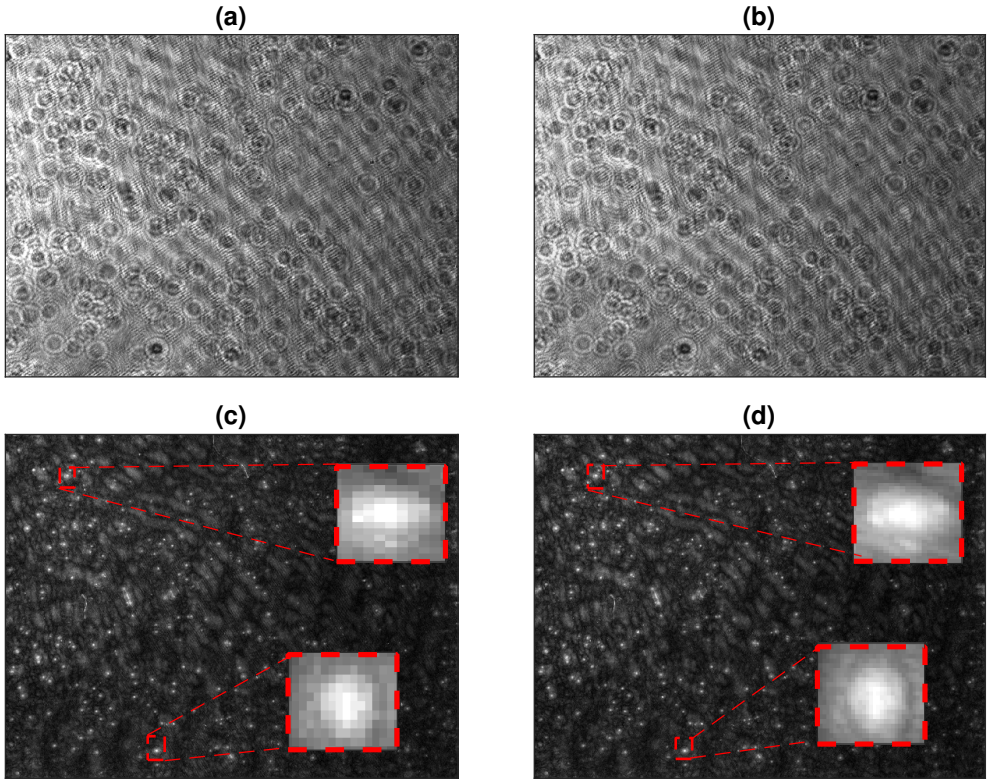

Figure 4.6: Experiment example: (a) original hologram of size 1280×1024 pixels corresponding to distribution of spherical particles of diameter $40\ \mu m$ (b) $2\times$ interpolated hologram (c) and (d) maximum intensity map computed from the stacks of images obtained by reconstructing the original and interpolated holograms, respectively. The cropped part at the red rectangular box part are shown in inset [186].

4.1.3 Conclusion

The proposed autoregressive hologram interpolation algorithm is found to provide significant improvement in the particle detection and size estimation accuracy based on the quantitative comparison with other hologram interpolation techniques. Since the algorithm is independent of particle type, it can be used for improving the non-spherical particle detection and size estimation accuracy as well. The simulation and experimental results substantiates the practical applicability of the proposed method.

5

Phase unwrapping methods

Phase estimation [188] is a key step in interferometric measurement techniques such as digital speckle pattern interferometry [189], digital holography [71], magnetic resonance imaging [190] and synthetic aperture radar interferometry [191, 192]. It is because the quantitative information on the physical quantity under investigation, for example, surface displacement, strain, object shape, magnetic field inhomogeneity, refractive index are available in the form of phase. However, the phase estimates obtained in these techniques are constrained in the range $(-\pi, \pi]$. Consequently, phase unwrapping is imperative for the quantitative measurement of physical parameters of interest from the phase estimates. Apart from optical interferometric measurement techniques, non-interferometric technique such as fringe projection profilometry [193] also records 3D shape information of the object in the form of phase.

Most of the phase retrieval techniques provide the phase estimates wrapped in the interval $(-\pi, \pi]$ due to the inverse tangent operation involved in them. However, the actual/true phase, which is proportional to the physical quantity, can lie outside this interval. *Phase unwrapping* is an operation of retrieving the estimate of true phase from the corresponding wrapped phase measurement. The relationship between wrapped phase and true phase can be given as,

$$\phi(x, y) = \psi(x, y) + 2\pi K(x, y) \tag{5.1}$$

where, ψ and ϕ represent the wrapped and true/unwrapped phase, respectively; K represents integer

[5]The chapter includes a phase unwrapping algorithm based on the breadth-first-search approach applied to the holographic phase images.

and (x, y) represents the pixel co-ordinate. Accordingly, in the absence of noise, the true phase can be obtained by simply adding or subtracting an appropriate integer multiple of 2π to each pixel in the wrapped phase. Thus, the problem of phase unwrapping can be considered as evaluating K at each pixel. One of the simple algorithm is based on the integration of wrapped phase differences [194] which works under certain assumptions, that is, the difference between two consecutive pixel's phase value is in the interval of $(-\pi, \pi]$. This algorithm, however, fails in practical scenarios wherein the fringe patterns are corrupted by the additive and multiplicative noise. In addition, there may exist inherent phase discontinuities in which case the assumptions do not hold. In light of these challenges, phase unwrapping becomes a non-trivial problem [195, 196].

5.1 Phase unwrapping algorithm using breadth-first-search and multi-level segmentation of phase quality interval in digital holography

In this section, we propose a quality-guided phase unwrapping algorithm based on the breadth-first-search approach in combination with a multi-level segmentation of the phase quality interval. The proposed method is noise robust and is capable of handling phase discontinuities. The algorithm is described in the Section 5.1.1. Simulation and experimental results are provided in Sections 5.1.2. A comparative study with state-of-art algorithms such as Goldstein [197], PUMA [117] and FastPU [116] is provided in these sections followed by the conclusion in Section 5.1.3.

5.1.1 Methodology

5.1.1.1 Phase Quality Map :

Performance of quality guided phase unwrapping algorithms mainly depends on the phase quality map. Different types of phase quality maps have been reported in the literature, for example, the pseudo-correlation coefficient map, the phase derivative variance map, the first difference map, the second phase difference map, etc. A comparative study on the performance of these different quality maps has been reported by Zhao et. al.[101]. In the proposed algorithm, we utilize the phase quality map generated based on the algorithm described in [116] as,

$$Q(x, y) = \sqrt{H^2(x, y) + V^2(x, y) + D_1^2(x, y) + D_2^2(x, y)}, \tag{5.2}$$

where,

$$\begin{aligned} H(x,y) &= \gamma[\psi(x-1,y) - \psi(x,y)] - \gamma[\psi(x,y) - \psi(x+1,y)] \\ V(x,y) &= \gamma[\psi(x,y-1) - \psi(x,y)] - \gamma[\psi(x,y) - \psi(x,y+1)] \\ D_1(x,y) &= \gamma[\psi(x-1,y-1) - \psi(x,y)] - \gamma[\psi(x,y) - \psi(x+1,y+1)] \\ D_2(x,y) &= \gamma[\psi(x-1,y+1) - \psi(x,y)] - \gamma[\psi(x,y) - \psi(x+1,y-1)]. \end{aligned} \tag{5.3}$$

$\gamma[\cdot]$ represents unwrapping operation to remove any 2π jumps between two consecutive pixels. The quality map is normalized such that the phase quality value lies in the interval of $[0, 1]$ with 0 and 1 indicating highest and lowest phase quality, respectively. Since the second phase difference can not be calculated at boundary pixels, the phase quality values at these pixels are set equal to 1. The phase quality index is considered as $1 - Q$ in this study.

5.1.1.2 Phase Quality Interval Segmentation :

The common strategy of quality guided phase unwrapping algorithms is to unwrap the pixels starting with the highest quality pixel. The pixels with low quality are pushed towards the end of unwrapping operation so that the unwrapping errors are localized and are not propagated. However, this approach is demanding from the point of view of memory requirement and computation time. As a result, different data structures have been employed to improve the performance of phase unwrapping with respect to these aspects [101].

The proposed method can be considered as multi-level phase unwrapping algorithm wherein the phase quality interval is uniformly or non-uniformly divided into multiple levels. In the proposed unwrapping strategy, a particular phase quality value (for example, segment boundary) is considered as a threshold for each segment of the phase quality interval. At a given time, the pixels with phase quality value below this threshold are unwrapped. Subsequently, another threshold value is selected to unwrap next set of pixels. Although such a multi-level phase unwrapping have been reported in the literature [98, 101], the levels have been limited to either two or three with uniform segmentation of phase quality interval. However, in the present work, phase quality interval is divided into comparatively higher number of levels. The algorithm starts with threshold value of zero and it is incremented at every iteration. For unwrapping pixels having phase quality value lower than the threshold, at least one unwrapped neighboring pixel is essential.

The selection of threshold values depend upon the type of segmentation of phase quality interval. Fig. 5.1 shows the three types of segmentation considered in this work. The width of the segments are equal in *uniform* segmentation, whereas the same changes linearly and exponentially in *linear* segmentation

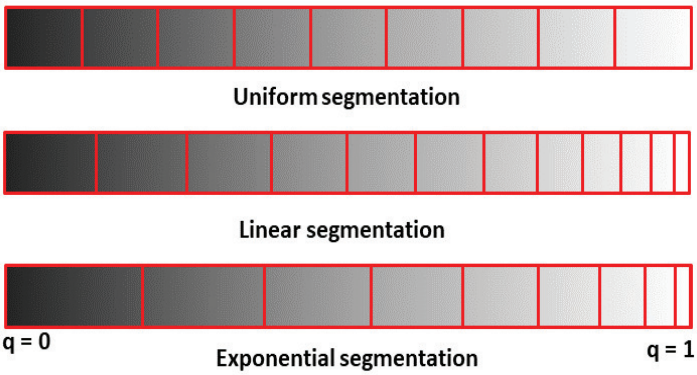

Figure 5.1: Different strategies of phase quality interval segmentation [198].

and *exponential* segmentation strategies, respectively. Let us consider that the phase quality interval $[0, 1]$ is divided into $L + 1$ number of segments. Let t represents an array with segment boundaries as its elements given as,

$$t(l) = \frac{l}{L} \; for \; l = 0, \cdots, L - 1. \tag{5.4}$$

The threshold values corresponding to different segmentation strategies are considered as,

$$\begin{aligned} q_{uniform}(l) &= t(l) \\ q_{linear}(l) &= t^2(l) \\ q_{exp}(l) &= \exp(\alpha t(l)), \end{aligned} \tag{5.5}$$

for $l = 0, \cdots, L - 1$, and α is a constant.

5.1.1.3 Phase Map Traversal based on Breadth-First-Search :

Different data structure employed for phase unwrapping approaches basically tackle the problem of memory and computation time efficient traversal of the phase image. In the proposed work, the breadth-first search (BFS) based approach is utilized. The BFS is a traversal technique for graph or tree data structure [199]. This algorithm begins at a root node (any arbitrary starting node in case of a graph) and explores to all other nodes that can be reached from the root node along the edges of the graph. The BFS follows one path in the graph along the branches as long as it keeps finding new nodes. If it does not find a new node, it backtracks to previous visited nodes and begins to visit other nodes of the graph. The algorithm keeps a track on the nodes which are visited, so that the processing is not repeated and each node is visited only once. In this particular case, nodes represent unwrapped pixels which satisfy the phase quality threshold criteria.

Algorithm 2 : BFS1

Input: Wrapped Phase (ψ), Phase Quality map (Q)
Output: Unwrapped Phase (ϕ)
Function funcBFS1(ψ, L, Q, ϕ)
for $l = 0, 1, .., L-1$ **do**
  if $l == 0$ **then**
    $linearIndex = find(Q <= q_{uniform}(l)/q_{linear}(l)/q_{exp}(l))$
    $[x, y] = ind2sub(size(Q), linearIndex)$
    Initialize: $x = x(1)$, $y = y(1)$, $\phi(x, y) = \psi(x, y)$, $queuePixel = [x, y]$ $treated(x, y) = 1$, $counter = 0$
    while $queuePixel \neq empty$ **do**
      $counter = counter + 1$
      $h = queuePixel(1)$, $x_{seed} = h(1)$, $y_{seed} = h(2)$
      for $x_{seed} = 2 : x-1, y_{seed} = 2 : y-1, i = x_{seed}-1 : x_{seed}+1, j = y_{seed}-1 : y_{seed}+1$ **do**
        if $treated(m, n) == 0$ *and* $Q(m, n) < q(l)$ **then**
          $\phi(m, n) = unwrap(\psi(m, n), \phi(x_{seed}, y_{seed}))$
          mark: $treated(m, n) = 1$
          $queuePixel(end + 1) = [m, n]$
        end
      end
    end
    $linIndex = find(treated == 1)$
    $[x_\phi, y_\phi] = ind2sub(size(treated), linIndex)$
  else
  end
  for $\kappa = 1 : numel(x_\phi)$ **do**
    if $y_\phi = empty$ **then**
      $linIndex = find(treated == 1)$
      $[x_\phi, y_\phi] = ind2sub(size(treated), linIndex)$
    end
    $m_1 = x_\phi(1)$, $n_1 = y_\phi(1)$, $x_\phi(1) = [\,]$, $y_\phi(1) = [\,]$
    if $treated(min(m_1 + 1, M), n_1) == 0$ *or* $treated(m_1, min(n_1 + 1, N), n_1) == 0$ *or* $treated(max(1, m_1 - 1), n_1) == 0$ *or* $treated(m_1, max(1, n_1 - 1)) == 0$ **then**
      $queuePixel = [m_1, n_1]$
      $counter = 0$
      while $queuePixel \neq empty$ **do**
        $counter = counter + 1$
        $h = queuePixel(1)$, $x_{seed} = h(1)$, $y_{seed} = h(2)$
        for $x_{seed} = 2 : x-1, y_{seed} = 2 : y-1, m = x_{seed}-1 : x_{seed}+1, n = y_{seed}-1 : y_{seed}+1$ **do**
          if $treated(m, n) == 0,$ *and* $Q(m, n) < q(l)$ **then**
            $\phi(m, n) = unwrap(\psi(m, n), \phi(x_{seed}, y_{seed}))$
            mark: $treated(m, n) = 1$
            $queuePixel(end + 1) = [m, n]$
            $x_{seed} = [x_{seed}; m]$, $y_{seed} = [y_{seed}; n]$
          end
        end
        $queuePixel(1) = [\,]$
      end
    end
  end
end

Algorithm 3 : BFS2

Input: Wrapped Phase (ψ), Phase Quality map (Q)
Output: Unwrapped Phase (ϕ)
Function funcBFS2(ψ, Q, ϕ)
for each $l \in l = 0, 1, .., L-1$, **do**
for each pixel (x, y), **do**
if $visited(x,y) == 0$ *and* $treated(x,y) == 1$ *and* $Q(x,y) < q(l)$ **then**
  initialize: $counter = 0$
  Function funcSearch($\psi(x,y)$, $Q(x,y)$, $\phi(x,y)$, $treated(x,y)$, $q(l)$, $visited(x,y)$, x, y, $counter$)
  mark: $visited(x,y) = 1$
  for *m = x-1:x+1* **do**
    for *n = y-1:y+1* **do**
      if $m > 1$, $n > 1$ *and* $treated(m,n) == 0$ **then**
        $\phi(m,n) = unwrap(\psi(m,n), \psi(x,y))$
        mark: $Treated(m,n) = 1$
        if $Q(m,n) < q(l)$ *and* $counter < CounterMax$ **then**
          $counter = counter + 1$
          $(x,y) = (m,n)$
          Function funcSearch($\psi(m,n)$, $Q(m,n)$, $\phi(m,n)$, $treated(m,n)$, $q(l)$, $visited(m,n)$, m, n, $counter$)
        end
      end
    end
  end
end

The BFS method can be implemented in two ways [200]. BFS 1 algorithm unwraps a pixel and maintains a record of 'treated' pixels. The condition 'treated' indicates whether a pixel has been unwrapped or not. An unwrapped pixel is considered as a seed pixel $(x_{seed},\ y_{seed})$ and it is used to unwrap its neighbouring wrapped pixels at (m,n), where $m = \{x_{seed} - 1,\ x_{seed},\ x_{seed} + 1\}$ and $n = \{y_{seed} - 1,\ y_{seed}, y_{seed} + 1\}$. During the traversal of phase image, if pixel (m,n) is not 'treated' and its phase quality value is less than a threshold (q), then (m,n) pixels are unwrapped by the seed pixel (x_{seed}, y_{seed}). The newly unwrapped pixel is stored in a queue of seed pixels, denoted as $queuePixel$. Due to this strategy, BFS 1 algorithm requires huge computation time. The unwrapped pixel coordinates are denoted as (x_ϕ, y_ϕ). In the BFS 2 algorithm, During the traversal of phase image, a record of visited as well as treated pixels is maintained. If a pixel is visited, it is not processed again. For a given threshold (q), the phase image is traversed from left to right and then top to bottom. If a pixel (x,y) is not visited, it is first unwrapped and its phase quality value is checked against the threshold. If it is less than the threshold, then it is used to unwrap its surrounding pixels $(m,n), \forall\ m = \{x-1, x, x+1\}\ and\ n = \{y-1, y, y+1\}$ irrespective of their phase quality values. Now, if any of its surrounding pixel is freshly unwrapped and its phase reliability value is less than the threshold, it is processed in the same manner

as its unwrapping pixel and it is marked as visited. This way all the potential pixels are identified and are unwrapped in a single traversal of the matrix. Simultaneous utilization of the BFS 2 algorithm and the phase quality interval segmentation allows phase unwrapping to be performed in a computationally efficient manner and localization of unwrapping error. It is important to note that the BFS 2 algorithm uses extra memory to keep a track of visited pixels and extra recursion stack memory as recursion is used in the implementation of breadth-first-search. In the algorithm, the condition 'visited' and 'treated' indicates whether a pixel has been used in the unwrapping of one of its neighbours and whether a pixel has been unwrapped or not, respectively.

5.1.2 Results and Discussion

The performance of the proposed phase unwrapping algorithm is evaluated using simulation examples. Figure 5.2a and 5.2b show the wrapped phase images of size 512×512 corrupted by additive noise [78] and the speckle noise [201], respectively. It is important to note that the phase unwrapping algorithm is robust to noise and does not perform denoising. As a result, the unwrapped phase carries the noise component associated with the wrapped phase. Therefore, the unwrapping errors caused by the noise-induced unintended phase jumps should be considered as performance measure for the unwrapping algorithm. In the implementation of the proposed method, we have used $L = 300$ for each segmentation scheme in the following examples. It should be noted that, the computation time directly depends on L. That is, the computation time increases with a higher value of L and vice versa.

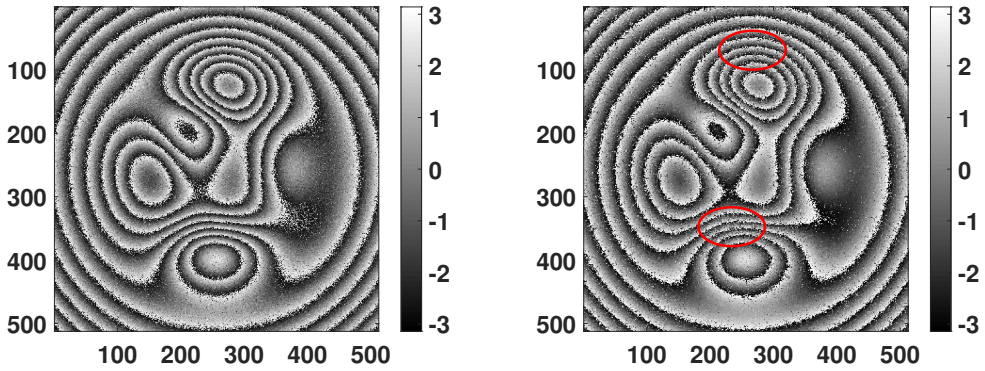

Figure 5.2: Simulated wrapped phase patterns corrupted with (a) additive noise and (b) speckle noise [198].

The BFS 1 and BFS 2 algorithms were implemented with the wrapped phase shown in Figure 5.2(a) and the root mean square error (RMSE) and peak-to-valley error (PVE) are calculated (tabulated in Table

5.1). For BFS 2 both the RMSE and PVE are less than BFS 1, at the same time it is computationally efficient than BFS 1. The BFS 2 algorithm was found to perform better with uniform and linear phase quality interval segmentation but the computation time is lower in case of linear interval segmentation. The unwrapping performance of the algorithms were studied considering exponential segmentation with α value in a range of $[1, 10]$. It was observed that the unwrapping errors are higher in comparison to the other segmentation strategies. Based on these observations, the BFS 2 algorithm with linear phase quality interval segmentation is chosen in the following examples.

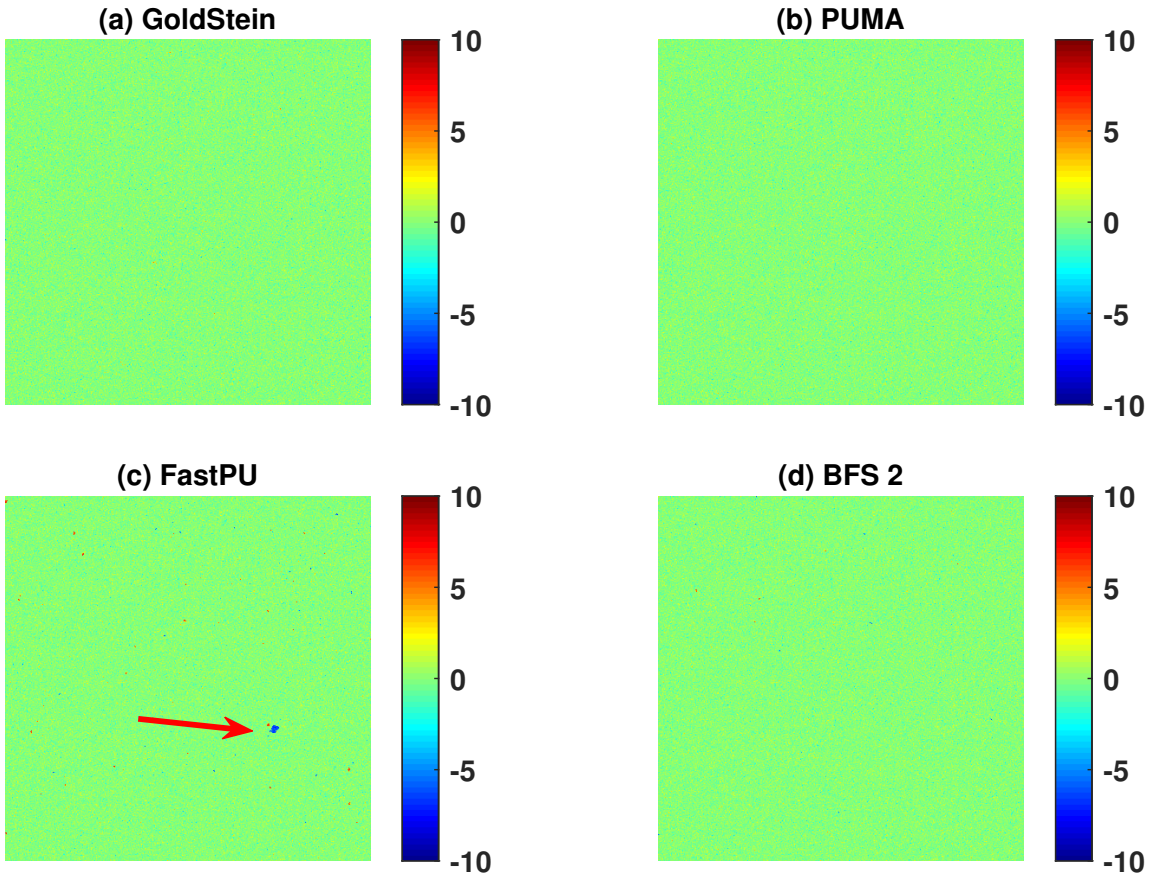

Figure 5.3: Error in the unwrapped phase estimates obtained using the (a) Goldstein, (b) PUMA, (c) FastPU and (d) BFS algorithms for the wrapped phase example shown in Fig. 5.2a. All error values are in radians [198].

Figure 5.3 shows the error maps in the unwrapped phase estimates obtained using BFS, PUMA, Goldstein, and FastPU algorithms for the additive noise corrupted wrapped phase shown in Fig. 5.2a with SNR = 2 dB. The RMSE and PVE evaluated for different algorithms are tabulated in Table 5.2. It can be observed that the PUMA, GoldsStein and BFS algorithms provided similar unwrapping performance whereas higher unwrapping errors were observed in the case of FastPU algorithm.

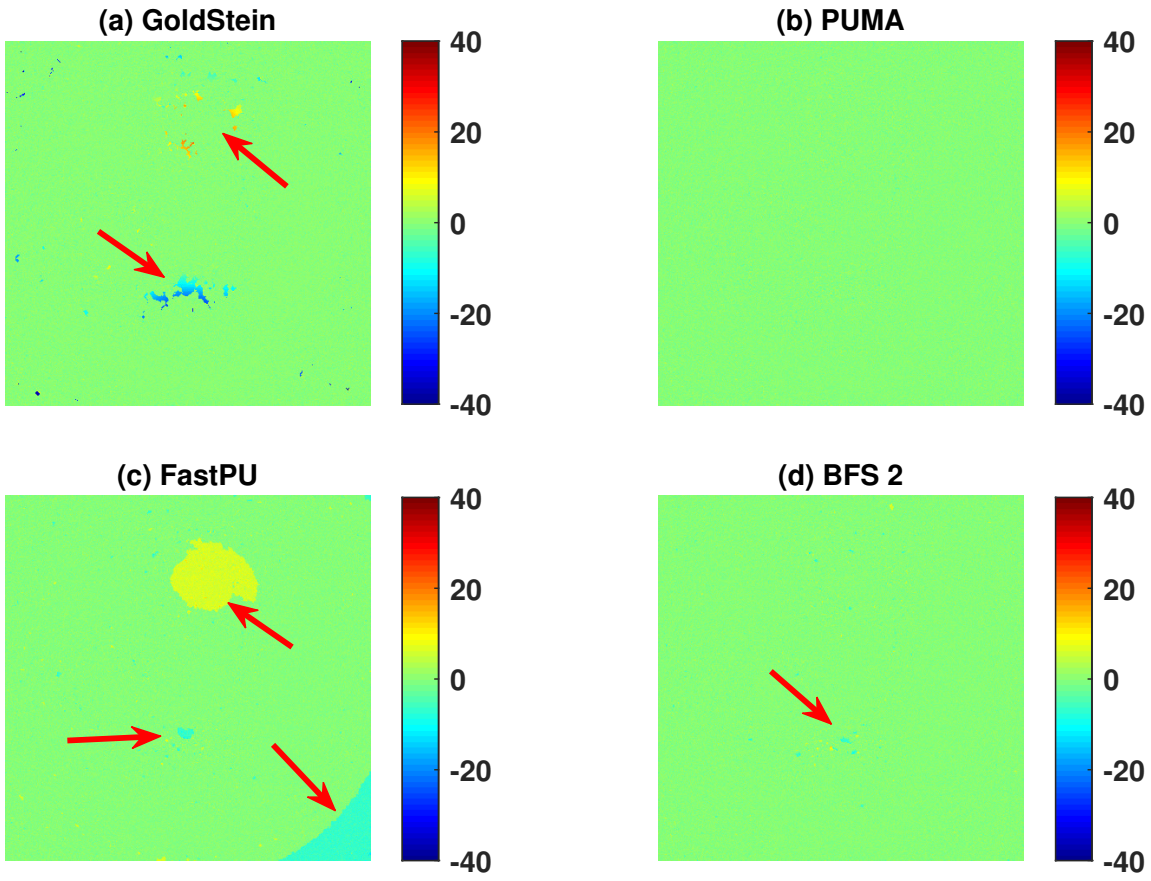

Figure 5.4: Error in the unwrapped phase estimates obtained using the (a) Goldstein, (b) PUMA, (c) FastPU and (d) BFS algorithms from the wrapped phase shown in Fig. 5.2b. All error values are in radians [198].

Figure 5.4 shows the error maps in the unwrapped phase estimates for the speckle noise corrupted wrapped phase shown in Fig. 5.2b. The speckle size was set to be four pixels. As a result, the regions of higher fringe density (encircled in red color) are more corrupted in comparison with the low fringe density regions. The RMSE and PVE evaluated for different algorithms are tabulated in Table 5.2. The PUMA algorithm provided best unwrapping results compared to the other algorithms. However, the computation time required is also largest for the PUMA algorithm. Although there exists some regions with high unwrapping errors in the case of BFS algorithm, these are highly localized. On the other hand, the unwrapping errors are significantly propagated to less noisy regions in the case of the Goldstein and the FastPU methods. The regions with high unwrapping errors are indicated with red color arrow. Computation time for different methods are tabulated in Table 5.3. It can be seen that, BFS 2 and FastPU are computationally more efficient compared to the GoldStein and PUMA.

The performance of the proposed BFS algorithm is evaluated with wrapped phase examples shown

Table 5.1: **Performance comparison of BFS 1 and BFS 2 algorithms with wrapped phase of Size** 512×512 **pixels (Fig.5.2a)**

	BFS 1			BFS 2		
	Uniform	**Linear**	**Exponential**	**Uniform**	**Linear**	**Exponential**
RMSE (in rad)	0.92	0.92	1.98	0.61	0.61	1.09
PVE (in rad)	37.31	30.08	70.07	12.71	12.71	41.42
Comp. time (sec)	23.53	22.32	20.41	0.91	0.86	0.83

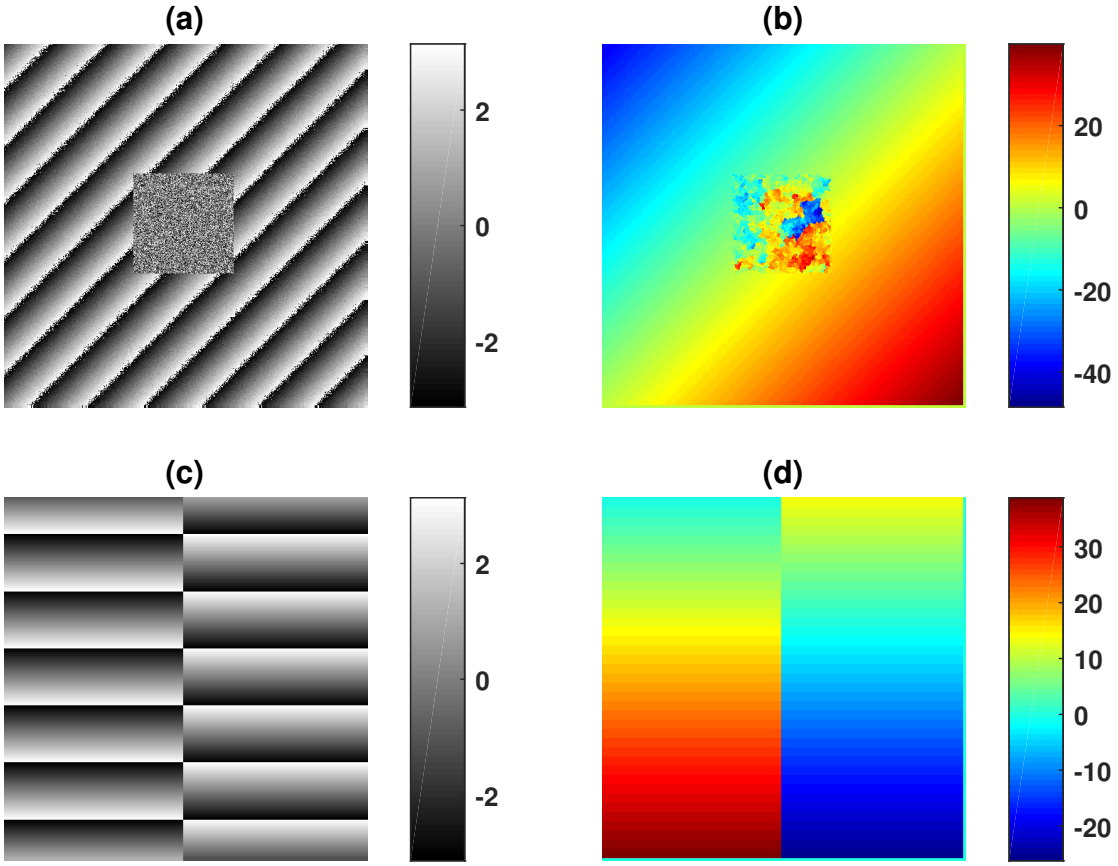

Figure 5.5: Simulated wrapped phase patterns consisting of (a) a random phase noise region and (c) an inherent phase discontinuity; (b) and (d) the unwrapped phase estimates obtained using the BFS method for the wrapped phase examples in (a) and (c), respectively. All phase values are in radians [198].

Table 5.2: **Performance comparison of different phase unwrapping algorithm for wrapped phase of Size** 512×512 **pixels**

Wrapped phase	RMSE (in rad)				PVE (in rad)			
	Goldstein	**PUMA**	**FastPU**	**BFS 2**	**Goldstein**	**PUMA**	**FastPU**	**BFS 2**
Fig. 5.2a	0.61	0.61	0.64	**0.61**	12.78	8.08	15.89	**12.71**
Fig. 5.2b	1.55	0.67	1.69	**0.72**	62.81	9.67	27.28	**24.85**

in Figs. 5.5(a) and (c) wherein they contain information-less random noise regions and inherent phase discontinuities, respectively. Figures 5.5(b) and (d) shows the capability of BFS 2 method to unwrap the above mentioned wrapped phase maps.

The validation of the proposed method was performed using the experimentally recorded phase images shown in Fig. 5.6(a) and Fig. 5.6(b). These are wrapped phases of size 950×1770 pixels and 950×700 pixels, respectively, associated with onion cells recorded in a digital holographic microscopy setup. Details of the hologram recording setup and parameters are described in [202]. Unwrapping of these phase maps were performed using the BFS 2, Goldstein, PUMA and FastPU algorithms. Figures 5.7 and 5.8 shows the unwrapped phase estimates obtained using different algorithms for the wrapped phases shown in Figs. 5.6(a) and 5.6(b), respectively. It can be clearly seen that the PUMA and BFS agree on the unwrapping results whereas the Goldstein and FastPU fail to provide reliable phase unwrapping.

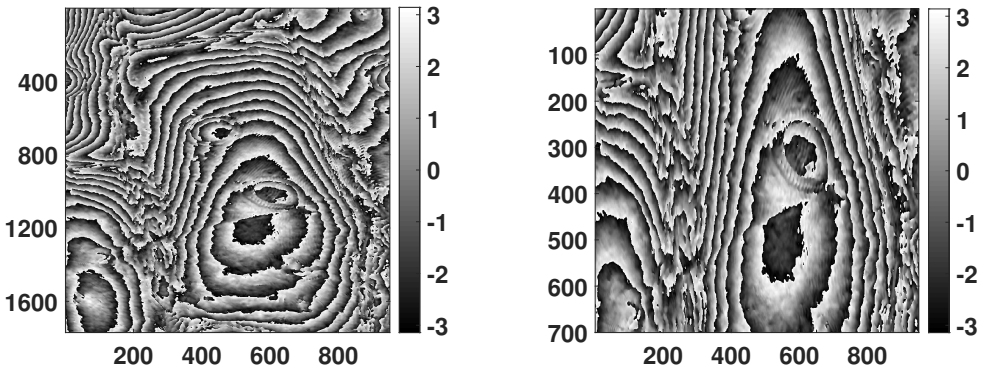

(a) (b)

Figure 5.6: Experimentally recorded wrapped phase patterns of onion cell specimen recorded in a digital holographic microscopy setup. All phase values are in radians [198].

Table 5.3: **Processing time required for the phase unwrapping by different algorithms**

Wrapped Phase Size	Processing time (in seconds)			
	GoldStein	PUMA	FastPU	BFS 2
512×512 (Fig. 5.2(a))	12.39	18.03	0.68	**0.86**
512×512 (Fig. 5.2(b))	12.41	18.96	0.68	**1.02**
950×1770 (Fig. 5.6(a))	64.91	649.23	9.33	**65.90**
950×700 (Fig. 5.6(b))	29.05	109.93	2.47	**20.15**

An important aspect associated with the proposed unwrapping algorithm is that the phase quality of that pixel which is used to unwrap the current pixel, is checked against a threshold rather than the phase quality of current pixel. The phase unwrapping is performed in recursive manner and a record of pixels

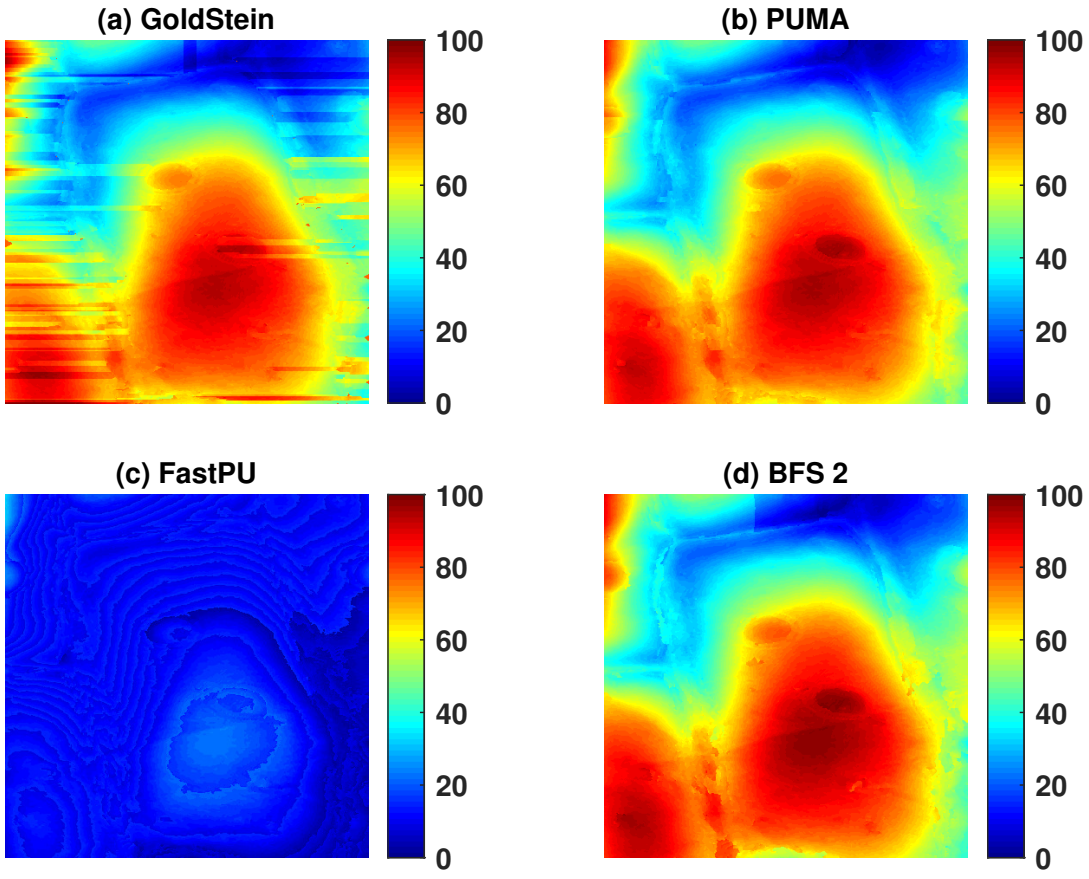

Figure 5.7: Unwrapped phase estimates obtained for the wrapped phase pattern shown in Fig. 5.6(a) using the (a) Goldstein (b) PUMA and (c) FastPU and (d) BFS algorithms. All phase values are in radians [198].

used to unwrap neighbor pixels is maintained in the BFS 2 algorithm. In the case of very low SNR, the number of segments should be increased (L) albeit at the cost of increased computation time. In the MATLAB implementation of the algorithm, it has been observed that at high SNR, the recursion memory of MATLAB is saturated. Therefore, the algorithm is modified accordingly to come out of the recursion process and continue the unwrapping operation. Based on these observations, it is recommended that if a wrapped phase pattern is heavily corrupted with speckle noise, a high value of L should be chosen to offer high noise robustness in phase unwrapping. On the other hand, if speckle noise is filtered out from the wrapped phase pattern to certain extent by some pre-processing operation, a small value of L should be selected which will provide a reliable unwrapped phase estimate at a low computation cost.

Table 5.3 provides the computation time required by each phase unwrapping method considered in the study. In each example, the time taken by the FastPU is the lowest. At the same time, its unwrapping reliability is also the lowest. On the other hand, although the PUMA algorithm provides highest unwrap-

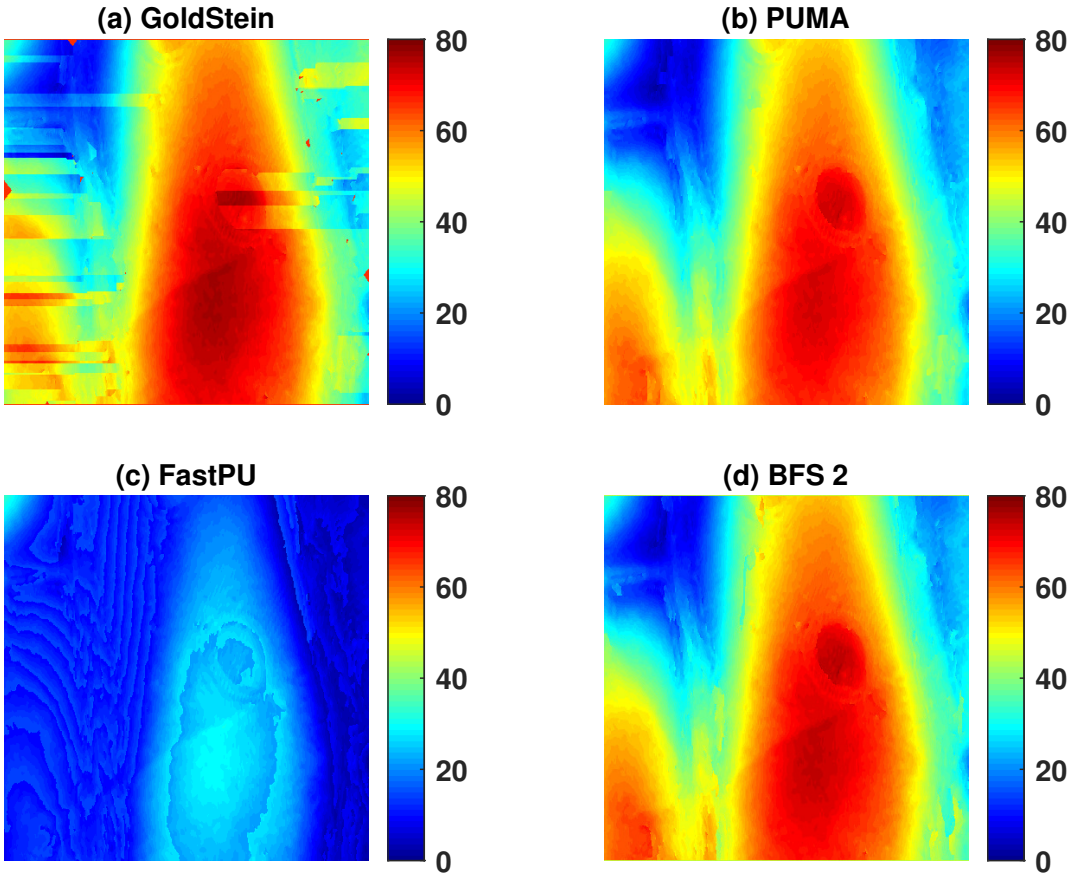

Figure 5.8: Unwrapped phase estimates obtained for the wrapped phase pattern shown in Fig. 5.6(b) using the (a) Goldstein (b) PUMA and (c) FastPU and (d) BFS algorithms [198].

ping reliability, its computation time is the highest. It has been observed that computation time taken by the PUMA algorithm varies significantly with the phase profile for the same size of the wrapped phase and SNR level. Thus, the BFS 2 algorithm provides an optimal compromise between the computation time and phase unwrapping reliability. In this work, all the unwrapping algorithms were implemented using the MATLAB 2019a on a laptop with 8 GB RAM and i5-9300U processor @2.4 GHz.

5.1.3 Conclusion

A computationally efficient and noise-robust phase unwrapping algorithm is proposed based on the breadth-first-search approach in combination with the multi-level segmentation of the phase quality interval. The proposed method is capable of unwrapping phase maps containing random phase regions and phase discontinuities. The proposed method unwraps the holographic wrapped phases efficiently. The flexibility in the phase quality interval segmentation offers an effective and efficient way of unwrapping phase images depending on the noise strength. Simulation and experimental results in comparison

with some of the previously proposed algorithms substantiate the practical applicability of the proposed method in digital holographic microscopy.

Part III

Autofocusing methods in digital holography

भारतीय प्रौद्योगिकी संस्थान गुवाहाटी
Indian Institute of Technology Guwahati

6

Autofocusing based on eigenvalues of hologram reconstructed images

6.1 Autofocusing based on eigenvalues of reconstructed images

In this section, we propose an autofocusing algorithm, named EIG, based on the eigenvalues of the reconstructed wavefield. The proposed algorithm is described in the Section 6.1.1. The simulation and experimental results are provided in Sections 6.1.2 followed by the conclusion in Section 6.1.3.

6.1.1 Methodology

In the present study, the lensless digital in-line holographic configuration with a spherical wave illumination of the object has been considered as shown in Fig. 1.2. The complex amplitude of the reconstructed optical wavefield at a distance z from the hologram plane is given by Eq. 1.10. The amplitude and phase images are obtained as

$$A_z(x,y) = |U_{r_z}(x,y)| \tag{6.1}$$

$$\phi_z(x,y) = \angle U_{r_z}(x,y). \tag{6.2}$$

Autofocusing in the digital in-line holographic configuration is more challenging compared to that in the off-axis digital holography as the reconstructed image contains the out-of-focus twin image contribution along with the in-focus image of the object. In addition, the reconstructed image contains a contribution

[6]The chapter presents two hologram autofocusing algorithms based on the eigenvalues of reconstructed images.

from the unscattered light wave. As a result, the effectiveness of the proposed algorithm in autofocusing is equally applicable to all digital holographic configurations.

In the proposed algorithm, the eigenvalue (EIG) based image sharpness estimation technique [203] is utilized for the automatic focal plane detection. Let us consider that the hologram reconstruction is performed starting from a distance z_s. The reconstruction distance is increased with z_{step} at each step. Let $M \times N$ and N_z represent the hologram size and the total number of reconstructed images, respectively. Using the set of reconstructed images, the automatic focal plane detection is performed. At a given reconstruction distance z, the corresponding amplitude image $A_z(x, y)$ is normalized by its energy as,

$$\bar{A}_z(x, y) = \frac{A_z(x, y)}{\sqrt{\sum_{x=0}^{N-1}\sum_{y=0}^{M-1}[A_z(x, y)]^2}}. \tag{6.3}$$

The mean value of normalized amplitude image is computed as

$$\mu_z = \frac{1}{MN}\sum_{x=0}^{N-1}\sum_{y=0}^{M-1}\bar{A}_z(x, y). \tag{6.4}$$

The covariance matrix $\boldsymbol{Q}_z$ is computed as

$$Q_z = \frac{1}{(M-1)}\tilde{A}_z\tilde{A}_z^T, \tag{6.5}$$

where, $\tilde{A}_z = \bar{A}_z - \mu_z$ and $(\cdot)^T$ represents the matrix transpose. A column vector E_z containing the eigenvalues of Q_z is obtained as

$$E_z = eig(Q_z), \tag{6.6}$$

where $eig(\cdot)$ represents eigenvalue computing function. Considering that the eigenvalues are arranged in an ascending order in the vector E_z, a metric for detecting the focal plane is defined as follows

$$\tau(z) = \sum_{k=1}^{M-\kappa} E_z(k), \tag{6.7}$$

where, κ is a user defined parameter. The metric is defined based on the fact that the in-focus image has higher amplitude variations compared to the out-of-focus images. In other words, the in-focus image sharpness is more compared to that of the out-of-focus images. In the present case, the components associated with the most dominant eigenvalues of the covariance matrix Q_z contains most of the information on the spatial variation in the reconstructed image. Therefore, all of these dominant eigenvalues should be utilized in the computation of the metric τ. However, the extent of the spatial variation in the reconstructed image changes almost monotonically in function of the reconstruction distance except at the focal plane. This behaviour is observed in the case of lensless digital in-line holographic configura-

tion due to the variable magnification associated with it. In order to compensate for this effect, a certain number of dominant eigenvalues need to be discarded in the computation of autofocusing metric. This number is given by the κ parameter. Typically, an appropriate value of κ depends on the size of the reconstructed image. Since Q_z has M number of eigenvalues, κ value can be selected as a percentage of M. It can be noted that we can set $\kappa = 0$ in the digital holographic configuration with fixed magnification. Finally, the value of corresponding $z_1 = z_f$ at which the metric τ takes the maximum/minimum value is selected as the location of focal plane. The proposed EIG algorithm is described below:

Algorithm 4 : EIG

Input: N_z number of reconstructed images each of size $M \times N$, z_s and z_{step}.
Output: z_f: Location of focal plane.
step 1: Calculate the normalized image $\bar{A}_z(x, y)$ (Eq. 6.3).
step 2: Calculate the mean μ_z of the normalized image (Eq. 6.4).
step 3: Calculate the covariance matrix Q_z (Eq. 6.5).
step 4: Calculate the eigenvalue vector E_z (Eq. 6.6).
step 5: Calculate the metric τ based on the user defined κ value (Eq.6.7).
Repeat step 1 to step 5 for each reconstruction distance z.
step 6: Calculate the estimate of the focal plane location as $z_f = \max_{z_1} \tau(z)$ or $z_f = \min_{z_1} \tau(z)$.

Note that the reconstruction distance z required in the algorithm is a function of z_1 and z_2. In the simulation and experimental study, z_1 and z_2 are varied such that $Z = (z_1 + z_2)$ is maintained constant. Therefore, the plots of autofocusing metrics are given in function of z_1.

6.1.2 Results and discussion

Simulation Results

The simulation study is performed considering a digital lensless in-line holographic setup with a spherical beam illumination of the object using a laser source of wavelength $\lambda = 500\ nm$ and camera pixel size of $4.8\ \mu m$. An amplitude, a phase and a mixed type object are considered during the simulation study. Simulation results are provided for objects placed at a single and two planes as described below:

Case 1: Single plane

Amplitude object : A simulated USAF target is used as an amplitude object of size 583×800 pixels as shown in Fig. 6.1(a). The object is placed such that $z_1 = 80\ mm$ and $z_2 = 20\ mm$. Thus, $M_g = 1.25$ and the object area is $2.7 \times 3.8\ mm^2$. The simulated hologram is shown in Fig. 6.1(b). The hologram reconstruction was performed with $z_s = 70\ mm$, $z_{step} = 0.5\ mm$ and $N_z = 40$ keeping $Z = 100\ mm$. Figure 6.1(c) shows the normalized plot of τ as a function of z_1 with $\kappa = [3, 5, 12, 18, 24, 30]$, where the κ values were selected as $[0.5\%, 1\%, 2\%, 3\%, 4\%, 5\%]$ of M, respectively. The metric has the maximum

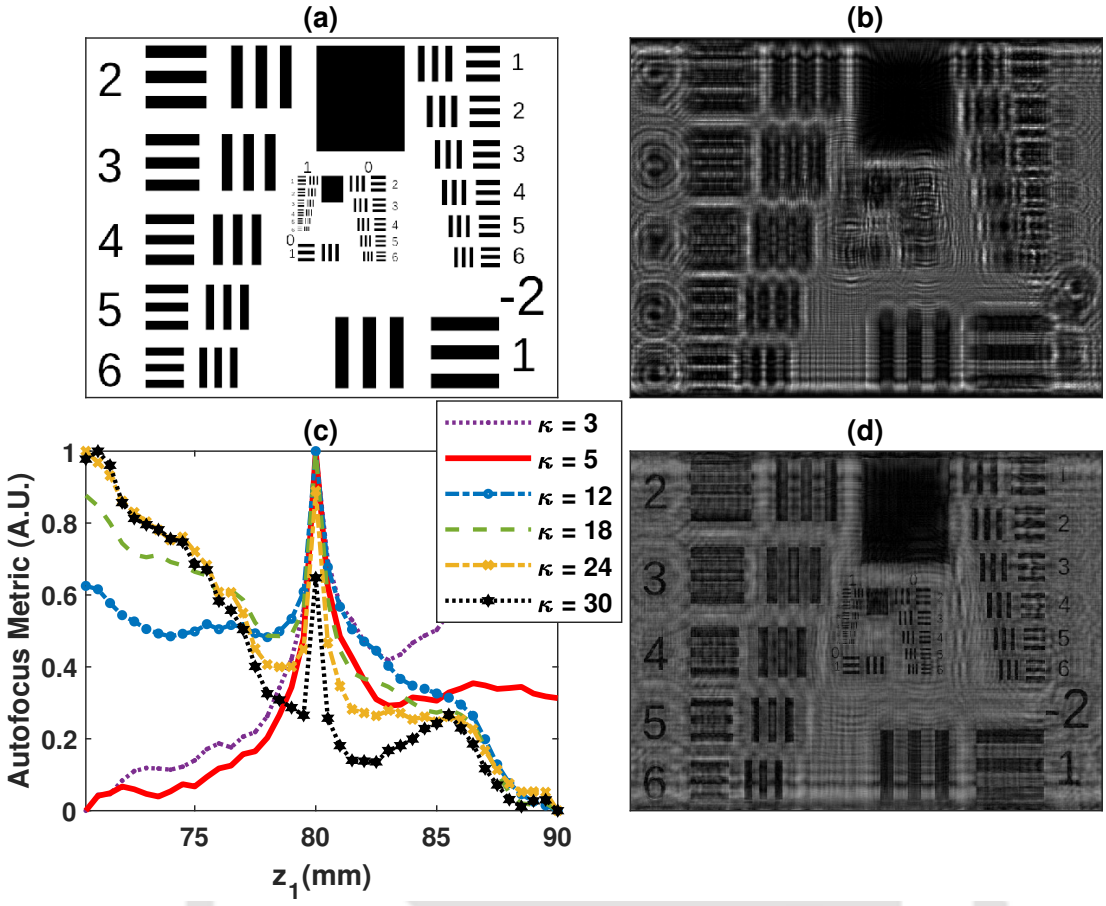

Figure 6.1: (a) The simulated amplitude object of size 583×800 pixels (b) the simulated hologram with $z_1 = 80\ mm$ and $z_2 = 20\ mm$ (c) the plot of L in function of z_1 for different κ and (d) the reconstructed amplitude image at the estimated focal plane [204].

value at $z_1 = 80\ mm$ corresponding to the focal plane. The distribution of τ with respect to the location of focal plane is approximately symmetric for $\kappa = 5$. Empirically, we found that the selection of 1%-3% of M as the κ value provides accurate estimate of location of the focal plane. The reconstructed amplitude image of the object at the detected focal plane is shown in Fig. 6.1(d) for the purpose of illustration.

Phase object : Similar to the amplitude object example, a simulation study was performed considering the USAF target is used as a phase object as shown in Fig. 6.2(a). The size of the object is 583×800 pixels. The simulated hologram is shown in Fig. 6.2(b). The hologram reconstruction was performed with $z_s = 70\ mm$, $z_{step} = 0.5\ mm$ and $N_z = 40$ keeping $Z = 100\ mm$. Figure 6.2(c) shows the normalized plot of τ as function of z_1 with $\kappa = [3, 5, 12, 18, 24, 30]$, where the κ values were selected as $[0.5\%, 1\%, 2\%, 3\%, 4\%, 5\%]$ of M, respectively. A single valley corresponding to the location of focal

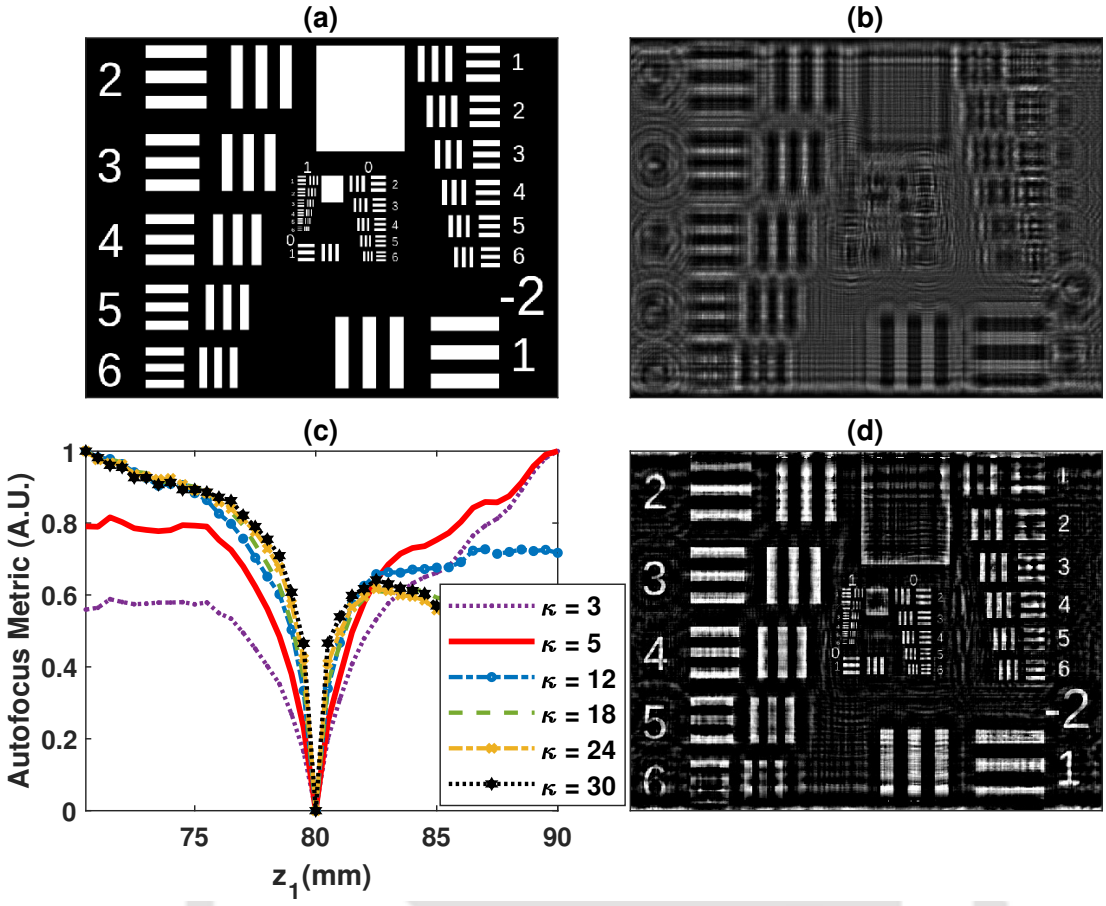

Figure 6.2: (a) The simulated phase object of size 583×800 pixels (b) the simulated hologram with $z_1 = 80\ mm$ and $z_2 = 20\ mm$ (c) the plot of $L(z_1)$ in function of κ and (d) the reconstructed phase image at the estimated focal plane [204].

plane at $z_1 = 80\ mm$ can be observed. In this case too, it was observed that the distribution of τ with respect to the focal plane is approximately symmetric for $\kappa = 5$. The reconstructed phase image of the object at the detected focal plane is shown in Fig. 6.2(d) for the purpose of illustration.

A comparison of the proposed algorithm with some of the previously established algorithms for the focal plane detection is given in Fig. 6.3. Figures 6.3(a) and 6.3(b) show the plots of autofocusing metrics of some representative algorithms in function of z_1 for the amplitude (Fig. 6.1(a)) and phase (Fig. 6.2(a)) objects, respectively. Note that the autofocusing metrics computed for all the methods are normalized for the purpose of comparison. It can be observed in Fig. 6.3(a) that although all the autofocusing metric curves exhibited a peak at the focal plane, peaks of the EIG, DFS and GRA curves are more sharper in comparison with the other curves. In fact, a monotonic variations in the metric curves are observed, except at the focal plane, for the algorithms other than the EIG, DFS and GRA. For these three algorithms, sharper peaks are observed in Fig. 6.3(b) for the phase object as well. Moreover, the

SEN algorithm could not provide accurate focal plane detection for the phase object. In the following simulation and experimental examples, the plot legends are the same as shown in Fig. 6.3. Therefore, the plot legends in the following examples are not shown due to the space constraints in the figures.

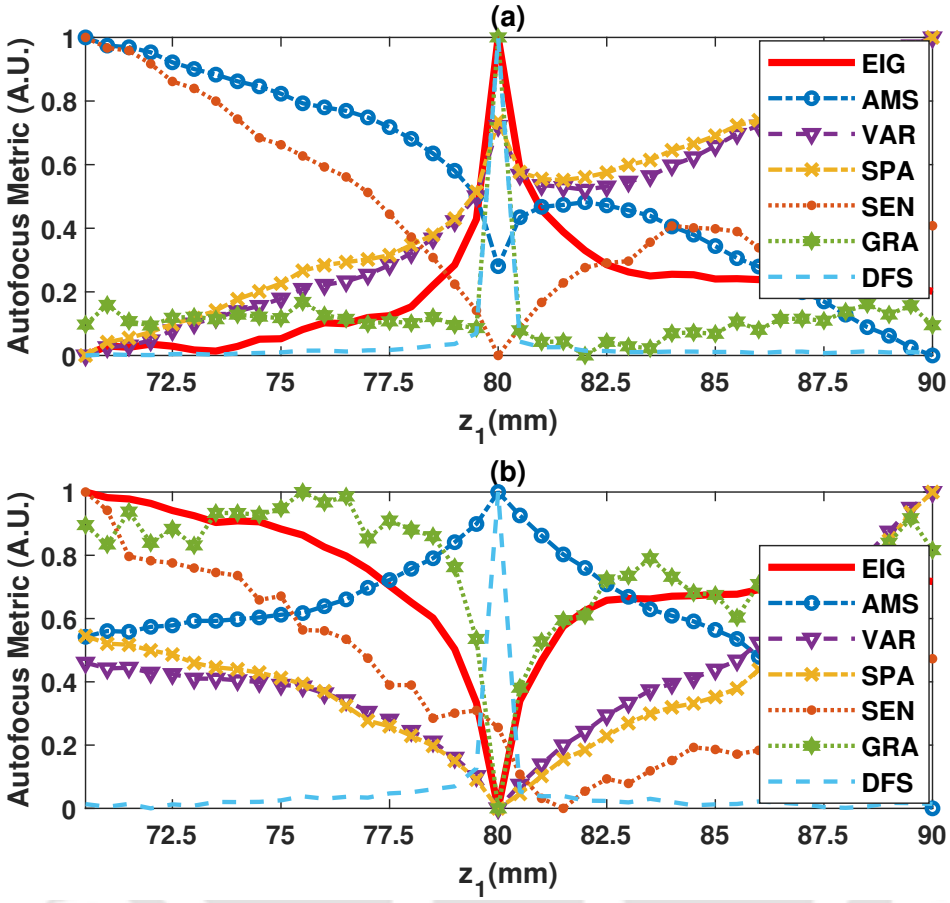

Figure 6.3: Plot of autofocusing metrics of representative algorithms in function of z_1 for (a) the amplitude object and (b) the phase object [204].

Mixed object : The performance of the proposed algorithm is also evaluated with a mixed type object having both amplitude and phase variations. The simulated amplitude and phase of the object each of size 200×200 pixels are shown in Figs. 6.4(a) and 6.4(b), respectively. Figure 6.4(c) shows the simulated hologram with $z_1 = 80\ mm$ and $z_2 = 20\ mm$. The autofocusing metrics evaluated using different algorithms are plotted as a function of z_1 as shown in Fig. 6.4(d). Since the object is of mixed type, the proposed eigenvalue based focal plane detection algorithm was implemented with the complex amplitude $U_{r_z}(x, y)$ instead of $A_z(x, y)$. It can be observed that only the proposed EIG and the DFS algorithm were successful in accurately detecting the focal plane at $z_1 = 80\ mm$. For the purpose of illustration, the reconstructed amplitude and reconstructed phase are shown in Figs. 6.4(e) and 6.4(f),

respectively.

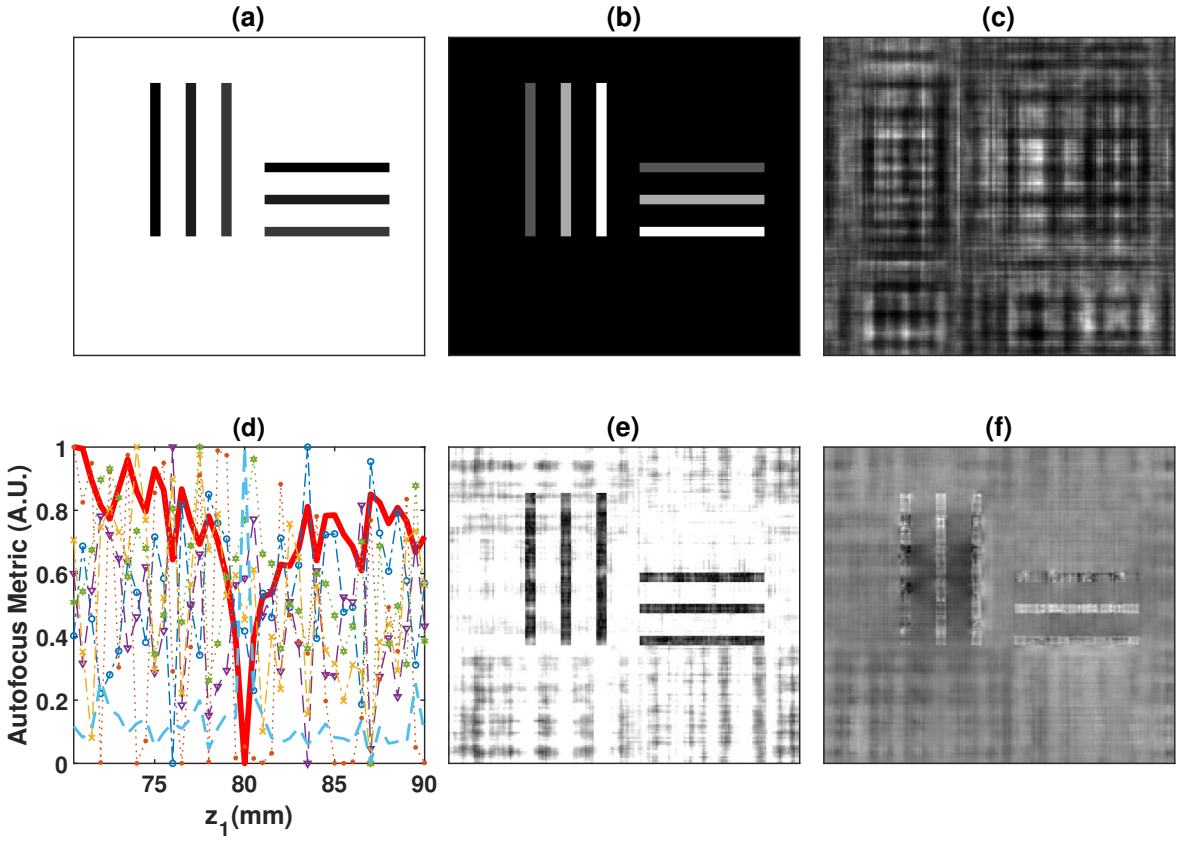

Figure 6.4: (a) The simulated amplitude and (b) the simulated phase of the mixed type object. (c) The simulated hologram with $z_1 = 80mm$ and $z_2 = 20\ mm$ (d) plot of autofocusing metrics of representative algorithms in function of z_1. The plot legends are same as those given in Fig. 6.3. The reconstructed (e) amplitude and (f) phase images at the estimated focal plane [204].

Case 2: Two plane

A simulated example of hologram autofocusing with two object planes is considered. In this example, randomly distributed particles representing pure amplitude objects are simulated at two different planes in the path of light propagation. Figures 6.5(a) and 6.5(b) show two images of size 200×200 pixel of the randomly distributed particles placed at $z_1 = 40\ mm$ and $z_1 = 60\ mm$, respectively, with total point source to hologram plane distance as $Z = 100\ mm$. The simulated hologram is shown in Fig. 6.5(c). Figure 6.5(d) shows the plot of autofocusing metrics evaluated using some representative algorithms as a function of z_1. Two peaks are observed at $z_1 = 40\ mm$ and $z_1 = 60\ mm$ by most of the algorithms. The reconstructed images at the estimated focal planes are shown in Figs. 6.5(e) and 6.5(f), respectively. Next, a similar exercise was performed as shown in Fig. 6.6 with two closely placed planes

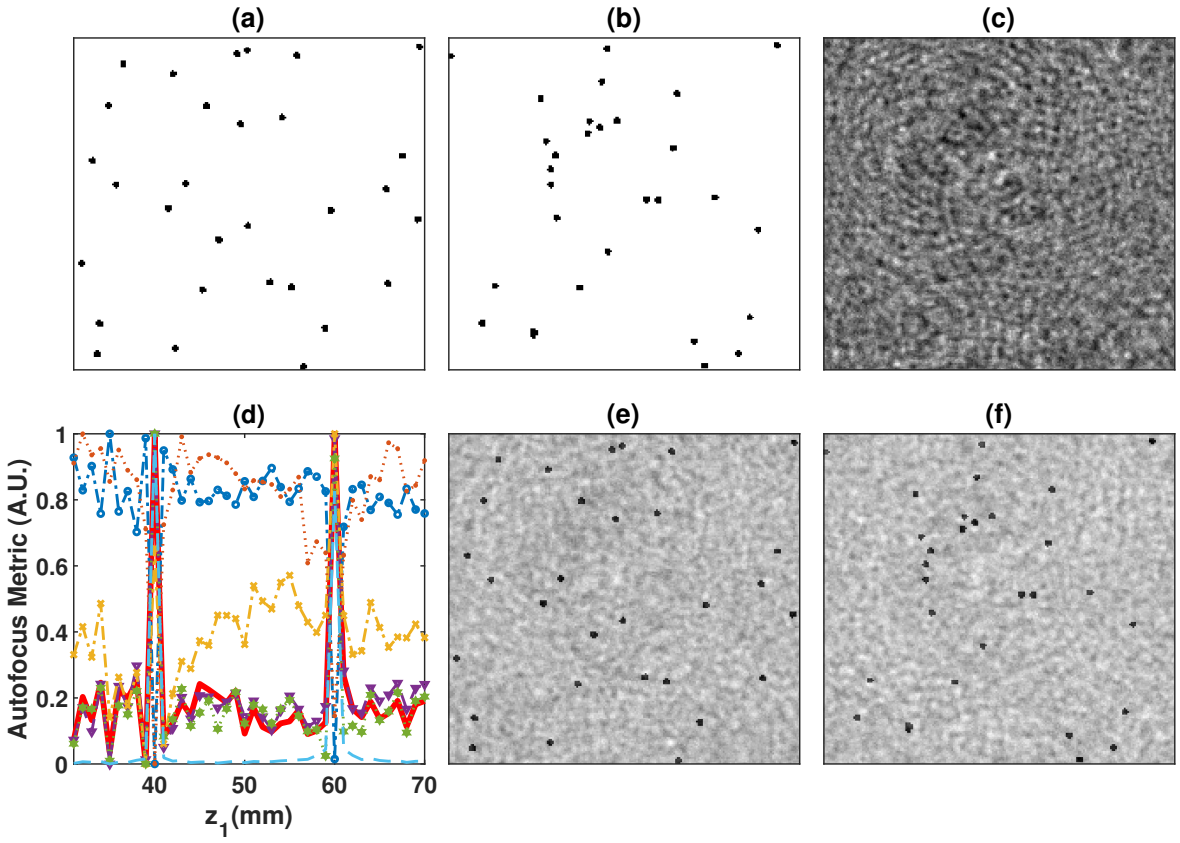

Figure 6.5: (a) and (b) The randomly distributed particles (amplitude objects) at the planes $z_1 = 40\ mm, z_2 = 60\ mm$ and $z_1 = 60\ mm, z_2 = 40\ mm$. (b) the simulated hologram and (c) plot of autofocusing metrics of some representative algorithms in function of z_1. The plot legends are same as those given in Fig. 6.3. (d) and (e) Reconstructed amplitude images at the estimated focal planes [204].

at $z_1 = 59\ mm$ and $z_1 = 60\ mm$ containing randomly distributed particles. The results shown in 6.6 show that the proposed algorithm was able to accurately detect the location of the focal plane in this case as well.

Experimental Results

The experimental validation of the proposed method is performed using the holograms recorded in a digital lensless in-line holographic setup with spherical light beam illumination. The experimental setup has been described in detail in [132]. A light source of wavelength $\lambda = 450\ nm$ was used to illuminate object sample, a chamber containing polystyrene microbeads immersed in an aqueous medium. The microbeads 90 μm and 45 μm sizes were used. The holograms were recorded using a monochrome camera with 2040×2040 pixels and 5.5 μm pixel size. Figure 6.7(a) shows the hologram recorded

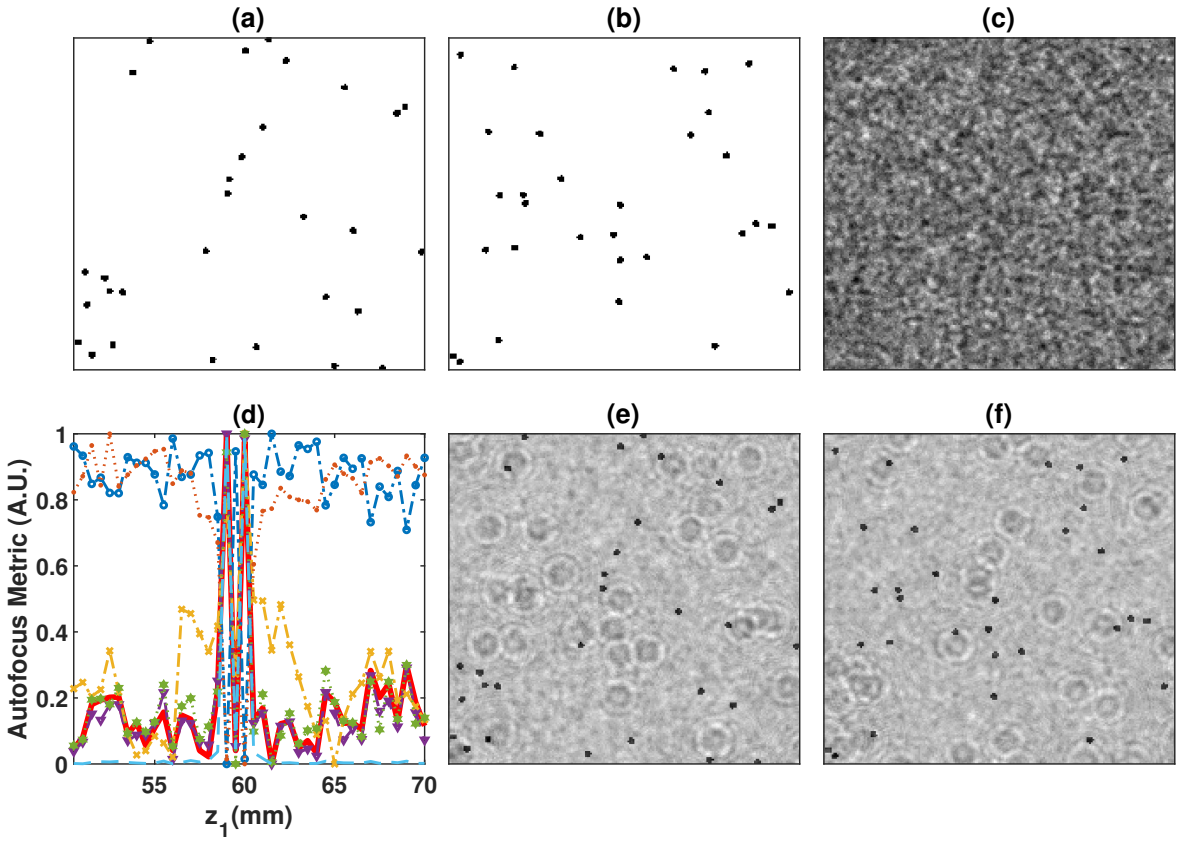

Figure 6.6: (a) and (b) The randomly distributed particles (amplitude objects) at the planes $z_1 = 59\ mm, z_2 = 41\ mm$ and $z_1 = 60\ mm, z_2 = 40\ mm$, respectively. (b) Simulated hologram and (c) plot of autofocusing metrics of some representative algorithms in function of z_1, The plot legends are same as those given in Fig. 6.3. (d) and (e) The reconstructed amplitude images at the estimated focal planes [204].

with $z_1 = 150\ mm$ and $z_2 = 150\ mm$ for a single object sample. Thus magnification of the setup was $M_g = 2$ and the object area was $5.61 \times 5.61\ mm^2$. The plots of autofocusing metrics as a function of z_1 are shown in Fig. 6.7(b). The estimated focal plane location was found at $z_1 = 149.1\ mm$. The reconstructed image at the estimated focal plane location is shown in Fig. 6.7(c) wherein the particles at focus are clearly visible. In the same experimental setup, another hologram was recorded as shown in Fig. 6.8(a) for two object samples placed at two different planes, $z_1 = 190\ mm, z_2 = 110\ mm$ and $z_1 = 235\ mm, z_2 = 65\ mm$. The plots of autofocusing metrics in function of z_1 is shown in Fig. 6.8(b). It can be observed that the two focal plane locations can be accurately estimated by detecting the peak locations. The reconstructed images at the estimated focal planes are shown in Figs. 6.8(c) and 6.8(d). Another experiment was performed using $45\ \mu m$ microbeads sandwitched between coverslip-microscope

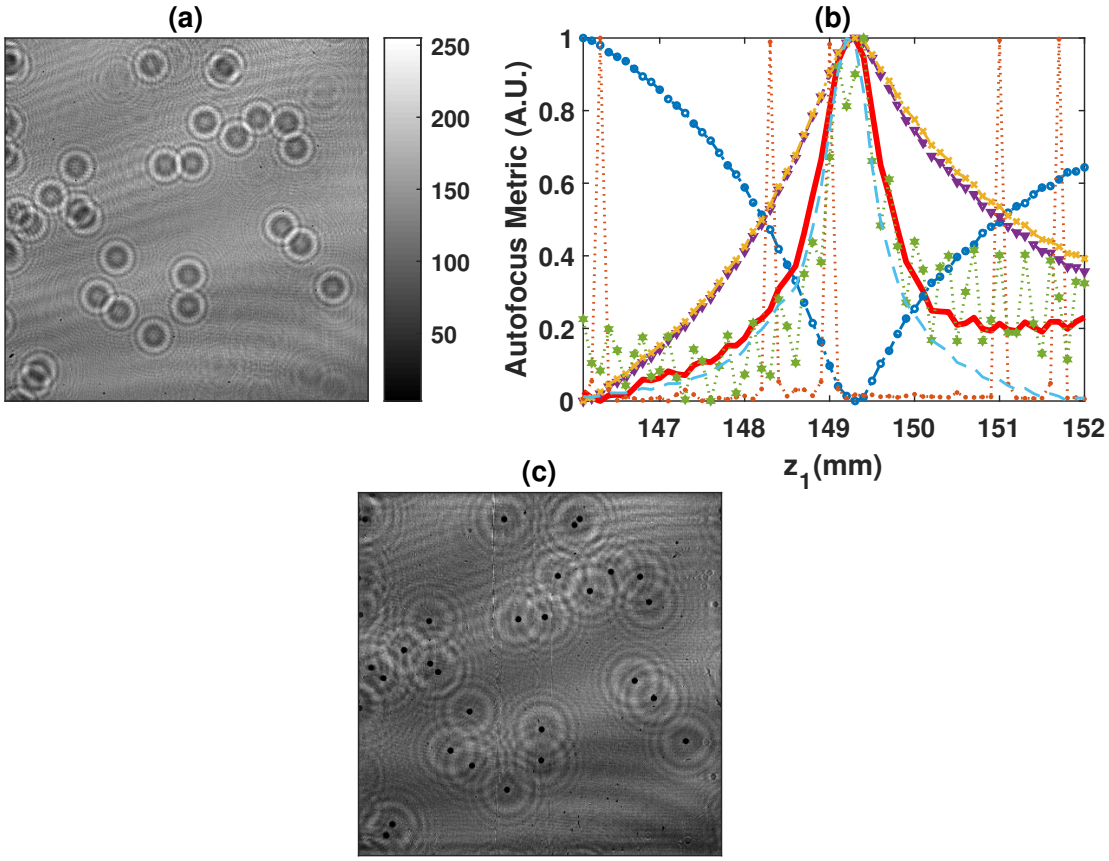

Figure 6.7: (a) Experimentally recorded in-line hologram associated with microbeads at $z_1 = 150\ mm$ and $z_2 = 150\ mm$ (b) plots of autofocusing metrics of some representative algorithms in function of z_1. The plot legends are same as those given in Fig. 6.3. (c) The reconstructed image at the estimated focal plane location.[204]

slide-coverslip such that the distance betweeb two object sample planes was around $1.1\ mm$. The slide was placed so that the two object samples planes were at around $z_1 = 150\ mm, z_2 = 150\ mm$ and $z_1 = 151.1\ mm, z_2 = 148.9\ mm$. Figure 6.9(a) shows the recorded hologram. The Laplacian filtering is applied to the hologram prior to the reconstruction during the autofocusing operation to improve the sensitivity of the autofocusing algorithms. The plots of autofocusing metrics of some representative algorithms in function of z_1 is shown in Fig. 6.9(b). The EIG algorithm detected two object planes at $z_1 = 149.9\ mm$ and $z_1 = 150.6\ mm$ based on the peak locations. The reconstructed images evaluated at the estimated focal planes using the original, unfiltered hologram are shown in Figs. 6.10(a) and 6.10(b). The selected regions of these reconstructed images indicated with the red colored rectangle are shown separately in Figs. 6.10(c) and 6.10(d), respectively. The micro-beads at focus in the individual planes are indicated with red colored arrows.

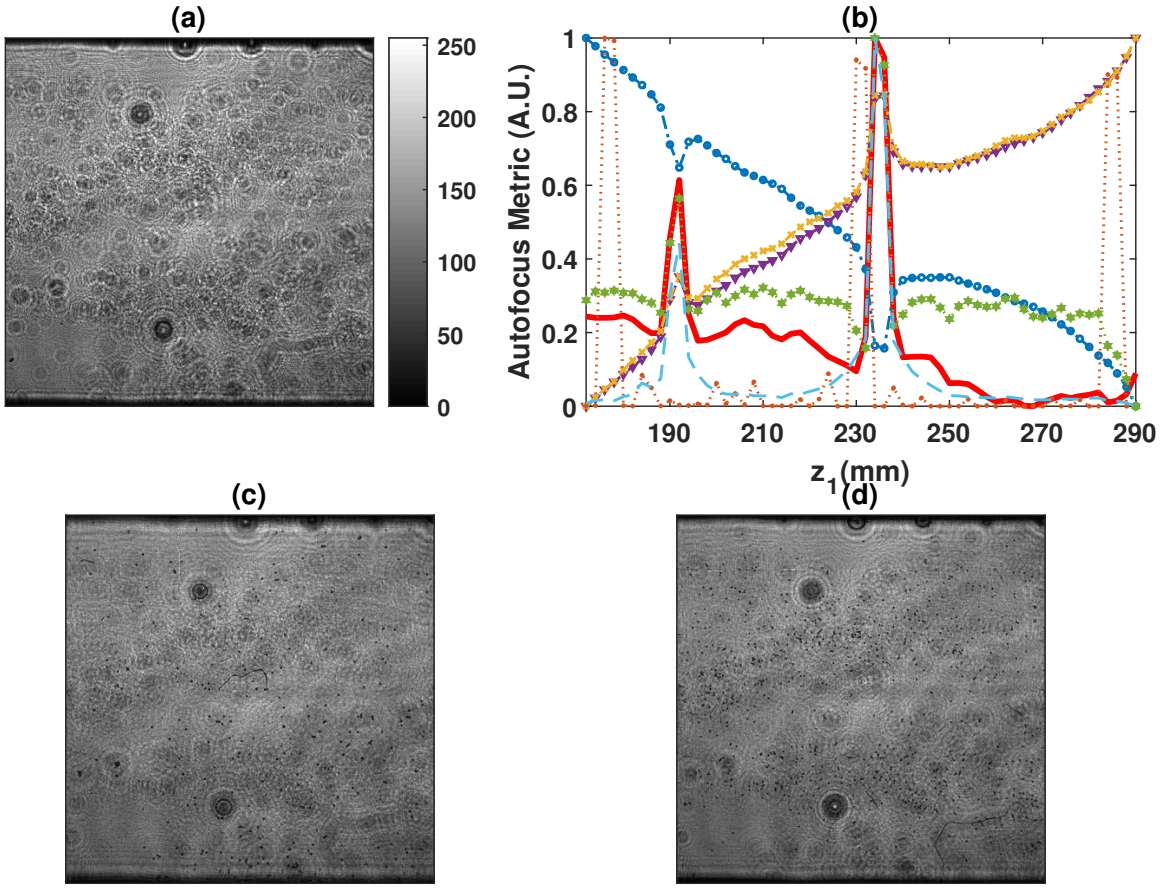

Figure 6.8: Experimentally recorded in-line hologram associated with microbeads placed at two planes $z_1 = 190\ mm$, $z_2 = 110\ mm$ and $z_1 = 235\ mm$, $z_2 = 65\ mm$ (b) plots of autofocusing metrics of some representative algorithms in function of z_1. The plot legends are same as those given in Fig. 6.3. (c) and (d) The reconstructed images at the estimated focal plane locations.[204]

Discussion

In the present study, the algorithms were implemented using the MATLAB 19a on a computer with the 9^{th} generation Intel-i5 processor with 2.4 GHz Hexacore and 8 GB RAM. The computation time taken by the autofocusing algorithms as a function of hologram size are tabulated in Table 6.1. The computation time required for the EIG algorithm is reported for two cases, $\text{EIG}^{(1)}$ and $\text{EIG}^{(2)}$. While in the first case, the algorithm was implemented using the full size reconstructed image, in the second case, the reconstructed image was divided into four parts and the autofocusing metric (Eq. 6.7) was computed for each part separately. In the end, an average of these four metrics was assigned to the corresponding reconstruction distance. In both the cases, the EIG algorithm provided similar performance in automatic detection of the focal plane. However, the computation time in the second case was found to be less compared to the first.

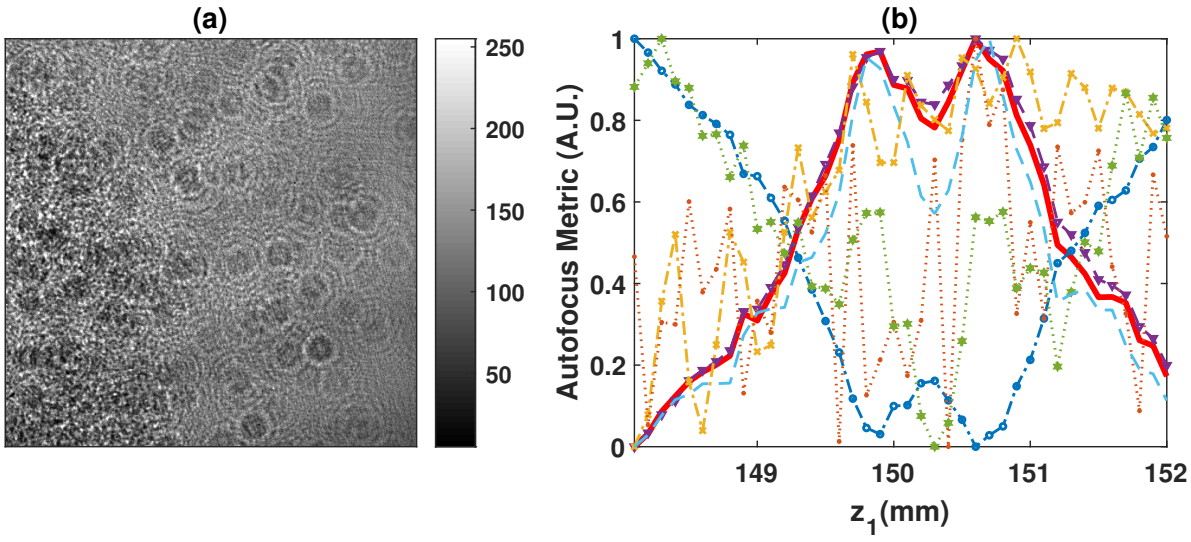

Figure 6.9: Experimentally recorded in-line hologram corresponding to the two object planes at $z_1 = 150\ mm$, $z_2 = 150\ mm$ and $z_1 = 151.1\ mm$, $z_2 = 148.9\ mm$ (b) plots of autofocusing metrics of some representative algorithms in function of z.[204]

The EIG algorithm can be implemented using either the magnitude images $A_{\tilde{z}}(x, y)$ or complex amplitude images $U_{r_{\tilde{z}}}(x, y)$. It has been observed that in the case of amplitude objects, the magnitude image based focal plane detection provides satisfactory results. This is also true for other methods considered for comparison. On the other hand, in the case of mixed object, the complex amplitude image based approach is found to provide comparatively better performance.

The EIG and DFS methods provide good performance irrespective of the object type. On the other hand, other methods provide poor results in the case of certain objects, especially objects of both amplitude and phase type. Therefore, the EIG and DFS methods can be considered to be the best. The computation time required for the EIG method is a little less compared to the DFS method.

Table 6.1: Computation time taken by autofocusing methods in function of hologram sizes (in seconds)

Autofocusing method	**Hologram size (in no. of pixels)**				
	200×200	400×400	583×800	1024×1280	2040×2040
AMS	0.05	0.15	0.43	1.90	4.51
DFS	0.24	0.67	1.63	5.32	24.21
GRA	0.10	0.44	1.29	3.91	12.79
SEN	0.22	0.46	1.42	6.23	34.47
SPA	0.24	0.35	1.45	5.31	24.53
VAR	0.06	0.18	0.53	2.61	7.08
$EIG^{(1)}$	0.15	0.67	1.62	5.90	28.42
$EIG^{(2)}$	0.16	0.59	1.27	4.80	20.48

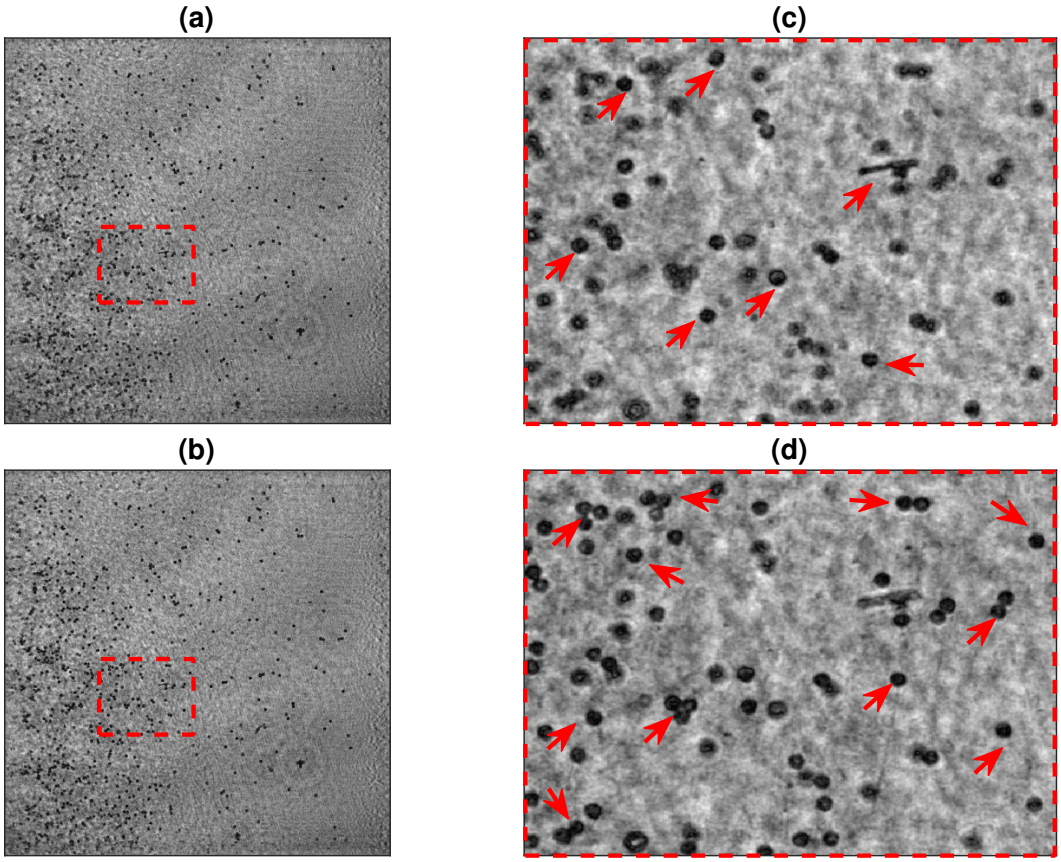

Figure 6.10: (a) and (b) Reconstructed images at the estimated focal planes using the unfiltered hologram in Fig. 6.9(a). (c) and (d) The selected regions of Figs. 6.10(a) and (b) reconstructed images indicated with the red colored rectangle, respectively.[204]

6.1.3 Conclusion

A novel hologram autofocusing algorithm is proposed based on a metric defined using the eigenvalues of the reconstructed optical wave-fields evaluated at different reconstruction distances. The proposed method performs equally well with amplitude object, phase object and mixed type object. The simulation and experimental results also demonstrate the capability of the proposed algorithm in locating the focal planes of closely spaced objects. The performance comparison of the proposed algorithm with some representative algorithms reported earlier in the literature substantiates the suitability of its use in practical applications.

6.2 Autofocusing based on distribution of eigenvalues of the reconstructed images

6.2.1 Methodology

A lensless digital in-line holographic configuration with a spherical wave illumination of the object as shown in Fig. 1.1(d) is considered for this present study. A spherical light beam of wavelength λ is used to illuminate an object placed at a distance of z_1 from the point light source located at the origin of the coordinate system. The object beam and reference beam propagates at a distance of z_2 from the object plane to the camera plane. The hologram is recorded as the intensity $H(X, Y)$ of the interference pattern between these two beams. In the hologram reconstruction process, under the paraxial approximation of wavefield propagation, the complex amplitude of the object wavefield can be computed as Eq. 1.10. The effectiveness of the proposed algorithm in autofocusing is equally applicable to the other digital holographic configurations as well.

In the proposed algorithm, the eigenvalue distribution is used for image sharpness estimation in the automatic focal plane detection technique. In the process of autofocusing, A_z is computed at different values of z within the measurement volume. At every reconstruction distance z, the corresponding amplitude image $A_z(x, y)$ is normalized by its energy as Eq. 6.3. The mean value of normalized amplitude image μ_z is evaluated using Eq. 6.4. A covariance matrix Q_z of mean subtracted normalized amplitude image is computed as Eq. 6.5. Subsequently, the eigenvalues of Q_z are evaluated and are arranged in an ascending order in a vector E_z using Eq. 6.6. In general, the eigenvalues decrease in approximately exponential manner up to a certain value of E_z. Beyond this value, the eigenvalue distribution is almost uniform. Accordingly, the eigenvalue distribution above a certain threshold can be modeled as,

$$E_z = E_{z0} e^{-n/\tau_z} \tag{6.8}$$

where, n and τ_z represent index and eigenvalue decay parameters, respectively. E_{z0} represents the value of E_z for $n = 0$. A linear model for τ_z estimation is obtained by taking logarithm of both sides of the above equation as,

$$\log E_z = -n/\tau_z + \log E_{z0}. \tag{6.9}$$

Thus, the logarithm of eigenvalue distribution below a threshold can be fit with a line of slope $-1/\tau_z$. The least square estimation of τ_z evaluated using the eigenvalues corresponding to each reconstructed image is used as autofocus metric. The corresponding distance $z_1 = z_f$, at which τ_z value is maximum or minimum is considered to be the image focus position. The in-focus image has higher amplitude

variations compared to the out-of-focus images, which means, the in-focus image sharpness is more compared to that of the out-of-focus images. The metric is defined based on the above fact.

In this case, the components associated with the most dominant eigenvalues of the covariance matrix Q_z contains most of the information on the spatial variation in the reconstructed image. Therefore, the metric τ_z should be calculated utilizing all of these dominant eigenvalues. However, monotonic changes of the the extent of the spatial variation in the reconstructed image as a function of the reconstruction distance can be found other than the focal plane in case of lensless digital in-line holographic configuration. This is due to the variable magnification associated with reconstructed image. This effect can be compensated by discarding a certain number of dominant eigenvalues in the computation of autofocusing metric. This number is given by the κ parameter whose value depends on the size of the reconstructed image. Since Q_z has M number of eigenvalues, κ value can be selected as a percentage of M and hence $E_z = E_z(m)$, where $m = 1, 2, \ldots, (M - \kappa)$. It can be noted that we can set $\kappa = 0$ in the digital holographic configuration with fixed magnification (i.e. parallel beam illumination). The distribution of eigenvalues E_z is exponential in nature. But for some cases, the exponential nature does not remains all over the distribution. It becomes almost linear after some extent. In that case, the slope of the eigenvalues distribution can be calculated only from the part of the distribution where its nature is exponential. Finally, the location of focal plane is selected as the value of $z_1 = z_f$ at which the metric τ_z takes the maximum/minimum value. The proposed algorithm (TOW) is described in Algorithm 5 below: Note

Algorithm 5 : TOW

Input: N_z number of reconstructed images each of size $(x \times y)$, z_s and z_{step}.
Output: z_f: Location of focal plane.
step 1: Calculate the normalized image $\bar{A}_z(x, y)$ (Eq. 6.3).
step 2: Calculate the mean μ_z of the normalized images (Eq. 6.4).
step 3: Calculate the covariance matrix Q_z (Eq. 6.5).
step 4: Calculate the metric τ_z based on the user defined κ value (Eq. 6.6, Eq. 6.8 and Eq. 6.9).
Repeat step 1 to step 4 for each reconstruction distance z.
step 5: Calculate the estimate of the focal plane location as $z_f = \max_{z_1} \tau(z)$ or $z_f = \min_{z_1} \tau(z)$.

that in the simulation and experimental study, z_1 and z_2 are varied such that $Z = z_1 + z_2$ is maintained constant. Therefore, the plots of autofocusing metrics are given in function of z_1.

6.2.2 Results and discussion

Simulation Results

A digital lensless in-line holographic setup with a spherical beam illumination of the object using a laser source of wavelength $\lambda = 500\ nm$ and camera pixel size of $4.8\ \mu m$ is considered for simulation

study. The hologram simulation and reconstruction is performed based on the algorithm described in [15]. A pure amplitude, a pure phase and a mixed type object are considered during the simulation study. Simulation results are provided for objects placed at a single and two planes as described below:

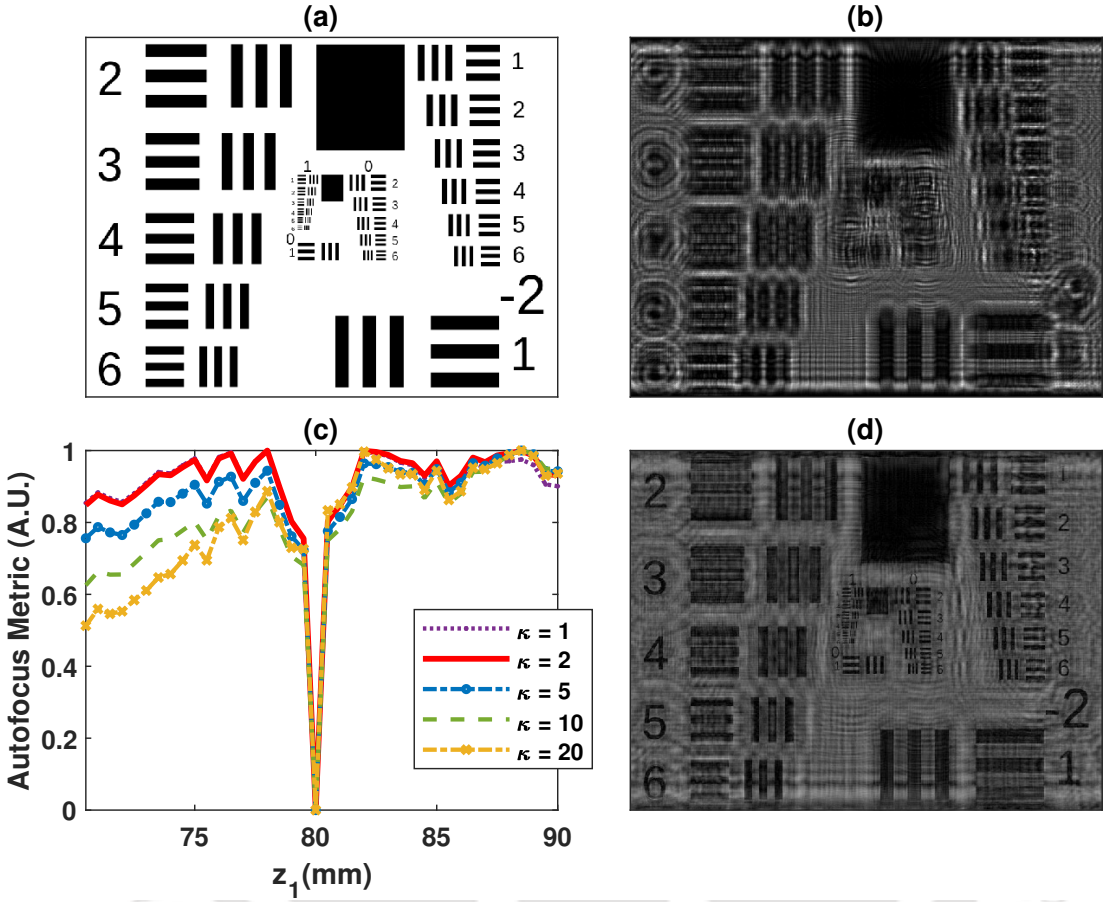

Figure 6.11: (a) The simulated amplitude object of size 583×800 pixels (b) the simulated hologram with $z_1 = 80\ mm$ and $z_2 = 20\ mm$ (c) the plot of $\boldsymbol{\tau}$ in function of z_1 for different κ and (d) the reconstructed amplitude image at the estimated focal plane [205].

Case 1: Single plane

Amplitude object : A USAF target amplitude object of size 583×800 pixels as shown in Fig. 6.11(a) is simulated such that, the object is placed at $z_1 = 80\ mm$ and $z_2 = 20\ mm$. Thus, $M_g = 1.25$ and the object area is $2.7 \times 3.8\ mm^2$. The simulated hologram is shown in Fig. 6.11(b). The hologram reconstruction was performed with $z_s = 70\ mm$, $z_{step} = 0.5\ mm$ and $N_z = 40$ keeping $z_1 + z_2 = 100\ mm$. Figure 6.11(c) shows the normalized plot of $\boldsymbol{\tau}$ in function of z_1 with $\kappa = [1, 2, 5, 10, 20]$, where the κ values were selected as $[0.2\%, 0.3\%, 1\%, 2\%, 4\%]$ of M, respectively. The metric has the minimum value at $z_1 = 80\ mm$ corresponding to the focal plane. The distribution of $\boldsymbol{\tau}$ with respect

to the location of focal plane is approximately symmetric for $\kappa = 1$ and 2. We can found that the κ values are most suitable in the range of 0.2%-1% of M as it provides accurate estimate of location of the focal plane. The reconstructed amplitude image of the object at the detected focal plane is shown in Fig. 6.11(d) for the purpose of illustration.

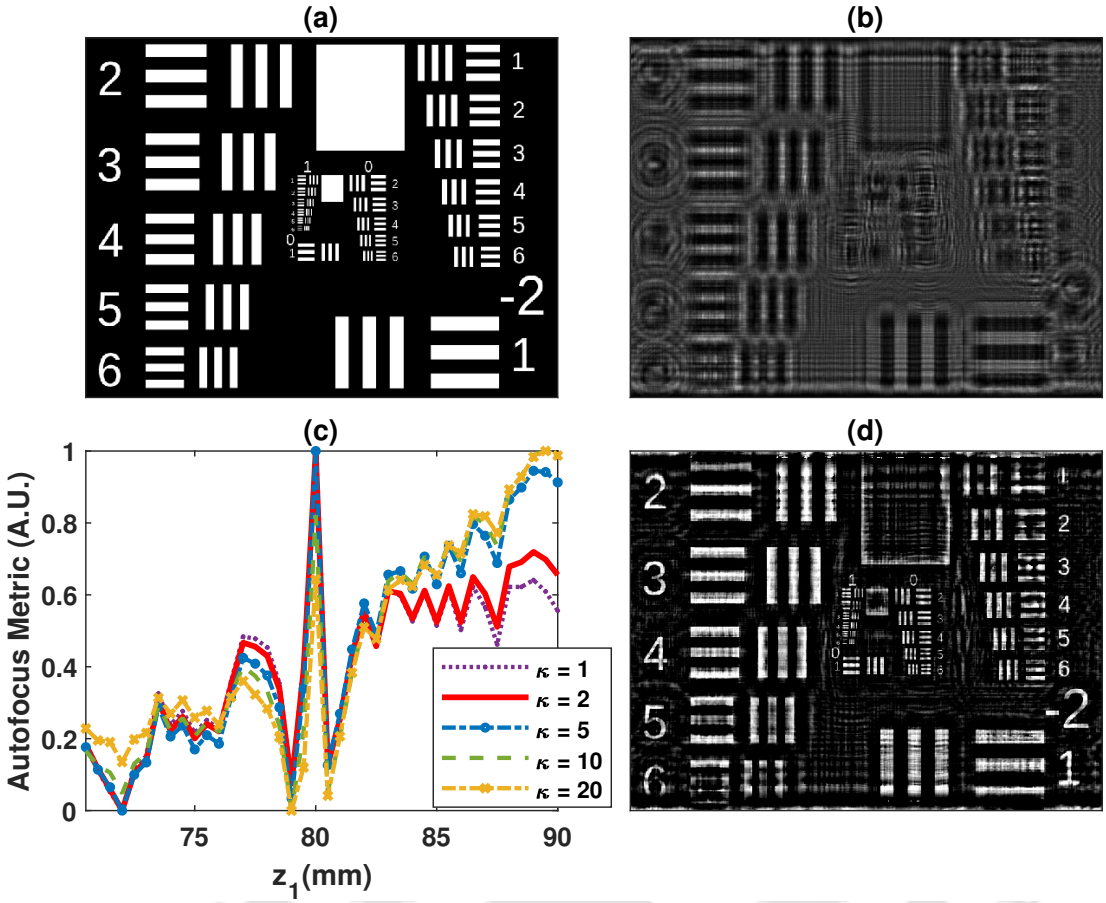

Figure 6.12: (a) The simulated phase object of size 583×800 pixels (b) the simulated hologram with $z_1 = 80\ mm$ and $z_2 = 20\ mm$ (c) the plot of $\boldsymbol{\tau}$ in function of z_1 for different κ and (d) the reconstructed phase image at the estimated focal plane [205].

Phase object : Similar to the amplitude object example, a USAF target phase object of the object is 583×800 pixels is simulated as shown in Fig. 6.12(a). The simulated hologram is shown in Fig. 6.12(b). The hologram reconstruction was performed with $z_s = 70\ mm$, $z_{step} = 0.5\ mm$ and $N_z = 40$ keeping $z_1 + z_2 = 100\ mm$. Figure 6.12(c) shows the normalized plot of $\boldsymbol{\tau}$ in function of z_1 with $\kappa = [1, 2, 5, 10, 20]$, where the κ value can be selected as $[0.2\%, 0.3\%, 1\%, 2\%, 4\%]$ of M, respectively. A single peak corresponding to the location of focal plane at $z_1 = 80\ mm$ can be observed. In this case too, it was observed that the distribution of $\boldsymbol{\tau}$ with respect to the focal plane is approximately symmetric

for $\kappa = 1$ and 2. The reconstructed phase image of the object at the detected focal plane is shown in Fig. 6.12(d) for the purpose of illustration.

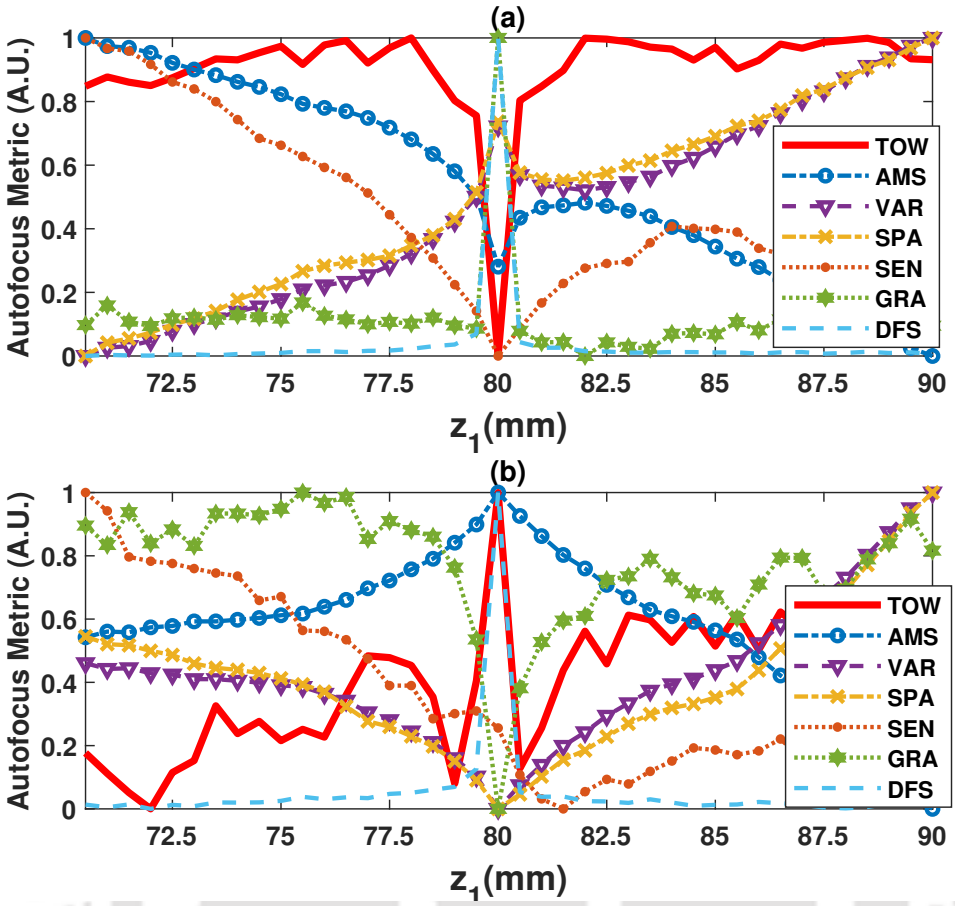

Figure 6.13: Plot of autofocusing metrics of representative algorithms in function of z_1 for (a) the amplitude object and (b) the phase object [205].

The proposed algorithm is compared with some of the previously established algorithms for the focal plane detection is given in Fig. 6.13. Figures 6.13(a) and 6.13(b) show the plots of autofocusing metrics of some representative algorithms in function of z_1 for the amplitude (Fig. 6.11(a)) and phase (Fig. 6.12(a)) objects, respectively. Note that the autofocusing metrics computed for all the methods are normalized for the purpose of comparison. It can be observed in Fig. 6.13(a) that although all the autofocusing metric curves exhibited a peak or dip at the focal plane, peaks of the DFS and GRA and dip of TOW curves are more sharper in comparison with the other curves. In fact, a monotonic variations in the metric curves are observed, except at the focal plane, for the algorithms other than the TOW, DFS and GRA. For these three algorithms, sharper peaks and dip are observed in Fig. 6.13(b) for the phase object as well. Moreover, the SEN algorithm could not provide accurate focal plane detection for the phase object. In the following simulation and experimental examples, the plot legends are the same as

shown in Fig. 6.13. Therefore, the plot legends in the following examples are not shown due to the space constraints in the figures.

Mixed object : The performance of the proposed algorithm is also evaluated with a mixed type object having both amplitude and phase variations. The simulated amplitude and phase of the object each of size 200×200 pixels are shown in Figs. 6.14(a) and 6.14(b), respectively. Figure 6.14(c) shows the simulated hologram with $z_1 = 80\ mm$ and $z_2 = 20\ mm$. The autofocusing metrics evaluated using different algorithms are plotted in function of z_1 as shown in Fig. 6.14(d). Since the object is of mixed type, the proposed focal plane detection algorithm was implemented with the complex amplitude $U_{r_z}(x, y)$ instead of $A_z(x, y)$. It can be observed that only the proposed TOW and the DFS algorithm were successful in accurately detecting the focal plane at $z_1 = 80\ mm$. For the purpose of illustration, the reconstructed amplitude and reconstructed phase are shown in Figs. 6.14(e) and 6.14(f), respectively.

Case 2: Two plane

A simulated example of hologram autofocusing with two object planes is considered. In this example, randomly distributed particles representing pure amplitude objects are simulated at two different planes in the path of light propagation. Figures 6.15(a) and 6.15(b) show two images of size 200×200 pixel of the randomly distributed particles placed at $z_1 = 40\ mm$ and $z_1 = 60\ mm$, respectively, with total point source to hologram plane distance as $Z = 100\ mm$. The simulated hologram is shown in Fig. 6.15(c). Figure 6.15(d) shows the plot of autofocusing metrics evaluated using some representative algorithms in function of z_1. Two peaks are observed at $z_1 = 40\ mm$ and $z_1 = 60\ mm$ by most of the algorithms. The reconstructed images at the estimated focal planes are shown in Figs. 6.15(e) and 6.15(f), respectively. Next, a similar exercise was performed as shown in Fig. 6.16 with two closely placed planes at $z_1 = 59\ mm$ and $z_1 = 60\ mm$ containing randomly distributed particles. The results shown in Fig. 6.16 show that the proposed algorithm was able to accurately detect the location of the focal plane in this case as well.

Experimental Results

The experimental validation of the proposed method is performed using the holograms recorded in a digital off-axis holographic setup with spherical light beam illumination. A light source of wavelength $\lambda = 532\ nm$ was used to illuminate a Buddha statue. The holograms were recorded using a monochrome camera with 1200×1600 pixels and $4.4\ \mu m$ pixel size. Figure 6.17(a) shows the recorded hologram,

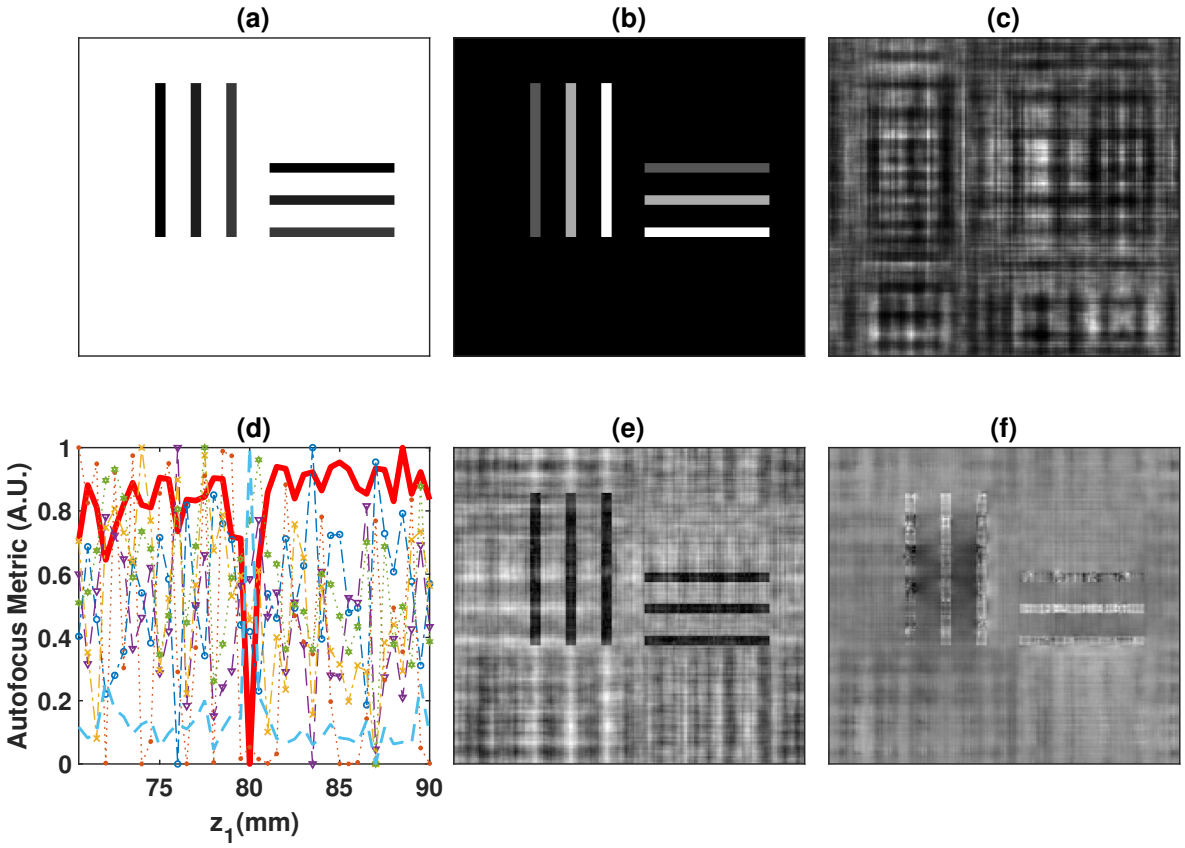

Figure 6.14: (a) The simulated amplitude and (b) the simulated phase of the mixed type object. (c) The simulated hologram with $z_1 = 80mm$ and $z_2 = 20\ mm$ (d) plot of autofocusing metrics of representative algorithms in function of z_1. The plot legends are same as those given in Fig. 6.13. The reconstructed (e) amplitude and (f) phase images at the estimated focal plane [205].

whereas the comparison among the autofocusing methods are shown in Fig. 6.17(b). The reconstructed image of the off-axis hologram has a DC part, a real image and a virtual image. The autofocusing algorithm can be applied on either real image or virtual image part. In the present study 700×700 pixels sized real image part of the reconstructed images are cropped. The autofocusing algorithm is applied on the set of these cropped images. The focus position is estimated as $z_f = 940\ mm$. Figure 6.17(c) shows the reconstructed image at focus.

Discussion

In the present study, the algorithms were implemented using the MATLAB 19a on a computer with the 9^{th} generation Intel-i5 processor with 2.4 GHz Hexacore and 8 GB RAM. The computation time taken by the autofocusing algorithms as a function of hologram size are tabulated in Table 6.2. The

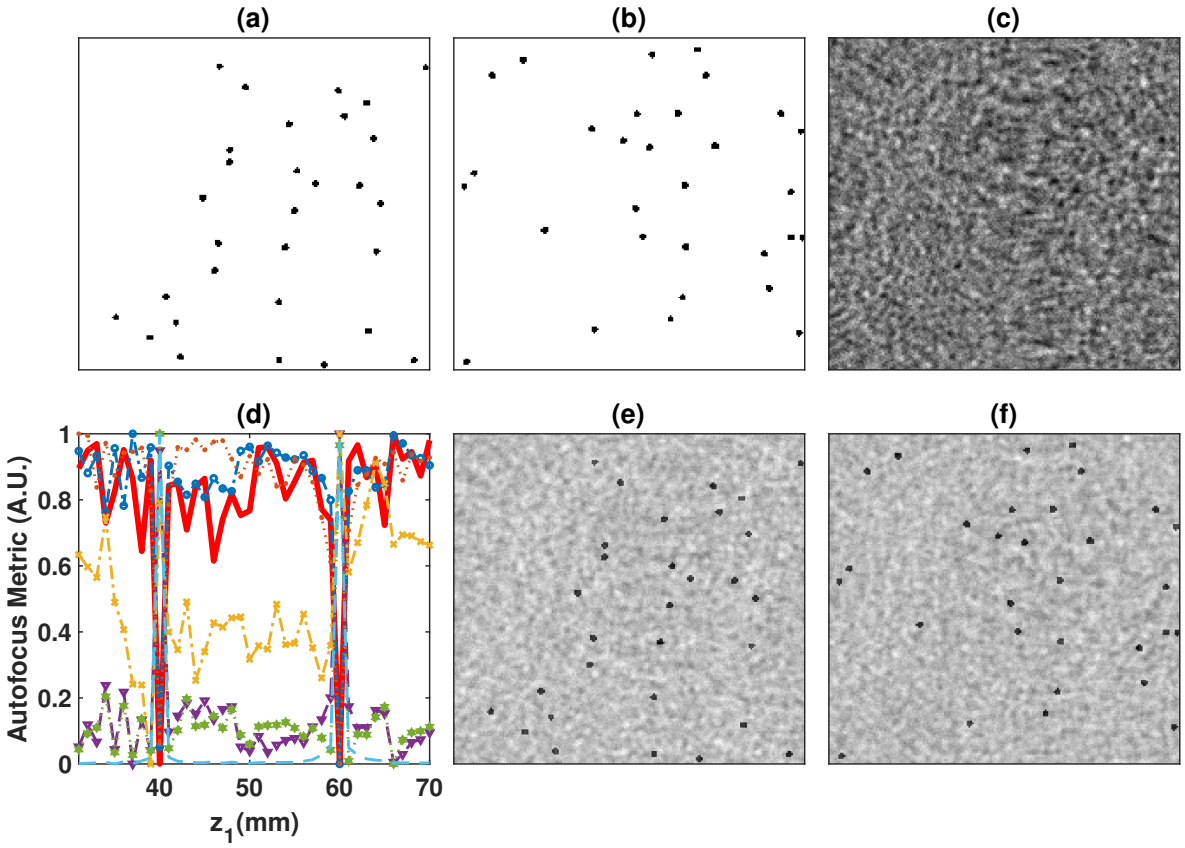

Figure 6.15: (a) and (b) The randomly distributed particles (amplitude objects) at the planes $z_1 = 40\ mm, z_2 = 60\ mm$ and $z_1 = 60\ mm, z_2 = 40\ mm$. (b) the simulated hologram and (c) plot of autofocusing metrics of some representative algorithms in function of z_1. The plot legends are same as those given in Fig. 6.13. (d) and (e) Reconstructed amplitude images at the estimated focal planes [205].

computation time in TOW implementation is found to be comparable to the other methods.

The TOW algorithm can be implemented using either the magnitude images $A_z(x, y)$ or complex amplitude images $U_{r_z}(x, y)$. It has been observed that in the case of amplitude and phase objects, the magnitude image based focal plane detection provides satisfactory results. This is also true for other methods considered for comparison. On the other hand, in the case of mixed object, the complex amplitude image based approach is found to provide comparatively better performance.

Both the methods EIG and TOW are able to detect the focal plane irrespective of object type and shape. They work fine in case of single plane and multiple plane objects. The algorithms are capable to find the closely spaced object focal plane. The computation time taken by both the methods in function of hologram size are tabulated in Table 6.3. It can be seen that, both the methods provide similar accuracy with comparable computation cost.

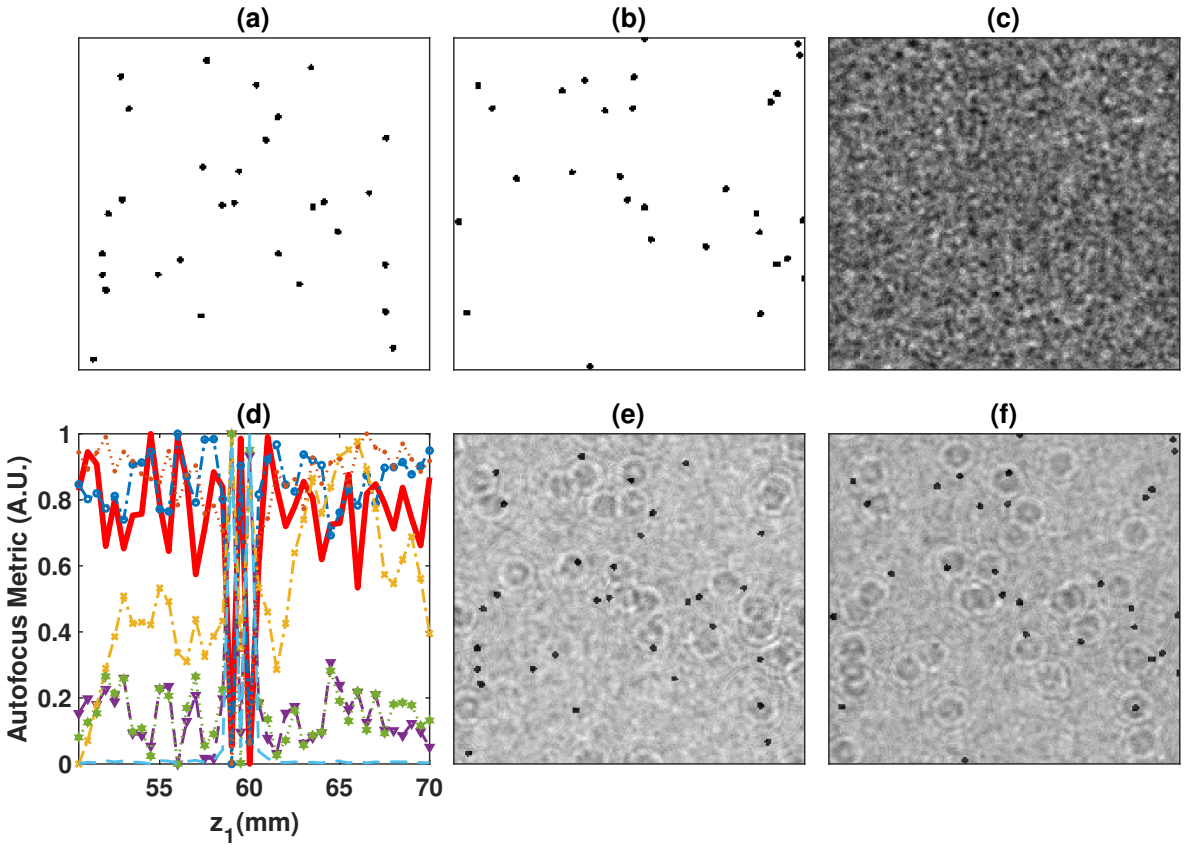

Figure 6.16: (a) and (b) The randomly distributed particles (amplitude objects) at the planes $z_1 = 59\ mm, z_2 = 41\ mm$ and $z_1 = 60\ mm, z_2 = 40\ mm$. (b) the simulated hologram and (c) plot of autofocusing metrics of some representative algorithms in function of z_1. The plot legends are same as those given in Fig. 6.13. (d) and (e) Reconstructed amplitude images at the estimated focal planes [205].

Table 6.2: Computation time taken by autofocusing methods in function of hologram sizes (in milliseconds)

Autofocusing	**Hologram size (in no. of pixels)**					
	In-line Hologram					**Off-axis Hologram**
method	200 × 200	400 × 400	583 × 800	1000 × 1000	2040 × 2040	700 × 700
AMS	0.38	2.4	8	15	50	5.6
DFS	0.99	6.3	29	42	190	23
GRA	0.98	5.5	28	40	190	20
SEN	0.76	3.3	10	19	75	7.5
SPA	0.43	2.4	7	16	66	5.6
VAR	0.52	2.9	7	18	65	7.6
TOW	1.05	5.7	26	36	170	22

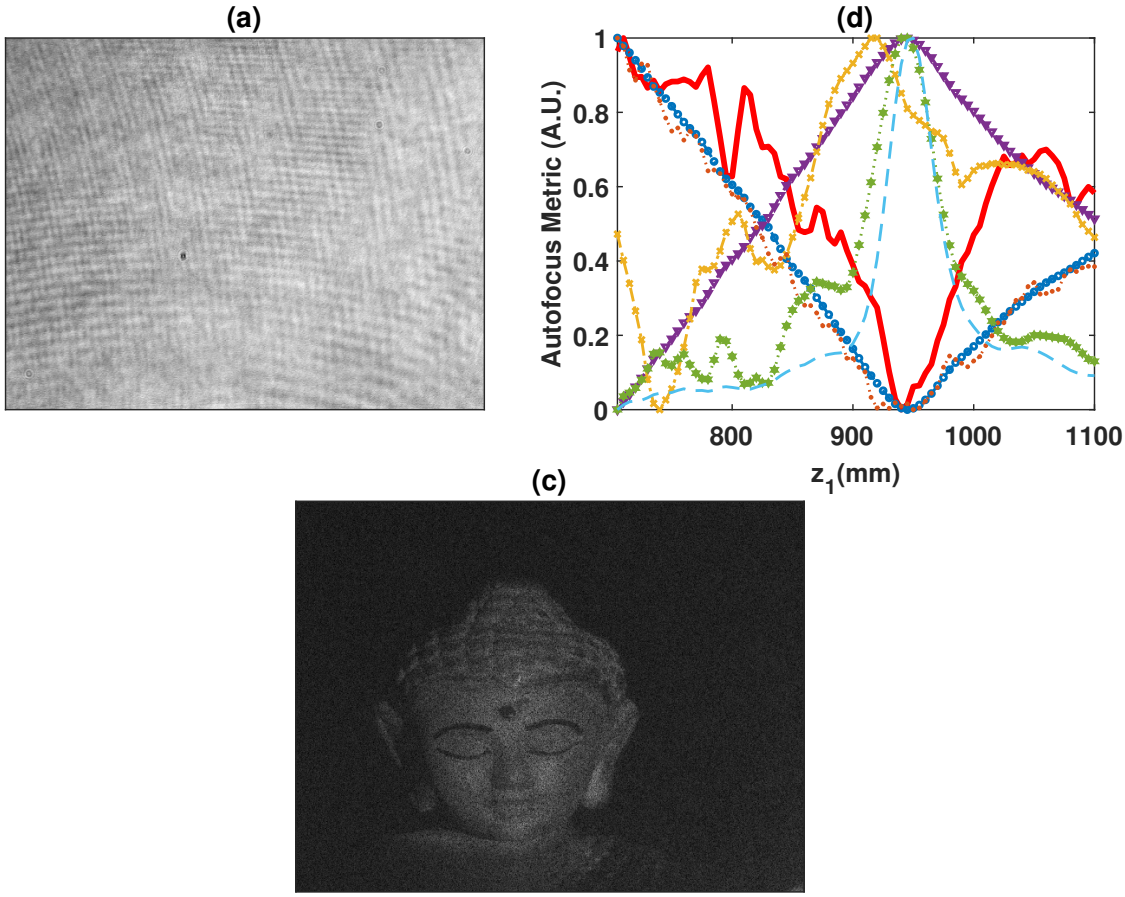

Figure 6.17: (a) Experimentally recorded hologram and (b) plot of autofocusing metrics of some representative algorithms in function of z_1, The plot legends are same as those given in Fig. 6.13. (c) reconstructed image at the estimated focal planes. The Buddha statue is clearly visible here [205].

Table 6.3: Computation time taken by proposed EIG and TOW algorithm in function of hologram sizes (in milliseconds)

Autofocusing method	**Hologram size (in no. of pixels)**				
	200×200	400×400	583×800	1000×1000	2040×2040
EIG	0.917	5.76	26.1	37.3	164.9
TOW	1.047	5.66	25.8	35.7	169.9

6.2.3 Conclusion

A novel hologram autofocusing algorithm is proposed based on a metric defined using the slope of the eigenvalues distribution of the reconstructed optical wave-fields evaluated at different reconstruction distances. The proposed method is equally suitable well with amplitude object, phase object and mixed type object. The simulation and experimental results also demonstrate the capability of the proposed algorithm in locating the focal planes of closely spaced objects. The performance comparison of the

proposed algorithm with some representative algorithms reported earlier in the literature substantiates the suitability of its use in practical applications.

7

Autofocusing based on particle swarm optimization

The conventional or direct autofocusing (AF) algorithms are able to detect the focal plane accurately utilizing reconstructed images evaluated at multiple planes as a part of focal plane detection procedure. However, evaluation of large number of reconstructed images is time consuming. As a result, although the computation time required in the execution of AF algorithm is low, the total time complexity required in the focal plane detection procedure including the hologram reconstruction and AF is significantly high. In this section, we propose a particle swarm optimization (PSO) [206] based technique to reduce the total computation time in the automatic detection of the focal plane. Note that any one of the previously mentioned image quality metric can be utilized in the implementation of the proposed method. For the purpose of demonstration we have considered different AF algorithms EIG [204], TOW [205], AMS [135], DFS [132], GRA [207] and VAR [134]. The details of the proposed algorithm is described below.

7.1 Methodology

Let $\boldsymbol{f(A_z)}$ represent the image quality metric defined ias a function of reconstruction distance z. The function $\boldsymbol{f}(A_z)$ corresponds to one of the AF algorithms among EIG, TOW, AMS, DFS, GRA and VAR. This function takes the object image reconstructed at distance z corresponding to a z_2 (as shown in Fig. 1.1(c)) as an input and returns the image quality metric.

[7]This chapter presents the hologram autofocusing algorithm based on the particle swarm optimization.

Algorithm 6 : Particle swarm optimization based focal plane detection

Input: N_z,T_h, w, ϕ_g, ϕ_p, z_{min}, z_{max}, $A_z(x,y)$
Output: z_f : focal plane distance
Initialize: $z_{prev} = z_{min}$, $maxItr$
HashMap: F_h stores $(z_i, \boldsymbol{f}(A_{z_i}))$
for $i = 1, \ldots, N_z$ **do**
  $z_i \sim \mathcal{U}(z_{min}, z_{max})$
  $\overline{z_i} = z_i$
  $v_i \sim \mathcal{U}(-|z_{max} - z_{min}|, |z_{max} - z_{min}|)$
  if $(i == 1)$ **then**
    $z_f = z_i$, $F_h(z_i) = \boldsymbol{f}(\boldsymbol{A_{z_f}})$
  end
  else if $\boldsymbol{f}(\boldsymbol{A_{\overline{z_i}}}) < F_h(z_f)$ **then**
    $z_f = \overline{z_i}$, $F_h(z_i) = \boldsymbol{f}(\boldsymbol{A_{z_f}})$
  end
end
while $|z_{prev} - z_f| > T_h$ & $maxItr > 0$ **do**
  for $i = 1, \ldots, N_z$ **do**
    if $(|z_{prev} - z_f| < T_h)$ **then**
      Break
    end
    $r_p, r_g \sim \mathcal{U}(0,1)$
    $v_i = w \cdot v_i + \phi_p \cdot r_p \cdot (\overline{z_i} - z_i) + \phi_g \cdot r_g \cdot (z_f - z_i)$
    $z_i = z_i + v_i$
    $\tilde{f}_{z_i} = \boldsymbol{f}(A_{z_i})$
    if $\tilde{f}_{z_i} < \boldsymbol{f}(A_{\overline{z_i}})$ **then**
      $\overline{z_i} = z_i$
      if $(z_f$ *in* $F_h)$ **then**
        if $(\tilde{f}_{z_i} < F_h(z_f))$ **then**
          $z_{prev} = z_f$, $z_f = \overline{z_i}$, $F_h(z_i) = \tilde{f}_{z_i}$
        end
      end
      else
        $\tilde{f}_{z_f} = \boldsymbol{f}(A_{z_f})$
        if $\tilde{f}_{z_i} < \tilde{f}_{z_f}$ **then**
          $z_{prev} = z_f$, $z_f = \overline{z_i}$, $F_h(z_i) = \tilde{f}_{z_i}$
        end
        else
          $F_h(z_i) = \tilde{f}_{z_f}$
        end
      end
    end
  end
  $maxItr = maxItr - 1$
end

The proposed method of focal plane position estimation is given in Algorithm 6. At first, the PSO algorithm parameters T_h, w, ϕ_g, ϕ_p are initialized. The focal plane position search space is set as $[z =$

$z_{min}, z_2 = z_{max}]$ as shown in Fig. 1.1(c). In the proposed method reconstruction distances z_i with $i \in [1, N_z]$ are treated as particles. The best position of the individual particle is indicated with $\overline{z_i}$. At the start of the algorithm, these particles are equispaced between z_{min} and z_{max} and the initial focal plane estimate z_f is set equal to z_{min}. The maximum number of iterations is set as $maxItr$. The particle velocity is initialized with a value chosen from a uniform distribution $\mathcal{U}(-|z_{max} - z_{min}|, |z_{max} - z_{min}|)$. The best particle positions are set as $\overline{z_i} = z_i$. A HashMap F_h is defined to store previously computed function values of $\boldsymbol{f}(A_z)$ at z_i's while returning the stored value in constant time (i.e. $\mathcal{O}(1)$). As a result, it helps in avoiding re-computation of the metric at the same position and effectively increases the computational efficiency of the algorithm. The first **for** loop in the algorithm identifies the best particle position among z_i's and assigns it to z_f. The following **while** loop is executed till the difference between the current and previous estimates of the focal plane location falls below the specified threshold T_h or maximum number of iterations are performed. The i^{th} particle position z_i is updated by moving it with a velocity v_i. The particle velocity v_i is evaluated based on the algorithm hyper-parameters w, ϕ_p and ϕ_g and previously estimated focal plane position. r_p and r_g are random numbers taken from a uniform distribution for velocity normalization to assure that, the particles remain inside the search space. Subsequently, the reconstructed image quality metrics evaluated for the updated particle position and its previously best known position are compared and the focal plane position estimate z_f is updated accordingly. Once the termination criteria is reached, the last value of z_f corresponding to z is considered to be the final focal plane position estimate.

7.2 Results and discussion

A simulation study was performed considering a digital lensless in-line holographic setup with a plane beam illumination (as shown in Fig. 1.1(c)) using a laser source of wavelength $\lambda = 500\ nm$. A USAF amplitude type sample of size 583×800 pixels shown in Fig. 7.1(a) is used as an object under investigation. A hologram is generated with the pixel size of $4.8\ \mu m \times 4.8\ \mu m$. The hologram simulation and reconstruction were performed based on the angular spectrum approach of wave propagation as described in [187]. The object to camera distance was set to $z_2 = 80\ mm$. Figure 7.1(b) shows the simulated hologram. The focal plane detection algorithms EIG, TOW, AMS, VAR, GRA and DFS were implemented using 80 hologram reconstructed images such that the reconstruction planes were equispaced between $z_2 = 70\ mm$ and $z_2 = 90\ mm$ away from the camera. The plots of image quality metrics in function of the reconstruction distances are shown in Fig. 7.1(c). It can be observed that the extremum values of the image quality metrics correspond to the reconstruction distance close to the true value. All

of the AF algorithms estimated the focal plane position at $z_2 = 80\ mm$. The total computation times, that is, the time taken for reconstruction of 80 images and evaluation of focal plane position estimate by each AF algorithm are reported in Table 7.1. For the purpose of illustration, the reconstructed image at the focal plane position estimated using the EIG algorithm is shown in Fig. 7.1(d).

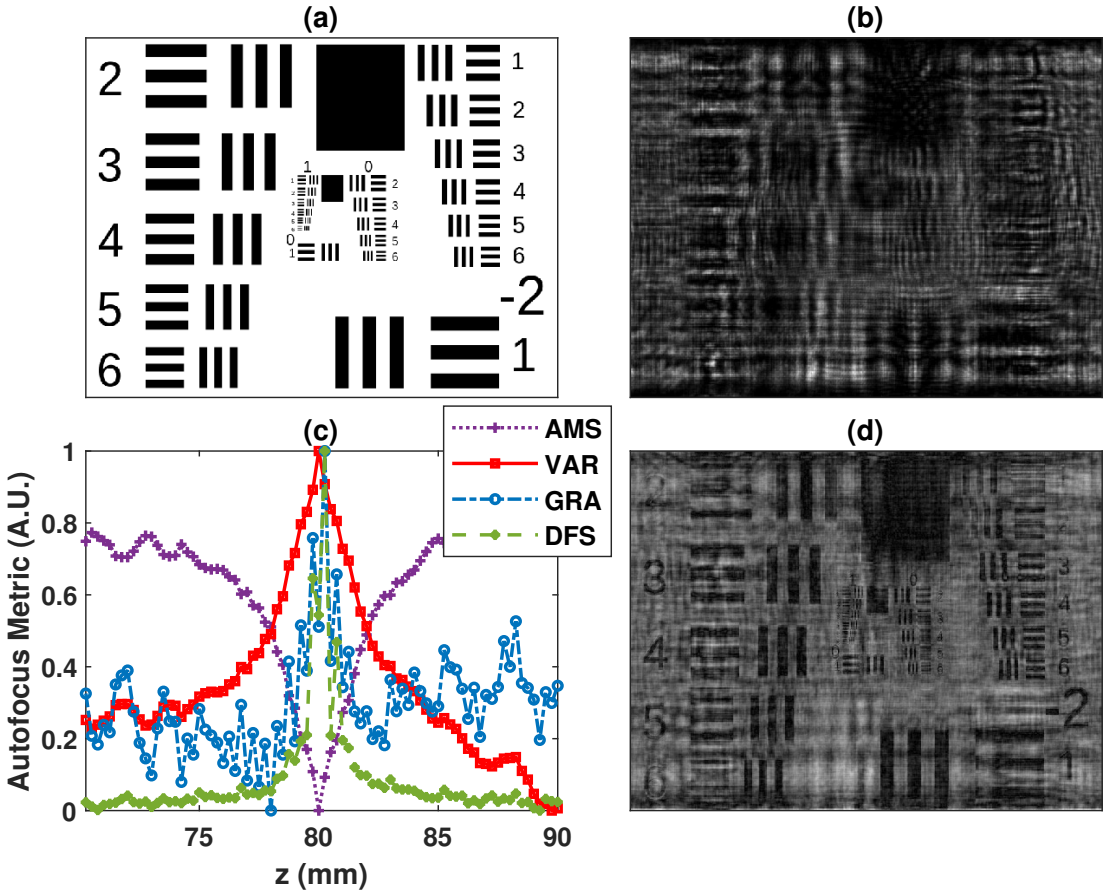

Figure 7.1: Simulation example: (a) USAF amplitude object, (b) hologram generated with camera to object distance $z_2 = 80\ mm$, (c) autofocus metric plots for conventional EIG, TOW, AMS, DFS, VAR and GRA methods and (d) reconstructed image at the detected focal plane of $z_f = 80\ mm$ obtained using the EIG method [208].

For the same simulation example, the proposed PSO algorithm was implemented with $N_z = 6$, $T_h = 0.00001$, $w = 0.0357$, $\phi_p = 0.7$, $maxItr = 10$ and $\phi_g = 1.05$ for each AF algorithm. The parameters are chosen as suggested in [209]. Let $\epsilon = |z_2 - z_f|$ define the absolute difference between the true and estimated reconstruction distances at each iteration. Figure 7.2 shows the plots of ϵ as a function of number of swarm iterations in the implementation of the proposed PSO algorithm using each AF algorithm. The plots are provided for five independent simulation runs. It can be noted that in each case the ϵ value converges towards zero as the algorithm progresses. The total time taken by the

proposed PSO based algorithm for each AF metric is reported in Table 7.1. It is evident that the proposed method significantly improves the computational efficiency of the AF algorithm without sacrificing the focal plane position estimation accuracy. For the same simulation example, the hologram was simulated with $z_2 = 80.15\ mm$. The errors in the focal plane position estimation using the conventional and PSO assisted EIG, TOW, AMS, VAR, GRA and DFS algorithms were 0.015, 0.015, 0.015, 0.015, 0.015, 0.015 and 0.005, 0.005, 0.005, 0.005, 0.015, 0.005, respectively. In this case, it can be noted that the PSO algorithm provided accurate focal plane position estimates compared to conventional approaches.

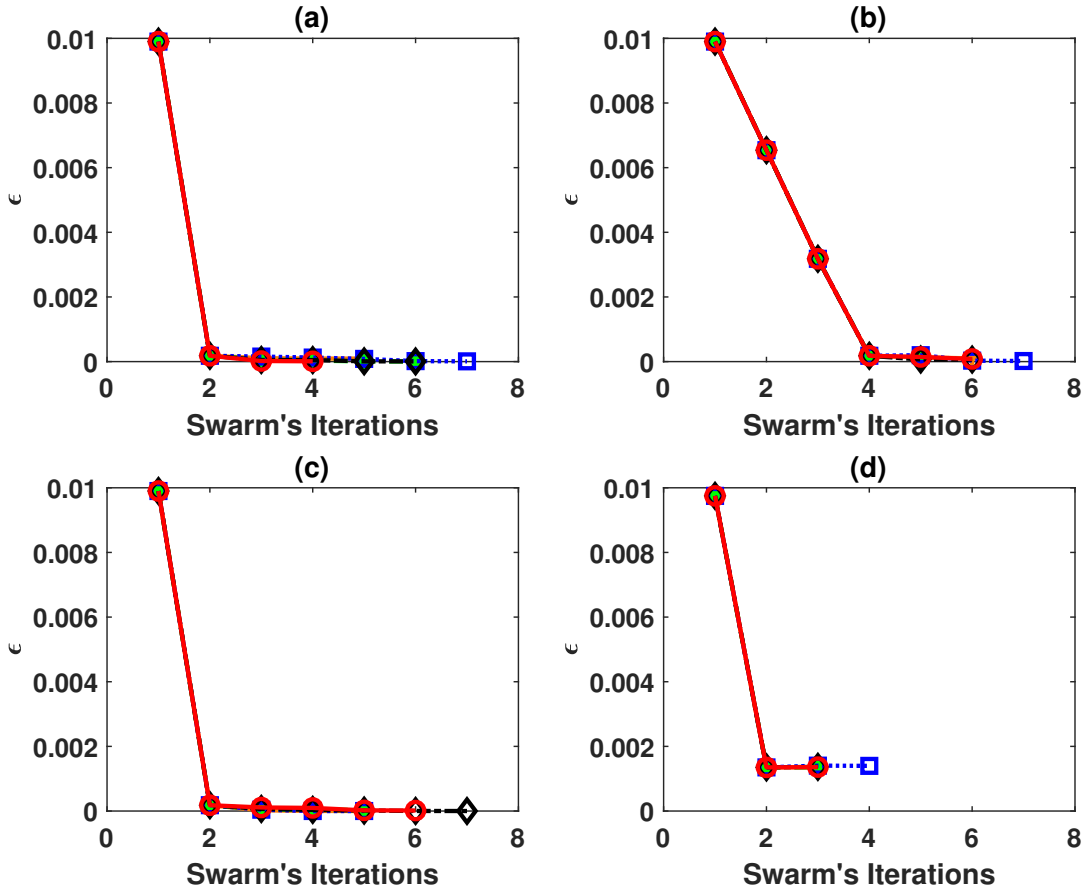

Figure 7.2: Plot of ϵ in function of number of swarm iterations with the implementation of the proposed PSO algorithm using (a) AMS (b) DFS (c) VAR and (d) GRA. The plots are provided for five independent simulation runs marked with different color [208].

A parametric study was conducted to evaluate the algorithm performance in function of the hyper-parameters. For the same simulation example in Fig. 7.1, ϵ values were evaluated by varying one of the hyper-parameters while keeping other parameters constant. Figures 7.3(a), 7.3(b) and 7.3(c) show the changes in ϵ in function of number of iterations considering different values of w, ϕ_p and ϕ_g, respectively. In each case, the estimated focal plane position estimate was found to converge towards the true value.

Table 7.1: Comparison of computation time (in seconds) in function of hologram size

AF method	Hologram size (in pixels)											
	200 × 200		400 × 400		583 × 800		1000 × 1000		2040 × 2040		1200 × 1600	
	Conv	**PSO**	Conv	**PSO**	Conv	**PSO**	Conv	**PSO**	Conv	**PSO**	Conv	**PSO**
AMS	0.73	**0.17**	3.08	**0.83**	4.08	**1.24**	20.21	**3.78**	104.0	**37.19**	8.86	**3.64**
DFS	1.09	**0.31**	3.47	**1.06**	5.40	**1.35**	22.93	**8.01**	120.9	**37.79**	10.14	**4.27**
EIG	0.95	**0.27**	3.39	**1.04**	5.40	**1.34**	23.40	**8.17**	127.7	**39.88**	10.93	**4.60**
GRA	1.08	**0.34**	3.39	**1.11**	5.33	**1.51**	22.68	**8.41**	115.2	**46.84**	9.93	**4.24**
TOW	1.08	**0.31**	3.33	**1.02**	5.40	**1.35**	22.77	**7.95**	131.6	**41.10**	12.46	**5.25**
VAR	0.75	**0.24**	3.14	**0.85**	4.92	**1.65**	20.54	**9.10**	105.6	**25.92**	8.98	**3.73**

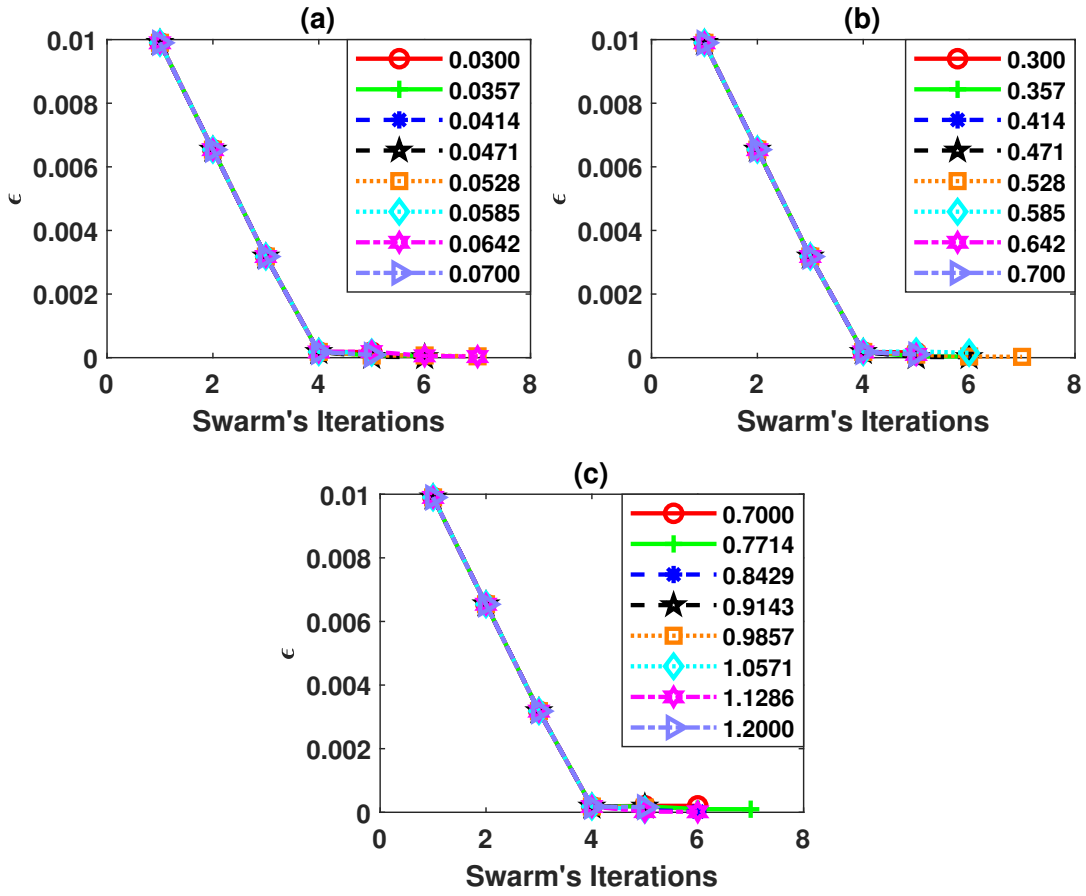

Figure 7.3: Plots of ϵ in function of number of iterations with the implementation of the proposed PSO algorithm using DFS for different values of (a) w with $\phi_p = 0.7$, $\phi_g = 1.05$, (b) ϕ_p with $w = 0.0357$, $\phi_g = 1.05$ and (c) ϕ_g with $w = 0.0357$, $\phi_p = 0.7$ [208]

.

The experimental validation was performed using the hologram recorded in a digital off-axis holographic setup with a Buddha statue as an object. The statue was illuminated with a laser light source of wavelength $\lambda = 532\ nm$. The hologram was recorded using a CCD camera (XCL-U1000, Sony Cor-

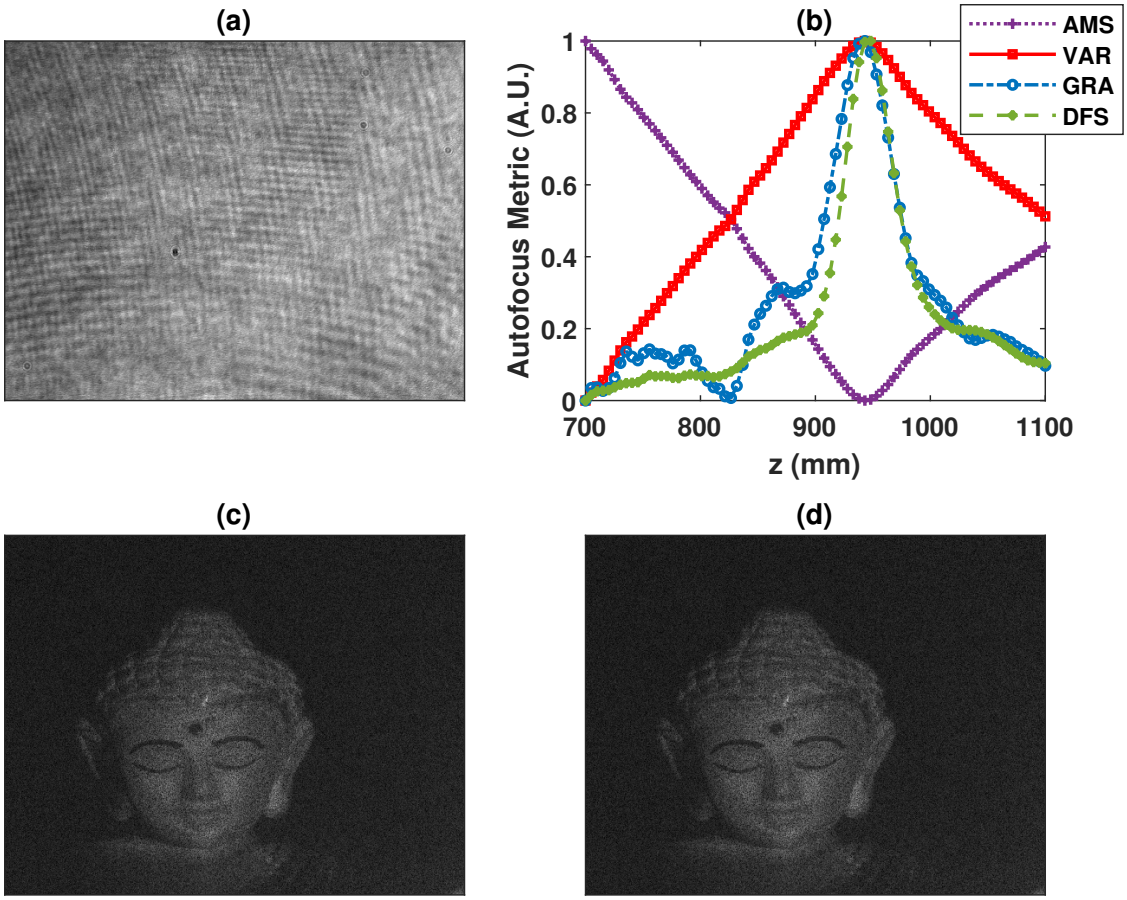

Figure 7.4: Experimental results: (a) digital hologram of a statue recorded in a digital holographic off-axis configuration (b) autofocus metric plots of convectional AMS, VAR, GRA and DFS algorithms. Reconstructed image obtained at the focal plane position (c) $z_f = 945\ mm$ estimated using conventional EIG algorithm and (d) $z_f = 938\ mm$ estimated using the PSO with EIG algorithm [208].

poration, Japan) of size 1600×1200 pixels and cell size of $4.4\ \mu m$. Figure 7.4(a) shows the recorded hologram corresponding to the statue. The Fresnel transform based hologram reconstructions were performed for the reconstruction distances between $700\ mm$ to $1100\ mm$. The object associated parts of size 700×700 were cropped from the reconstructed images and hologram AF algorithms were applied to these cropped images. The plots of AF metrics computed at 80 reconstruction planes are given in Fig. 7.4(b). The focal plane position estimates obtained using conventional EIG, TOW, AMS, DFS, VAR and GRA methods are $z_f = 945, 940, 945, 950, 945$ and $945\ mm$. The proposed PSO algorithm was applied using each AF algorithm with $N_z = 6$ within the search space. The corresponding focal plane position estimates are $z_f = 938\ mm$. As the object is three dimensional, the focal plane is estimated as a mean object position. It can be noted that the PSO algorithm could successfully estimate the focal plane location similar to the conventional AF algorithm. For the purpose of illustration, the reconstructed image

at the focal position estimated using the PSO and conventional methods with AMS algorithm are shown in Fig. 7.4(c) and Fig. 7.4(d), respectively, where, the statue is clearly visible in both reconstructed images. At the same time, the computation time associated with PSO algorithm is significantly less in comparison to the conventional method as reported in Table 7.1.

The proposed algorithm was implemented using the MATLAB R2019a on a computer with 9th-generation Intel-i5 processor with 2.4 GHz dual-core and 8 GB RAM. It is important to note that the accuracy achieved with the PSO algorithm in equivalent to the traditional AF methods. Thus, the main advantage of the PSO algorithm over the conventional AF methods is that the time complexity is significantly reduced.

7.3 Conclusion

The particle swarm optimization based autofocusing in digital holography is found to provide significant reduction in the computation time in comparison to the conventional approach. Furthermore, this improvement is achieved along with increased autofocusing accuracy. The simulation results indicate the quantitative improvement in the computational efficiency offered by the proposed method. The experimental result further substantiates its practical applicability.

8

Autofocusing based on an iterative algortihm

In this section, we propose another iterative technique to reduce the computation time in the total focal plane detection procedure in digital holography. Several autofocusing algorithms have been proposed which provide accurate detection of focal plane. Although the computation times required in the execution of these algorithms are low, the typical time required for generating reconstructed images at multiple planes as a part of focal plane detection procedure is significantly high. The proposed method computes a focal plane estimate using one of the conventional autofocusing algorithms in each iteration. In the subsequent iteration, the focal plane search range and resolution is varied based on the focal plane estimate obtained in the previous iteration. In this study, we have considered five autofocusing algorithms AMS [135], DFS [132], EIG [204], GRA [207] and VAR [134].

8.1 Methodology

In the proposed ierative autofocusing algorithm, for an input hologram of size $M \times N$ and range of reconstruction distances z, we will achieve the actual focus position of the object z_f as the output. First, for range of z, the starting position z_{start} and stopping position z_{end} are initialized. N_z is the number of equidistant planes in which the holograms are reconstructed at every iteration. In the n^{th} iteration, the hologram is reconstructed starting from a distance $z_1 = z_{start}$ up to a distance $z_1 = z_{end}$ at N_z

[8]This chapter presents the hologram autofocusing algorithm based on the iterative approach of metric computation and comparison.

number of equidistant planes using Eq. 1.10. The step increment in z_1 is given as,

$$z_{step} = z_{range}/N_z \tag{8.1}$$

where, $z_{range} = (z_{end} - z_{start})$. The autofocus metric τ_z is calculated at each z_1 location. Depending on whether the object is amplitude or phase type, the focal plane estimate z_f is evaluated as the location z_1 where τ_z is found to be $maximum$ or $minimum$, respectively. Subsequently, in the $(n+1)^{th}$ iteration, z_{range} is taken as the half of that in the n^{th} iteration. The values of z_{start} and z_{end} are updated as per z_f evaluated in the n^{th} iteration and z_{range} of the current $(n+1)^{th}$ iteration. The difference between z_f evaluated in two consecutive iterations is calculated. The iteration is terminated when this difference is less than a given threshold value. The final z_f is selected as the object focal plane. The proposed algorithm is described in Algorithm 7 below:

Algorithm 7 : ITR

Input: Hologram of size $M \times N$, z_{start}, z_{end}, threshold, N_z
Output: z_f: Location of focal plane.
step 1: Reconstruction of hologram $H(X,Y)$ starting at $z_1 = z_{start}$ up to a distance $z_1 = z_{end}$ in N_z equidistance planes with $z_{step} = z_{range}/N_z$, where $z_{range} = (z_{end} - z_{start})$.
step 2: Calculation of autofocus metric τ_z as a function of z_1.
step 3: Determine z_f based on either $\tau_z = \tau_{z_{max}}$ or $\tau_z = \tau_{z_{min}}$.
step 4: Update:
$z_{range}(n+1) = z_{range}(n)/2$
$z_{end}(n+1) = z_f(n) + (z_{range}(n+1)/2)$
$z_{start}(n+1) = z_f(n) - (z_{range}(n+1)/2)$
$n = n+1$
step 5: Repeat the **steps 1** to **steps 3** and check if $z_f(n+1) - z_f(n) < threshold$. If true, set $z_f(n+1)$ as the final focal plane, else repeat **steps 4** and **steps 5**.

8.2 Results and Discussion

A digital in-line holographic setup with a spherical beam illumination using a laser source of wavelength $\lambda = 450\ nm$ and camera pixel size of $5.5\ \mu m$ is considered for the simulation study. The hologram simulation and reconstruction were performed utilizing the algorithm described in [15]. A simulated USAF target amplitude object of size 583×800 pixels, as shown in Fig. 8.1(a), was placed such that $z_1 = 50.275\ mm$ and $z_2 = 49.725\ mm$. The simulated hologram with magnification $M_g = 1.99$ and object area $1.61 \times 2.21\ mm^2$ is shown in Fig. 8.1(b). In the first iteration, z_{start} and z_{end} were initialized as $40\ mm$ and $60\ mm$, keeping $Z = 100\ mm$ and $N_z = 10$. The algorithm terminated after 4^{th} iteration and the focal plane was detected as $z_f = 50.25\ mm$. The conventional techniques estimate the focal plane at $z_f = 50.5\ mm$ (shown in Fig. 8.1(c)). The reconstructed amplitude image at the detected focal

plane by iterative method is shown in Fig. 8.1(d).

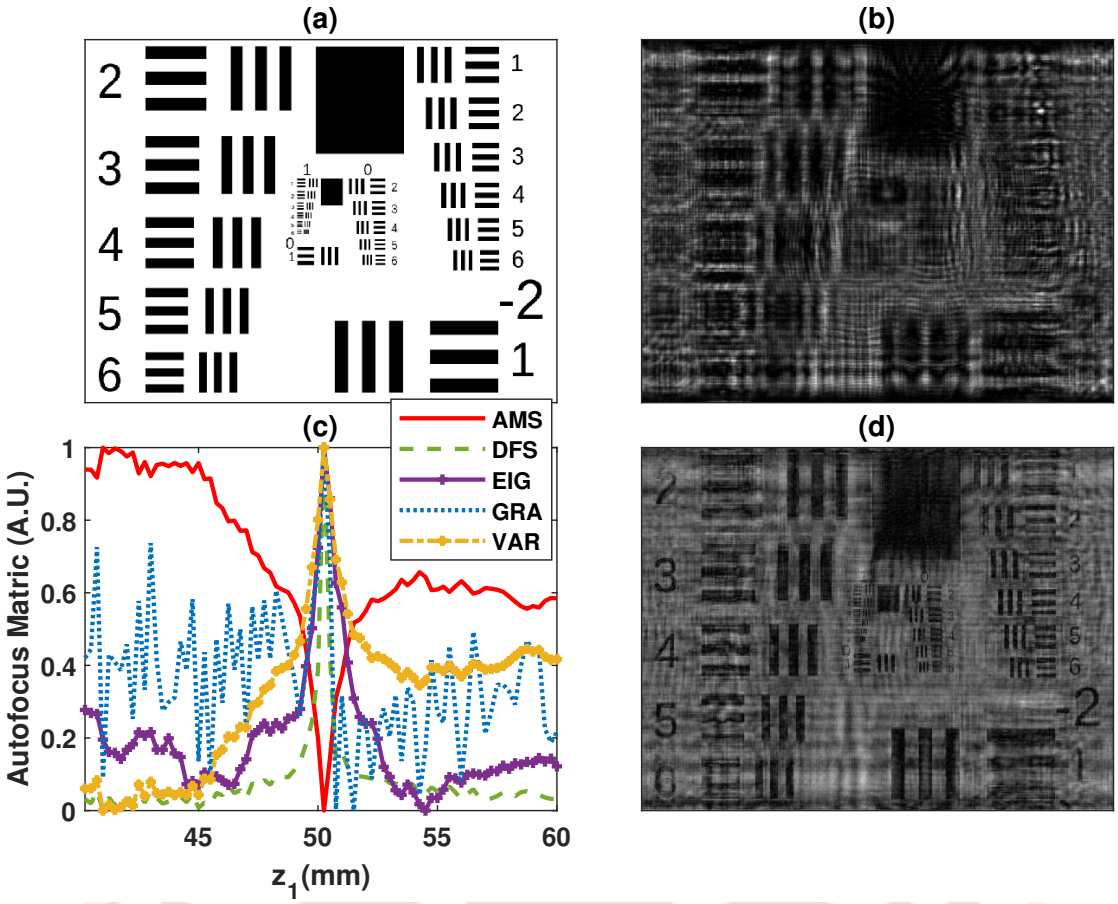

Figure 8.1: Simulation result: (a) USAF amplitude object, (b) hologram at a distance $z_1 = 50.275\ mm$, $z_2 = 49.725\ mm$, (c) autofocus metric plot for conventional method and (d) reconstructed image at the detected focal plane of $z_f = 50.25\ mm$ obtained using the iterative method.

.

To validate the applicability of the proposed method in the case of holographic configuration, a digital in-line holography setup was considered with spherical beam illumination. A hologram of size 2040×2040 pixels (as shown in Fig. 8.2(a)) was recorded considering polystyrene particle object of diameter $90\ \mu m$ at $z_1 = 150\ mm$, where $Z = 300\ mm$. The laser light source of wavelength $\lambda = 450\ nm$ and camera of pixel pitch $5.5\ \mu m$ is used. Autofocus metric plots of conventional methods are shown in Fig. 8.2(b), where focal plane is detected at $z_1 = 149.1\ mm$ using all the conventional techniques. The ITR detected the focal plane at $149.3\ mm$. The reconstructed image at the detected focal plane using ITR method is shown in Fig. 8.2(c), where the particles are clearly visible.

Another experimental study was done considering a digital off-axis holographic setup with a parallel light beam illumination. A Buddha statue was illuminated using a laser light source of wavelength $\lambda = 532\ nm$. The hologram shown in Fig. 8.3(a) was recorded using a camera of size 1200×1600

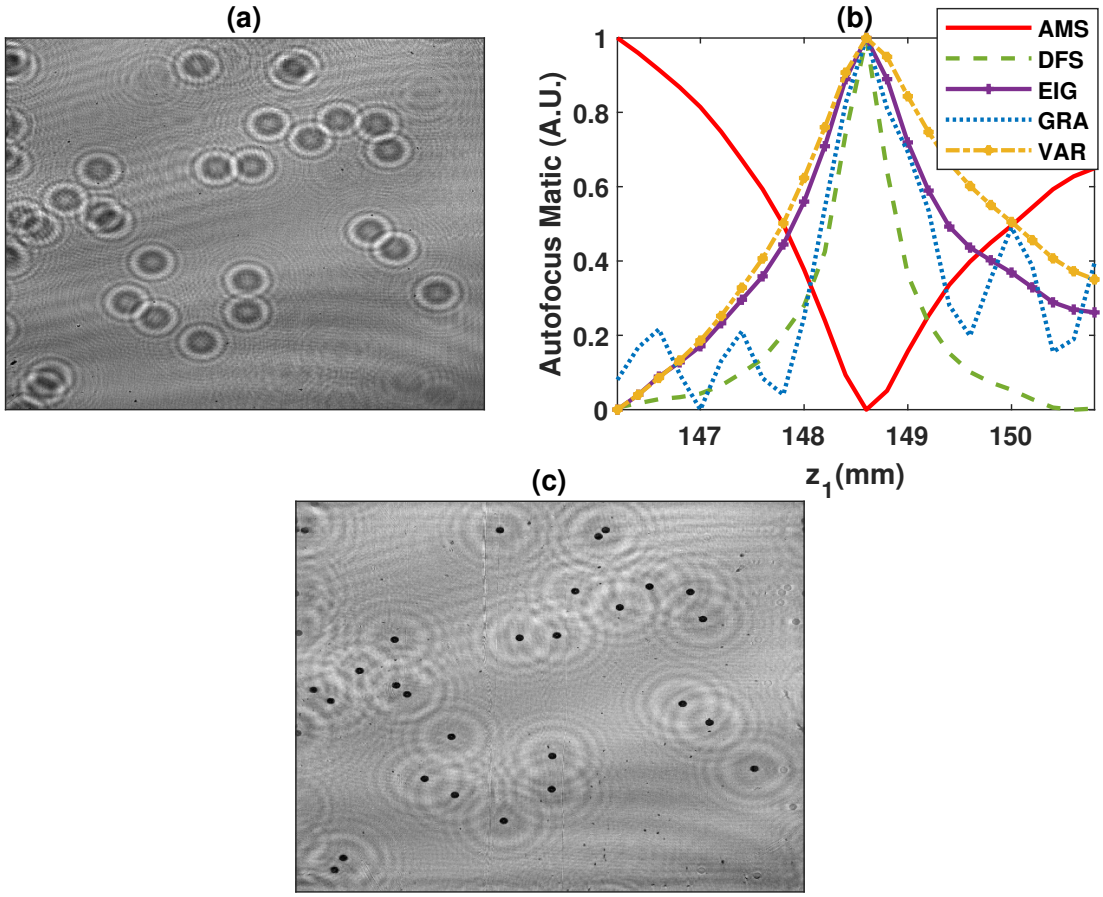

Figure 8.2: Experimental result: (b) Recorded hologram at a distance $z_1 = 150\ mm$, $z_2 = 150\ mm$, (c) autofocus metric plot for conventional method and (d) reconstructed image at the detected focal plane of $z_f = 149.3\ mm$ obtained using the ITR method.

pixels with the object placed at $z_2 = 937.5\ mm$. In case of off-axis holography the reconstructed image has three parts, i.e., real image, DC value and virtual image. The autofocusing algorithm is applied on the real image part, which is a cropped part of 700×700 pixels from reconstructed images at every reconstruction distances. The autofocus metric plot for conventional methods are shown in Fig. 8.3(b), where conventional methods find the focal plane at $z_f = 945, 950, 945, 945, 940, 945\ mm$ using AMS, DFS, EIG, GRA TOW and VAR metric respectively. The estimated focal plane location was found at $z_f = 940\ mm$ in iterative algorithm using all the above metrices. The reconstructed image at the detected focal plane using ITR method is shown in Fig. 8.3(c), wherein the Buddha face is clearly visible.

All the algorithms were implemented using the MATLAB 19a on a computer with 9^{th}-generation Intel-i5 processor with 2.4 GHz Hexacore and 8 GB RAM. It can be seen that the algorithm is able to efficiently detect the focal plane. The accuracy of the iterative algorithm in automatic focal plane detection is almost same as the traditional autofocusing methods. The main advantage of the iterative algorithm

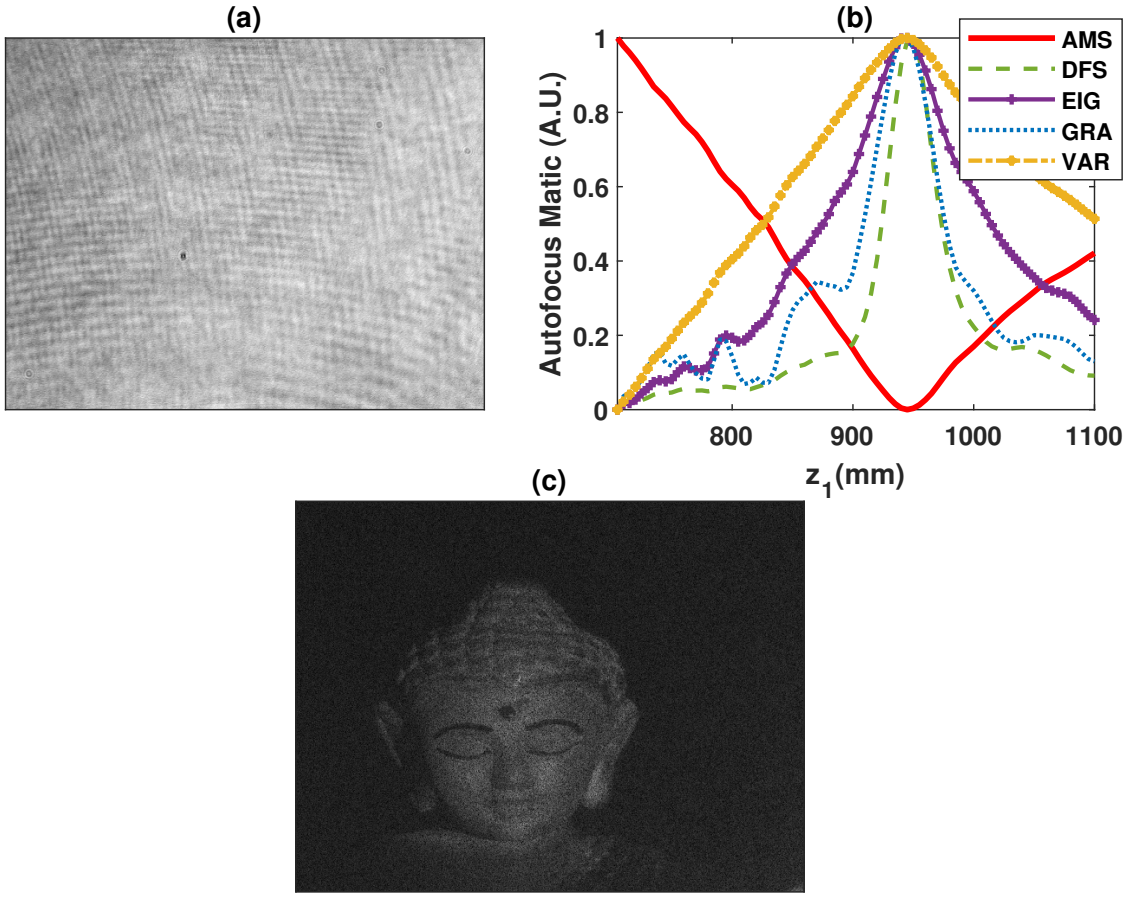

Figure 8.3: Experimental result: (a) Hologram of Buddha statue in off-axis holography set up at a distance $z_2 = 937.5\ mm$, (b) autofocus metric plot for conventional method and (c) reconstructed image at the detected focal plane of $z_f = 940\ mm$ obtained using the ITR method.

.

is that the time complexity is significantly reduced compared to the conventional autofocusing methods. The comparison of the computation time taken by different autofocusing algorithms in function of hologram size is tabulated in Table 8.1. The conventional autofocusing methods and PSO based autofocusing methods are mentioned as 'Conv' and 'PSO'. The proposed iterative methods are mentioned as 'ITR'. In the case of conventional autofocusing methods, the focal plane detection was performed with the hologram reconstructions computed with $N_z = 80$.

8.3 Conclusion

A strategy of reducing the computation time required for automatic focal plane detection is proposed in digital holography. The iterative approach of focal plane detection allows to refine the focal plane estimate in each iteration. The simulation and experimental results indicate that the proposed iterative

Table 8.1: Comparison of computation time (in seconds) in function of hologram size

AF method	Hologram size (in pixels)																	
	In-line holography															off-axis holography		
	200 × 200			400 × 400			583 × 800			1000 × 1000			2040 × 2040			1200 × 1600		
	Conv	PSO	**ITR**	Conv	PSO	**ITR**	Conv	PSO	**ITR**	Conv	PSO	**ITR**	Conv	PSO	**ITR**	Conv	PSO	**ITR**
AMS	0.73	0.17	**0.19**	3.08	0.83	**0.73**	4.08	1.24	**1.15**	20.21	3.78	**4.81**	104.0	37.19	**30.1**	8.86	3.64	**2.29**
DFS	1.09	0.31	**0.22**	3.47	1.06	**0.86**	5.40	1.35	**1.31**	22.93	8.01	**5.44**	120.9	37.79	**32.9**	10.14	4.27	**2.65**
EIG	0.95	0.27	**0.21**	3.39	1.04	**0.81**	5.40	1.34	**1.29**	23.40	8.17	**5.47**	127.7	39.88	**34.4**	10.93	4.60	**2.81**
GRA	1.08	0.34	**0.22**	3.39	1.11	**0.83**	5.33	1.51	**1.28**	22.68	8.41	**5.30**	115.2	46.84	**32.5**	9.93	4.24	**2.56**
TOW	1.08	0.31	**0.24**	3.33	1.02	**0.80**	5.40	1.35	**1.29**	22.77	7.95	**5.32**	131.6	41.1	**35.4**	12.46	5.25	**3.20**
VAR	0.75	0.24	**0.20**	3.14	0.85	**0.76**	4.92	1.65	**1.17**	20.59	9.10	**4.80**	105.6	25.9	**30.7**	8.98	3.73	**2.34**

strategy is about 75% more computationally efficient compared to the conventional autofocusing methods. This efficiency in achieved without compromising the focal plane detection accuracy.

Part IV

Particle Imaging Applications

भारतीय प्रौद्योगिकी संस्थान गुवाहाटी
Indian Institute of Technology Guwahati

9

Particle detection and size estimation

DIH has found numerous applications especially in particle detection and size estimation. For example, three-dimensional particle size distribution has been obtained in a DIH setup using machine learning [210]. Dual-beam interferometry is utilized for the determination of two-dimensional position detection of opaque particle. In [176], particle density on dust cloud dynamics in a minimum ignition energy apparatus has been investigated using the DIH. Single-pixel holographic rod-shaped particle size has been detected using Wigner-Ville distribution [211]. In DIH, different approaches have been reported for determining particle object properties, such as particle size, shape and location, either directly from the hologram [61, 212, 213] or from the hologram reconstructed images [214, 215, 216]. In the later approaches, the hologram is reconstructed at a set of reconstruction distances. Subsequently, particle detection algorithms are applied to the reconstructed images ($A_z(x, y)$) to determine the object properties. Some of these algorithms are based on a minimum intensity metric [217, 218, 219] and maximum edge sharpness metric [220, 221]. A hybrid method [222, 178, 223] developed by combining these methods is shown to provide improvement in estimating the object properties. The ultimate detectable particle size limit has been studied]and a hologram interpolation scheme has been suggested to lower this limit [66].

Since the DIH is able to reconstruct the object wavefield at any desired plane within the measurement volume, it offers an important advantage of accurate determination of both the particle size and depth. Various automatic algorithms have been proposed for determining accurate particle depths and

[9]This chapter presents the application of hologram processing algorithms for the improvement of particle detection and size estimation.

sizes from the hologram reconstructed images. Most of these algorithms involve numerical reconstruction of the hologram at different planes and subsequent application of one of the image quality metrics to identify positions of in-focus particles. Since the camera field-of-view and resolution is fixed in a given DIH setup, the particle detection and size estimation accuracy is limited. The accuracy of particle detection and size estimation can be improved with improvement of hologram or reconstructed image resolution. Some hologram resolution enhancement methods have been reported recently. For example, improvement of the spatial dynamic range of digital holography with super-sampling using Lanczos interpolation is shown to provide better particle detection performance [66]. Bicubic interpolation of the hologram is used to enhance the low-frequency terms of the object in conjunction with the iterative extrapolation approach for high resolution hologram imaging [67].

9.1 Improvement of particle detection and size estimation accuracy using autoregressive interpolation of hologram

In this section, we discuss interpolation of digital hologram using autoregressive (AR) algorithm (as described in 4.1) to improve the particle detection accuracy in the DIH setup. The major factors affecting the accuracy of particle detection and size determination in the DIH are camera sensor pixel size, number of pixels, magnification, etc. The aim of this proposed algorithm is to improve the resolution of the hologram reconstructed images which essentially increases the accuracy of particle detection and size determination. The Hough transform based edge detection technique can be used to locate the spherical particles in the images obtained from the interpolated hologram reconstruction. In general, the particles occupy minimum area in the reconstructed images at focus. As a result, circular object areas of equivalent diameters are detected in the case of spherical objects. We propose to utilize the maximum intensity metric to determine the location of particles. For obtaining the size of the particle, the circular Hough transform based edge detection algorithm is utilized. The proposed method mainly focuses on the improvement of particle detection and size estimation accuracy with an autoregressive interpolation of a hologram. However, the particle analysis accuracy certainly depends on the choice of different particle detection methods as well. A number particle analysis methods and their comparative studies have been reported in [222, 178, 223, 61, 212, 213, 214, 215, 216, 217, 218, 219, 220, 221, 224, 225]. In the present work, we have used maximum intensity projection with Hough transform based edge detection technique for particle analysis [217, 218, 219]. It is done so as to provide an explicit performance comparison among different hologram interpolation algorithms only. This algorithm provides the two-dimensional position and diameter of the particles from the maximum intensity map. The diameter is computed in

terms of number of pixels. Accordingly, the diameter estimate is obtained as $d = d_p\Delta$, where d_p and Δ represent number of pixels and the pixel width, respectively. The proposed algorithm is implemented using MATLAB R2019a. It is important to emphasize that although the proposed method is investigated for spherical particles in the present study, it can work equally well in the case of non-spherical particles.

A simulation study is shown in Fig. 4.2 with a simulated single particle object of diameter $d = 27.5\ \mu m$ placed at $z_1 = 80\ mm$. The AR interpolation is applied once and twice on the LR hologram. Both the original LR and $2\times$, $4\times$ interpolated HR holograms are reconstructed and circular Hough transform based edge detection algorithm is applied on the reconstructed images. The diameter estimates of the particles in the reconstructed images from the original, $2\times$ and $4\times$ interpolated holograms are found to be $31.6\ \mu m$, $28.1\ \mu m$ and $27.6\ \mu m$, respectively. It is quite clear that the hologram interpolation algorithm provides improvement in the particle size estimation accuracy.

Similar simulation study is shown in Fig. 4.3 with two closely spaced particles, each of diameter $d = 24.5\ \mu m$ with a spacing of $5.5\ \mu m$ corresponding to a single pixel. No particles were detected in the object image obtained with the original LR hologram reconstruction due to close spacing between two particles. On the other hand, both the particles were detected with diameters $23.7\ \mu m,\ 24.2\ \mu m$ and $24.4\ \mu m,\ 24.4\ \mu m$ in the images obtained from the reconstruction of $2\times$ and $4\times$ interpolated holograms, respectively. This results indicate that the hologram interpolation algorithm provides accurate particle detection even in the case of closely spaced particles.

For the example of multiple particle of same size, shown in Fig. 4.4, the performance of the proposed AR hologram interpolation algorithm is compared with the other interpolation techniques, such as, bicubic (BC), bilinear (BL), nearest neighbour (NN) and Lanczos (LZ). These interpolations are performed using built-in imresize function available in MATLAB. A number of holograms were simulated each with a distinct number of particles and particle diameter. These holograms were interpolated using above mentioned techniques. The hologram reconstructions were performed with each original non-interpolated (NI) hologram and interpolated hologram. The quantitative performance comparison among the interpolation techniques is provided in Table 9.1 in terms of the percentage of number of detected particles (n), and mean diameter (d_m) and standard deviation (σ) of estimated particle diameter. These results clearly indicates that the AR hologram interpolation provides better accuracy in particle detection and size estimation in comparison with the other interpolation techniques.

Similarly, for the example of multiple particle of same size, shown in Fig. 4.5, the percentage number of detected particles and their size distribution are given in Table 9.2.

Table 9.1: Performance comparison among hologram interpolation techniques in terms of percentage of number of detected particles and estimated size distribution parameters in the case of object plane containing multiple particles of same diameter

Diameter (μm)	Method	Number of particles														
		200			100			50			25			10		
		n (%)	d_m (μm)	σ (μm)	n (%)	d_m (μm)	σ (μm)	n (%)	d_m (μm)	σ (μm)	n (%)	d_m (μm)	σ (μm)	n (%)	d_m (μm)	σ (μm)
40	NI	51.31	47.7	11.48	60.58	45.96	8.95	72.96	47.57	5.69	70.88	46.35	3.25	75.8	47.81	4.25
	AR	**95.35**	**42.17**	**2.19**	**99.6**	**42.13**	**1.91**	**99.92**	**41.97**	**1.58**	**99.76**	**42.87**	**1.26**	**99.6**	**42.74**	**1.13**
	BC	94.02	44.2	2.56	97.8	44.18	2.05	99.12	44.27	1.71	99.28	44.4	1.56	99.6	43.63	1.29
	BL	95.25	43.87	2.38	98	43.85	1.93	99.2	43.76	1.7	99.44	43.58	1.47	99.6	43.37	1.27
	NN	93.17	44.2	2.77	97.1	44.19	2.28	98.88	44.07	1.84	99.36	44.41	1.66	99.6	44.31	1.5
	LZ	94	44.21	2.65	97.3	44.11	1.98	99.16	44.24	1.8	99.36	43.35	1.4	99.6	43.66	1.24
20	NI	46.66	28.34	13.19	31.4	27.21	7.04	58	27.4	5.82	49.36	25.54	3.42	39	27.1	3.95
	AR	**93.43**	**21.52**	**1.81**	**95.9**	**21.04**	**1.09**	**97.76**	**21.33**	**1.03**	**98.4**	**20.32**	**0.73**	**98.6**	**20.59**	**0.69**
	BC	90.21	22.34	2.26	82.62	22.1	1.63	93.12	22.11	1.62	94.88	22.21	1.07	96	22.34	0.88
	BL	89.26	25.44	2.54	82.76	25.32	1.93	94.28	25.39	2.29	94.64	20.54	0.85	94.8	25.31	0.75
	NN	86.32	22.21	2.18	67.6	21.86	1.61	88.28	21.74	1.56	87.28	21.69	1.04	82.6	21.55	0.81
	LZ	78.86	25.19	2.53	73.62	24.9	2.11	84.88	24.86	1.22	82.56	20.92	0.85	79.8	24.95	0.57
10	NI	X	X	X	X	X	X	X	X	X	X	X	X	X	X	X
	AR	**94.52**	**10.2**	**2.33**	**94.22**	**10.17**	**1.7**	**94.32**	**10.23**	**1.69**	**89.84**	**10.02**	**1.05**	**96.2**	**10.08**	**1.11**
	BC	79.75	10.75	2.66	73.46	10.64	2.26	68.72	10.77	1.88	72.32	10.95	1.82	81	10.61	1.23
	BL	85.72	10.99	2.89	79.12	10.96	2.55	70.52	10.96	2.33	71.28	10.94	2.08	76.6	10.54	1.56
	NN	71.04	10.56	2.63	60.3	10.41	2.07	52.64	10.37	1.79	36.72	10.27	1.59	64.2	9.92	1.34
	LZ	78.95	10.73	2.66	73.02	10.62	2.19	67.64	10.7	1.89	52.32	10.75	1.64	64.6	10.66	1.44

Table 9.2: Performance comparison among hologram interpolation techniques in terms of percentage of number of detected particles and estimated size distribution parameters in the case of object plane containing multiple particles of different diameters

Diameter (μm)	n (%)						d_m (μm)						σ (μm)					
	NI	AR	BC	BL	NN	LZ	NI	AR	BC	BL	NN	LZ	NI	AR	BC	BL	NN	LZ
80	63.5	**85.3**	75.3	82.0	73.9	75.4	86.32	**82.16**	83.61	83.87	83.71	83.56	5.91	**2.62**	2.97	2.86	2.57	3.06
40	80.87	**98.53**	97.47	98.07	96.73	98.03	45.23	**42.29**	43.31	42.98	43.23	43.36	3.36	**1.80**	2.17	2.18	2.11	2.08
20	39.04	**96.48**	94.66	93.08	87.96	86.52	25.06	**21.12**	21.23	22.08	21.32	21.36	5.80	**1.84**	2.09	2.35	2.03	2.09

In the experimental result shown in Fig. 4.6 with a glass cuvette of width 10 mm containing polystyrene spherical particles of diameter 40 μm suspended in distilled water and spherical laser illumination of DIH setup. The circular Hough transform based particle detection algorithm was applied to these maximum intensity maps. The particle size distributions were obtained as $n = 48$, $d_m = 46.1\ \mu m$, $\sigma = 9.5\ \mu m$ and $n = 86$, $d_m = 40.01\ \mu m$, $\sigma = 2.32\ \mu m$ for the original and AR interpolated hologram, respectively. Here, n represents number of particles. The coefficient of variance of the polystyrene particles is up to 5% as per the manufacturing company "Micro-beads". In case of proposed method the same is calculated as $\approx 5.8\%$ which is close to the actual value. The comparison of performance is tabulated in Table 9.3. From these results, it can be deduced that the AR hologram interpolation offers significant improvement in the particle detection and size estimation accuracy over conventional method. The performance of AR interpolation method is comparable with the existing interpolation methods.

Table 9.3: Performance comparison among hologram interpolation techniques in the case of experimental study with polystyrene micro-particles of diameter $40\mu m$ taking hologram size 1280×1024 pixels

Interpolation methods	NI	AR	BC	BL	NN	LZ
Number of particles	48	**86**	80	73	58	78
$d_m(\mu m)$	46.1	**40.01**	39.25	40.34	40.64	40.64
$\sigma(\mu m)$	9.5	**2.32**	1.88	4.68	2.22	2.41

The autoregressive hologram interpolation algorithm discussed here, is found to provide significant improvement in the particle detection and size estimation accuracy based on the quantitative comparison with other hologram interpolation techniques. Since the algorithm is independent of particle type, it can be used for improving the non-spherical particle detection and size estimation accuracy as well. The simulation and experimental results substantiates the practical applicability of the proposed method.

9.2 Improvement of particle detection and size estimation accuracy using iterative estimation

Since the major factors affecting the accuracy of particle detection and size determination in the DIH are camera sensor pixel size, number of pixels, magnification, etc., the particle detection and size estimation accuracy is limited due to camera specifications. The particle size estimation accuracy can be increased by improving reconstructed image quality. In the section 3.1, we have described the in-line hologram reconstruction algorithm using iterative estimation. This method improves the reconstructed image quality of digital in-line hologram (shown in section 3.1.2), which results in increase in particle size estimation accuracy. The reconstructed images after 50 iteration is considered for the study of particle detection accuracy. The circular Hough transform based edge detection algorithm is applied on this estimated reconstructed images as well as conventional reconstructed images. The diameter of detected particles are estimated as described in the previous section.

In the simulation example shown in Fig. 3.3 with simulated amplitude type particle objects, the Hough transform based particle analysis algorithm is applied on the reconstructed images of conventional reconstruction and iterative reconstruction. The comparative study of particle size estimation is tabulated in Table 9.4. It can be clearly seen that the particle size estimation accuracy improves significantly using proposed iterative algorithm for hologram reconstruction.

Table 9.4: Performance comparison between proposed iterative algorithm and conventional DIH in terms of estimated size distribution parameters in the case of object plane containing multiple particles of same diameter.

Diameter (μm)	**Method**	**Number of particles**									
		200		**100**		**50**		**25**		**10**	
		d_m (μm)	σ (μm)	d_m (μm)	σ (μm)	d_m (μm)	σ (μm)	d_m (μm)	σ (μm)	d_m (μm)	σ
100	Conv.	88.31	12.05	95.20	7.04	96.24	5.93	96.08	5.94	97.47	3.36
	Proposed	**94.25**	**9.73**	**97.67**	**3.97**	**98.50**	**2.82**	**98.43**	**3.49**	**97.88**	**2.05**
80	Conv.	74.39	8.48	77.09	4.26	77.83	4.66	78.53	3.24	78.35	3.93
	Proposed	**78.14**	**4.15**	**78.72**	**3.58**	**78.99**	**3.09**	**80.07**	**1.65**	**80.38**	**1.88**
50	Conv.	48.44	7.56	53.20	7.65	52.77	5.84	51.61	4.02	49.22	2.53
	Proposed	**49.98**	**3.89**	**49.73**	**2.62**	**49.47**	**2.45**	**49.90**	**1.74**	**50.07**	**1.52**
40	Conv.	42.29	7.18	45.86	8.11	42.04	4.86	38.69	2.81	39.09	3.17
	Proposed	**40.74**	**3.95**	**39.62**	**3.42**	**40.04**	**2.74**	**40.18**	**1.82**	**39.94**	**1.46**
20	Conv.	25.12	6.33	24.64	6.05	22.84	4.11	22.31	3.15	22.54	3.03
	Proposed	**21.39**	**3.97**	**20.86**	**3.12**	**20.31**	**2.08**	**20.04**	**1.87**	**20.83**	**1.56**

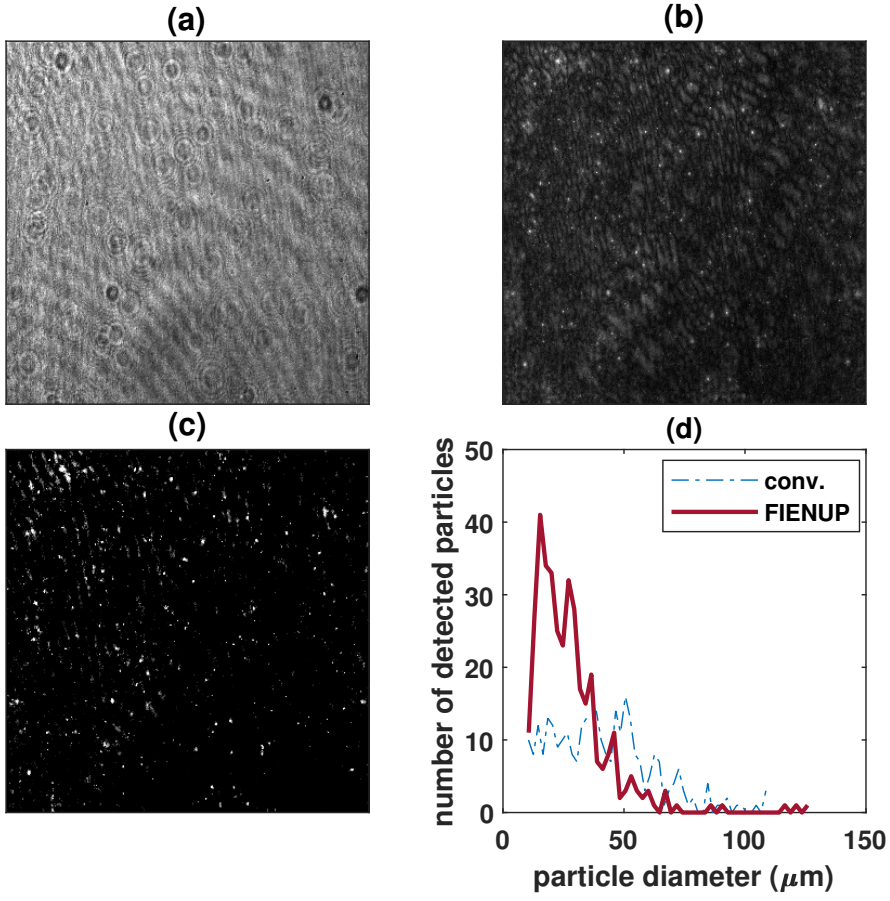

Figure 9.1: Experimental result: (a) Recorded hologram of size 1024×1280 pixels with Farakka fly ash particles. (b) maximum intensity map of the reconstructed amplitude images with conventional in-line holography, (c) maximum intensity map of the reconstructed amplitude images with Fienup's iterative method, (d) particle size distribution with both methods [182].

For experimental validation, the example shown in Fig. 3.4 is considered, where a glass cuvette of width $1\ cm$ containing polystyrene spherical particles of diameter $40\ \mu m$ suspended in distilled water is illuminated with spherical laser to record digital in-line hologram. The circular Hough transform based edge detection algorithm is applied on maximum intensity map of both the conventional and iteratively reconstructed images. The polystyrene particle's average diameter is estimated in the conventional reconstructed image as $d_{avg} = 46.1\ \mu m$, where same is estimated as $d_{avg} = 40.6\ \mu m$ in the reconstructed images obtained using the iterative algorithm.

Another experimental study was performed with Farakka fly ash particles as object for holographic imaging. Experimentally recorded in-line hologram, maximum intensity map of reconstructed images using conventional and proposed methods are shown in Fig. 9.1(a), Fig. 9.1(b) and Fig. 9.1(c), respectively. The particle distribution obtained using circular Hough transform method for both the methods are compared in Fig. 9.1(d). The distribution achieved from the proposed iterative estimation based method is significantly better than the same obtained from conventional DIH.

This iterative estimation based reconstruction technique in digital in-line holography is able to provide accurate particle detection and size estimation. The improved detection accuracy is achieved due to the removal of twin image effect and the background noise by the iterative estimation. The simulation and experimental results substantiate the practical applicability of the proposed method.

भारतीय प्रौद्योगिकी संस्थान गुवाहाटी
Indian Institute of Technology Guwahati

10

Measurement of particle size distribution

10.1 Measurement of fly ash particle size distribution using lensless digital in-line holography

Out of India's total installed capacity of 160000 MW electric power, 65% comes from thermal power plant. These thermal power plats produce around 200 million ton fly ash per year in India. An estimated about 70,000 acres of land is occupied by fly ash ponds. The consensus is that by 2025, coal-burning power stations will provide more than half of the India's energy needs. The nation uses only about 38% of its total produced fly ash for cement manufacturing. Under these circumstances and with the continued reliance on coal, India will have huge supplies of ash in the years to come, an estimated 300-400 million ton. Occasional failure of these ash ponds affects vast tracts of agricultural land nearby. Improper use of fly ash pollutes river water even up to 100 kilometers endangering aquatic and human life. For proper utilization of fly ash, physical, chemical and engineering characterization of fly ash is essential. Material properties varies for different plants, same plant over period of time due to different coal supply [226, 227] and methods of operation of plant and fluctuation in power generation [228]. Due to that, the characterization of fly ash from different sources is necessary [229, 230].

In the last decade, numerous methods are applied to investigate the particle size distribution (PSD) of fly ash. The conventional method adopted is sieve analysis coupled with hydrometer analysis (ASTM D422-63)[231]. Hydrometer analysis is based on sedimentation principle and requires 24 hours to com-

[10]This chapter presents the practical applications of digital holographic microscopy in the measurement of particle size distribution.

plete the test. Some other state-of-the-art method for particle size analysis include electrical low pressure impactor [232, 233, 234], scanning mobility particle spectrometer [235], and laser particle size analyzer [236]. These techniques suffer from high costs, complex operations, high test duration and/ or special sample preparation requirements [38]. Many a times, the factors contributing to errors in PSD are hidden and not anticipated in advance. For example: the choice of dispersion media and its refractive index is an important consideration for laser particle size analysis. The charged particles and its reactivity would influence the accuracy of particle size determination. It is explicit that any technology that requires less residence time of particle in the dispersive media or the one with no dispersive media will be advantageous. Any initiative to improve these limitations is important for improving the accuracy of particle size characterization of materials.

Digital in-line holography is an interferometric technique for three-dimensional imaging of the object under investigation [1]. It has been extensively used in many applications such as quantitative particle characterization [38], particle tracking [237], microfluidics [238, 239], bioimaging [51, 17, 240, 180, 241], etc. due to its simple and low-cost optical configuration [242, 243, 244, 245]. The intensity pattern generated by the interference between a reference light wave and an object wave scattered from or transmitted through the object is recorded as the hologram consisting of both the amplitude and phase information of the object wavefield. In a digital holography setup, the hologram recording is performed using a digital sensor such as a CCD/CMOS camera. Consequently, the reconstruction of the object wavefield is performed *numerically* by back-propagating the complex optical wavefield evaluated at hologram plane to the object plane separated by the reconstruction distance [246]. Various methods have been reported for imaging and estimation of particle shape [247], size, temperature [248] and velocity [249] using digital in-line holography. Berg et al. was able to image aerosol particles in situ ranging from $15 - 500$ μm using digital in-line holography [161]. An improved algorithm was presented to determine that, the particle to be measured can be either spherical or fibroid [215]. Three-dimension positions and PSD of glass beads with size of 20–100 μm were located in the upper dilute zone of a cold CFB riser [250]. The impact of particle concentration and turbidity was also investigated with standard particles of 39.82 μm suspended in the samples [251]. Recently, fly ash PSD in a range of $0 - 4$ μm was also determined using digital holographic microscopy in a microfluidic setup [38].

In this section, a lenless digital in-line holography system is proposed to determine the PSD of different fly ash samples in a range of 10-90 μm. The hologram interpolation is incorporated to enhance the reconstructed image quality. Circular Hough transform based edge detection and extrapolation algorithms are used to detect and measure the fly ash PSD. The detailed methods and materials used are

described below in section **Materials and methods**. The simulated and experimental results are shown in section **Results** followed by the **Conclusion**. The proposed method is able to determine the fly ash PSD better than the laser particle size analyser and similar to the conventional hydrometer method with a reduced experimental and time complexity.

10.1.1 Materials and methods

10.1.1.1 Particle size determination by conventional method

Table 10.1 summarizes the physical properties of four fly ashes (Badarpur fly ash-BFA, Farakka fly ash-FFA, Neyveli fly ash-NFA, Pond ash-PA sourced from the thermal power plants in India) used in this study. The particle grain-size distribution was determined by following the method stated in ASTM D 422-63 (ASTM, 2007)[231]. The specific gravity of the parent material were determined as per ASTM D854-92 [252]. The total specific surface area (SSA) was determined using ethylene glycol monoethyl ether method [253]. The cation exchange capacity (CEC) was measured using ammonium replacement method [254, 255]. Except NFA, all FAs showed very low CEC and SSA. X-Ray Diffraction (XRD) was conducted using (Rigaku, Model, Micromax-007HF) on all parent materials to understand their mineralogy. The step size, 2θ range and scan speed was kept at 0.02°, (3 - 70°) and (20°2θ/min), respectively and obtained XRD response was analyzed using Match software. The pH values of the FAs were tested by using a systronics (India) pH meter.

The particle size determination of fly ash by the standard test method (ASTM D422-63) involves both sieve analysis and sedimentation analysis by hydrometer method. For particles coarser than 75 μm (No. 200 sieve), the particle size is determined by sieving. For this purpose, a set of sieves was stacked in decreasing order of size one over the other. A predetermined quantity of fly ash is added to the upper most sieve and it is subjected to shaking in a sieve shaker. After sieving, the weight of particles retained on each sieve was used to obtain the PSD according to ASTM D422-63 [231]. The portion of fly ash finer than 75 μm was subjected to sedimentation analysis by hydrometer method for determining the PSD.

For conducting hydrometer analysis, air dried fly ash sample of approximately $50-100$ g was placed in a 250 ml beaker. About 125 ml of sodium hexametaphosphate solution was added as a dispersing agent. The solution was stirred and allowed to soak for at least 16 h. At the end of soaking period, water was added to the solution and stirred again. The fly ash slurry was then transferred to the graduated cylinder and sufficient water was added so that the total volume is 1000 ml. The sedimentation cylinder was shaken back and forth by placing the palm at the open end. Care was taken that the solution does

Table 10.1: Physical properties of fly ashes used in this study

Properties	Material			
	BFA	FFA	NFA	PA
Specific gravity	2.20	2.16	2.64	2.20
PSD (%):				
Coarse sand (4.75-2 mm)	0	0	0	0
Medium sand (2-0.425 mm)	0	0	3	0
Fine sand (0.425-0.075 mm)	8	24	55	36
Silt (0.075-0.002 mm)	88	74	42	61
Clay (¡ 0.002 mm)	4	2	0	3
Classification	F	F	C	F
Total specific surface area (EGME method) (m^2/g)	11.54	12.59	13.24	10.45
CEC ($m_{eq}/100\ g$)	1.44	1.89	9.04	0.99
pH (Liquid/Solid = 20)	8.45	10.5	12.45	8.52
Minerals present	Mullite Quartz Hematite Agragonite Anhydrite	Mullite Quartz Hematite Agragonite Anhydrite	Mullite Quartz Hematite Agragonite Anhydrite Calcium oxide	Mullite Quartz Hematite Agragonite Anhydrite

not spill out. After careful agitation of the fly ash slurry, it was placed on a level surface for hydrometer readings at regular intervals of time ($2, 5, 15, 30, 60, 250$ and 1440 minutes). The hydrometer readings were used to determine PSD (ASTM D422-63) [231].

Laser diffraction particle size analysis of fly ash was performed using Malvern Mastersizer 2000 [256] with its particle size range varying from $0.02\ \mu m - 2000\ \mu m$. Approximately $1\ g$ of fly ash was added slowly using a spatula into a $1000\ ml$ beaker containing $750\ ml$ of distilled water. A stirrer rotating at 3000 RPM ensures proper agitation of the solution during the addition of fly ash. The fly ash particles were made to pass through a focused laser beam. The particles scatter light at an angle that is inversely proportional to its size. The photosensitive detectors capture the angular intensity of scattered light. The scattering intensity versus angle was used to develop PSD. Multiple measurements were made and the results were averaged to ensure repeatability of results. The FESEM images of the fly ash samples are shown in Fig. 10.1. The dry fly ash samples are shown in Fig. 10.2(a-d).

10.1.1.2 Particle size determination by digital in-line holography

10.1.1.2.1 Sample Preparation Fly ash samples are prepared by adding some dispersing agent for holographic experiment. About $33\ g$ Sodium hexametaphosphate ($(NaPO_3)_6$) and $7\ g$ Sodium Carbonate (Na_2CO_3) are added as a dispersing agent to prepare $1000\ ml$ solution. $50\ g$ of fly ash sample

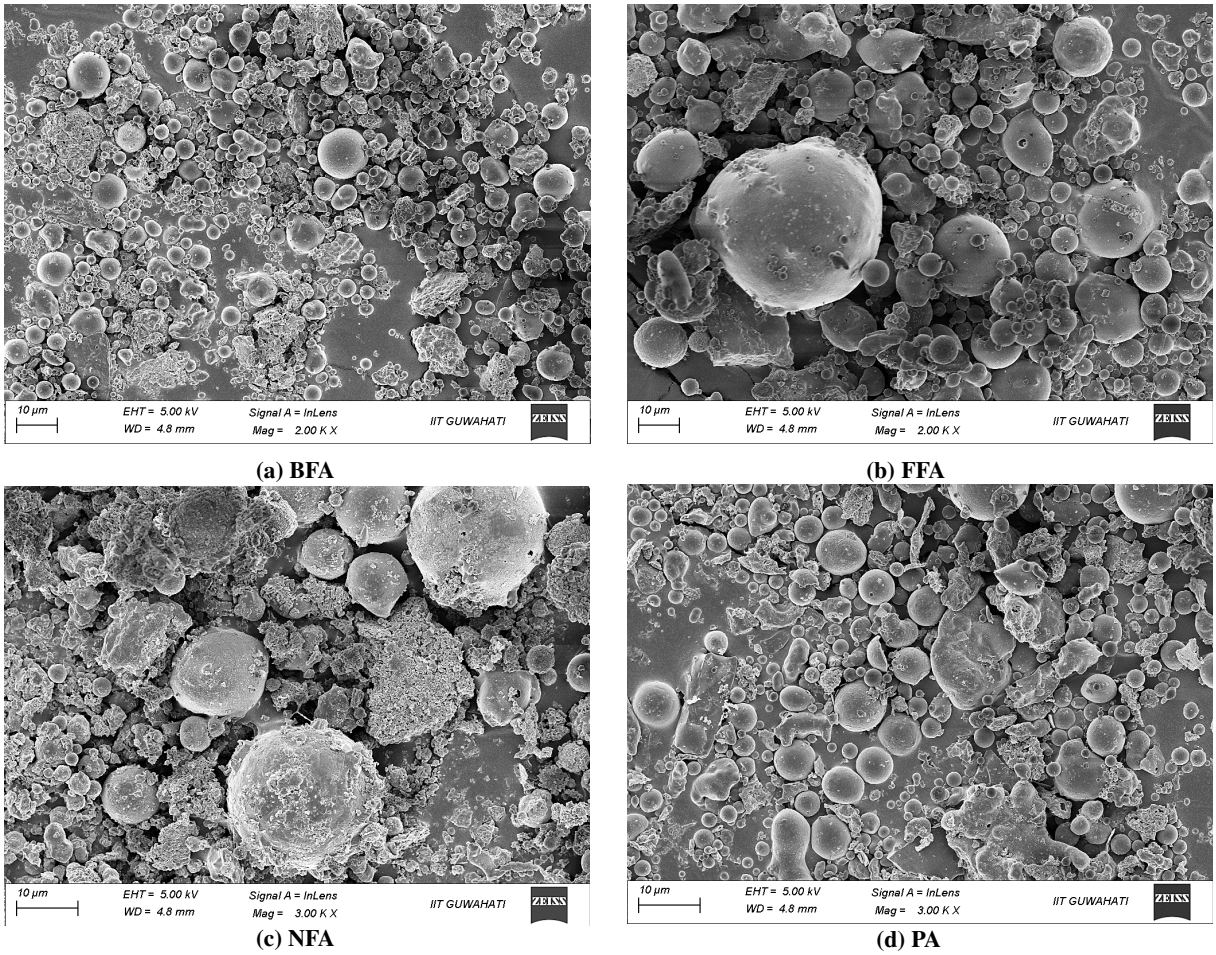

Figure 10.1: The FESEM images of the fly ash samples.

is added to 100 ml of this solution. The fly ash solution is stirred to allow fly ash particles disperse properly. Finally 1 ml of this solution is diluted by adding 40 ml distilled water. The prepared sample is spread on a microscopic glass slide and dried properly to record the holograms. The sample preparation process is shown in Fig. 10.3. The prepared samples used for holographic experiments are shown in Fig. 10.2(e-h).

10.1.1.2.2 Hologram Recording Figure 10.4 shows a schematic of lensless digital in-line holographic imaging setup utilized for obtaining PSD. A He-Ne laser of wavelength $\lambda = 632.8\ nm$ (LASOS, LGK 7628, 5 mW) was used as a light source. A set of particles under investigation was spread and fixed over a microscopic glass slide. The laser beam is filtered using a pinhole (Holmarc, HPRA-3-25) of size 25 μm to achieve spherical and spatially-coherent beam illumination of the glass slide. The parts of the illumination beam that are scattered and not scattered by the object are considered as object beam and reference beam, respectively, both of which propagate in the same direction. An

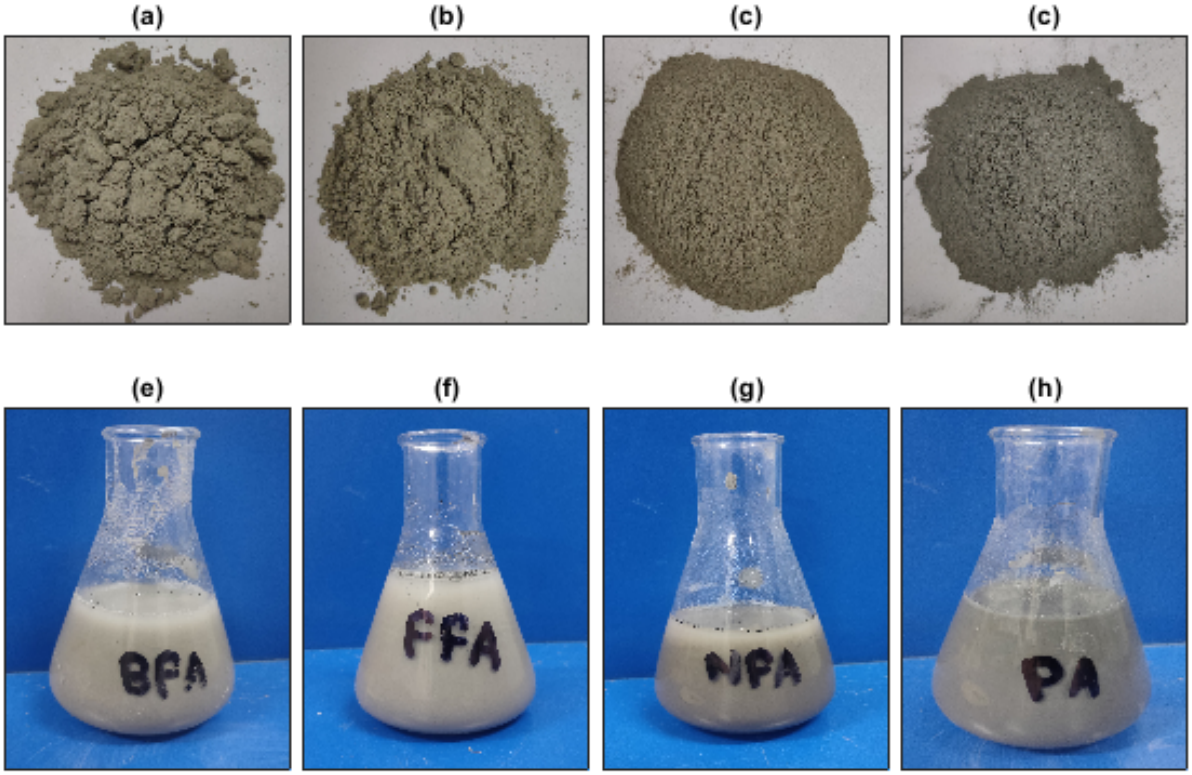

Figure 10.2: Dry fly ash samples: (a) BFA, (b) FFA, (c) NFA, (d) PA. Fly ash samples prepared for holographic experiments: (e) BFA, (f) FFA, (g) NFA, (h) PA.

Figure 10.3: Fly ash sample preparation for digital holographic experiments.

interference pattern generated by reference and object beams is recorded as a hologram using the CMOS camera sensor (Pixelink, PL-D734MU-T, Pixels: 2048×2048, Pixel size: $5.5\ \mu m \times 5.5\ \mu m$) connected to a computer. The pinhole-to-camera distance ($Z = 100\ cm$) is kept constant. The pinhole-to-glass slide distance z_1 was varied in the range $96\ cm - 98\ cm$ to obtain the required magnification and field of view.

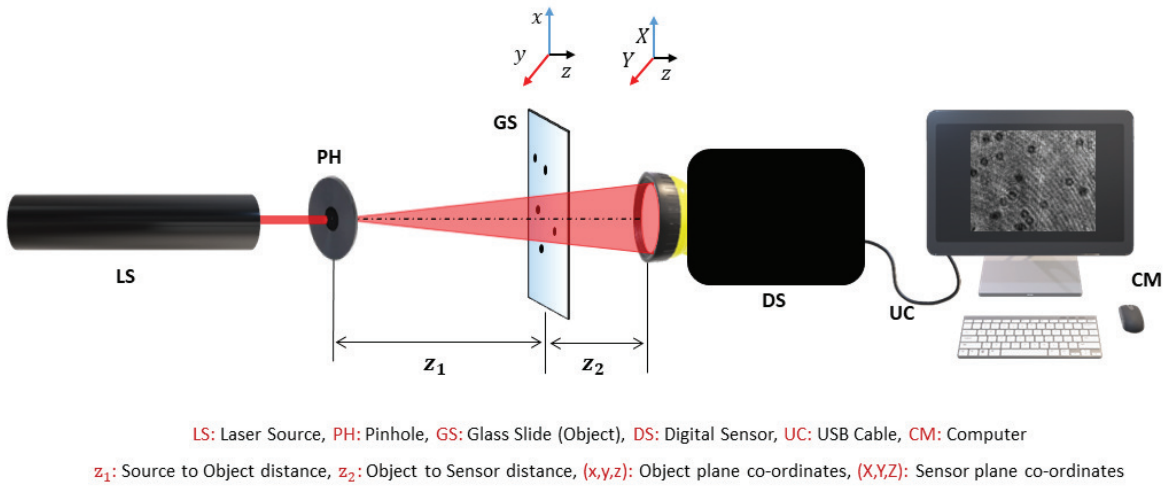

Figure 10.4: Experimental setup of digital in-line holography with spherical beam illumination

In the particle distribution measurement, a maximum of 50 holograms (H_O) were recorded corresponding to different regions of the glass slide. The hologram recording was performed carefully making sure that there was no overlap between imaged regions. Initially, a separate reference hologram (H_R) was recorded in the absence of particles on the glass slide. Subsequently, the background subtracted holograms are obtained as,

$$H_{BR}(X,Y) = H_O(X,Y) - H_R(X,Y). \tag{10.1}$$

These background subtracted holograms are reconstructed to obtain the particle images using the technique described below.

10.1.1.2.3 Hologram Reconstruction Prior to reconstruction, the holograms are interpolated to generate holograms $H(X,Y)$ of double the size of the original using bicubic interpolation technique. [67]. The hologram interpolation helps in increasing the apparent pixel density and in turn the quality of hologram reconstructed images. The holograms were reconstructed using the angular spectrum method [1] following the Eq. 1.10. For the setup in Figure 10.4, the complex amplitude of the object wave can be reconstructed by setting z as $\tilde{z} = z_1 z_2 / Z$ in Eq. 3.5. The amplitude image $A_z(x,y)$ and the phase image $\phi_z(x,y)$ of the object specimen can be computed using Eq. 6.1 and Eq. 6.2. The object focal plane $z_f = z_1$ is accurately determined by using the eigenvalue based autofocusing method [204]. The numerical reconstruction of hologram at any given plane within the measurement volume allows to obtain the three-dimensional PSD from a single hologram recording. In the case of lens-less holographic configura-

tion shown in Figure 10.4, unit magnification is achieved considering plane wave illumination, whereas magnification greater than one can be achieved with spherical wave illumination [222, 178, 223, 66].

10.1.1.2.4 Particle Detection Different approaches have been reported in digital in-line holography for determining particle object parameters, such as shape, size and location of the particles, either directly from hologram [61, 212, 213] or from reconstructed images [214, 215, 216]. The hologram is reconstructed at the object focal plane and subsequently a particle detection algorithm is applied on the reconstructed amplitude image ($A_z(x, y)$). Several particle detection algorithms have been proposed in the literature based on a maximum edge sharpness metric [220, 221], minimum intensity metric [217, 218, 219] and hybrid method [222, 178, 223]. A hologram interpolation is suggested to enhance the detectable particle size limit towards smaller size range [66]. At the object focal plane, particles occupy minimum area in the reconstructed images. As a result, spherical particle object can be detected as circular objects of equivalent diameters in the reconstructed images. In the present work, we have utilized circular Hough transform based edge detection technique on reconstructed amplitude images $A_z(x, y)$ for particle analysis [217, 218, 219]. This algorithm provides the two-dimensional position and radius of the particles from reconstructed amplitude images in terms of number of pixels. Accordingly, the particle diameter estimate is computed as $d = 2r_p\Delta$, where r_p represents the radius in number of pixels and Δ represents sensor pixel width.

10.1.1.2.5 Data Processing The particle detection algorithm provides the quantitative information on the diameter and number of particles of specific diameters. For the purpose of evaluating PSD, the particle size range is divided into N number of bins with bin centers at $90\ \mu m, 85\ \mu m, \cdots, 10\ \mu m$ and each bin of size $5\ \mu m$. The plot of number of detected particles from the reconstructed images belonging to specific bins in function of bin centers provides the PSD. Similarly, particle volume distribution and percentage finer (PF) can also be calculated as follows:

(i) Particle volume is evaluated as

$$V(j) = \frac{4\pi}{3} r^3(j), \tag{10.2}$$

where $j \in [1, N]$; $r(j)$ represents particle radius associated with j^{th} bin center.

(ii) Total volume of particles belonging to each bin is calculated as

$$V_b(j) = V(j)n(j), \tag{10.3}$$

where $n(j)$ represents the number of particles belonging to the j^{th} bin.

(iii) Total volume of all the detected particles is calculated as,

$$V_T = \sum_{j=1}^{N} V_b(j). \tag{10.4}$$

(iv) Percentage of particles belonging to j^{th} bin is calculated as,

$$P(j) = V_b(j) \times \frac{100}{V_T}. \tag{10.5}$$

(v) The cumulative percentage of particles belonging to bins below and including j^{th} bin is calculated as,

$$CM(j) = CM(j-1) + P(j). \tag{10.6}$$

(vi) Finally, the percentage finer for j^{th} bin is evaluated as,

$$PF(j) = 100 - CM(j). \tag{10.7}$$

We considered two modalities for PSD estimation: one with particles spread and fixed over a microscopic glass slide as described above and one with particles suspended in distilled water in a cuvette (Sky Technology, AC-SP 10P, volume: $3.5\ ml$, wavelength range = $340-2500\ nm$). For the PSD estimation using cuvette, the center of cuvette was placed at a distance of $z_1 = 97\ cm$ from the pinhole. The above described procedure of PSD estimation was performed at various reconstruction distances ($\tilde{z}$) corresponding to the cuvette volume. Total 200 hologram reconstructions were performed. Subsequently, a single particle image is obtained based on the maximum intensity at each pixel evaluated from the stack of reconstructed images. It is important to note that in the case of cuvette and glass slide, single and multiple holograms need to be recorded, respectively. The numbers of particles in each bin which were evaluated from multiple holograms obtained using glass slide were added together to obtain the PF_c.

The PFs evaluated using the proposed method were compared with those obtained using the conventional hydrometer technique. In addition, the PSD of fly ashes was obtained using laser particle size analyzer (Mastersizer 2000). Whereas the hydrometer can provide the PSD for sizes below $10\ \mu m$, the proposed technique is limited to measure PSD for particle sizes $\geq 10\ \mu m$ due the pixel size of $5.5\ \mu m$. In order to compensate for the missing data on number of particles of sizes below $10\ \mu m$, an extrapolation approach has been proposed in this study. In general, the PSD exhibits an exponentially decaying profile which can be represented as follows

$$PSD(j) = PSD(0)\exp(-f(j)). \tag{10.8}$$

In the above equation, $f(j) = \tau_n j^n + \tau_{n-1} j^{n-1} + \cdots + \tau_1 j$, where, $\tau_n, \tau_{n-1}, \ldots, \tau_1$ represent decay parameters. Evaluating logarithm of both sides of Eq. 10.8, we obtain

$$\log PSD(j) = -f(j) + \log PSD(0). \tag{10.9}$$

Since the above equation represents a polynomial, the distribution $\log\ PSD(j)$ is fitted with n^{th} order polynomial as a function of j to obtain the estimates of $\tau_n, \tau_{n-1}, \ldots, \tau_1$. These values are plugged into Eq. 10.8 to extrapolate the PSD to obtain the estimates of number of particles with size below $10\ \mu m$.

10.1.2 Results

Four fly ash samples: BFA, FFA, NFA, and PA were used for the validation of proposed technique. It is understood from the literature that fly ash exhibit close to uniform PSD and clearly encompass the size range suitable for testing the efficacy of the proposed holographic method. Glass slides were prepared and 50 holograms were recorded for each sample. Figure 10.5(a) shows one of the representative holograms associated with FFA sample recorded with $z_1 = 96.65\ cm$. The reference and reference

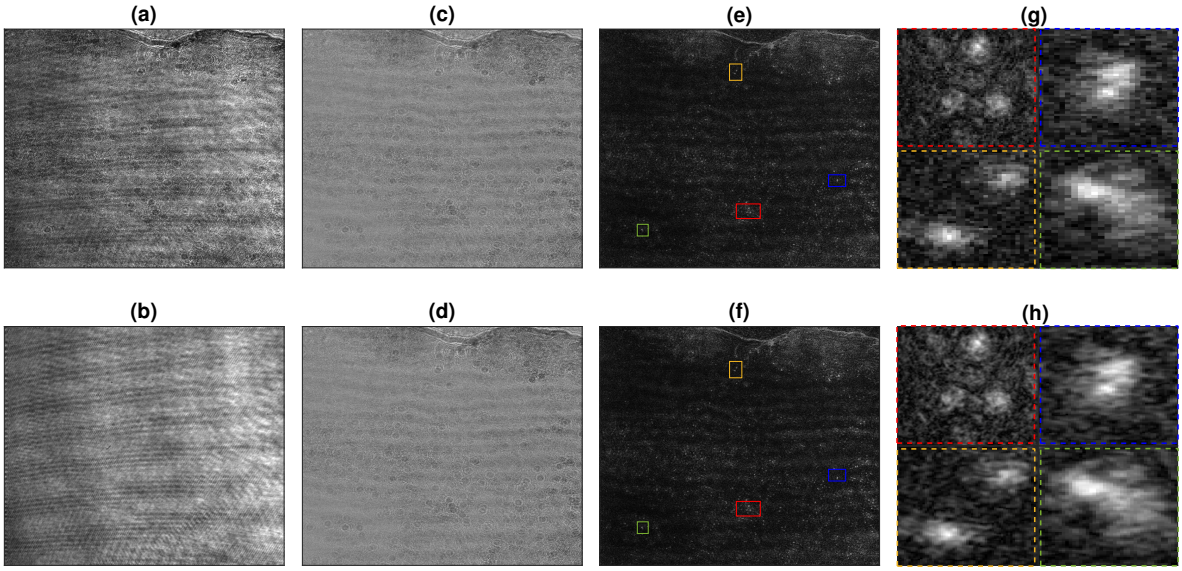

Figure 10.5: (a) Raw hologram corresponding to one of the representative holograms of fly ash samples, (b) reference hologram, (c) reference subtracted hologram, (d) interpolated hologram of size double than that of raw hologram computed using bicubic interpolation. (e) and (f) Particle images obtained from the reconstruction of holograms shown in (c) and (d), respectively, (g) and (h) zoomed-in view of some of the parts of reconstructed images shown with colored rectangles.

subtracted holograms are shown in Figs. 10.5(b) and 10.5(c). The $2\times$ interpolated reference subtracted hologram shown in Fig. 10.5(d). Figures 10.5(e) and 10.5(f) show the particle images reconstructed from original and interpolated holograms, respectively. For the purpose of illustration, zoomed-in parts of the

reconstructed images indicated with squares of different colors are shown in Figs. 10.5(g) and 10.5(h). The hologram interpolation provides improved particle image resolution which essentially results in accurate PSD [186]. The detailed hologram recording and reconstruction process was implemented as described in the "Methods" section and PSD is computed for each hologram.

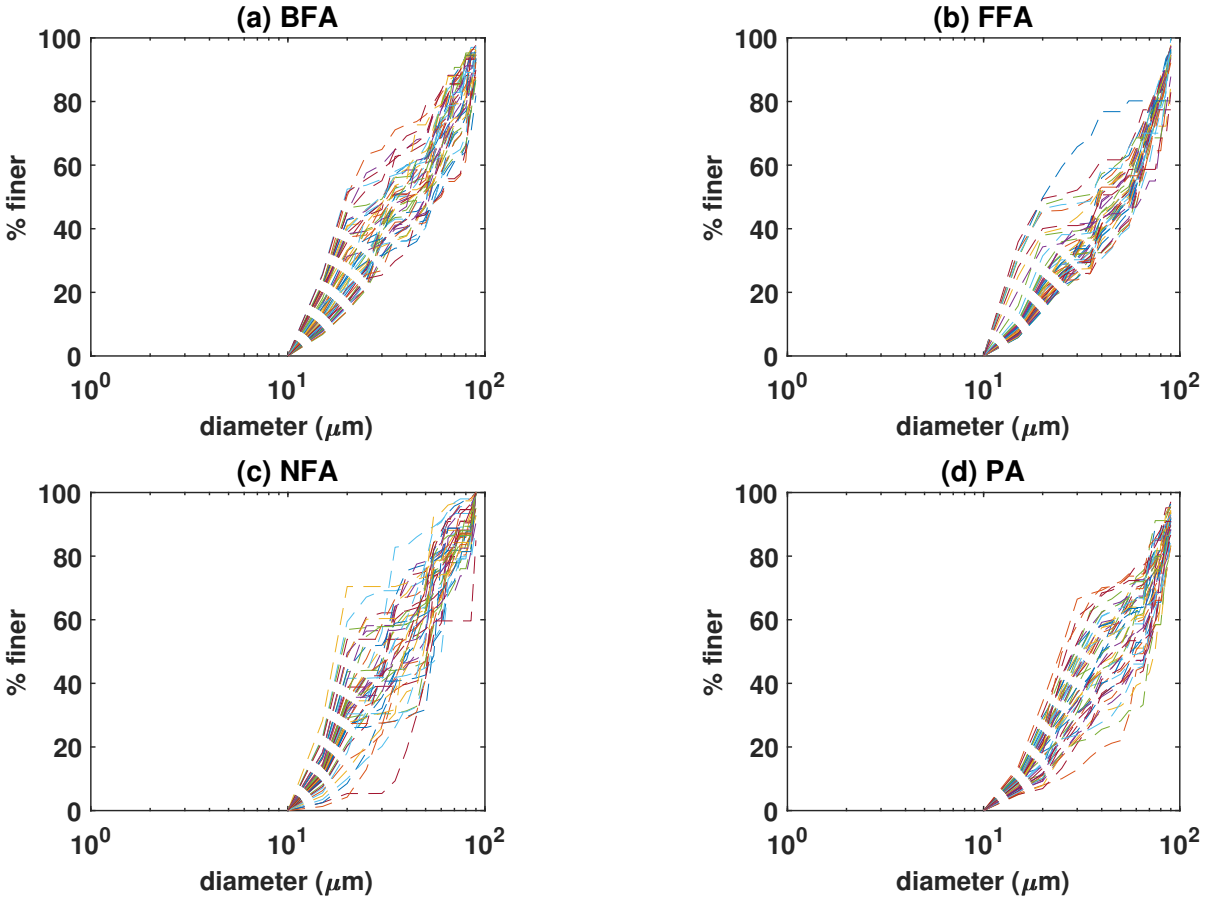

Figure 10.6: Plots of PFs evaluated for (a) BFA, (b) FFA, (c) NFA, and (d) PA samples.

Figure 10.6 shows the plots of PFs evaluated for each sample and each of their corresponding holograms. Due to the non-uniform spreading of fly-ash samples on the glass slides, the field-of-views corresponding to different holograms do not contain same number of particles and do not follow similar PSDs. As a result, the PFs of different holograms given in Fig. 10.6 show significant variations. Therefore, as mentioned previously, the numbers of particles in each bin obtained for multiple holograms are added together to estimate the percentile finer PF_c. Figure 10.7 shows the plots of PF_c for each sample in function of number of holograms (N_h). For the purpose of comparison, the PFs obtained using the hydrometer technique is also provided. It can be noted that increase in number of holograms, which effectively increases the number of imaged particles, improves the PF_c estimation accuracy. To

further emphasize this observation, correlation between PF_c and hydrometer data PF_{hyd} in function of N_h were computed as given in Table 10.2. It can be noted that correlation increases with N_h. Therefore, a larger value of N_h provides higher accuracy in the estimation of PF_c.

Table 10.2: Study of correlation coefficient between PF_c and PF_{hyd} for different values of N_h

	BFA	**FFA**	**NFA**	**PA**
$N_h = 5$	0.9955	0.9977	0.9895	0.9907
$N_h = 10$	0.9954	0.9974	0.9826	0.9814
$N_h = 15$	0.9962	0.9956	0.9835	0.9909
$N_h = 20$	0.9980	0.9979	0.9810	0.9908
$N_h = 25$	0.9989	0.9984	0.9848	0.9946
$N_h = 30$	0.9971	0.9985	0.9890	0.9953
$N_h = 40$	0.9989	0.9986	0.9862	0.9984
$N_h = 50$	**0.9991**	**0.9992**	**0.9988**	**0.9986**

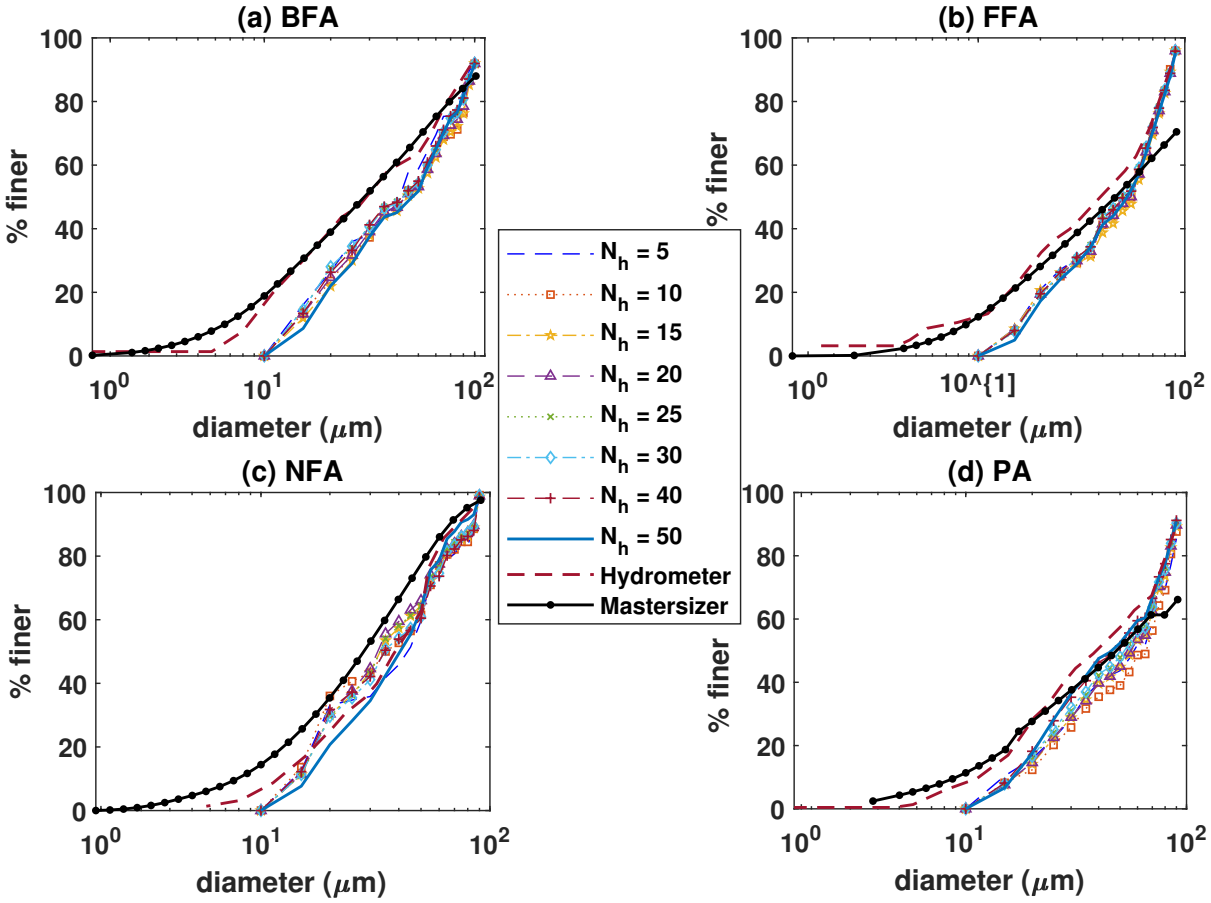

Figure 10.7: Plots of PF_c evaluated for (a) BFA, (b) FFA, (c) NFA, and (d) PA samples in function of number of holograms.

Further, a performance comparison between cuvette and glass slide based methods is provided in

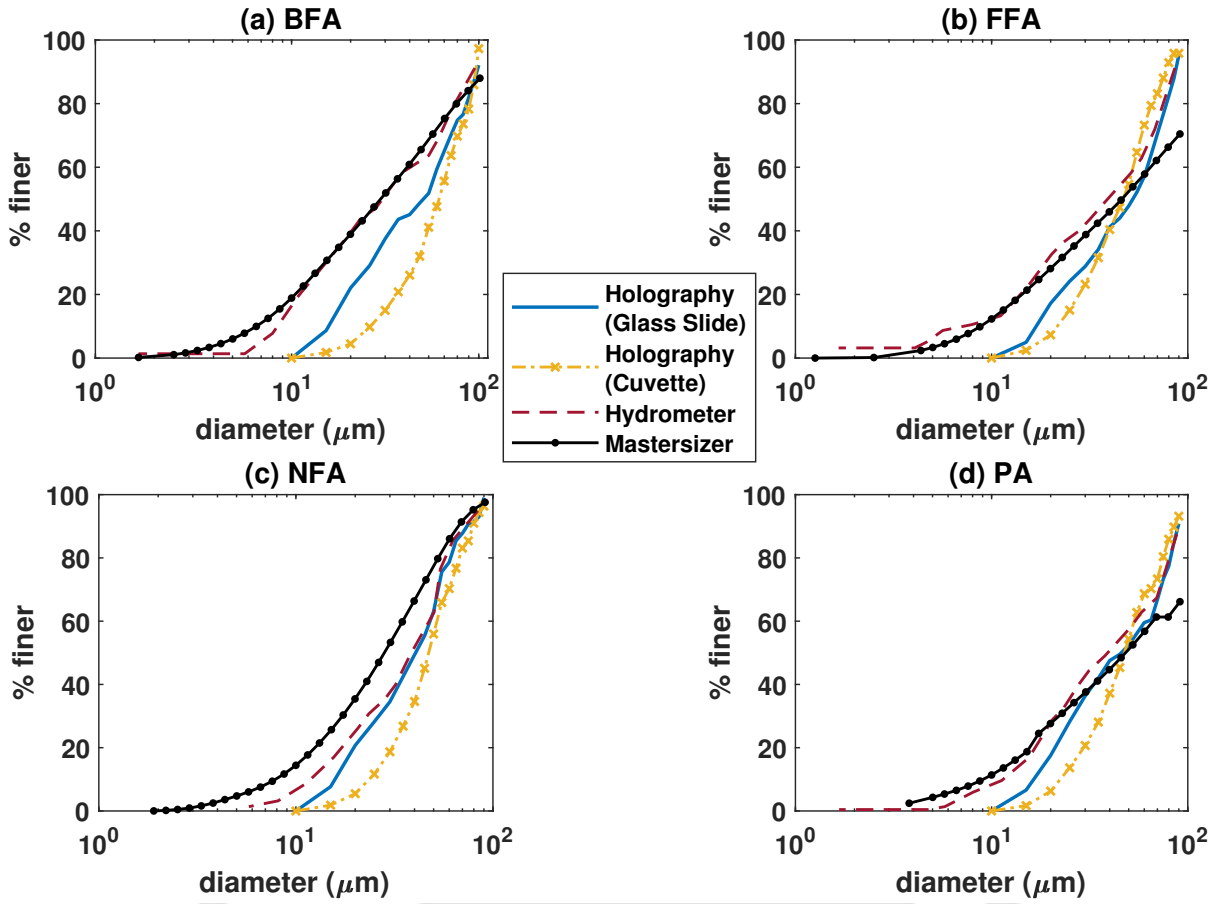

Figure 10.8: Plots of PF_c evaluated for (a) BFA, (b) FFA, (c) NFA, and (d) PA samples using glass slide and cuvette based methods.

Fig. 10.8. It is evident that the glass slide based method provides better PF estimation performance in comparison to cuvette based method. Fly ash particles float inside the cuvette and precipitate. Due to that, less number of particles are detected, which results in poor PF_c measurement. It is important to note that PFs shown in Figs. 10.6-10.8 are obtained without application of the proposed extrapolation technique.

Figure 10.7 shows the parametric study of PF_c for each sample considering cumulatively 5, 10, 15, 20, 25, 30, 40 and 50 holograms. The fly-ash samples are non-uniformly spread on the glass slides. Therefore, the particle distribution PF_c using the proposed method comparable to PF_{hyd} is obtained by adding number of particles in each bin associated with all 50 holograms for each samples. The proposed method is limited in providing the PSD for particle sizes above 10 μm. On the other hand, hydrometer is capable of providing the distribution for particle sizes below 10 μm as well. In order to compare these two methods, the PFcs estimated with the proposed method need to be modified for the number of

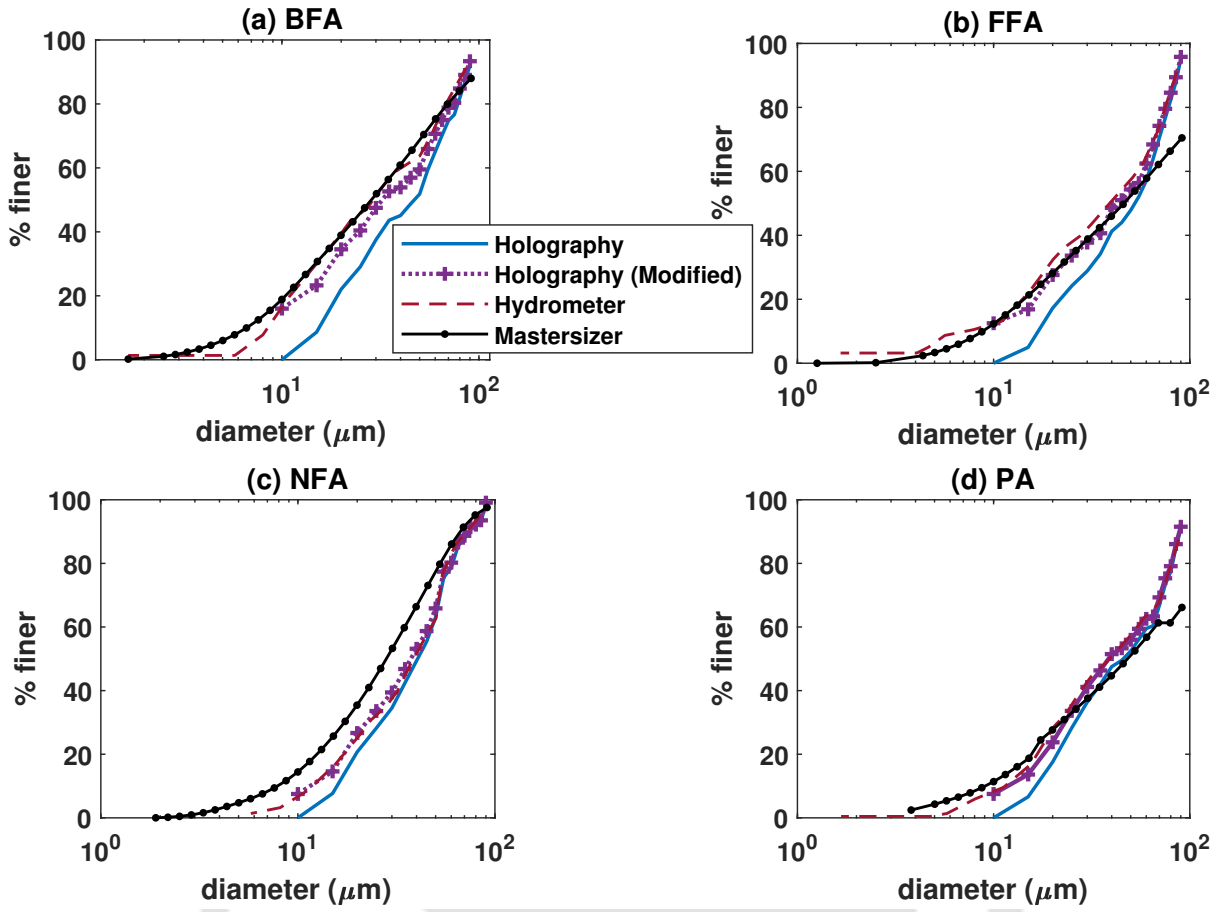

Figure 10.9: Plots of modified PF_c evaluated for (a) BFA with 16%, (b) FFA with 12.5%, (c) NFA with 7.5% and (d) PA with 7.5% volume modification.

particles with sizes below 10 μm. In the BFA, FFA, NFA and PA samples, volumes of particles with sizes below 10 μm were measured using the hydrometer to be 16%, 12.5%, 7.5% and 7.5% of total volume, respectively. Subsequently, these values were used to modify the PFcs estimated with the proposed method as shown in Fig. 10.9. It can be noted that the modified PF_cs are indeed similar to the PF_{hyd} for all samples.

A data extrapolation scheme has been proposed to estimate the number of particles of sizes below 10 μm in evaluating PF_cs using the proposed holographic technique. The distribution $\log\ PSD(i)$ in Eq. 10.9 is fitted with n^{th} order polynomial as a function of i. The PSDs of holographic measurement for each sample are extrapolated by fitting with $n = 1, 2, 3, 4, 5$ order polynomial in function of i. The PF_cs evaluated from the extrapolated PSDs for each sample are shown in Figure 10.10. The extrapolated PSD after fitting with 4^{th} order polynomial provides a PF_c estimate close to the hydrometer measurement PF_{hyd}. The goodness-of-fit is quantified in terms of coefficient of regression parameter,

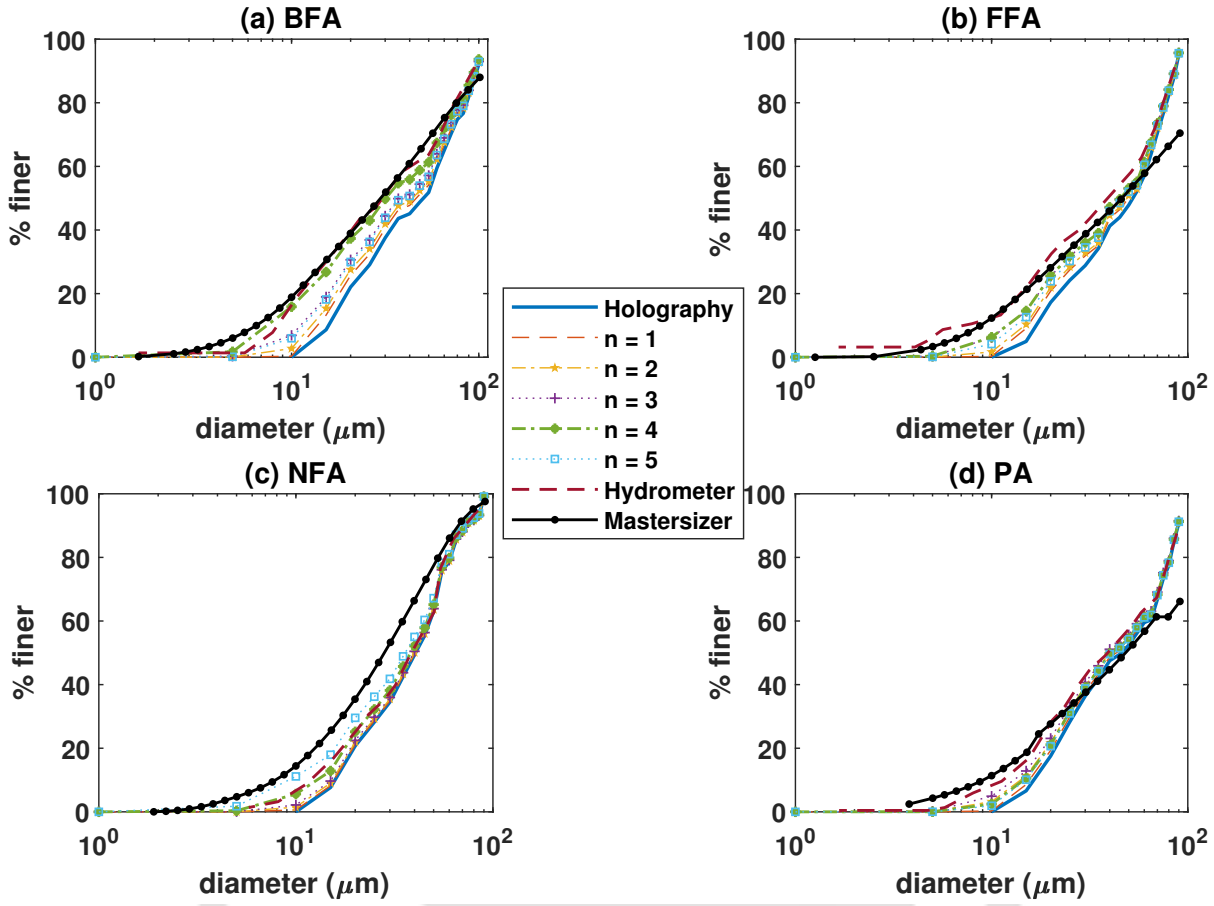

Figure 10.10: Plots of PF_c obtained from extrapolated PSDs after fitting with n^{th} order polynomial for (a) BFA, (b) FFA, (c) NFA, and (d) PA samples.

R^2. The values of R^2 evaluated for each fly ash sample in function of n are given in Table 10.3. It can be noted that highest fitting accuracy is achieved with $n = 4$ for all samples. Note that for BFA and FFA samples, the values of R^2 could not be evaluated for $n = 5$ due to ill-conditioned matrix. The final PF_c of the proposed method, Mastersizer PF_M and hydrometer measurement PF_{hyd} for each sample are compared in Figure 10.11. The performance comparison indicates that the proposed method provides similar performance as that of the hydrometer. However, the total processing time required for the proposed method is about $5-10$ minutes, wheres the hydrometer method requires about 24 hours. Thus, the proposed method is found to be more feasible to measure the fly ash PSD in a computationally efficient manner. In the present study, the numerical implementation is performed using the MATLAB-19a on a computer with the Intel(R) Core(TM) i7-8700 processor with 3.2 GHz Octacore and 16 GB RAM.

Table 10.3: Study of coefficient of regression (R^2) for different values of n

	BFA	FFA	NFA	PA
n = 1	0.287	0.322	0.366	0.350
n = 2	0.588	0.641	0.694	0.679
n = 3	0.806	0.855	0.890	0.879
n = 4	**0.926**	**0.957**	**0.972**	**0.991**
n = 5	-	-	0.973	0.964

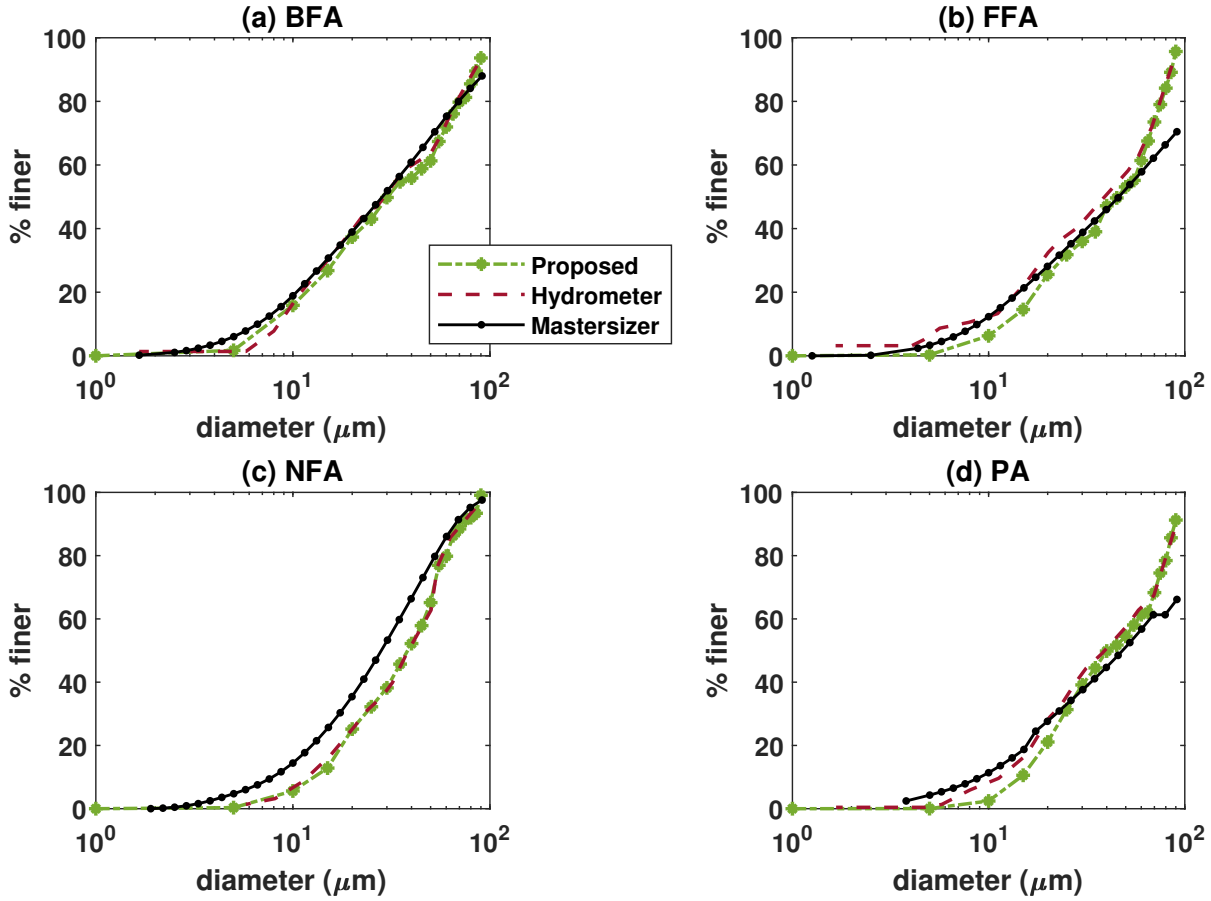

Figure 10.11: Comparison of proposed method with conventional hydrometer and Mastersizer in the PF measurement of (a) BFA, (b) FFA, (c) NFA, and (d) PA samples.

10.1.3 Conclusion

The lensless digital in-line holographic method was utilized for the measurement of PSD. The proposed method involves a simple sample preparation step wherein the fly ash sample are non-uniformly spread over a glass slide. The holograms of different regions on the glass slide provide measurement of respective PSDs. The overall sample PSD can be easily obtained by using the total number of detected particles. The performance of the proposed method is found to be similar to that of the hydrometer in the

range of $10 - 90$ μm. The proposed scheme of PSD extrapolation allows to estimate the number of particles with sizes below 10 μm. A simple sample preparation mechanism and numerical hologram image reconstruction of particles makes the proposed method a suitable candidate for the PSD measurement of fly ash samples in an accurate and computationally efficient manner.

भारतीय प्रौद्योगिकी संस्थान गुवाहाटी
Indian Institute of Technology Guwahati

Part V

Conclusion or status of thesis work

भारतीय प्रौद्योगिकी संस्थान गुवाहाटी
Indian Institute of Technology Guwahati

11

Status of Thesis Work

This section summarizes the work presented in the thesis. A number of digital hologram processing algorithms are reported for hologram reconstruction, numerical autofocusing, improved particle size estimation, phase unwrapping, etc. The practical validation of these algorithms has been performed through number of experiments. In the present thesis, digital in-line hologram recording and reconstruction process is derived considering object placed at any plane inbetween the source and camera. A new iterative estimation based reconstruction technique is proposed to reduce twin image effect and background noise of reconstructed image. The developed digital hologram reconstruction algorithm based on Toeplitz Matrix based Deconvolution is found to provide the reconstruction quality similar to the conventional algorithm with better computational efficiency. This increase in computational efficiency is more prominent when the hologram reconstruction is performed in an iterative manner. An autoregressive hologram interpolation algorithm is developed to provide significant improvement in reconstructed image quality, which results in improved particle detection and size estimation accuracy. A computationally efficient and noise-robust phase unwrapping algorithm is proposed based on the breadth-first-search approach in combination with the multi-level segmentation of the phase quality interval. Two efficient autofocusing algorithms are developed based on eigenvalues and eigenvalue distribution, respectively. The particle swarm optimization based autofocusing in digital holography is found to provide significant reduction in the computation time in comparison to the conventional approach. The iterative approach of focal plane detection allows to refine the focal plane estimate in each iteration. The proposed iterative

[11] This chapter presents the summary of the thesis work.

strategy is about 75% more computationally efficient compared to the conventional autofocusing methods. The lensless digital in-line holographic method was utilized to measure the particle size distribution (PSD) of different fly ash samples. The proposed method is capable of detecting the PSD in the range of $10-90$ μm. The below 10 μm is estimated using extrapolation technique. The proposed method provides accuracy similar to conventional hydrometer methods. A simple sample preparation mechanism and numerical hologram image reconstruction of particles makes the proposed method a suitable candidate for the PSD measurement of fly ash samples in an accurate and computationally efficient manner.

- **Journal Published : 8**
- **Conference Publication : 1**
- **Conference Presentation : 1**
- **Manuscript Submitted : 2**

12

Future Direction

- **Digital in-line holography for particle imaging in microfluidics**

  Digital in-line holography has been widely used in many applications such as quantitative particle characterization, particle tracking in microfluidcs, particles and flow measurement in 3D space, etc due to its simple and low-cost optical configuration. We have done some preliminary work in the field of particle tracking in microfluidic channel. A microfluidic channel carrying particle sample was considered as the object in the holographic microscopy setup with plane wave illumination as shown in Fig. 1.1(a). The aim of our study to holographically image the fluid flow under different flow conditions and channel types such as straight channel, channel with T-junction, converging-diverging channel, etc. The proposal is to track particles in 3-D dimensions to characterize fluid flow and compare it with numerical simulation.

- **Fluid characterization using lensless digital in-line holography**

  The flow a particle in fluid is affected by different fluid and particle parameters such as fluid viscosity, densities of fluid and particle, particle size, etc. Digital lensless in-line holography can be effectively utilized for fluid characterization by quantifying the particle flow within the fluid. Due to compact setup associated with the DIH, the fluid sample volume requirement is less.

- **3D-Deconvolution of digital hologram with reduced computation cost**

[12]This chapter presents future directions of the research associated with the thesis work.

In general, for the 3D particle field imaging in digital holography, the hologram reconstructions need to be performed individually at different plane which is a computationally expensive process. The state-of-art methods for 3D deconvolution is performed using Fast Fourier transform routines which has limitations on the hologram size that can be processed. At the same time, the point spread function derived at a single plane is utilized during deconvolution which may not be a valid assumption in several cases. In future, we will try to focus on the development of 3D-deconvolution algorithms to overcome these limitations.

- **Characterization of micro-particles with arbitrary size and shape in digital holography**

  The present thesis mainly focused on the characterization of spherical particles. In future, we aim to develop algorithms for characterization of micro-particles with arbitrary size and shape in digital holography.

List of Publications

Conference Paper:

1. Autofocusing in Digital Holography based on Eigenvalue Distribution.

   Anik Ghosh and Rishikesh Kulkarni

   Presented and published in the conference, *OSA Imaging and Applied Optics Congress 2021*, July 2021. [ch. 6.2]

Published/Accepted/Revision Submitted Papers:

1. Autofocusing in digital holography using eigenvalues.

   Anik Ghosh, Rishikesh Kulkarni and Pranab Kumar Mondal (2021).

   Applied Optics, **60-4**, 1031-1040. [ch. 6]

2. Improving particle detection and size estimation accuracy in digital in-line holography using autoregressive interpolation.

   Anik Ghosh and Rishikesh Kulkarni (2021).

   Applied Optics, **8**, 6. [ch. 4.1 and ch. 9.1]

3. Fast and accurate autofocusing algorithm in digital holography based on particle swarm optimization.

   Subham Rathor, Anik Ghosh and Rishikesh Kulkarni (2021).

   Optik, **247**, 167946. [ch. 7]

4. Improved particle size estimation in digital in-line holography based on Fienup's iterative algorithm.

   Anik Ghosh, Rishikesh Kulkarni, Chandra Bhanu Gupt and Sreedeep Sekharan (2022).

   Asian Journal of Physics, **30-(10-11)**, 1437-1446. [ch. 3.1 and ch. 9.2]

5. Phase unwrapping algorithm using breadth-first-search and multi-level segmentation of phase quality interval in digital holography.

   Anik Ghosh, Rishikesh Kulkarni and Rajshekhar Gannavarpu (2022).

   Journal of Modern Optics, **69-16**, 957-967. [ch. 5.1]

6. Fast hologram reconstruction algorithm in digital in-line holography using Toeplitz matrix based deconvolution (2022).

Anik Ghosh, Rishikesh Kulkarni, Seunghyup Shin and Pranab Kumar Mondal (2022).

Optics and Lasers in Engineering, **159-27**, 107198. [ch. 3.2]

7. Fast Iterative Autofocusing Algorithm in Digital Holography.

   Anik Ghosh, Rishikesh Kulkarni and Pramod Rastogi (2021).

   Asian Journal of Physics, **30-7**, 1051-1057. [ch. 8]

8. Measurement of fly ash particle size distribution using lensless digital in-line holography.

   Anik Ghosh, Rishikesh Kulkarni, Chandra Bhanu Gupt and Sreedeep Sekharan (2022).

   Journal of Testing and Evaluation, **51-4**. [ch. 10]

Bibliography

[1] J. W. Goodman, *Introduction to Fourier optics*. Roberts and Company Publishers, 2005.

[2] D. Gabor, "A new microscopic principle," 1948.

[3] ——, "Microscopy by reconstructed wave-fronts," *Proceedings of the Royal Society of London. Series A. Mathematical and Physical Sciences*, vol. 197, no. 1051, 1949.

[4] ——, "Microscopy by reconstructed wave fronts: 2," *Proceedings of the Physical Society. Section B*, vol. 64, no. 6, 1951.

[5] T. Tahara, X. Quan, R. Otani, Y. Takaki, and O. Matoba, "Digital holography and its multidimensional imaging applications: a review," *Microscopy*, vol. 67, no. 2, 2018.

[6] Y. Takaki and N. Okada, "Hologram generation by horizontal scanning of a high-speed spatial light modulator," *Applied optics*, vol. 48, no. 17, 2009.

[7] T. Yamaguchi and H. Yoshikawa, "Computer-generated image hologram," *Chinese Optics Letters*, vol. 9, no. 12, 2011.

[8] Y. Takaki, Y. Matsumoto, and T. Nakajima, "Color image generation for screen-scanning holographic display," *Optics express*, vol. 23, no. 21, 2015.

[9] T. Ito, T. Shimobaba, H. Godo, and M. Horiuchi, "Holographic reconstruction with a 10-μm pixel-pitch reflective liquid-crystal display by use of a light-emitting diode reference light," *Optics letters*, vol. 27, no. 16, 2002.

[10] J. W. Goodman and R. Lawrence, "Digital image formation from electronically detected holograms," *Applied physics letters*, vol. 11, no. 3, 1967.

[11] M. Takeda, H. Ina, and S. Kobayashi, "Fourier-transform method of fringe-pattern analysis for computer-based topography and interferometry," *JosA*, vol. 72, no. 1, 1982.

[12] M. K. Kim, "Digital holographic microscopy," in *Digital Holographic Microscopy*. Springer, 2011.

[13] L. J.-C. Picart. P, *Digital Holography*. Wiley, Hoboken, 2013.

[14] T.-C. Poon and J.-P. Liu, *Introduction to modern digital holography: with MATLAB*. Cambridge University Press, 2014.

[15] T. Latychevskaia and H.-W. Fink, "Practical algorithms for simulation and reconstruction of digital in-line holograms," *Applied optics*, vol. 54, no. 9, 2015.

[16] E. Mahoney, J. Kun, M. Smieja, and Q. Fang, "Point-of-care urinalysis with emerging sensing and imaging technologies," *Journal of The Electrochemical Society*, vol. 167, no. 3, 2020.

[17] V. Bianco, L. Miccio, P. Memmolo, F. Merola, B. Mandracchia, T. Cacace, M. Mugnano, M. Paturzo, M. Villone, P. L. Maffettone, and P. Ferraro, "3d imaging in microfluidics: New holographic methods and devices," in *Progress in Biomedical Optics and Imaging - Proceedings of SPIE*, vol. 10875, 2019.

[18] M. Kumar.S and Dutta.K.P, "Photonic crystal fiber for high resolution lensless in-line holographic microscopy," in *Physics Optics*, 2020.

[19] S. Agarwal, V. Kumar, and C. Shakher, "Onion cell imaging by using Talbot/self-imaging effect," *SPIE*, vol. 10453, 2017.

[20] ——, "Analysis of red blood cell parameters by Talbot-projected fringes," *Journal of Biomedical Optics*, vol. 22, no. 10, 2017.

[21] E. Cuche, F. Bevilacqua, and C. Depeursinge, "Digital holography for quantitative phase-contrast imaging," *Optics letters*, vol. 24, no. 5, 1999.

[22] Y. Takaki, H. Kawai, and H. Ohzu, "Hybrid holographic microscopy free of conjugate and zero-order images," *Applied optics*, vol. 38, no. 23, 1999.

[23] S. Murata and N. Yasuda, "Potential of digital holography in particle measurement," *Optics & Laser Technology*, vol. 32, no. 7-8, 2000.

[24] C. J. Mann, L. Yu, C.-M. Lo, and M. K. Kim, "High-resolution quantitative phase-contrast microscopy by digital holography," *Optics Express*, vol. 13, no. 22, 2005.

[25] T. Javidi.B, "Three-dimensional object recognition by use of digital holography." *Optics Letter*, vol. 25, no. 9, 2000.

[26] J. Gass, A. Dakoff, and M. Kim, "Phase imaging without 2π ambiguity by multiwavelength digital holography," *Optics letters*, vol. 28, no. 13, 2003.

[27] A. Alfalou and C. Brosseau, "Optical image compression and encryption methods," *Advances in Optics and Photonics*, vol. 1, no. 3, 2009.

[28] M. Takeda and M. Kitoh, "Spatiotemporal frequency multiplex heterodyne interferometry," *JOSA A*, vol. 9, no. 9, 1992.

[29] P. Clemente, V. Durán, E. Tajahuerce, J. Lancis *et al.*, "Single-pixel digital ghost holography," *Physical Review A*, vol. 86, no. 4, 2012.

[30] P. Clemente, V. Durán, E. Tajahuerce, P. Andrés, V. Climent, and J. Lancis, "Compressive holography with a single-pixel detector," *Optics letters*, vol. 38, no. 14, 2013.

[31] T. Noda, S. Kawata, and S. Minami, "Three-dimensional phase-contrast imaging by a computed-tomography microscope," *Applied optics*, vol. 31, no. 5, 1992.

[32] K. Delikoyun, E. Cine, M. Anil-Inevi, M. Ozuysal, E. Ozcivici, and H. C. Tekin, "Lensless digital in-line holographic microscopy for space biotechnology applications," *Proceedings of 9th International Conference on Recent Advances in Space Technologies, RAST 2019*, 2019.

[33] R. Aniruddha, K. M. Arslan, D. Andriejus, D. Mustafa, T. Derek, R. Julien, C. J. M, and O. Aydogan, "Holographic detection of nanoparticles using acoustically actuated nanolenses," *Nature communications*, vol. 11, no. 1, pp. 1–10, 2020.

[34] A. Tikan, S. Bielawski, and C. Szwaj, "Single-shot measurement of phase and amplitude by using a heterodyne time-lens system and ultrafast digital time-holography," *Nature Photonics*, vol. 12, 2018.

[35] J. H. Park, T. Go, and S. J. Lee, "Label-free sensing and classification of old stored blood," *Annals of Biomedical Engineering*, vol. 45, no. 11, 2017.

[36] S. Gupta and S. A. Vanapalli, "Microfluidic shear rheology and wall-slip of viscoelastic fluids using holography-based flow kinematics," *Physics of Fluids*, vol. 32, no. 1, 2020.

[37] P. Ferraro, F. Merola, P. Memmolo, L. Miccio, M. Mugnano, M. Villone, and P. L. Maffettone, "Label-free imaging of cancer cells by in-flow tomography," in *Progress in Biomedical Optics and Imaging - Proceedings of SPIE*, vol. 10890, 2019.

[38] H. Zhou, Z. Yang, Z. Yao, and K. Cen, "Application of digital holographic microscopy and microfluidic chips to the measurement of particle size distribution of fly ash after a wet electrostatic precipitator," *Flow Measurement and Instrumentation*, vol. 60, 2018.

[39] P. Memmolo, L. Miccio, F. Merola, M. Mugnano, and P. Ferraro, "Hydrodynamic red blood cells deformation by quantitative phase microscopy and zernike polynomials," *Frontiers in Physics*, vol. 7, no. JULY, 2019.

[40] P. Ferraro, F. Merola, L. Miccio, P. Memmolo, and M. Mugnano, "Holographic processing pipeline for tomographic flow cytometry," *Proceedings of SPIE - The International Society for Optical Engineering*, vol. 11060, 2019.

[41] V. Bianco, T. Cacace, B. Mandracchia, V. Pagliarulo, M. Paturzo, and P. Ferraro, "Compact modules for off-axis holography in microfluidics: Features and design solutions," *Progress in Biomedical Optics and Imaging - Proceedings of SPIE*, vol. 10869, 2019.

[42] P. Memmolo, M. Villone, F. Merola, M. Mugnano, L. Miccio, P. L. Maffettone, and P. Ferraro, "Holographic imaging for 3d cells morphology in microfluidic flow," *Progress in Biomedical Optics and Imaging - Proceedings of SPIE*, vol. 11076, 2019.

[43] H. Kreuzer, M. Jericho, I. Meinertzhagen, and W. Xu, "Digital in-line holography with photons and electrons," *Journal of Physics: Condensed Matter*, vol. 13, no. 47, 2001.

[44] H. Meng and F. Hussain, "In-line recording and off-axis viewing technique for holographic particle velocimetry," *Applied Optics*, vol. 34, no. 11, 1995.

[45] S. Kumar, M. Mahadevappa, and P. K. Dutta, "Lensless in-line holographic microscopy with light source of low spatio-temporal coherence," *arXiv preprint arXiv:2002.03369*, 2020.

[46] V. N. Manoharan, *holographic-microscopy*. Harvard university, 2022.

[47] N. Pavillon, J. Kühn, C. Moratal, P. Jourdain, C. Depeursinge, P. J. Magistretti, and P. Marquet, "Early cell death detection with digital holographic microscopy," *PloS one*, vol. 7, no. 1, p. e30912, 2012.

[48] X. Fan, J. J. Healy, K. O'Dwyer, J. Winnik, and B. M. Hennelly, "Adaptation of the standard off-axis digital holographic microscope to achieve variable magnification," in *Photonics*, vol. 8, no. 7. MDPI, 2021, p. 264.

[49] B. Kemper and G. Von Bally, "Digital holographic microscopy for live cell applications and technical inspection," *Applied optics*, vol. 47, no. 4, pp. A52–A61, 2008.

[50] M. Tarn and N. Pamme, *Microfluidics*. Elsevier, 2014.

[51] M. Ugele, M. Weniger, M. Stanzel, M. Bassler, S. W. Krause, O. Friedrich, O. Hayden, and L. Richter, "Label-free high-throughput leukemia detection by holographic microscopy," *Advanced Science*, vol. 5, no. 12, 2018.

[52] A. Ghosh, R. Kulkarni, S. Shin, and P. K. Mondal, "Fast hologram reconstruction algorithm in digital in-line holography using toeplitz matrix based deconvolution," *Optics and Lasers in Engineering*, vol. 159, p. 107198, 2022.

[53] W. H. Carter, "Computational reconstruction of scattering objects from holograms," *JOSA*, vol. 60, no. 3, pp. 306–314, 1970.

[54] T. S. Huang, "Digital holography," *Proceedings of the IEEE*, vol. 59, no. 9, pp. 1335–1346, 1971.

[55] L. Yu and M. K. Kim, "Wavelength-scanning digital interference holography for tomographic three-dimensional imaging by use of the angular spectrum method," *Optics letters*, vol. 30, no. 16, pp. 2092–2094, 2005.

[56] S. De Nicola, A. Finizio, G. Pierattini, P. Ferraro, and D. Alfieri, "Angular spectrum method with correction of anamorphism for numerical reconstruction of digital holograms on tilted planes," *Optics express*, vol. 13, no. 24, pp. 9935–9940, 2005.

[57] C. J. Mann and M. Kim, "Quantitative phase-contrast microscopy by angular spectrum digital holography," in *Three-Dimensional and Multidimensional Microscopy: Image Acquisition and Processing XIII*, vol. 6090. SPIE, 2006, pp. 50–57.

[58] M. K. Kim, L. Yu, and C. J. Mann, "Interference techniques in digital holography," *Journal of Optics A: Pure and Applied Optics*, vol. 8, no. 7, p. S518, 2006.

[59] C. J. Pellizzari, M. T. Banet, M. F. Spencer, and C. A. Bouman, "Demonstration of single-shot digital holography using a bayesian framework," *JOSA A*, vol. 35, no. 1, pp. 103–107, 2018.

[60] D. Lebrun, S. Belaïd, and C. Özkul, "Hologram reconstruction by use of optical wavelet transform," *Applied optics*, vol. 38, no. 17, pp. 3730–3734, 1999.

[61] C. Buraga-Lefebvre, S. Coëtmellec, D. Lebrun, and C. Özkul, "Application of wavelet transform to hologram analysis: three-dimensional location of particles," *Optics and Lasers in Engineering*, vol. 33, no. 6, pp. 409–421, 2000. [Online]. Available: https://doi.org/10.1016/S0143-8166(00)00050-6

[62] A. Sharma, G. Sheoran, Z. Jaffery, and Moinuddin, "Improvement of signal-to-noise ratio in digital holography using wavelet transform," *Optics and lasers in engineering*, vol. 46, no. 1, pp. 42–47, 2008.

[63] J. T. Sheridan and R. Patten, "Holographic interferometry and the fractional fourier transformation," *Optics letters*, vol. 25, no. 7, pp. 448–450, 2000.

[64] N. K. Nishchal, J. Joseph, and K. Singh, "Securing information using fractional fourier transform in digital holography," *Optics communications*, vol. 235, no. 4-6, pp. 253–259, 2004.

[65] J. C. Marron and K. S. Schroeder, "Three-dimensional lensless imaging using laser frequency diversity," *Applied optics*, vol. 31, no. 2, pp. 255–262, 1992.

[66] Z. Falgout, Y. Chen, and D. R. Guildenbecher, "Improving the spatial dynamic range of digital inline particle holography," *Applied optics*, vol. 58, no. 5, pp. A65–A73, 2019. [Online]. Available: https://doi.org/10.1364/AO.58.000A65

[67] Z. Huang and L. Cao, "Bicubic interpolation and extrapolation iteration method for high resolution digital holographic reconstruction," *Optics and Lasers in Engineering*, vol. 130, p. 106090, 2020. [Online]. Available: https://doi.org/10.1016/j.optlaseng.2020.106090

[68] R. W. Gerchberg, "A practical algorithm for the determination of plane from image and diffraction pictures," *Optik*, vol. 35, no. 2, pp. 237–246, 1972.

[69] J. R. Fienup, "Phase retrieval algorithms: a comparison," *Applied optics*, vol. 21, no. 15, pp. 2758–2769, 1982.

[70] F. Momey, L. Denis, T. Olivier, and C. Fournier, "From fienup's phase retrieval techniques to regularized inversion for in-line holography: tutorial," *JOSA A*, vol. 36, no. 12, pp. D62–D80, 2019.

[71] H. Xia, S. Montresor, R. Guo, J. Li, F. Olchewsky, J.-M. Desse, and P. Picart, "Robust processing of phase dislocations based on combined unwrapping and inpainting approaches," *Optics letters*, vol. 42, no. 2, pp. 322–325, 2017.

[72] R. M. Goldstein, H. A. Zebker, and C. L. Werner, "Satellite radar interferometry: Two-dimensional phase unwrapping," *Radio science*, vol. 23, no. 4, pp. 713–720, 1988.

[73] D. Zheng and F. Da, "A novel algorithm for branch cut phase unwrapping," *Optics and Lasers in Engineering*, vol. 49, no. 5, pp. 609–617, 2011.

[74] J. De Souza, M. Oliveira, and P. Dos Santos, "Branch-cut algorithm for optical phase unwrapping," *Optics letters*, vol. 40, no. 15, pp. 3456–3459, 2015.

[75] D. C. Ghiglia and L. A. Romero, "Minimum lp-norm two-dimensional phase unwrapping," *JOSA A*, vol. 13, no. 10, pp. 1999–2013, 1996.

[76] J. M. Dias and J. M. Leitão, "The z/spl pi/m algorithm: a method for interferometric image reconstruction in sar/sas," *IEEE Transactions on Image processing*, vol. 11, no. 4, pp. 408–422, 2002.

[77] M. Servin, F. J. Cuevas, D. Malacara, J. L. Marroquin, and R. Rodriguez-Vera, "Phase unwrapping through demodulation by use of the regularized phase-tracking technique," *Applied Optics*, vol. 38, no. 10, pp. 1934–1941, 1999.

[78] V. Katkovnik, J. Astola, and K. Egiazarian, "Phase local approximation (phasela) technique for phase unwrap from noisy data," *IEEE Transactions on Image Processing*, vol. 17, no. 6, pp. 833–846, 2008.

[79] J. C. Estrada, M. Servin, and J. A. Quiroga, "Noise robust linear dynamic system for phase unwrapping and smoothing," *Optics express*, vol. 19, no. 6, pp. 5126–5133, 2011.

[80] S. S. Gorthi and P. Rastogi, "Piecewise polynomial phase approximation approach for the analysis of reconstructed interference fields in digital holographic interferometry," *Journal of Optics A: Pure and Applied Optics*, vol. 11, no. 6, p. 065405, 2009.

[81] X. M. Xie and Q. N. Zeng, "Efficient and robust phase unwrapping algorithm based on unscented kalman filter, the strategy of quantizing paths-guided map, and pixel classification strategy," *Applied Optics*, vol. 54, no. 31, pp. 9294–9307, 2015.

[82] R. Kulkarni and P. Rastogi, "Simultaneous estimation of phase and its pth order derivatives," *Journal of Optics*, vol. 18, no. 5, p. 055603, 2016.

[83] O. Loffeld, H. Nies, S. Knedlik, and W. Yu, "Phase unwrapping for sar interferometry—a data fusion approach by kalman filtering," *IEEE Transactions on Geoscience and Remote Sensing*, vol. 46, no. 1, pp. 47–58, 2007.

[84] X. Xie, "Iterated unscented kalman filter for phase unwrapping of interferometric fringes," *Optics Express*, vol. 24, no. 17, pp. 18 872–18 897, 2016.

[85] X. Xie and G. Dai, "Unscented information filtering phase unwrapping algorithm for interferometric fringe patterns," *Applied Optics*, vol. 56, no. 34, pp. 9423–9434, 2017.

[86] R. Kulkarni and P. Rastogi, "Phase unwrapping algorithm using polynomial phase approximation and linear kalman filter," *Applied optics*, vol. 57, no. 4, pp. 702–708, 2018.

[87] D. C. Ghiglia and L. A. Romero, "Robust two-dimensional weighted and unweighted phase unwrapping that uses fast transforms and iterative methods," *JOSA A*, vol. 11, no. 1, pp. 107–117, 1994.

[88] X. Wang, S. Fang, and X. Zhu, "Weighted least-squares phase unwrapping algorithm based on a non-interfering image of an object," *Applied Optics*, vol. 56, no. 15, pp. 4543–4550, 2017.

[89] Z. Zhao, H. Zhao, L. Zhang, F. Gao, Y. Qin, and H. Du, "2d phase unwrapping algorithm for interferometric applications based on derivative zernike polynomial fitting technique," *Measurement Science and Technology*, vol. 26, no. 1, p. 017001, 2014.

[90] Y. Guo, X. Chen, and T. Zhang, "Robust phase unwrapping algorithm based on least squares," *Optics and Lasers in Engineering*, vol. 63, pp. 25–29, 2014.

[91] H. A. Aebischer and S. Waldner, "A simple and effective method for filtering speckle-interferometric phase fringe patterns," *Optics Communications*, vol. 162, no. 4-6, pp. 205–210, 1999.

[92] Q. Kemao, L. Feng, S. H. Soon *et al.*, "Comparative analysis on some filters for wrapped phase maps," *Applied optics*, vol. 46, no. 30, pp. 7412–7418, 2007.

[93] Q. Kemao, "Two-dimensional windowed fourier transform for fringe pattern analysis: principles, applications and implementations," *Optics and Lasers in Engineering*, vol. 45, no. 2, pp. 304–317, 2007.

[94] J. M. N. Leitão and M. A. T. Figueiredo, "Absolute phase image reconstruction: A stochastic nonlinear filtering approach," *IEEE Transactions on Image Processing*, vol. 7, no. 6, pp. 868–882, 1998.

[95] M. A. Navarro, J. C. Estrada, M. Servin, J. A. Quiroga, and J. Vargas, "Fast two-dimensional simultaneous phase unwrapping and low-pass filtering," *Optics Express*, vol. 20, no. 3, pp. 2556–2561, 2012.

[96] R. Kulkarni and P. Rastogi, "Simultaneous unwrapping and low pass filtering of continuous phase maps based on autoregressive phase model and wrapped kalman filtering," *Optics and Lasers in Engineering*, vol. 124, p. 105826, 2020.

[97] X. Su and W. Chen, "Reliability-guided phase unwrapping algorithm: a review," *Optics and Lasers in Engineering*, vol. 42, no. 3, pp. 245–261, 2004.

[98] S. Zhang, X. Li, and S. . Yau, "Multilevel quality-guided phase unwrapping algorithm for real-time three-dimensional shape reconstruction," *Applied Optics*, vol. 46, no. 1, pp. 50–57, 2007.

[99] Q. Kemao, W. Gao, and H. Wang, "Windowed fourier-filtered and quality-guided phase-unwrapping algorithm," *Applied optics*, vol. 47, no. 29, pp. 5420–5428, 2008.

[100] S. Li, X. Su, and W. Chen, "A new wavelet transform for reliability-guided phase unwrapping of optical fringe patterns," *Optics Communications*, vol. 284, no. 20, pp. 4879–4883, 2011.

[101] M. Zhao, L. Huang, Q. Zhang, X. Su, A. Asundi, and Q. Kemao, "Quality-guided phase unwrapping technique: Comparison of quality maps and guiding strategies," *Applied Optics*, vol. 50, no. 33, pp. 6214–6224, 2011.

[102] Y. Lu, W. Zhao, X. Zhang, W. Xu, and G. Xu, "Weighted-phase-gradient-based quality maps for two-dimensional quality-guided phase unwrapping," *Optics and Lasers in Engineering*, vol. 50, no. 10, pp. 1397–1404, 2012.

[103] H. Zhong, J. Tang, and S. Zhang, "Phase quality map based on local multi-unwrapped results for two-dimensional phase unwrapping," *Applied optics*, vol. 54, no. 4, pp. 739–745, 2015.

[104] H. Yu, Y. Lan, Z. Yuan, J. Xu, and H. Lee, "Phase unwrapping in insar: A review," *IEEE Geoscience and Remote Sensing Magazine*, vol. 7, no. 1, pp. 40–58, 2019.

[105] N. Pandey, A. Ghosh, and K. Khare, "Two-dimensional phase unwrapping using the transport of intensity equation," *Applied optics*, vol. 55, no. 9, pp. 2418–2425, 2016.

[106] R. R. Coifman and D. L. Donoho, "Translation-invariant de-noising," in *Wavelets and statistics*. Springer, 1995, pp. 125–150.

[107] D. Blinder, H. Ottevaere, A. Munteanu, and P. Schelkens, "Efficient multiscale phase unwrapping methodology with modulo wavelet transform," *Optics express*, vol. 24, no. 20, pp. 23 094–23 108, 2016.

[108] H. Y. Huang, L. Tian, Z. Zhang, Y. Liu, Z. Chen, and G. Barbastathis, "Path-independent phase unwrapping using phase gradient and total-variation (tv) denoising," *Optics express*, vol. 20, no. 13, pp. 14 075–14 089, 2012.

[109] F. Yang, T.-A. Pham, N. Brandenberg, M. P. Lütolf, J. Ma, and M. Unser, "Robust phase unwrapping via deep image prior for quantitative phase imaging," *IEEE Transactions on Image Processing*, vol. 30, pp. 7025–7037, 2021.

[110] X. Zhang, X. Zhang, M. Xu, H. Zhang, and X. Jiang, "Phase unwrapping in digital holography based on non-subsampled contourlet transform," *Optics Communications*, vol. 407, pp. 367–374, 2018.

[111] B. M. Hennelly and J. T. Sheridan, "Generalizing, optimizing, and inventing numerical algorithms for the fractional fourier, fresnel, and linear canonical transforms," *JOSA A*, vol. 22, no. 5, 2005.

[112] K. M. Molony, B. M. Hennelly, D. P. Kelly, and T. J. Naughton, "Reconstruction algorithms applied to in-line gabor digital holographic microscopy," *Optics Communications*, vol. 283, no. 6, 2010.

[113] T. Latychevskaia, F. Gehri, and H.-W. Fink, "Depth-resolved holographic reconstructions by three-dimensional deconvolution," *Optics express*, vol. 18, no. 21, pp. 22 527–22 544, 2010.

[114] T. Latychevskaia, "Iterative phase retrieval for digital holography," *JOSA A*, vol. 36, no. 12, 2019.

[115] T. Latychevskaia and H.-W. Fink, "Solution to the twin image problem in holography," *Physical review letters*, vol. 98, no. 23, 2007.

[116] M. A. Herráez, D. R. Burton, M. J. Lalor, and M. A. Gdeisat, "Fast two-dimensional phase-unwrapping algorithm based on sorting by reliability following a noncontinuous path," *Applied optics*, vol. 41, no. 35, pp. 7437–7444, 2002.

[117] J. M. Bioucas-Dias and G. Valadao, "Phase unwrapping via graph cuts," *IEEE Transactions on Image processing*, vol. 16, no. 3, pp. 698–709, 2007.

[118] I. Yamaguchi and T. Zhang, "Phase-shifting digital holography," *Optics letters*, vol. 22, no. 16, 1997.

[119] J. H. Bruning, D. R. Herriott, J. Gallagher, D. Rosenfeld, A. White, and D. Brangaccio, "Digital wavefront measuring interferometer for testing optical surfaces and lenses," *Applied optics*, vol. 13, no. 11, 1974.

[120] Y. Awatsuji, M. Sasada, and T. Kubota, "Parallel quasi-phase-shifting digital holography," *Applied physics letters*, vol. 85, no. 6, 2004.

[121] J. Millerd, N. Brock, J. Hayes, M. North-Morris, B. Kimbrough, and J. Wyant, "Pixelated phase-mask dynamic interferometers," in *Fringe 2005*. Springer, 2006.

[122] J. C. Wyant, "Dynamic interferometry," *Optics and photonics news*, vol. 14, no. 4, 2003.

[123] T. Shimobaba, Y. Sato, J. Miura, M. Takenouchi, and T. Ito, "Real-time digital holographic microscopy using the graphic processing unit," *Optics express*, vol. 16, no. 16, 2008.

[124] W. Bishara, T.-W. Su, A. F. Coskun, and A. Ozcan, "Lensfree on-chip microscopy over a wide field-of-view using pixel super-resolution," *Optics express*, vol. 18, no. 11, 2010.

[125] F. Merola, L. Miccio, M. Paturzo, A. Finizio, S. Grilli, and P. Ferraro, "Driving and analysis of micro-objects by digital holographic microscope in microfluidics," *Optics letters*, vol. 36, no. 16, 2011.

[126] L. Miccio, A. Finizio, R. Puglisi, D. Balduzzi, A. Galli, and P. Ferraro, "Dynamic dic by digital holography microscopy for enhancing phase-contrast visualization," *Biomedical optics express*, vol. 2, no. 2, 2011.

[127] V. Bianco, M. Paturzo, O. Gennari, A. Finizio, and P. Ferraro, "Imaging through scattering microfluidic channels by digital holography for information recovery in lab on chip," *Optics express*, vol. 21, no. 20, 2013.

[128] V. Bianco, M. Paturzo, A. Finizio, A. Calabuig, B. Javidi, and P. Ferraro, "Clear microfluidics imaging through flowing blood by digital holography," *IEEE Journal of Selected Topics in Quantum Electronics*, vol. 20, no. 3, 2013.

[129] A. Barroso, B. Kemper, S. Ketelhut, S. Graß, J. Reiber, and J. Schnekenburger, "Multimodal optical detection and toxicity testing of microplastics in the environment," in *Progress in Biomedical Optics and Imaging - Proceedings of SPIE*, vol. 10881, 2019.

[130] V. Kumar, G. S. Khan, and C. Shakher, "Phase contrast imaging of red blood cells using digital holographic interferometric microscope," *SPIE*, vol. 10453, 2017.

[131] O. B. Luro S., Potvin-Trottier L., "Isolating live cells after high-throughput, long-term, time-lapse microscopy," *Nature Methods*, vol. 17, 2020.

[132] M. Trusiak, J.-A. Picazo-Bueno, P. Zdankowski, and V. Micó, "Darkfocus: numerical autofocusing in digital in-line holographic microscopy using variance of computational dark-field gradient," *Optics and Lasers in Engineering*, vol. 134, p. 106195, 2020.

[133] J. Gillespie and R. A. King, "The use of self-entropy as a focus measure in digital holography," *Pattern recognition letters*, vol. 9, no. 1, pp. 19–25, 1989.

[134] L. Yu and L. Cai, "Iterative algorithm with a constraint condition for numerical reconstruction of a three-dimensional object from its hologram," *JOSA A*, vol. 18, no. 5, pp. 1033–1045, 2001.

[135] F. Dubois, C. Schockaert, N. Callens, and C. Yourassowsky, "Focus plane detection criteria in digital holography microscopy by amplitude analysis," *Optics Express*, vol. 14, no. 13, 2006.

[136] M. Liebling and M. Unser, "Autofocus for digital fresnel holograms by use of a fresnelet-sparsity criterion," *JOSA A*, vol. 21, no. 12, pp. 2424–2430, 2004.

[137] P. Memmolo, M. Paturzo, B. Javidi, P. A. Netti, and P. Ferraro, "Refocusing criterion via sparsity measurements in digital holography," *Optics letters*, vol. 39, no. 16, pp. 4719–4722, 2014.

[138] M. L. Tachiki, M. Itoh, and T. Yatagai, "Simultaneous depth determination of multiple objects by focus analysis in digital holography," *Applied optics*, vol. 47, no. 19, pp. D144–D153, 2008.

[139] H. A. Ilhan, M. Doğar, and M. Özcan, "Fast autofocusing in digital holography using scaled holograms," *Optics Communications*, vol. 287, pp. 81–84, 2013.

[140] M. Lyu, C. Yuan, D. Li, and G. Situ, "Fast autofocusing in digital holography using the magnitude differential," *Applied Optics*, vol. 56, no. 13, pp. F152–F157, 2017.

[141] M. León-Rodríguez, R. Rodríguez-Vera, J. A. Rayas, and J. Flores-Moreno, "One-shot dual-wavelength in-line digital holographic microscopy," *Optics and Lasers in Engineering*, vol. 51, no. 7, pp. 883–889, 2013.

[142] M. F. Toy, J. Kühn, S. Richard, J. Parent, M. Egli, and C. Depeursinge, "Accelerated autofocusing of off-axis holograms using critical sampling," *Optics letters*, vol. 37, no. 24, pp. 5094–5096, 2012.

[143] C. A. Trujillo and J. Garcia-Sucerquia, "Automatic method for focusing biological specimens in digital lensless holographic microscopy," *Optics letters*, vol. 39, no. 9, pp. 2569–2572, 2014.

[144] Y. Zhang, H. Wang, Y. Wu, M. Tamamitsu, and A. Ozcan, "Edge sparsity criterion for robust holographic autofocusing," *Optics Letters*, vol. 42, no. 19, pp. 3824–3827, 2017.

[145] H. Pinkard, Z. Phillips, A. Babakhani, D. A. Fletcher, and L. Waller, "Deep learning for single-shot autofocus microscopy," *Optica*, vol. 6, no. 6, pp. 794–797, 2019.

[146] H. Wang, Z. Dong, S. Wang, and Y. Lou, "Comparison of the refocus criteria for the phase, amplitude, and mixed objects in digital holography," *Optical Engineering*, vol. 57, no. 5, 2018.

[147] C. Zheng, Z. Shen, Q. Chang, Q. Su, X. Zhu, and X. Gao, "Experimental study on electrostatic precipitation of low-resistivity high-carbon fly ash at high temperature," *Energy & Fuels*, vol. 31, no. 6, pp. 6266–6273, 2017.

[148] P. Briard, J. Wang, and Y. Han, "Electromagnetic scattering of an aggregate of particles illuminated by an arbitrary shaped beam," in *AOPC 2015: Advances in Laser Technology and Applications*, vol. 9671. SPIE, 2015, pp. 219–225.

[149] G. Videen, E. Zubko, J. A. Arnold, B. MacCall, A. J. Weinberger, Y. Shkuratov, and O. Muñoz, "On the interpolation of light-scattering responses from irregularly shaped particles," *Journal of Quantitative Spectroscopy and Radiative Transfer*, vol. 211, pp. 123–128, 2018.

[150] M. R. Hajihashemi and H. Jiang, "Gaussian random ellipsoid geometry-based morphometric recovery of irregular particles using light scattering spectroscopy," *Journal of Quantitative Spectroscopy and Radiative Transfer*, vol. 118, pp. 86–95, 2013.

[151] A. J. Hickey and N. M. Concessio, "Descriptors of irregular particle morphology and powder properties," *Advanced drug delivery reviews*, vol. 26, no. 1, pp. 29–40, 1997.

[152] S. J. Blott and K. Pye, "Particle shape: a review and new methods of characterization and classification," *Sedimentology*, vol. 55, no. 1, pp. 31–63, 2008.

[153] J. W. Bullard and E. J. Garboczi, "Defining shape measures for 3d star-shaped particles: Sphericity, roundness, and dimensions," *Powder technology*, vol. 249, pp. 241–252, 2013.

[154] G. Bagheri, C. Bonadonna, I. Manzella, and P. Vonlanthen, "On the characterization of size and shape of irregular particles," *Powder Technology*, vol. 270, pp. 141–153, 2015.

[155] X. Wu, L. Shi, Z. Lin, Y. Wu, M. Brunel, J. Jacquot, and G. Gréhan, "Dual-beam interferometric particle imaging for size and shape characterization of irregular coal micro-particle: Validation with digital inline holography," *Journal of Quantitative Spectroscopy and Radiative Transfer*, vol. 241, p. 106728, 2020.

[156] C. Tropea, "Optical particle characterization in flows," *Annual Review of Fluid Mechanics*, vol. 43, pp. 399–426, 2011.

[157] H.-E. Albrecht, N. Damaschke, M. Borys, and C. Tropea, *Laser Doppler and phase Doppler measurement techniques*. Springer Science & Business Media, 2013.

[158] D. Asahina and M. Taylor, "Geometry of irregular particles: Direct surface measurements by 3-d laser scanner," *Powder technology*, vol. 213, no. 1-3, pp. 70–78, 2011.

[159] C. Lin and J. Miller, "3d characterization and analysis of particle shape using x-ray microtomography (xmt)," *Powder Technology*, vol. 154, no. 1, pp. 61–69, 2005.

[160] J. Katz and J. Sheng, "Applications of holography in fluid mechanics and particle dynamics," *Annual Review of Fluid Mechanics*, vol. 42, no. 1, pp. 531–555, 2010.

[161] M. J. Berg and G. Videen, "Digital holographic imaging of aerosol particles in flight," *Journal of Quantitative Spectroscopy and Radiative Transfer*, vol. 112, no. 11, pp. 1776–1783, 2011.

[162] A. Wang, T. G. Dimiduk, J. Fung, S. Razavi, I. Kretzschmar, K. Chaudhary, and V. N. Manoharan, "Using the discrete dipole approximation and holographic microscopy to measure rotational dynamics of non-spherical colloidal particles," *Journal of Quantitative Spectroscopy and Radiative Transfer*, vol. 146, pp. 499–509, 2014.

[163] G. König, K. Anders, and A. Frohn, "A new light-scattering technique to measure the diameter of periodically generated moving droplets," *Journal of aerosol science*, vol. 17, no. 2, pp. 157–167, 1986.

[164] A. Glover, S. Skippon, and R. Boyle, "Interferometric laser imaging for droplet sizing: a method for droplet-size measurement in sparse spray systems," *Applied optics*, vol. 34, no. 36, pp. 8409–8421, 1995.

[165] S. Dehaeck and J. Van Beeck, "Multifrequency interferometric particle imaging for gas bubble sizing," *Experiments in fluids*, vol. 45, no. 5, pp. 823–831, 2008.

[166] J. Shen, H. Wang, B. Wang, H. Yu, and B. Yu, "Stability in debye series calculation for light scattering by absorbing particles and bubbles," *Journal of Quantitative Spectroscopy and Radiative Transfer*, vol. 111, no. 5, pp. 772–781, 2010.

[167] L. Qieni, H. Kan, G. Baozhen, and W. Xiang, "High-accuracy simultaneous measurement of particle size and location using interferometric out-of-focus imaging," *Optics express*, vol. 24, no. 15, pp. 16 530–16 543, 2016.

[168] J. Sun, H. Zhang, Z. Li, D. Jia, T. Liu, and M. Zhai, "Determining speckle orientation of interferometric out-of-focus images," *Journal of Quantitative Spectroscopy and Radiative Transfer*, vol. 226, pp. 73–80, 2019.

[169] T. Kobayashi, T. Kawaguchi, and M. Maeda, "Measurement of spray flow by an improved interferometric laser imaging droplet sizing (ilids) system," *Department of System Design Engineering, Japan*, 2000.

[170] H. Shen, S. Coetmellec, and M. Brunel, "Cylindrical interferometric out-of-focus imaging for the analysis of droplets in a volume," *Optics letters*, vol. 37, no. 19, pp. 3945–3947, 2012.

[171] ——, "Simultaneous 3d location and size measurement of spherical bubbles using cylindrical interferometric out-of-focus imaging," *Journal of Quantitative Spectroscopy and Radiative Transfer*, vol. 131, pp. 153–159, 2013.

[172] M. Brunel, S. G. Ruiz, J. Jacquot, and J. van Beeck, "On the morphology of irregular rough particles from the analysis of speckle-like interferometric out-of-focus images," *Optics Communications*, vol. 338, pp. 193–198, 2015.

[173] Y. Wu, Z. Lin, X. Wu, and K. Cen, "Dual-beam interferometric particle imaging for size measurement of opaque metal droplet," *Powder Technology*, vol. 356, pp. 31–38, 2019.

[174] S. Shao, K. Mallery, and J. Hong, "Machine learning holography for measuring 3d particle distribution," *Chemical Engineering Science*, vol. 225, p. 115830, 2020.

[175] C. Li, R. Panday, X. Gao, J. Hong, and W. A. Rogers, "Measuring particle dynamics in a fluidized bed using digital in-line holography," *Chemical Engineering Journal*, vol. 405, p. 126824, 2021.

[176] S. Prasad, C. Schweizer, P. Bagaria, A. Saini, W. D. Kulatilaka, and C. V. Mashuga, "Investigation of particle density on dust cloud dynamics in a minimum ignition energy apparatus using digital in-line holography," *Powder Technology*, vol. 384, pp. 297–303, 2021.

[177] S. Li, Y. Zhao, and Y. Ye, "Improved minimum intensity projection in holographic reconstruction via snr-enhanced holography," *Journal of Modern Optics*, vol. 68, no. 6, pp. 322–326, 2021.

[178] D. R. Guildenbecher, J. Gao, P. L. Reu, and J. Chen, "Digital holography simulations and experiments to quantify the accuracy of 3d particle location and 2d sizing using a proposed hybrid method," *Applied optics*, vol. 52, no. 16, pp. 3790–3801, 2013. [Online]. Available: https://doi.org/10.1364/AO.52.003790

[179] E. Porcheron, P. Lemaitre, J. Van Beeck, R. Vetrano, M. Brunel, G. Grehan, and L. Guiraud, "Development of a spectrometer for airborne measurement of droplet sizes in clouds," *Journal of the European Optical Society-Rapid publications*, vol. 10, 2015.

[180] Y.-C. Chen, C.-S. Kuo, Z.-Z. Wang, H.-Y. Lei, C.-H. Yang, and C.-H. Huang, "Lens-free holographic microscopy for complete blood analysis on a chip," in *Optical Diagnostics and Sensing XX: Toward Point-of-Care Diagnostics*, vol. 11247. International Society for Optics and Photonics, 2020.

[181] M. Kumar, X. Quan, Y. Awatsuji, C. Cheng, M. Hasebe, Y. Tamada, and O. Matoba, "Common-path multimodal three-dimensional fluorescence and phase imaging system," *Journal of Biomedical Optics*, vol. 25, no. 3, 2020.

[182] A. Ghosh, R. Kulkarni, C. B. Gupt, and S. Sekharan, "Improved particle size estimation in digital in-line holography based on fienup's iterative algorithm," *Asian Journal of Physics*, vol. 30, no. 10-11, pp. 1437–1446, 2022.

[183] P. C. Hansen, "Deconvolution and regularization with toeplitz matrices," *Numerical Algorithms*, vol. 29, no. 4, pp. 323–378, 2002.

[184] W. Zhang, H. Zhang, L. Cao, M. E. Gehm, Q. Jiang, D. J. Brady, and G. Jin, "Resolution and sampling analysis in digital in-line holography with spherical wave illumination," *Optical Engineering*, vol. 59, no. 10, p. 102402, 2019.

[185] X. Zhang and X. Wu, "Image interpolation by adaptive 2-d autoregressive modeling and soft-decision estimation," *IEEE transactions on image processing*, vol. 17, no. 6, pp. 887–896, 2008. [Online]. Available: http://doi.org/10.1109/TIP.2008.924279

[186] A. Ghosh and R. Kulkarni, "Improving particle detection and size estimation accuracy in digital in-line holography using autoregressive interpolation," *Applied Optics*, vol. 60, no. 28, pp. 8728–8736, 2021.

[187] T. Latychevskaia and H.-W. Fink, "Practical algorithms for simulation and reconstruction of digital in-line holograms," *Applied optics*, vol. 54, no. 9, pp. 2424–2434, 2015.

[188] P. Rastogi and E. Hack, *Phase estimation in optical interferometry*. CRC Press, 2014.

[189] S. Wu, L. Zhu, S. Pan, and L. Yang, "Spatiotemporal three-dimensional phase unwrapping in digital speckle pattern interferometry," *Optics letters*, vol. 41, no. 5, pp. 1050–1053, 2016.

[190] M. Jenkinson, "Fast, automated, n-dimensional phase-unwrapping algorithm," *Magnetic Resonance in Medicine: An Official Journal of the International Society for Magnetic Resonance in Medicine*, vol. 49, no. 1, pp. 193–197, 2003.

[191] B. Osmanoğlu, F. Sunar, S. Wdowinski, and E. Cabral-Cano, "Time series analysis of insar data: Methods and trends," *ISPRS Journal of Photogrammetry and Remote Sensing*, vol. 115, pp. 90–102, 2016.

[192] R. Bamler and P. Hartl, "Synthetic aperture radar interferometry," *Inverse problems*, vol. 14, no. 4, p. R1, 1998.

[193] X. Su and Q. Zhang, "Dynamic 3-d shape measurement method: a review," *Optics and Lasers in Engineering*, vol. 48, no. 2, pp. 191–204, 2010.

[194] K. Itoh, "Analysis of the phase unwrapping algorithm," *Applied optics*, vol. 21, no. 14, pp. 2470–2470, 1982.

[195] D. C. Ghiglia and M. D. Pritt, *Two-Dimensional Phase Unwrapping: Theory, Algorithms, and Software*. Wiley, 1998.

[196] E. Zappa and G. Busca, "Comparison of eight unwrapping algorithms applied to fourier-transform profilometry," *Optics and Lasers in Engineering*, vol. 46, no. 2, pp. 106–116, 2008.

[197] B. Spottiswoode, "2d phase unwrapping algorithms," *MATLAB Cent File Exch*, vol. 12, no. 2, 2008.

[198] A. Ghosh, R. Kulkarni, and R. Gannavarpu, "Phase unwrapping algorithm using breadth-first-search and multi-level segmentation of phase quality interval in digital holography," *Journal of Modern Optics*, vol. 69, no. 16, pp. 957–967, 2022.

[199] T. H. Cormen, C. E. Leiserson, R. L. Rivest, and C. Stein, *Introduction to Algorithms, Third Edition*, 3rd ed. The MIT Press, 2009.

[200] L. L. García, A. G. Arellano, and W. Cruz-Santos, "A parallel path-following phase unwrapping algorithm based on a top-down breadth-first search approach," *Optics and Lasers in Engineering*, vol. 124, p. 105827, 2020.

[201] S. Montresor and P. Picart, "Quantitative appraisal for noise reduction in digital holographic phase imaging," *Optics Express*, vol. 24, no. 13, pp. 14 322–14 343, 2016.

[202] A. Vishnoi and R. Gannavarpu, "Single shot quantitative phase gradient estimation using wigner-ville distribution in digital holographic microscopy," *OSA Continuum*, vol. 4, no. 9, pp. 2452–2459, 2021.

[203] C. . Wee and R. Paramesran, "Image sharpness measure using eigenvalues," in *International Conference on Signal Processing Proceedings, ICSP*, 2008, pp. 840–843.

[204] A. Ghosh, R. Kulkarni, and P. K. Mondal, "Autofocusing in digital holography using eigenvalues," *Applied Optics*, vol. 60, no. 4, pp. 1031–1040, 2021.

[205] A. Ghosh and R. Kulkarni, "Autofocusing in digital holography based on eigenvalue distribution," in *Sensors and Sensing congress*. Optical Society of America, 2021, pp. JTu5A–32.

[206] J. Kennedy, *Particle Swarm Optimization*. Boston, MA: Springer US, 2010, pp. 760–766.

[207] P. Langehanenberg, B. Kemper, D. Dirksen, and G. Von Bally, "Autofocusing in digital holographic phase contrast microscopy on pure phase objects for live cell imaging," *Applied optics*, vol. 47, no. 19, pp. D176–D182, 2008.

[208] S. Rathod, A. Ghosh, and R. Kulkarni, "Fast and accurate autofocusing algorithm in digital holography based on particle swarm optimization," *Optik*, vol. 247, p. 167946, 2021.

[209] Y. Li and Y. Zhang, "Hyper-parameter estimation method with particle swarm optimization," *arXiv preprint arXiv:2011.11944*, 2020.

[210] S. Shao, K. Mallery, and J. Hong, "Machine learning holography for measuring 3d particle distribution," *Chemical Engineering Science*, vol. 225, 2020. [Online]. Available: https://doi.org/10.1016/j.ces.2020.115830

[211] C. Li, R. Panday, X. Gao, J. Hong, and W. A. Rogers, "Measuring particle dynamics in a fluidized bed using digital in-line holography," *Chemical Engineering Journal*, vol. 405, 2021. [Online]. Available: https://doi.org/10.1016/j.cej.2020.126824

[212] L. Denis, C. Fournier, T. Fournel, C. Ducottet, and D. Jeulin, "Direct extraction of the mean particle size from a digital hologram," *Applied Optics*, vol. 45, no. 5, pp. 944–952, 2006. [Online]. Available: https://doi.org/10.1364/AO.45.000944

[213] S. Soontaranon, J. Widjaja, and T. Asakura, "Extraction of object position from in-line holograms by using single wavelet coefficient," *Optics communications*, vol. 281, no. 6, pp. 1461–1467, 2008. [Online]. Available: https://doi.org/10.1016/j.optcom.2007.11.027

[214] T. Khanam, E. Darakis, A. Rajendran, V. Kariwala, A. K. Asundi, and T. J. Naughton, "On-line digital holographic measurement of size and shape of microparticles for crystallization processes," in *Ninth International Symposium on Laser Metrology*, vol. 7155. International Society for Optics and Photonics, 2008, p. 71551K. [Online]. Available: https://doi.org/10.1117/12.814557

[215] E. Darakis, T. Khanam, A. Rajendran, V. Kariwala, T. J. Naughton, and A. K. Asundi, "Microparticle characterization using digital holography," *Chemical Engineering Science*, vol. 65, no. 2, pp. 1037–1044, 2010. [Online]. Available: https://doi.org/10.1016/j.ces.2009.09.057

[216] T. Khanam, M. N. Rahman, A. Rajendran, V. Kariwala, and A. K. Asundi, "Accurate size measurement of needle-shaped particles using digital holography," *Chemical engineering science*, vol. 66, no. 12, pp. 2699–2706, 2011. [Online]. Available: https://doi.org/10.1016/j.ces.2011.03.026

[217] J. Sheng, E. Malkiel, and J. Katz, "Digital holographic microscope for measuring three-dimensional particle distributions and motions," *Applied optics*, vol. 45, no. 16, pp. 3893–3901, 2006. [Online]. Available: https://doi.org/10.1364/AO.45.003893

[218] D. K. Singh and P. Panigrahi, "Improved digital holographic reconstruction algorithm for depth error reduction and elimination of out-of-focus particles," *Optics Express*, vol. 18, no. 3, pp. 2426–2448, 2010. [Online]. Available: https://doi.org/10.1364/OE.18.002426

[219] L. Tian, N. Loomis, J. A. Domínguez-Caballero, and G. Barbastathis, "Quantitative measurement of size and three-dimensional position of fast-moving bubbles in air-water mixture flows using digital holography," *Applied optics*, vol. 49, no. 9, pp. 1549–1554, 2010. [Online]. Available: https://doi.org/10.1364/AO.49.001549

[220] V. Ilchenko, T. Lex, and T. Sattelmayer, "Depth position detection of the particles in digital holographic particle image velocimetry (dhpiv)," in *Fundamental Problems of Optoelectronics and Microelectronics II*, vol. 5851. International Society for Optics and Photonics, 2005, pp. 123–128. [Online]. Available: https://doi.org/10.1117/12.634069

[221] J. P. Fugal, T. J. Schulz, and R. A. Shaw, "Practical methods for automated reconstruction and characterization of particles in digital in-line holograms," *Measurement Science and Technology*, vol. 20, no. 7, p. 075501, 2009. [Online]. Available: https://doi.org/10.1088/0957-0233/20/7/075501

[222] J. Gao, D. R. Guildenbecher, P. L. Reu, and J. Chen, "Uncertainty characterization of particle depth measurement using digital in-line holography and the hybrid method," *Optics express*, vol. 21, no. 22, pp. 26 432–26 449, 2013. [Online]. Available: https://doi.org/10.1364/OE.21.026432

[223] D. R. Guildenbecher, P. L. Reu, H. L. Stuaffacher, and T. Grasser, "Accurate measurement of out-of-plane particle displacement from the cross correlation of sequential digital in-line holograms," *Optics letters*, vol. 38, no. 20, pp. 4015–4018, 2013. [Online]. Available: http://doi.org/10.1364/OL.38.004015

[224] J. Huang, S. Li, Y. Zi, Y. Qian, W. Cai, M. Aldén, and Z. Li, "Clustering-based particle detection method for digital holography to detect the three-dimensional location and in-plane size of particles," *Measurement Science and Technology*, vol. 32, no. 5, p. 055205, 2021.

[225] G. Pan and H. Meng, "Digital holography of particle fields: reconstruction by use of complex amplitude," *Applied optics*, vol. 42, no. 5, pp. 827–833, 2003.

[226] H. Y. Yudhbir and Y. Honjo, "Application of geotechnical engineering to environmental control," *Theme lecture*, vol. 5, no. 9, pp. 431–469, 1991.

[227] M. Winter and B. Clarke, "Improved use of pulverised fuel ash as general fill," *Proceedings of the Institution of Civil Engineers-Geotechnical Engineering*, vol. 155, no. 2, pp. 133–141, 2002.

[228] S. H. Lee, E. Sakai, M. Daimon, and W. K. Bang, "Characterization of fly ash directly collected from electrostatic precipitator," *Cement and concrete research*, vol. 29, no. 11, pp. 1791–1797, 1999.

[229] S. K. Das *et al.*, "Geotechnical properties of low calcium and high calcium fly ash," *Geotechnical & Geological Engineering*, vol. 24, no. 2, pp. 249–263, 2006.

[230] S. Baskar and M. Murali Krishna, "Innovative studies on the potential use of pond ash on large scale in building & construction sectors," *International Journal of Civil Engineering and Technology*, vol. 9, no. 5, pp. 766–770, 2018.

[231] D. ASTM *et al.*, *Standard test method for particle-size analysis of soils*. West Conshohocken, PA, 2007.

[232] T.-M. Chen, C.-J. Tsai, S.-Y. Yan, and S.-N. Li, "An efficient wet electrostatic precipitator for removing nanoparticles, submicron and micron-sized particles," *Separation and Purification Technology*, vol. 136, pp. 27–35, 2014.

[233] Y. Xu, X. Liu, J. Cui, D. Chen, M. Xu, S. Pan, K. Zhang, and X. Gao, "Field measurements on the emission and removal of pm2. 5 from coal-fired power stations: 4. pm removal performance of wet electrostatic precipitators," *Energy & Fuels*, vol. 30, no. 9, pp. 7465–7473, 2016.

[234] Z. Sui, Y. Zhang, Y. Peng, P. Norris, Y. Cao, and W.-P. Pan, "Fine particulate matter emission and size distribution characteristics in an ultra-low emission power plant," *Fuel*, vol. 185, pp. 863–871, 2016.

[235] A. Bologa, H.-R. Paur, M. Lehner, H. Seifert, T. Wascher, and K. Woletz, "Collection of fine particles by novel wet electrostatic precipitator," *IEEE Transactions on Industry Applications*, vol. 45, no. 6, pp. 2170–2177, 2009.

[236] P. K. Mandal and A. Bandyopadhyay, "Characterizing fly ash particles followed by prediction of removal efficiencies of fly ash and co2 in an indian wet esp," *Journal of environmental chemical engineering*, vol. 4, no. 1, pp. 167–177, 2016.

[237] F. Verpillat, F. Joud, P. Desbiolles, and M. Gross, "Dark-field digital holographic microscopy for 3d-tracking of gold nanoparticles," *Optics express*, vol. 19, no. 27, pp. 26 044–26 055, 2011.

[238] P. AntonioáNetti *et al.*, "Imaging adherent cells in the microfluidic channel hidden by flowing rbcs as occluding objects by a holographic method," *Lab on a Chip*, vol. 14, no. 14, pp. 2499–2504, 2014.

[239] H. B. Evans, S. Gorumlu, B. Aksak, L. Castillo, and J. Sheng, "Holographic microscopy and microfluidics platform for measuring wall stress and 3d flow over surfaces textured by micro-pillars," *Scientific reports*, vol. 6, no. 1, pp. 1–12, 2016.

[240] A. Brodoline, N. Rawat, D. Alexandre, N. Cubedo, and M. Gross, "4d compressive sensing holographic microscopy imaging of small moving objects," *Optics Letters*, vol. 44, no. 11, pp. 2827–2830, 2019.

[241] M. Kumar, X. Quan, Y. Awatsuji, C. Cheng, M. Hasebe, Y. Tamada, and O. Matoba, "Common-path multimodal three-dimensional fluorescence and phase imaging system," *Journal of Biomedical Optics*, vol. 25, no. 3, p. 032010, 2020.

[242] A. Greenbaum, W. Luo, T.-W. Su, Z. Göröcs, L. Xue, S. O. Isikman, A. F. Coskun, O. Mudanyali, and A. Ozcan, "Imaging without lenses: achievements and remaining challenges of wide-field on-chip microscopy," *Nature methods*, vol. 9, no. 9, pp. 889–895, 2012.

[243] A. Ozcan and E. McLeod, "Lensless imaging and sensing," *Annual review of biomedical engineering*, vol. 18, pp. 77–102, 2016.

[244] E. McLeod and A. Ozcan, "Unconventional methods of imaging: computational microscopy and compact implementations," *Reports on Progress in Physics*, vol. 79, no. 7, p. 076001, 2016.

[245] Y. Wu and A. Ozcan, "Lensless digital holographic microscopy and its applications in biomedicine and environmental monitoring," *Methods*, vol. 136, pp. 4–16, 2018.

[246] U. Schnars and W. Jüptner, "Direct recording of holograms by a ccd target and numerical reconstruction," *Applied Optics*, vol. 33, no. 2, pp. 179–181, 1994.

[247] R. Luo and L. Wang, "Liquid velocity distribution in slug flow in a microchannel," *Microfluidics and nanofluidics*, vol. 12, no. 1, pp. 581–595, 2012.

[248] B. Skarman, K. Wozniak, and J. Becker, "Digital in-line holography for the analysis of bénard-convection," *Flow Measurement and Instrumentation*, vol. 10, no. 2, pp. 91–97, 1999.

[249] S. J. Lee and S. Kim, "Advanced particle-based velocimetry techniques for microscale flows," *Microfluidics and Nanofluidics*, vol. 6, no. 5, pp. 577–588, 2009.

[250] X. WU, X. PU, S. PU, Z. YUAN, and K. CEN, "Particle sizing for gas-solids flow with digital in-line holography," *Journal of Chemical Industry and Engineering (China)*, 2009.

[251] M. N. Rahman, A. Rajendran, V. Kariwala, and A. K. Asundi, "Effect of particle concentration and turbidity on particle characterization using digital holography," *Chemical Engineering Research and Design*, vol. 92, no. 2, pp. 249–255, 2014.

[252] A. (D854-92), "Standard test method for specific gravity of soils," 1984.

[253] A. B. Cerato and A. J. Lutenegger, "Determination of surface area of fine-grained soils by the ethylene glycol monoethyl ether (egme) method," *Geotechnical Testing Journal*, vol. 25, no. 3, pp. 315–321, 2002.

[254] D. A. Horneck, J. M. Hart, K. Topper, and B. Koepsell, *Methods of soil analysis used in the soil testing laboratory at Oregon State University*. Oregon State University, 1989.

[255] H. Chapman, "Cation-exchange capacity," *Methods of soil analysis: Part 2 Chemical and microbiological properties*, vol. 9, pp. 891–901, 1965.

[256] M. Instruments, *Brochure for Mastersizer 2000 Particle Size Analyzer*. M Instruments, 2006.

[257] Y. Shen, S. Lou, and X. Wang, "Estimation method of point spread function based on kalman filter for accurately evaluating real optical properties of photonic crystal fibers," *Applied optics*, vol. 53, no. 9, pp. 1838–1845, 2014.